

9-1-1993

Synthetic image generator model: Application of specular and diffuse reflectivity components and performance evaluation in the visible region

Richard Stark

Follow this and additional works at: <http://scholarworks.rit.edu/theses>

Recommended Citation

Stark, Richard, "Synthetic image generator model: Application of specular and diffuse reflectivity components and performance evaluation in the visible region" (1993). Thesis. Rochester Institute of Technology. Accessed from

This Thesis is brought to you for free and open access by the Thesis/Dissertation Collections at RIT Scholar Works. It has been accepted for inclusion in Theses by an authorized administrator of RIT Scholar Works. For more information, please contact ritscholarworks@rit.edu.

Synthetic Image Generator Model:
Application of
Specular and Diffuse Reflectivity Components
and
Performance Evaluation in the Visible Region

by
Richard B. Stark

A thesis submitted in partial fulfillment of the
requirements for the degree of Master of Science
in the Center for Imaging Science in the
College of Imaging Arts and Sciences
of the Rochester Institute of Technology

September 1993

Signature of the Author Richard B. Stock

Accepted by Dana G. Marsh

Sept 30, 1993
Coordinator, M.S. Degree Program

COLLEGE OF IMAGING ARTS AND SCIENCES
ROCHESTER INSTITUTE OF TECHNOLOGY
ROCHESTER, NEW YORK

CERTIFICATE OF APPROVAL

M.S. DEGREE THESIS

The M.S. Degree Thesis of Richard Stark
has been examined and approved by the
thesis committee as satisfactory for the
thesis requirement for the
Master of Science degree

Dr. John Schott, Thesis Advisor

Dr. Mark Fairchild

Mr. Carl Salvaggio

9/29/93

Date

THESIS RELEASE PERMISSION
ROCHESTER INSTITUTE OF TECHNOLOGY
COLLEGE OF IMAGING ARTS AND SCIENCES

Title of Thesis

Synthetic Image Generator Model:
Application of Specular and Diffuse Reflectivity Components
and
Performance Evaluation in the Visible Region

I, Richard B. Stark, hereby grant permission to the Wallace Memorial Library of R.I.T. to reproduce my thesis in whole or in part. Any reproduction will not be for commercial use or profit.

Signature: _____

Date: 17 Sep 93

Abstract

This study focused on the operation of the RIT Digital Imaging and Remote Sensing Lab's synthetic image generation (DIRSIG) software model in the 0.4 to 1.0 μm wavelength region. The overall intent was to create a baseline for future DIRSIG activity. This was achieved by modifying the infrared based software to account for the characteristics of visible energy, and then evaluating the model's overall performance. A modification was made to the model's radiance algorithm by dividing surface reflectivity into a combination of view angle dependent diffuse and specular components. Additionally a practical method was developed for generating these values. Performance evaluation of the model was accomplished by collecting truth data from an actual scene, generating an applicable reflectivity database, synthetically generating images of the scene, and then comparing the image data with the truth data. The generated images provided a good representation of the visible energy interactions occurring in a scene.

Acknowledgements

Over the course of 14 months, during different phases of this study, many people have provided crucial assistance.

I would like to thank:

my committee members,

the people involved in the Digital Imaging and Remote Sensing Laboratory,

my co-workers at Eastman Kodak, and

the US Air Force.

In particular, I'm grateful to:

Dr John Mason,
Mr Carl Salvaggio,
Mr Xiofan Feng,
Mr Rolando Raqueno,
Mr Tim Gallagher,
Ms Carolyn Kitchen, and
Ms Lisa Reniff.

Dedication

This work is dedicated to

Jennifer,
Regan,
and
Tierney

Table of Contents

1.	Introduction.....	1
2.	Background.....	3
2.1.	Synthetic Image Generation Modeling.....	3
2.1.1	Applications.....	4
2.1.2	Modeling of Environment.....	5
2.1.3	Ray Tracing and Radiosity.....	8
2.2.	Reflectivity Review.....	11
2.3.	Reflectivity in Existing Visible SIG Models...	17
2.4.	Obtaining Reflectivity Values.....	21
2.4.1	Actual Measurements.....	21
2.4.2	Reflection Models.....	23
2.4.3	Hybrid Approach.....	27
2.5.	DIRS Lab SIG.....	29
2.5.1	Scene Geometry Submodel.....	31
2.5.2	Ray Tracer Submodel.....	33
2.5.3	Radiometry Submodel.....	36
2.6.	DIRSIG and Reflectivity.....	41
3.	Objectives and Approach.....	43
4.	Modified DIRSIG Radiance Algorithm.....	45
5.	Reflectivity Components.....	51
5.1.	Surface Reflection Characteristics Observed in In-Plane Plots.....	52
5.2.	Characterizations of Surface Samples for this Study.....	59
5.3.	Generation of Reflectivity Components.....	69
5.3.1	Generating $R_d'(\theta_v)$	74
5.3.2	Generating $R_s'(\theta_v)$	79
5.3.3	Results of Generation of $R_d'(\theta_v)$ and $R_s'(\theta_v)$	80
5.3.4	Calculation of Diffuseness and Specularity.....	84
5.4.	Assessment of Reflectance Generation Method...	87
5.5.	Models for Non-BDRF Measured Surfaces.....	90

6.	Obtaining Truth Data.....	96
6.1.	The Scene.....	96
6.2.	Collection of Data.....	100
6.3.	Equipment Calibration.....	104
7.	Assessment of DIRSIG's Sensitivity of Radiance Reaching the Sensor.....	106
7.1.	Comparison of Truth and DIRSIG Parameters....	106
7.2.	Error Propagation.....	116
7.3.	Error Propagation Results.....	119
8.	DIRSIG Image Evaluation.....	123
8.1.	Quantitative Assessment.....	125
8.1.1	Comparison of Calibrated Image Pixel Values.....	125
8.1.2	Comparison of Corrected Image Pixel Values.....	131
8.1.3	Time Trend Comparisons in Image Pixel Values.....	136
8.2.	Qualitative Observations of Images.....	144
8.2.1	Observations of General Limitations..	144
8.2.2	Observations of Specific Phenomenon..	148
9.	Conclusions.....	154
9.1.	Summary.....	154
9.2.	Recommendations.....	158
9.3.	Closing.....	159
	References.....	161
	Appendix.....	164

List of Figures

<u>Figure</u>	<u>Title</u>	<u>Page</u>
2.1	Energy Interactions Within a Scene	6
2.2	Spectral Plots of Solar Energy Atmospheric Interaction	8
2.3	Sample Rays Within Ray Tracing	9
2.4	Incident Irradiance (E_i) and Reflected Radiance (L_r)	12
2.5	Geometric Relations of BRDF	13
2.6	Hemispherical-Directional Reflectivity	14
2.7	Reflectivity Characteristics	16
2.8	Surface Roughness	17
2.9	Phong Model Geometry	24
2.10	Light Intensity Distribution	26
2.11	Zero Bi-Static Measurement Geometry	28
2.12	Submodel Interactions Within DIRSIG	30
2.13	Facet Subnodes	31
2.14	Attribute Subnodes	32
2.15	Material Subnodes	32
2.16	Ideal Ray Tracer Assessments	34
2.17	Current Ray Tracer Assessments	35
2.18	Angles in Radiometric Equations	38
2.19	Four General Ray Tracer Interactions	38
4.1	Specular Acceptance Cone for Solar Illumination	49
4.2	Background Reflected Downwelling Illumination	50
5.1.a	Strong Specular Characteristics	54

<u>Figure</u>	<u>Title</u>	<u>Page</u>
5.1.b	Strong Directional Diffuse Characteristics	54
5.1.c	Strong Uniform Diffuse Characteristics	54
5.1.d	Grazing Angle Characteristics of Diffuse Surfaces	54
5.2.a	In-Plane BDRF of Roofing Material (@ 0 deg)	57
5.2.b	In-Plane BDRF of Roofing Material (@ 30 deg)	57
5.2.c	In-Plane BDRF of Roofing Material (@ 60 deg)	57
5.2.d	Hemispheric BDRF of Roofing Material	57
5.3.a	In-Plane BDRF of Sandpaper (@ 0 deg)	58
5.3.b	In-Plane BDRF of Sandpaper (@ 30 deg)	58
5.3.c	In-Plane BDRF of Sandpaper (@ 60 deg)	58
5.3.d	Hemispheric BDRF of Sandpaper	58
5.4	Angle Definition for In-Plane Scans	59
5.5	In-Plane BDRF Measurements of Green Panel Sample	62
5.6	In-Plane BDRF Measurements of White Panel Sample	63
5.7	In-Plane BDRF Measurements of Specular Panel Sample	64
5.8	Out-of-Plane BDRF Measurements of Green Panel Sample	66
5.9	Out-of-Plane BDRF Measurements of White Panel Sample	67
5.10	Out-of-Plane BDRF Measurements of Specular Panel Sample	68
5.11	Representation of DIRSIG Energy Assessment	70
5.11.A	Reflected Energy Assessment	73
5.12	Points used for Averaging to Determine $R_d'(\theta_v)$	76

<u>Figure</u>	<u>Title</u>	<u>Page</u>
5.13	A Look at Reflectivity Reciprocity	77
5.14	Reflectivity Components for Green Sample	81
5.15	Reflectivity Components for White Sample	82
5.16	Reflectivity Components for Specular Sample	83
5.17	Hemispherical-Directional Reflectivity Values for Subset of Samples	88
5.18	Model-Derived Reflectivity Components for Pavement	95
6.1	Top View of Scene	96
6.2	Side View of Scene	97
6.3	Illumination Angles of Truth Data	101
6.4	Measurement of Directional Downwelled Radiance	102
6.5	Sketch of Radiometer Placement for In-Scene Measurement	103
7.1	Measured Directional Downwelled Radiance vs LOWTRAN7's Calculated Directional Downwelled Radiance (in BLUE Band)	109
7.2	Measured Directional Downwelled Radiance vs LOWTRAN7's Calculated Directional Downwelled Radiance (in GREEN Band)	110
7.3	Measured Directional Downwelled Radiance vs LOWTRAN7's Calculated Directional Downwelled Radiance (in RED Band)	111
7.4	Percent RMS Error vs Time of Day for Both Directional and Hemispherical Downwelled Radiance	113
7.5	Relationship Establishing Upwelled Radiance and Atmospheric Transmission	114
8.1	Map of Digital Count Extraction Points	124
8.2	Calibrated Synthetic DC vs Truth DC	126

<u>Figure</u>	<u>Title</u>	<u>Page</u>
8.3	Corrected Synthetic DC vs Truth DC	132
8.4.A	Overall RMS Digital Count Error	133
8.4.B	Overall RMS Relative Reflectivity Error	134
8.5	Trend in Incident Energy for Green Band	137
8.6	Trend in Reflected Energy for Green Band	138
8.7	Digital Count Trends for Grey Level 3 Panel	140
8.8	Digital Count Trends for Specular Panel's Light and Dark Halves	141
8.9	Digital Count Trend for Top of White Panel	142
8.10	Digital Count Trend for Grass	143

List of Tables

<u>Table</u>	<u>Title</u>	<u>Page</u>
2.1	Definitions of Variables in Current Radiance Algorithm	40
4.1	Variable Definitions in New Radiance Algorithm	47
5.1	Measured Diffuseness and Specularity	86
5.2	RMS Error of In-Plane Assumption	89
5.3	Reflectivity Curves (Incremental Percent Increases)	91
5.4	Diffuseness and Specularity	92
5.5	$R_d'(0)$ and $R_s'(0)$ Values of Non-BDRF Measured Surfaces	94
6.1	Primary and Secondary In-Scene Objects	98
6.2	CCD Camera Calibration Transformations	104
6.3	QED Radiometer Calibration Transformations	105
7.1	RMS Error for Directional Downwelled Radiance	108
7.2	RMS Error for Hemispherical Downwelled Radiance	112
7.3	Summary of Errors Associated With Each Variable	116
7.4	Observed Parameter Values and Associated Error for Green Band at 1230 Hours	118
7.5	Error Contributions of Variables	119
8.1	Matrix of Assessed Images	123
8.2	Spearman Rank Order Correlation Coefficient (r) and Z Statistics	130
8.3	Overall Percent RMS Reflectivity Error and Performance Rankings	134
8.4	Truck Reflectivity Component Values	150

1. Introduction

This study focuses on operation of the RIT Digital and Remote Sensing Lab's synthetic image generation (DIRSIG) software model within the 0.4 to 1.0 μm wavelength region. DIRSIG is a robust model which generates a remotely viewed image by simulating the many interactions affecting energy reaching the sensor. The model provides for treatment of the solar, atmospheric, target, and sensor interactions.

Evaluations of DIRSIG operating in the thermal (8-14 μm) and midwave (3-5 μm) infrared regions have recently been accomplished, highlighting potential problems with how well the model simulates radiance-surface interactions. These difficulties are hard to isolate in the midwave and thermal IR regions due to the complicating presence of surface emissions. Therefore, improvements should be made and assessed by operation in the visible region, where surface emissions do not exist. This study is intended to set the groundwork for future enhancements in this area.

Currently, DIRSIG only allows for ideal specular or ideal diffuse reflectance behavior. In reality, the treatment of reflectance should account for the effects of a mixture of specular and diffuse characteristics. The difficulty in

such treatment lies with actual acquisition of the values for the reflectivity components. Many models have been developed over the years to describe reflectivity. Unfortunately, the literature doesn't contain any reflectance models that describe the reflectivity as it is required by DIRSIG. DIRSIG's rendering technique requires view angle dependent components used to modify ideal radiance-scene interactions.

The approach to this study was two-fold. First, an improved method was established for modeling reflectivity characteristics. This included the generation of a reflectivity component database by a practical approximation method based on existing theories. Second, the performance of DIRSIG in the visible region was evaluated. This evaluation included the collection of truth data from an actual scene and comparing it to data from a synthetically generated image of the same scene.

The hypothesis is that the modifications will result in realistic radiance-surface interactions within the scene and that any significant errors will be attributable to known aspects of the model. This evaluation will serve as an initial overall assessment of the model's performance in this wavelength region.

2. Background

2.1 Synthetic Image Generation Modeling

Today's information dependent society increasingly craves imagery for many different applications. One of the major imaging categories is remote sensing. Remote sensing generally pertains to acquiring an image of an outdoor scene by a distantly located sensor. The sensors can be carried aboard a variety of platforms to include aircraft, spacecraft, surface ships and submarines.

Under some circumstances, it may be prohibitive to record the image of an actual scene. Whether the prohibition is levied by money, time, or accessibility constraints, there is a great need for the ability to simulate realistic images. The creation of realistic artificial images using detailed computer software algorithms, is referred to as synthetic image generation (SIG). The degree of realism required of SIG varies with the particular application of the imagery. For instance, some applications may only require accurate spatial information, while others may require accurate spatial, spectral, and radiometric detail.

2.1.1. Applications

Raqueno, et al (1991) describes various applications appropriate for SIG techniques. One example is resource management, where images from airborne sensors are used to assess a particular phenomenon occurring over large areas. Simulations can be used to 'pre-fly' a target to determine the best geometry and environmental conditions for observing the phenomenon of interest. The actual collection can then concentrate on a few designated "flights" to record the desired information, saving both time and money.

Another application is training for image exploitation. From the tedious human assessment of detailed reconnaissance images to the high speed machine interpretations of terrain following radar, image exploitation techniques involve applying decision algorithms to assess image characteristics. Training or evaluating both human and automated analysts is limited by the availability of imagery incorporating desired combinations of sensing geometry and environmental conditions. Synthetic images can be used to depict scenes normally restricted to actual collection and depict them under various conditions. Therefore humans and machines can be presented images which provide the needed challenge to their respective capabilities.

2.1.2. Modeling of Environment

To create realistic synthetic images of remotely sensed scenes, all potential sources of energy that may be directed into a sensor must be modeled. Of this energy, only the region of the electromagnetic spectrum that can be detected by a particular sensor must be accounted for. Even though SIG techniques are useful for a variety of sensors sensitive to all wavelengths, much of the related research focuses on electro-optical applications in the 0.4 to 15.0 μm region. The primary energy sources within this region are solar and thermal emission.

As these energies propagate, they are potentially modified by atmospheric and/or surface interactions. The extent of effects depend on the relation between the energy wavelength and molecular particle size making up the atmosphere or surface it interacts with. For many remote sensing applications, the surface interaction with energy is of primary interest because understanding this provides an opportunity for in-scene exploitation (Lillisand and Kiefer, 1987).

According to the principle of conservation of energy, incident energy onto a surface must either be absorbed,

reflected, or allowed to transmit. Since transmission is not a factor for solid surfaces of interest within a typical scene, interactions are in the form of either reflection or absorption. Absorption is proportional to emission if the surface is in thermal equilibrium with its surroundings. Generally, the predominant surface interaction for incident energy below 3 μm is reflection. For longer wavelengths, the predominant effect is emission (Lillisand and Kiefer, 1987).

Figure 2.1 displays the various energy interactions occurring within a given scene. A scene will normally consist of solar energy reflected from the surface, thermal energy emitted by the surface, atmospheric downwelling energy, and atmospheric upwelling energy. The upwelling and downwelling energy are a result of the atmosphere's molecules scattering, absorbing, and re-emitting energy.

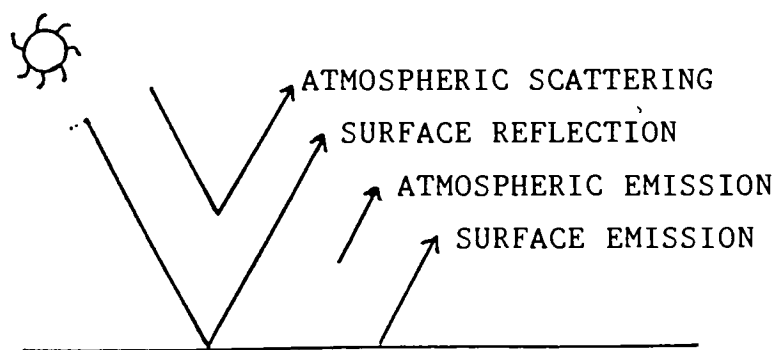


Figure 2.1 Energy Interactions Within a Scene

The bulk of published work regarding operating SIG models focuses on the thermal infrared region (8 - 15 μm) in support of research on infrared sensors for defense and resource management applications. Within this region the solar surface reflection is very small compared to surface emission. Some SIG models will also operate within the midwave IR region (3-5 μm) where both surface reflection and emission are equally important. However, these simulations are usually restricted to night to avoid the solar reflection effects. Raqueno, *et al* (1991) provides a good review of existing IR based models.

This study focused on the 0.4 - 1.0 μm range, which I refer to as the visible region. Many silicon based charged couple device (CCD) sensors are sensitive within this spectrum. The visible region is normally thought of as limited to 0.4 - 0.7 μm , as defined by the sensitivity of the human eye. The wavelength region of 0.7 - 1.0 μm includes part of a region normally referred to as the "near IR" or "reflective IR", which extends to 3.0 μm .

Within this "extended" visible spectrum, solar energy is the primary source and attenuation of this energy from atmospheric interaction is generally minor (Figure 2.2). The primary energy interaction is due to surface scattering

and absorption. Therefore, effective visible SIG modeling is highly dependent on proper treatment of these surface effects.

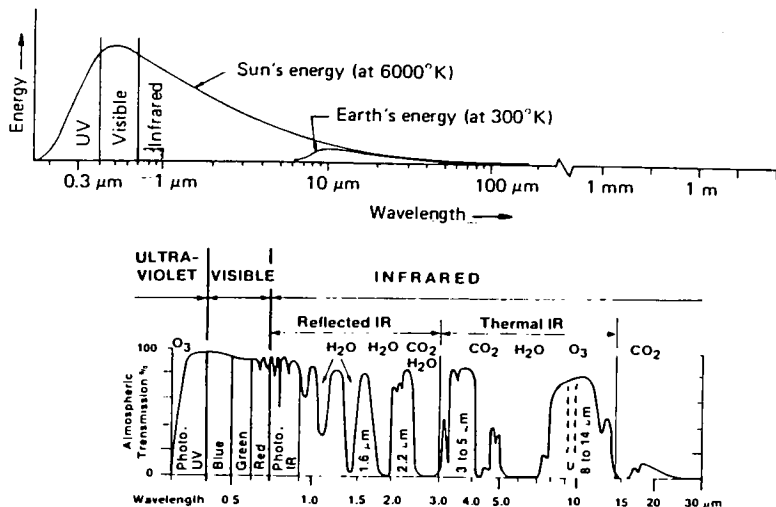


Figure 2.2 Spectral Plots of Solar Energy and Atmospheric Interaction (Lillisand and Kiefer, 1987)

2.1.3 Ray Tracing and Radiosity

Prior to reviewing reflectivity, a brief look is made of how many SIG models account for the interaction of energies within a scene. Comprehensive treatments of energy propagation are generally complex, cumbersome algorithms created for theoretical purposes and not meant for practical use. Therefore, early SIG models relied on relatively simplistic methods. However, with dramatic increases in computer processing power in the 1980's, development efforts

have focused on providing practical methods of applying complex theoretical energy propagation algorithms. Two such methods are ray tracing and radiosity (Goral, *et al*, 1984).

Ray tracing is a backward reconstruction process that determines the energy reaching a sensor's pixels by casting rays into the scene and "back tracking" until all energy sources are accounted for. Figure 2.3 shows a few simple rays. This method is restricted since it employs point sampling of energy contributions along the ray. Outside the ray vector, the energy contributions are approximated by constant ambient terms. This results in some loss of differential energy information which may result in inability to adequately simulate detail within shadow areas. A complete discussion of ray tracing is presented by Bouville and Bouatouch (1991).

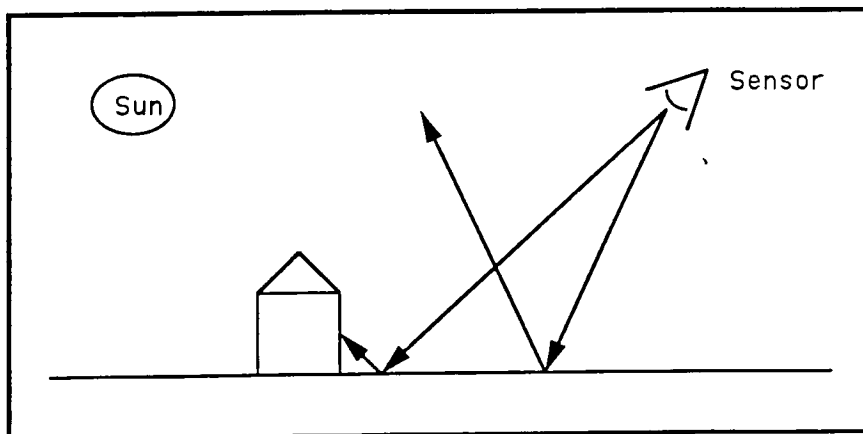


Figure 2.3 Sample Rays Within Ray Tracing

Radiosity is a method which separates the calculation of energy leaving the surfaces within a scene from the propagation of the energies to the sensor. First, the energy leaving the surfaces for the entire scene are determined through illumination and reflectance calculations. All objects are considered diffuse and inter-object illumination is determined by geometric relations between the objects. Following this, the energy reaching the sensor is assessed from any particular view angle. The appeal of this process is that the "...environmental intensity information can be pre-processed and subsequently used for multiple views." However, due to this large preprocessing cost, radiosity is limited to static scenes. Also, only diffuse scenes can be generated and the final image is only as accurate as the degree of resolution for discrete elements within the scene model (Greenberg, 1989).

This study is concerned with application of both specular and diffuse reflectivity characteristics in an existing ray tracing SIG model. Therefore, only direct ray tracing approaches were considered.

2.2 Reflectivity Review

In general, reflectivity is the scattering and absorption phenomenon of incident energy by a surface. The reflective characteristics of a surface can be characterized by the amount, relative spectral content, and degree of angular dispersion of the energy reflected. There are an abundance of reflectance terms used to describe various aspects of the relation between incident and reflected light. The most general term relates the energy reflected into the entire hemisphere to the total energy incident onto a surface. Lillisand and Kiefer (1987) define this unitless value as a surface's *Reflectance (R)*.

$$R = \text{total scattered energy} / \text{total incident energy} \quad (2.1)$$

The energy incident from a distant source will be considered uniform and defined as the *incident irradiance (Ei)*, with units of watts per meters². The energy reflected from a point on the surface will propagate radially outward and is defined as the *reflected radiance (Lr)*, with units of Watts per meters² per steradian (Nicodemus, 1965). These terms are depicted in figure 2.4.

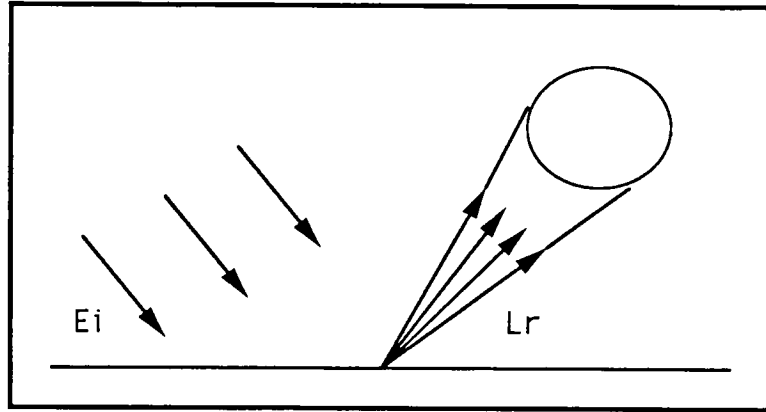


Figure 2.4 Incident Irradiance (E_i) and Reflected Radiance (L_r)

An intuitive characteristic of reflectivity is that it varies as a function of incident and viewing angles. According to Schott, *et al* (1990), "data acquired at fixed illumination angles indicate that common backgrounds can vary in their reflectance factors by 100 to 400 % for view angles ranging from nadir to 75 degrees off nadir." For most modeling applications, the geometrical dependence of the reflectance is an important consideration and therefore the basic definition of reflectance is usually insufficient. Feng, *et al* (1992), characterize this geometric reflection phenomenon as the *Bidirectional Reflectance Distribution Function (BRDF)*. BRDF is defined as the ratio of the radiance reflected by a surface into a particular direction to the irradiance incident on the sample within a small solid angle, with units of inverse steradians.

This relation is depicted in equation 2.2 and figure 2.5.

$$\text{BRDF} = (L_r) / (L_i \cos\theta_i d\omega_i) = L_r / E_i \quad (2.2)$$

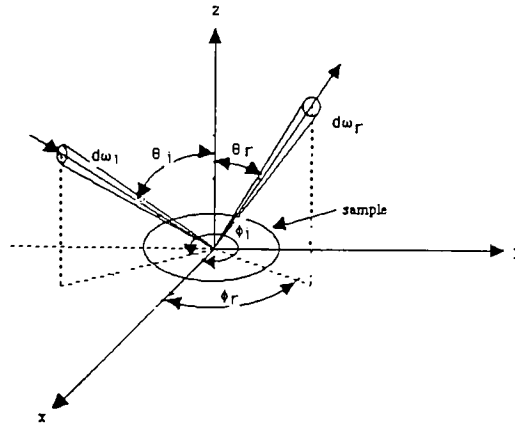


Figure 2.5 Geometric Relations of BRDF [Feng,1990]

To characterize a surface's BRDF at a particular geometry, both the incident irradiance and reflected radiance would need to be known. These values are difficult to measure simultaneously with a typical laboratory set-up. Therefore another quantity is often used to characterize a surface reflectivity. This is the *bidirectional reflectance factor (BDRF)*. The BDRF is the "ratio of the radiant flux actually reflected by a sample surface to that which would be reflected into the same reflected beam geometry by an ideal (lossless) perfectly diffuse (Lambertian) standard surface

irradiated in exactly the same way as the sample." This unitless value is closely related to the BRDF as shown in equation 2.3 (Feng, et al, 1992).

$$\text{BDRF} = \pi \text{ BRDF} \quad \text{where} \quad \pi = \sum_{\theta} \sum_{\phi} \cos \theta_r \sin \theta_r \Delta \theta_r \Delta \phi_r \quad (2.3)$$

Another important reflectivity relation describes "the reflected intensity into one direction resulting from incident radiation from all directions." This is depicted in figure 2.6.

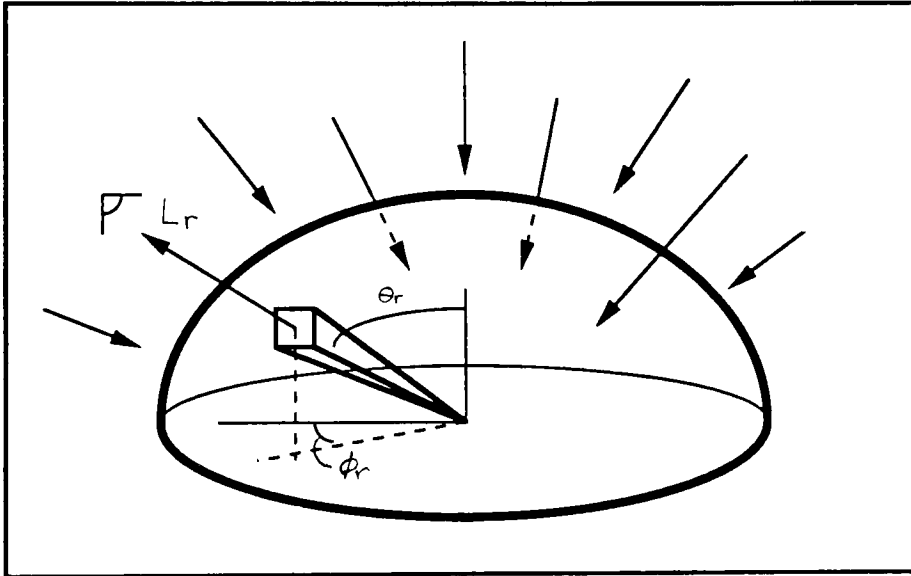


Figure 2.6 Hemispherical-Directional Reflectivity

The reflected radiance is equivalent to integrating equation 2.2 over all angles of incidence.

$$L_r = \int_{\text{hem}} \text{BRDF} L_i \cos \theta_i d\omega_i \quad (2.4)$$

This reflectance relation is referred to by Siegel and Howell (1982) as the *hemispherical-directional reflectivity*. The unitless term is defined as the ratio of the reflected radiance in a given direction to the integrated average incident radiance from the entire hemisphere (equation 2.5).

$$R_{\text{hem-dir}} = \frac{L_r}{\frac{1}{\pi} \int_{\text{hem}} L_i \cos\theta_i d\omega_i} = \frac{\int_{\text{hem}} \text{BRDF} L_i \cos\theta_i d\omega_i}{\frac{1}{\pi} \int_{\text{hem}} L_i \cos\theta_i d\omega_i} \quad (2.5)$$

The previous characterizations are very specific for a particular surface in describing the "amount" of energy reflected. Two other descriptions provide a more qualitative description of the "dispersive" behavior of reflectivity. When reflected energy is concentrated at an angle equal to the angle of incidence, but 180 azimuthal degrees away, it is referred to as *specular reflection*. An ideal specular surface has a BRDF which is a delta function at the reflection angle, and zero everywhere else. *Diffuse reflection* occurs when the reflected energy is spread in all directions. The BRDF of an ideal diffuse surface is equal at all view angles as described by Lambert's law. Such a surface is referred to as Lambertian (Sillion, et al, 1991).

In most real, non-ideal surfaces, the "dispersive" behavior will be a mixture of both specular and diffuse

characteristics. As shown in figure 2.7, the energy will reflect in all directions, but will build up a concentration in the specular direction. The degree of concentration will characterize surfaces as either more specular or more diffuse in behavior.

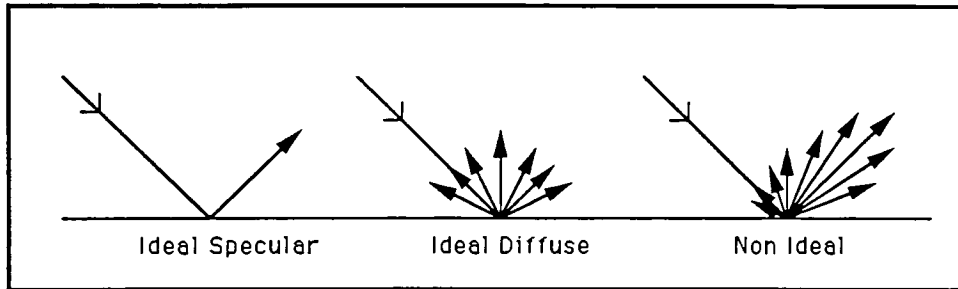


Figure 2.7 Reflectivity Characteristics

Another aspect to reflectivity is the relation of the angle of incidence and wavelength of the incoming energy, with the surface roughness features. He, et al, (1991) discuss how shadowing and masking (see figure 2.8) serve to attenuate reflected energy. As the incidence angle increases away from the surface normal, less energy is trapped by the surface features, and more is reflected into the specular direction. This phenomenon is sometimes referred to as "grazing angle" effects. Similarly, as the wavelength of the incident energy increases and becomes larger than the projected surface roughness, less interaction occurs with the surface and less energy suffers from attenuation.

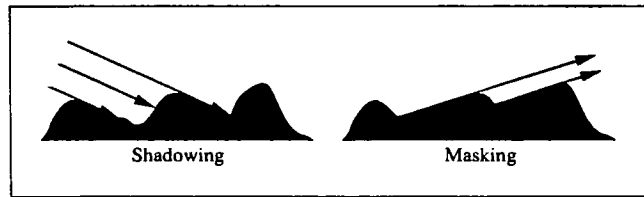


Figure 2.8 Surface Roughness [He, et al, 1991]

2.3 Reflectivity in Existing Visible SIG Models

The majority of the computer graphics literature discuss algorithms that forgo proper radiometry. Those concerned with realism care more about if the overall image simply appears correct, which can be accomplished by various artistic methods. In fact, only four operating SIG models were found to be concerned with creating realistic, radiometrically correct images in the visible region. Of these, all but one are infrared models that have been "extended" to operate in the visible. The fundamental algorithms for these models were probably designed to describe the nuances of thermal emissions as opposed to those of solar reflections.

This section provides a brief overview of how these visible SIG models treat surface reflection. The models are used in

a variety of applications whose requirements range from simple reflection approximations to detailed characterizations. In general, the more detailed models are slower to implement and require much more knowledge of the object surfaces. These trade-offs must be considered when rating the value of different SIG models and their surface reflectance treatments.

Two "crude" treatments of surface reflectance are found in SIGs developed by Texas Instruments and Photon Research. The *Texas Instrument* application generates synthetic images to create a database for testing automatic target recognition algorithms. These algorithms primarily seek to make decisions based on the general categorization of scene objects as distinguished from background. This categorization is mostly spatial with relative contrasts needed to further discern objects. The general nature of the Texas Instrument SIG model requires only a simple approximation of surface reflection. Therefore all objects are simply assumed to be diffuse and total diffuse reflectance values are used (Lindahl, et al, 1990).

The SIG model implemented by *Photon Research* generates high altitude earth background imagery and also requires only a simple approach to surface reflectance. This model also

uses a diffuse reflectance value to determine the surface effects within a scene. Justification for the simplistic approach is due to the high altitude nature of the imagery which reduces the resolution. Within the large ground sample spot size, the natural objects vary quite a bit and obtaining accurate reflectance values would not be beneficial (Reeves, *et al*, 1988).

The visible SIG model developed by the *Georgia Tech Research Institute* generates more detailed images. A rendering method called environment mapping is used which is described as a cross between radiosity and ray tracing. As in radiosity, the energy leaving the surfaces for the entire scene are precalculated. However, this is accomplished by considering six different geometrical arrangements, each using a common specular reflectance value. The energy leaving the surface due to diffuse reflectivity is found by simply averaging the six specular values. Final rendering is accomplished using ray tracing techniques that interrogate the scene and apply the appropriate specular reflected energy value plus the diffuse reflected energy. Thus only one reflectance value (which is specular in nature) is used for a particular surface (Cathcart, *et al*, 1990).

A visible SIG model that is based on a detailed characterization of reflectivity exists within the *Computer Graphics Program at Cornell University*. The reflectance model is an in-depth physics based algorithm that has evolved over the past twenty years and incorporates full BRDF effects. This model is referenced by most other journal articles found relating to visible SIG and reflectance theory. An important aspect of Cornell's SIG model is that it employs a combination of ray tracing and radiosity rendering methods to capture the benefits of both techniques (Wallace, *et al*, 1987).

However, there are some limitations of the Cornell SIG model. The detailed reflectance model may actually be too complex for many practical applications. Also, the radiometry algorithm, which governs the ray tracing and radiosity, does not incorporate many atmospheric effects on a scene. For these reasons, the Cornell SIG model is primarily used to image scenes with highly controlled environments which have a minimum number of objects and no atmospheric elements to contend with (i.e. the production of quality indoor images of simple objects). Such restrictions make the Cornell model unattractive for synthetically generating remotely sensed images.

2.4 Obtaining Reflectivity Values

An important part of SIG is actually obtaining values characterizing a surface's reflection characteristics. One method is to measure a complete BRDF set. Another way is to derive a particular reflectivity value using detailed, theoretical reflectivity models. Alternatively, a hybrid approach can be used to generate appropriate reflectivity data from a subset of measured reflectance values that represents the more important characteristics required for a given application. The appropriate technique to apply is, of course, one that balances out the required realism with practicality. The first two may provide more sensitive data, but the third will be more practical to apply. These three approaches will be discussed in this section.

2.4.1 Actual Measurements

Actually measuring BRDF (or BDRF) values for a surface should provide the most exact representation of reflectance. Feng (1990) describes how BDRF data is obtained by systematically measuring the reflectance at various illumination and viewing angles throughout the hemisphere. However, there are trade-offs to consider when acquiring this degree of precision.

First, the cost and complexity of the measurement apparatus is directly related to the resolution of the data. This equipment must be capable of adjusting the position of the source, sensor and sample to emulate a wide range of geometrical configurations. The sensor must be spectrally sensitive to measure over the desired wavelength bands. Also, the entire system must be extremely stable over the long period of time required for measurement.

Second, the large amount of BDRF data generated is a major concern for practical application. Even if the discrete measurements were spatially "spread out" and then interpolated, the amount of data is enormous. For example, if only five illumination angles were used, along with 15 view angles, nine azimuthal angles, and three spectral bands; the combined number of measurements would equal $5 \times 15 \times 9 \times 3 = 2,025$. Each of these measurements would need to be stored and then readily accessed by the SIG model, resulting in potentially large processing times.

The main objective of this study is supporting remote sensing applications of SIG. In many instances, samples cannot be acquired for all surfaces in the scene. The actual scene may be in a restricted area or may contain living surfaces such as plant life whose reflective

properties will change after removal. Therefore, many surface reflections still need to be approximated based on known characteristics of *similar* materials. This restriction limits the value of relying on an expensive, completely measured, BDRF data base.

2.4.2. Reflection Models

Use of models to predict reflectance values requires a thorough understanding of actual surface characteristics. There are many models available with varying levels of complexity. Like the choice of an overall SIG model, the choice of a reflectance model depends on the degree of accuracy required for the application.

Early reflection models simply treated all surfaces as diffuse. However in 1975, Phong introduced a more realistic model to account for the fact that more light is reflected in the specular direction. This was accomplished by adding a specular reflection component (R_s) to the simple diffuse component (R_d).

$$R = R_d + R_s \quad (2.6)$$

For a mirror surface, this added component would only be found at the specular reflection angle. Phong realized that most surfaces were not mirrors and the specular component is

more of a lobe which "falls-off" at varying rates. He incorporated these lobe effects by modifying the specular component with $\cos(\alpha)^n$. As shown in figure 2.9, α is the angle between the specular reflection vector (V) and the viewing vector (E). The value of "n" will be large for highly specular materials and small for more diffuse materials (Magenat-Thalman and Thalman, 1987).

$$R_s' = R_s(\cos \alpha)^n \quad (2.7)$$

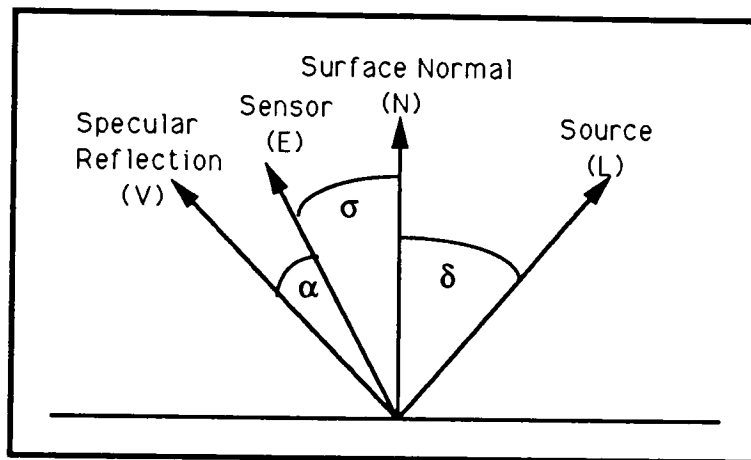


Figure 2.9 Phong Model Geometry

While the Phong reflectance model is more accurate, it is still heavily empirical. Blinn (1977) sought to overcome this by using the less empirical Torrance-Sparrow model for the specular reflectance component. While Phong treats the surface as a plane, the Torrance-Sparrow model assumes the surface is a collection of small mirror-like facets. The

specularity of the surface results from the orientation of the facets.

$$R_s = (D G F) / (\cos \sigma) \quad (2.8)$$

where: D represents the distribution function of the facet normals which is statistically derived
G is the attenuation due to shadowing and obscuration(function of roughness parameters)
F is the Fresnel factor of the surface, a function of index of refraction
 σ is the angle between the surface normal (N) and the viewing direction (E), see figure 2.9

As mentioned earlier, a complex reflectance model was developed at Cornell University by Cook and Torrence (1982). This heavily theoretical model incorporates BRDF effects and still allows for overt empirical adjustment. The adjustment is provided by characterizing a surface with percentages of specularity (s) and diffuseness (d).

$$R = d R_d + s R_s, \quad \text{where } s + d = 1 \quad (2.9)$$

The BRDF effects are incorporated into the specular component by accounting for the solid angle (π) defined by the sensor and illumination angle (δ) shown in figure 2.9.

$$R_s = (D G F) / \pi(\cos \sigma)(\cos \delta) \quad (2.10)$$

Also at Cornell, He, *et al* (1991) introduced a more accurate model for reflectance based on physical optics. This model

has a third term that represents the spread and direction of the specular lobe, as Phong tried to do empirically. This term is referred to as the directional diffuse component (Rdd). These components are displayed in figure 2.10.

$$R = R_s + R_d + R_{dd} \quad (2.11)$$

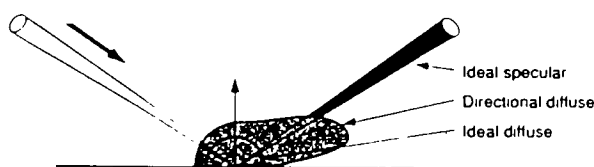


Figure 2.10 Light Intensity Distribution
(He, et al, 1991)

Determining values for these terms require extensive calculations and knowledge of such surface characteristic parameters as polarization effects, complex index of refraction, RMS roughness, and auto-correlation length. These components are fully derived in the reference.

The more complex models provide accurate reflectance data for a given surface. However, in order to use these models, a great deal of detailed surface information must be available. This information must be obtained through extensive laboratory testing. As with full BDRF measurements, using complex reflectance models may not be practical for remote sensing applications.

2.4.3. Hybrid Approach

Another method, developed by the Environmental Research Institute of Michigan (ERIM), generates reflectivity values by incorporating both measurements and modeling. In brief, the ERIM method requires a small subset of BRDF data for a particular surface. The BRDF for any geometric situation encountered can then be calculated from a theoretical reflection model using the BRDF subset and known surface parameters. This reflectance model is very similar, although less complex, to that of He, *et al.* Particular BRDF values can be found without having to measure and store large volumes of data, or without having to understand and use complex theoretical models (ERIM BRL Report, 1974).

The actual subset of reflectance data used by the ERIM model are referred to as "zero bi-static" reflectance values. Zero bi-static refers to the source-sensor angle being held near zero. As shown in figure 2.11, the vector representing the source-sensor location is at an angle θ_n from nadir. This angle is incremented from 0 to 90 degrees and BRDF values are recorded at each step. The scan is performed twice. First, with the sensor and source at the same polarization and then with sensor and source cross polarized. The surface characteristics are exploited by

assessing how the surface effectively reflects in different directions under the changes in polarization.

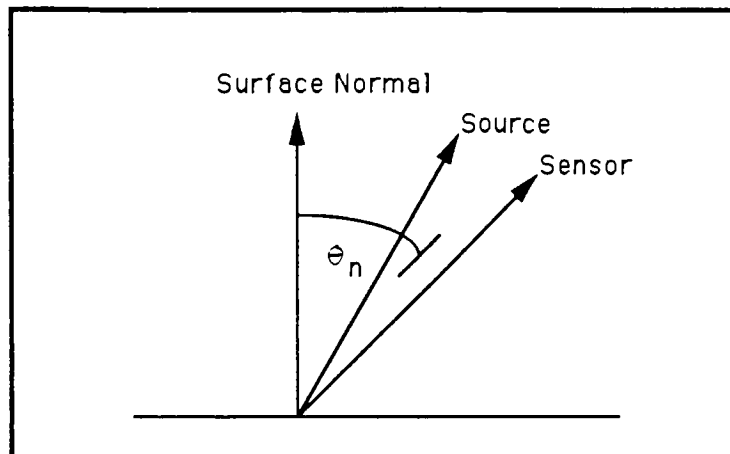


Figure 2.11 Zero Bi-static Measurement Geometry

All three techniques for generating reflectivity values share a common problem of relying on a material data base that may be difficult to populate. However, the hybrid concept offers the most practical method for remote sensing applications. Thus, the focus in this study was to develop and test a simplified hybrid method. The applied method incorporates many of the aspects found in all three techniques described above. Most importantly, the approach taken is only concerned with incorporating those reflectivity characteristics actually exploited by the available SIG model. The next section discusses this model.

2.5 DIRS Lab SIG

This study focused on modifying an existing infrared SIG model to operate in the visible (0.4 -1.0 μm) region to incorporate some of the reflectance concerns discussed. As mentioned in the introduction, the SIG model was developed by the Rochester Institute of Technology's Digital Imaging and Remote Sensing (DIRS) Lab, and is referred to as DIRSIG. This model is described in detail by Raqueno, *et al* (1991). DIRSIG provides treatment of the solar, atmospheric, scene object, and sensor effects for remotely sensed images.

The DIRSIG model consists of the following five submodels: scene geometry, ray tracer, temperature generator, radiometry, and sensor. Relevant scene input data include materials, weather, and atmosphere. The submodels interact to create the final synthetic image as shown in figure 2.12. Since this study evaluates only the radiance reaching the "front end" of the sensor and is restricted to the visible region, the sensor and temperature generator submodels will not be discussed. A description will be given to the applicable portions of the scene geometry, ray tracer, and radiometry submodels. Greater detail on the submodels can be found in the referenced document.

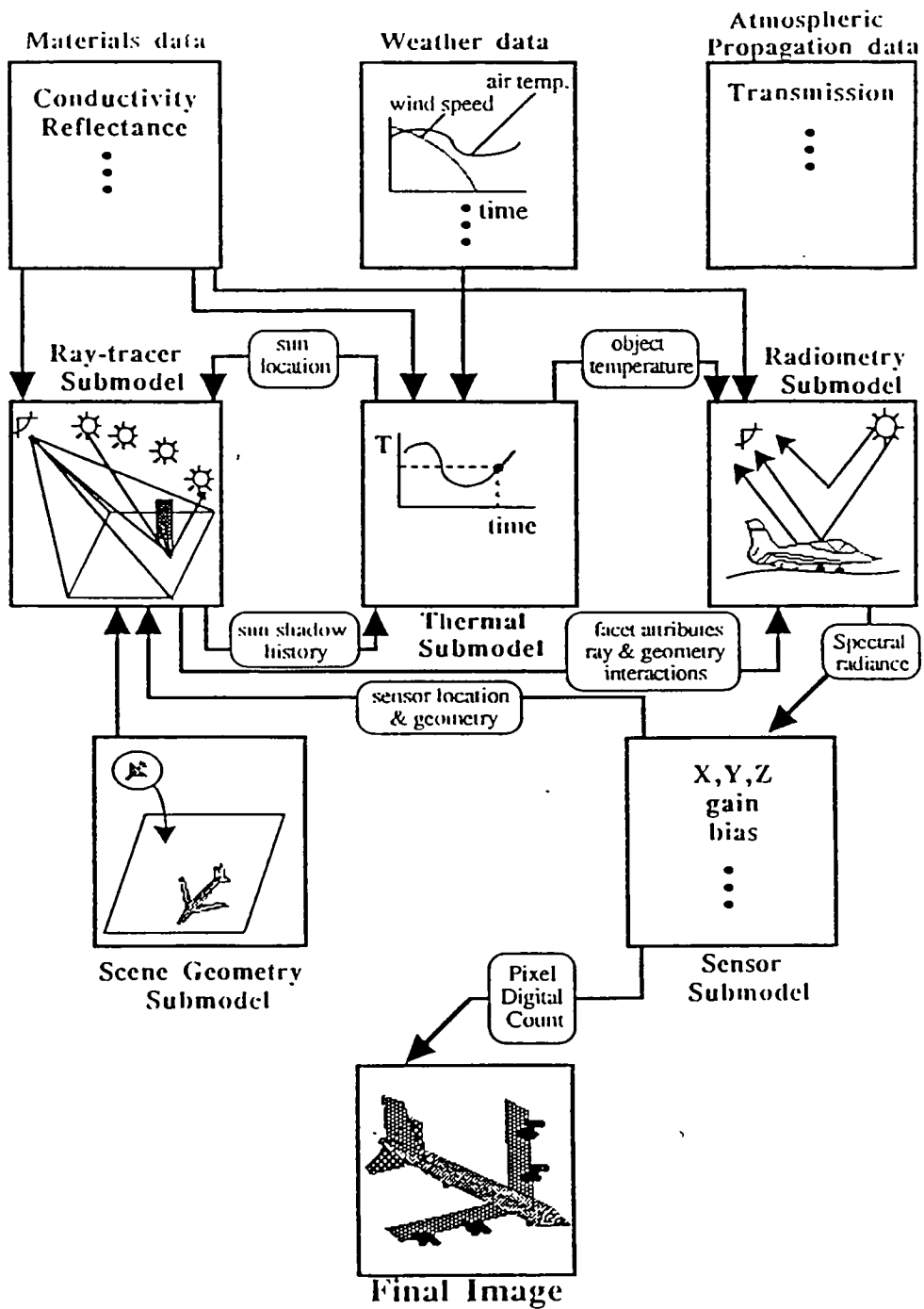


Figure 2.12 Submodel Interactions Within DIRSIG
[Raqueno, et al, 1991]

2.5.1. Scene Geometry Submodel

The starting point for generating a synthetic image is the scene geometry. This submodel uses a 3-D AutoCAD model of the objects, along with scaling and orientation algorithms, to create the desired scene. The scene objects are subdivided into facets which make-up the most basic element. Each facet is described by pointers to three nodes (geometry, orientation, and attribute) which serve to link the various properties designated by the model builder.

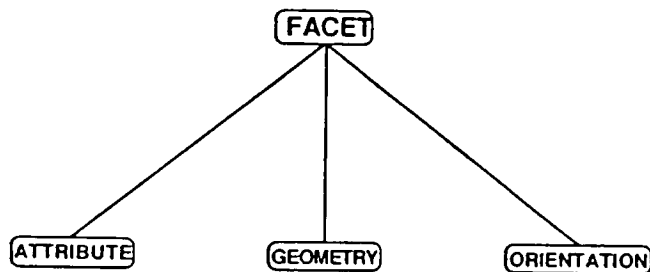


Figure 2.13 Facet Subnodes [Raqueno, et al, 1991]

The geometry node defines the coordinates of the facet's points as well as the normal vector from the facet plane. The orientation node provides angle information regarding the orientation of the facet normal with respect to the earth and sun. These two nodes provide the data needed to trace the basic interaction of a propagated ray. The attribute node contains additional parameters that define the facet's physical properties (see figure 2.14). The

primary property for this study is the material code, which points to a common materials database that can be accessed by any facet. Figure 2.15 displays the types of information that can be assigned to this database for use by the overall SIG process. It is this database that will contain the generated reflectance values.

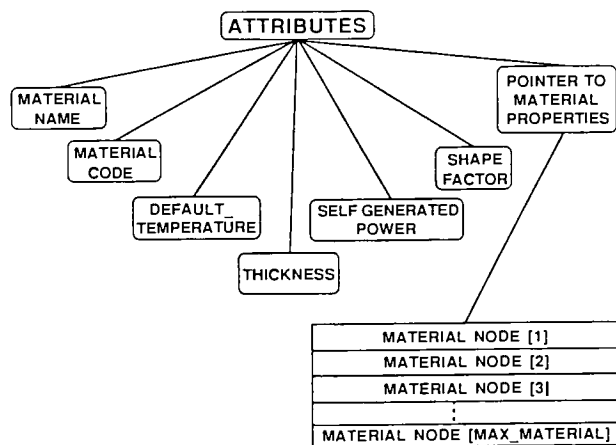


Figure 2.14 Attribute Subnodes [Raqueno, *et al*, 1991]

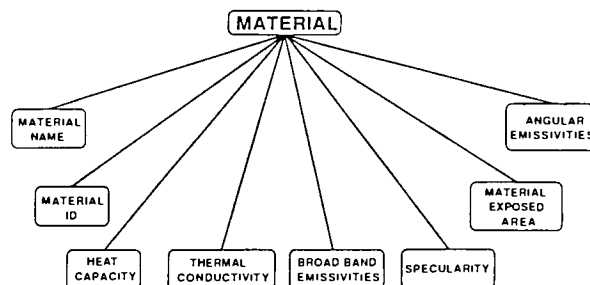


Figure 2.15 Material Subnodes [Raqueno, *et al*, 1991]

2.5.2. Ray Tracer Submodel

The ray tracer submodel is tasked with retracing the paths of photons reaching each sensor picture element into the scene itself. This allows for proper calculation of the radiance based on the originating source and intervening scene interactions such as atmospheric absorption and material reflection. In performing this task, the submodel also serves to coordinate the entire simulation process.

For an ideal tracing, each time a ray interacts with a facet, secondary rays would need to be sent out in *all* directions. Each secondary ray would determine the incoming energy to the facet from a particular direction. The energy from each direction would then be attenuated by a specific BRDF value based on the orientation of the primary ray and each secondary ray. This ideal assessment of the incident energy is depicted in figure 2.16.

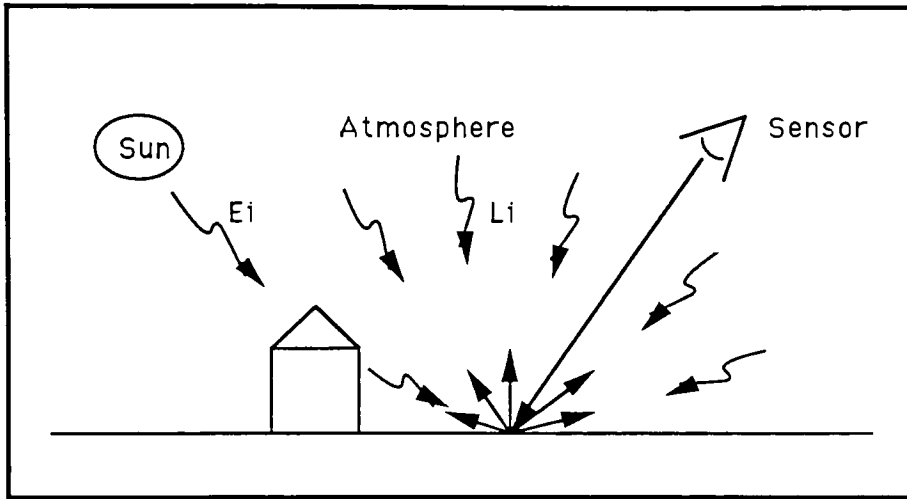


Figure 2.16 Ideal Ray Tracer Assessments

Although such an ideal scheme is feasible, there are reasons why it is not practical. First, generating all the specific BRDF values would require many resources as discussed in section 2.4.1. Thus, it is unlikely that a materials database would ever be sufficiently populated. Second, to fully exploit such BRDF phenomenon as sharp specular peaks, a high density of secondary rays are required to provide sufficient angular resolution. Assessing a high enough density of secondary rays will be similar to integrating the incident energy over the hemisphere, as shown in equation 2.4. Such a large volume of primary rays may result in prohibitive processing time.

For practical reasons, the current approach by DIRSIG avoids complete sets of secondary rays for each facet interaction by assuming each material is either completely specular or completely diffuse. If a surface is labelled as specular, then a secondary ray is cast at the "specular" angle and assessed for incoming energy content. If the surface is labelled as diffuse, then no secondary rays are traced and the incoming energy is assessed from the hemispheric downwelled radiance and effective solar radiance. These are depicted in figure 2.17. The incoming energy in the specular case is modified by a view angle dependent reflectance value, calculated from an angular emissivity value. For the diffuse case, the incoming energy is modified by a total diffuse reflectance value, also calculated from emissivity.

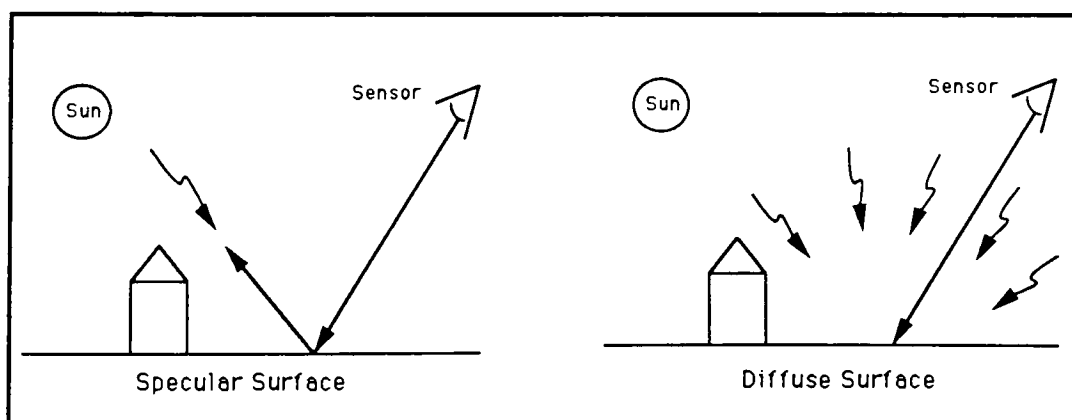


Figure 2.17 Current Ray Tracer Assessments

For the long wave infrared region, it has been determined by Shor (Raqueno, *et al*, 1991) that the maximum "depth" of ray-facet interactions to be traced is two. Computations of rays beyond this result in insignificant radiance contributions. No similar testing has been done in the midwave infrared and visible regions, but the same results will be assumed.

2.5.3. Radiometry Submodel

The radiometry submodel actually calculates the radiance reaching the front end of the sensor according to the interactions described by the scene geometry and ray tracer submodels. The ray-facet interactions are governed by the material characteristics database. The ray-atmosphere interactions are provided by an algorithm referred to as the spectral vector generation model (SVGM) which was developed by Salvaggio, *et al* (1991).

SVGM is a modified version of another algorithm called LOWTRAN7, developed by the Air Force Geophysics Laboratory. "LOWTRAN models the atmosphere as many individual layers, each of which exhibits either pre-defined or user-specified meteorological conditions, atmospheric composition of gases,

aerosol type and specific scattering phase functions, as well as sensitivity to global position" (Raqueno, *et al*). The modified model provides DIRSIG with such parameters as exoatmospheric solar irradiance, atmospheric transmission, and downwelling sky radiance.

The SIG algorithms required to determine the radiance reaching the sensor for each ray cast are straight forward. If the ray's primary target is considered specular, the radiance is found from an ideal specular treatment using equation 2.12. If the ray's primary target is diffuse, the radiance is determined from an ideal diffuse treatment using equation 2.13. In each case, the total radiance reaching the sensor for any primary ray is found by adding the atmospheric upwelled radiance. To further limit the extent of the calculations, the background objects are always considered diffuse.

The parameters required by these equations are either defined by the material database, generated by another submodel, or calculated by the SVGM. Table 2.1 provides definitions of these parameters. Figure 2.18 illustrates the angles used in the equations. Figure 2.19 displays the four general interactions incurred by the ray tracer in implementing the radiometry algorithm. The variable

referred to as shape factor (F) represents the percentage of the "sky dome" visible to a facet. For each facet, the model sends rays radially outward and tracks the relation between the number of rays intersecting an object and the number reaching the sky.

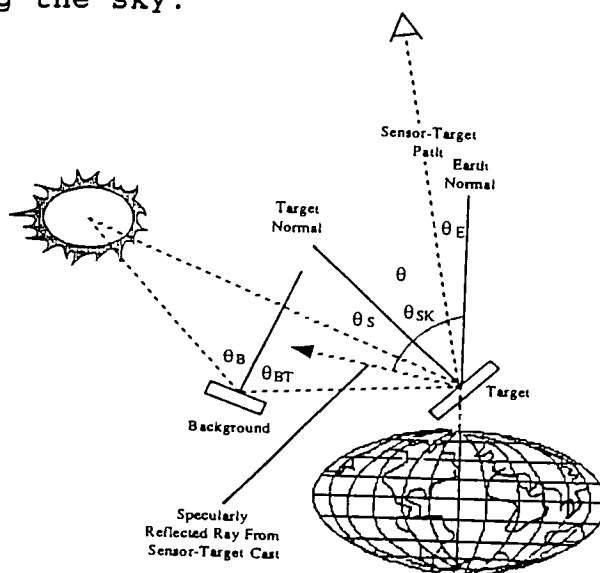


Figure 2.18 Angles in Radiometric Equations
[Raqueno, et al, 1991]

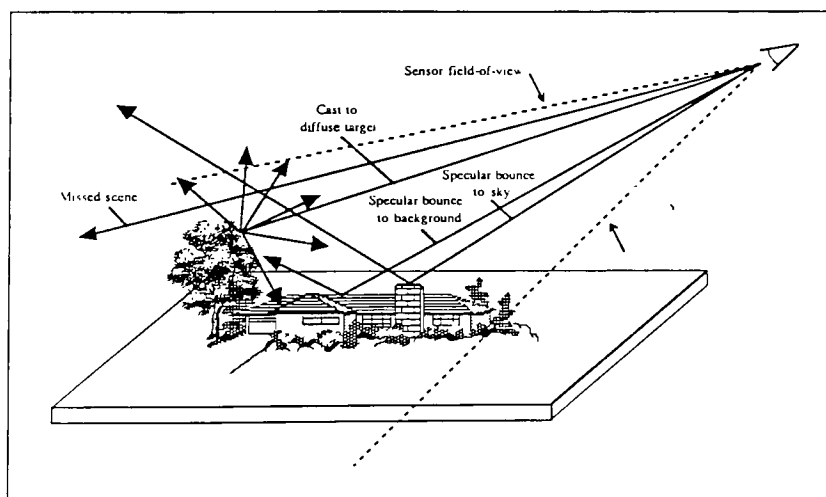


Figure 2.19 Four General Ray Tracer Interactions
[Raqueno, et al, 1991]

Current Radiance Algorithm

Surface Designated as Specular:

$$\begin{aligned}
 L(\theta_v) &= \text{Reflected Radiance} + \\
 &\quad \text{Upwelled Radiance} \\
 &= (\text{solar} + \text{downwelled} + \text{background}) (\text{reflectance}) (\text{atm transmission}) + \\
 &\quad \text{upwelled radiance} \\
 &= [(E_s/\pi) I'_s \tau_1 \cos\theta_s + L_d(\theta_{sky})(1-I'_{SH}) + (E_s/\pi) I'_b \tau_1 \cos\theta_b R_b(\theta_{bt}) I'_{SH}] R(\theta_v) \tau_2(\theta_E) + \\
 &\quad Lu(\theta_v)
 \end{aligned}
 \tag{2.12}$$

Surface Designated as Diffuse:

$$\begin{aligned}
 L(\theta_v) &= \text{Reflected Radiance} + \\
 &\quad \text{Upwelled Radiance} \\
 &= (\text{solar} + \text{downwelled} + \text{background}) (\text{reflectance}) (\text{atm transmission}) + \\
 &\quad \text{upwelled radiance} \\
 &= [(E_s/\pi) I'_s \tau_1 \cos\theta_s + FL_{dsky} + (1-F)((E_s/\pi) I'_b \tau_1 \cos\theta_b) R_b(30^\circ)] R(0^\circ) \tau_2(\theta_E) + \\
 &\quad Lu(\theta_v)
 \end{aligned}
 \tag{2.13}$$

R	target reflectance, calculated from $1-\varepsilon(\theta_v)$
R_b	background reflectance
$L(\theta_v)$	radiance reaching front of the sensor
L_{dsky}	downwelled radiance due to scattering integrated over the skydome
$L_d(\theta_{\text{sky}})$	directional downwelled radiance due to scattering
$L_u(\theta_v)$	upwelled radiance due to scattering along the target-sensor path
E_s/π	exoatmospheric solar radiance
τ_1	atmospheric transmission along the source-target path
$\tau_2(\theta_E)$	atmospheric transmission along the target-sensor path
I'_{SH}	secondary hit flag (1 or 0)
I'_s	target sun/shadow flag (1 or 0)
I'_b	background sun/shadow flag (1 or 0)
F	shape factor, the fraction of the exposed skydome
θ_s	angle between the normal to the surface and the sun-target path
θ_{sky}	angle between the normal to the earth and the specularly reflected ray from the sensor to target cast
θ_b	angle between the background normal and the sun-background path
θ_{bt}	angle between the background normal and the target hit point
θ_v	angle between the target normal and the sensor-target path
θ_E	angle between the earth normal at the target and sensor-earth path

Note: all reflectance, radiance, and transmission variables are spectrally dependent.

Table 2.1 Definitions of Variables in Current Radiance Algorithm

2.6. DIRSIG and Reflectivity

As stated, the current DIRSIG treatment of reflectivity allows for either ideal specular or ideal diffuse behavior. In reality, most objects' reflectivity exhibit some mixture of specular and diffuse characteristics. These reflectivities carry a strong dependence on illumination and view angle that result in phenomenon such as varied specular lobe width, back scatter peaks, and "grazing" angle peaks.

When surfaces are treated as ideal, the reflected energy may tend to be inaccurate. Such effects have been observed in DIRSIG evaluations in the thermal infrared and midwave infrared. In particular, for objects treated as specular, the "... assumption could lead to an over prediction of radiance when a background object is in the path of a reflected specular hit (Schott, *et al*, 1993)." It is assumed that similar problems will exist in the visible region.

With the DIRSIG algorithm designed for operation in the thermal region, the reflectivity values are actually derived from a surfaces' angular hemispheric emissivities. The angular hemispheric emissivity values are dependent on view angle only. However, the desired reflectivity is a function

of both view angle and illumination angle. Therefore, the conservation of energy law should not apply for BRDF values and angular hemispheric emissivity. A different technique of deriving reflectance values was obviously needed for operation in the visible region. The derivation and application of such a technique is addressed in section 5.

3. Objectives and Approach

The overall objectives of this thesis are modification of DIRSIG's treatment of reflectivity to exploit the visible spectrum and evaluation of DIRSIG's performance in this region. As mentioned, DIRSIG was developed for operation in the infrared wavelength region and therefore no baseline exists in the visible region to compare the effects of modifications. *The hypothesis is that the modifications will result in realistic energy-surface interactions within the scene and that any significant errors will be attributable to other aspects of the model.* The following was accomplished to meet the objectives:

First. The DIRSIG radiance algorithm was modified to provide a more realistic treatment of reflectivity. This includes use of DIRSIG specific, diffuse and specular reflectivity components.

Second. A technique was developed to generate the reflectivity component values and then applied to the materials used in this study.

Third. Ground truth data was obtained by imaging an actual scene from a fixed view angle with various solar illumination angles. This included establishing the actual scene, collecting the images, measuring atmospheric effects, monitoring the environment, and performing equipment calibrations.

Fourth. Selected images were generated of the ground truth scene using the modified DIRSIG model.

Fifth. Performance of the modified DIRSIG model was evaluated by comparing the generated images against the observed truth data.

All aspects of this project were performed in four specific spectral bands within the 400 - 1000 nm range. These bands were chosen based on available filters (see the filter transmissivity plots in the appendix) and are designated as:

- BLUE (420 - 510 nm)
- GREEN (510 - 570 nm)
- RED (610 - 750 nm)
- NIR (745 - 1000 nm)

The NIR band was included based on the capabilities of the sensor used to obtain the truth images. However, a thorough quantitative assessment of this band was not permissible because (1) the detector equipment used to measure much of the supporting data in this evaluation is only designed for use in the visible region, approximately 400-750 nm, and (2) complete documentation on the actual maximum wavelength limit of the camera's CCD detectors was not available.

4. Modified DIRSIG Radiance Algorithm

The modifications to DIRSIG's radiance algorithm focus on optimizing use of the existing variables. These changes involve the energy incident on a target and the scattering of this energy by the target's surface in the direction of the sensor. This algorithm is presented in equation 4.1.a and the variables are defined in table 4.1.

The modified algorithm considers each surface as having both specular and diffuse reflectivity characteristics. The characteristics are represented by two view angle dependent reflectivity components for a given surface, which are further described in section 5. These components represent the respective percentages of radiance reflected to the sensor. Therefore, the algorithm can be thought of as having two radiance components, one from diffuse interaction and the other from specular. The two radiance components are simply added to find the total radiance reflected from the target surface. The atmospheric upwellèd radiance is then added to the total reflected energy to find the total energy reaching the sensor for a particular primary ray.

Equation 4.1.b simply expands the algorithm to include a targets's emissivity, as it would be applied in the longer

wavelength regions. This is only included for completeness. The appendix contains a pseudo code version of the modified algorithm as it is implemented in the software. Note that implementation involves two passes of the algorithm for each pixel, once as diffuse and once as specular.

Modified Radiance Algorithm

For Visible Region:

$$\begin{aligned}
 L(\theta_V) &= \text{Specularly Reflected Radiance} + \\
 &\quad \text{Diffusely Reflected Radiance} + \\
 &\quad \text{Upwelled Radiance} \\
 &= \{(\text{solar} + \text{downwelled} + \text{background}) (\text{specular reflectance component}) + \\
 &\quad (\text{solar} + \text{downwelled} + \text{background}) (\text{diffuse reflectance component})\} \text{ atm transmission} + \\
 &\quad \text{upwelled radiance} \\
 &= \{[(E_s/\pi)I'_s I'_T \tau_1 \cos\theta_s + L_d(\theta_{sky})I'_{SH} + I'_{SH}((E_s/\pi)I'_b \tau_1 \cos\theta_b + FL_{dsky})R_{db}(\theta_{bt})]R_s(\theta_v) + \\
 &\quad [(E_s/\pi)I'_s \tau_1 \cos\theta_s + FL_{dsky} + I'_{SH}(1-F)((E_s/\pi)I'_b \tau_1 \cos\theta_b + FL_{dsky})R_{db}(\theta_{bt})]R_d(\theta_v)\} \tau_2(\theta_E) + \\
 &\quad Lu(\theta_V)
 \end{aligned} \tag{4.1.a}$$

For Visible and IR Regions:

$$\begin{aligned}
 L(\theta_V) &= \text{Specularly Reflected Radiance} + \\
 &\quad \text{Diffusely Reflected Radiance} + \\
 &\quad \text{Target's Emitted Radiance} + \\
 &\quad \text{Upwelled Radiance} \\
 &= \{(\text{solar} + \text{downwelled} + \text{background}) (\text{specular reflectance component}) + \\
 &\quad (\text{solar} + \text{downwelled} + \text{background}) (\text{diffuse reflectance component}) + \\
 &\quad \text{target emissivity}\} \text{ atm transmission} + \\
 &\quad \text{upwelled radiance} \\
 &= \{[(E_s/\pi)I'_s I'_T \tau_1 \cos\theta_s + L_d(\theta_{sky})I'_{SH} + I'_{SH}((E_s/\pi)I'_b \tau_1 \cos\theta_b + FL_{dsky} + \epsilon_B(\theta_{BT}))R_{db}(\theta_{bt})]R_s(\theta_v) + \\
 &\quad [(E_s/\pi)I'_s \tau_1 \cos\theta_s + FL_{dsky} + I'_{SH}(1-F)((E_s/\pi)I'_b \tau_1 \cos\theta_b + FL_{dsky} + \epsilon_B(\theta_{BT}))R_{db}(\theta_{bt})]R_d(\theta_v) + \\
 &\quad \epsilon_T(\theta_v)\} \tau_2(\theta_E) + \\
 &\quad Lu(\theta_V)
 \end{aligned} \tag{4.1.b}$$

where, $\epsilon_T(\theta_v)$ = target emissivity
 $\epsilon_B(\theta_{BT})$ = background emissivity

R_s	specular reflectivity component
R_d	diffuse reflectivity component
R_{db}	diffuse reflectivity component of the background
$L(\theta_v)$	radiance reaching front of the sensor
L_{dsky}	downwelled radiance due to scattering integrated over the skydome
$L_d(\theta_{sky})$	directional downwelled radiance due to scattering
$L_u(\theta_v)$	upwelled radiance due to scattering along the target-sensor path
E_s/π	exoatmospheric solar radiance
τ_1	atmospheric transmission along the source-target path
$\tau_2(\theta_E)$	atmospheric transmission along the target-sensor path
I'_{SH}	secondary hit flag (1 or 0)
I'_s	target sun/shadow flag (1 or 0)
I'_b	background sun/shadow flag (1 or 0)
I'_T	specular incidence/sun intersection flag (1 or 0)
F	shape factor, the fraction of the exposed skydome
θ_s	angle between the normal to the surface and the sun-target path
θ_{sky}	angle between the normal to the earth and the specularly reflected ray from the sensor to target cast
θ_b	angle between the background normal and the sun-background path
θ_{bt}	angle between the background normal and the target hit point
θ_v	angle between the target normal and the sensor-target path
θ_E	angle between the earth normal at the target and sensor-earth path

Note: all reflectance, radiance, and transmission variables
are spectrally dependent.

Table 4.1 Variable Definitions in New Radiance Algorithm

Description of Changes

The methods used to find the specular and diffuse radiance components are similar to those used previously to find each ideal case. Changes were made as to what energy is assessed and its subsequent attenuation by the surface interaction.

One area of change involved the direct solar energy effects. When computing the specular component, the direct solar radiance will not be included unless the secondary ray cast from the target actually intersects the solar disk, which is defined as a two degree angular diameter (figure 4.1).

Previously, the effects of the sun were considered for the specular as long as it was in line-of-sight of the target. This was sufficient in the thermal region when only the amount of absorption of solar energy was important.

However, this is inappropriate in the visible due to reflectivity's bidirectional dependence. For diffuse, the solar effects will continue to be treated as before, irrespective of the azimuthal illumination angle. In effect, this simply treats the reflection of the solar energy towards the sensor as diffuse unless the sun happens to be located within the specular angle defined by the sensor.

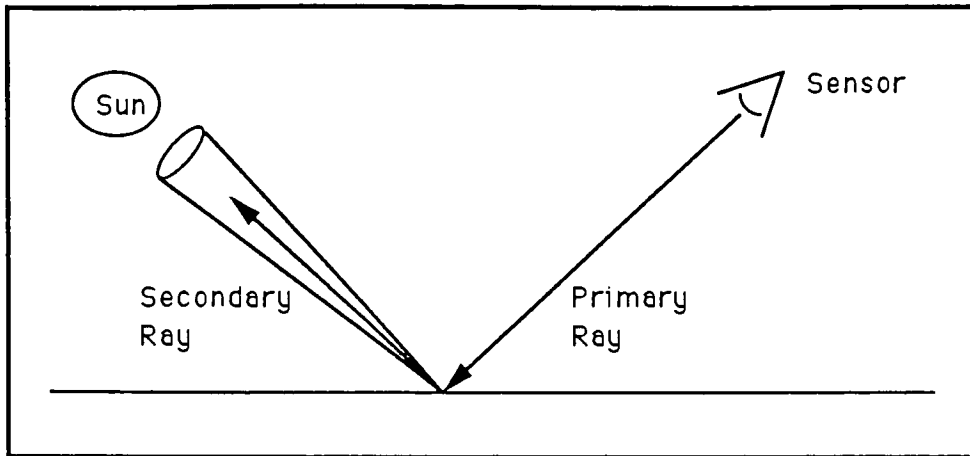


Figure 4.1 Specular Acceptance Cone for Solar Illumination

Another change involved illumination from a background object. Previously, only the reflection of solar illumination from a background was accounted for. When the sun was no longer within line-of-sight of the background, no energy was reflected and potential background contrast information was lost. Now, the reflection off the background from the downwelled radiance from the sky is included as well. When the sun is no longer illuminating the background, the sky radiance may still be sufficient enough to be a factor (figure 4.2).

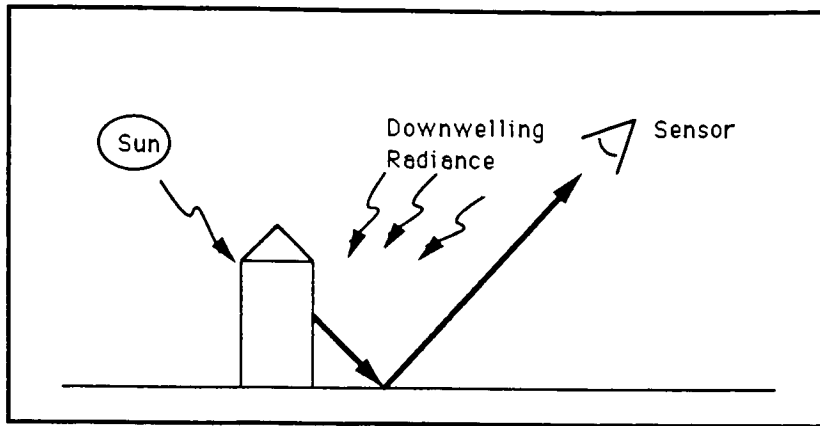


Figure 4.2 Background Reflected Downwelling Illumination

Two assumptions were made that should add only a small percentage of error to the overall radiance. First, the background object is still always considered diffuse to limit the extent of the calculations. Second, the full hemispherical downwelling radiance incident onto the background is modified by the same shape factor determined for the primary target. In reality, the background's actual shape factor could be a little different. However, this approximation is acceptable considering the added computation that would be required to determine additional shape factors.

5. Reflectivity Components

The underlying philosophy for the treatment of reflectivity components in this study is as stated by Beard and Arnold (1989).

"It is our [ERIM] opinion that, for materials of interest, we cannot gather all the empirical data that are necessary to completely describe the scattering characteristics of the particular material. We can only afford to measure enough data to characterize the type of scattering...to represent or approximate the scattering characteristics of the material.... Our challenge, therefore, is to extend the... techniques...to capture the expected variation in the BRDF."

Dividing a surface's reflectivity into specular and diffuse components generally follows the treatment applied at Cornell and ERIM (section 2.4.2). However, their methods are not very practical to implement. This study applies a more practical approach to generating a reflectivity component database. Specifically, a series of "in-plane" plots of bidirectional reflectance are used to derive a complete reflectivity component database. Before describing how the reflectivity components are generated, a review is presented of the surface reflection characteristics observed in in-plane plots.

5.1 Surface Reflection Characteristics Observed in In-Plane Plots

The reflective behavior of a surface is often observed by plotting the reflected energy at varying view angles, with respect to a particular illumination angle. These are referred to as "in-plane" plots. The main reflectance characteristics described in such a plot include; (1) existence of a specular lobe, (2) degree of spread within an existing lobe, (3) magnitude of the lobe, (4) existence of a level, non-specular plateau, (5) increased reflectivity at large "grazing" view angles, and (6) back scatter effects.

In most instances, the in-plane plots will sufficiently characterize the surface's reflective behavior. This behavior can be classified into three general categories; *specular*, *directional diffuse*, and *uniform diffuse*. In reality, the in-plane plots of most surfaces will tend to display some combination of the three behavior types.

Theoretical in-plane plots for these classifications are displayed in the polar plots of figure 5.1., as published by He, *et al* (1991). These plot the BRDF for a series of illumination angles (normalized to the BRDF for the respective specular angles). Figure 5.1.a displays strong specular behavior with a narrow lobe width. Figure 5.1.b

shows strong directional diffuse with a 'fattening' of the lobe and an increase in the magnitude as the illumination angle increases. Figure 5.1.c shows strong uniform diffuse characteristics with a fairly uniform lobe that becomes more directional at increased illumination angles. Finally, figure 5.1.d displays the dramatically increasing reflectivity at high view angles (grazing angles) for diffuse surfaces.

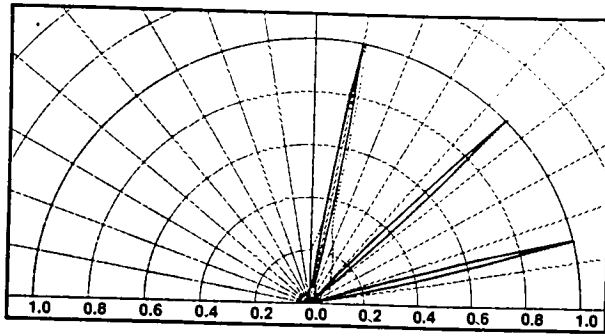


figure 5.1.a Strong Specular Characteristic
(for incidence angles 10, 45, & 75)

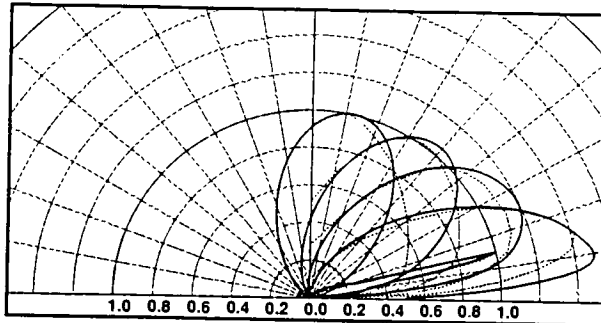


figure 5.1.b Strong Directional Diffuse Characteristic
(for incidence angles 10, 30, 45, 60, & 75)

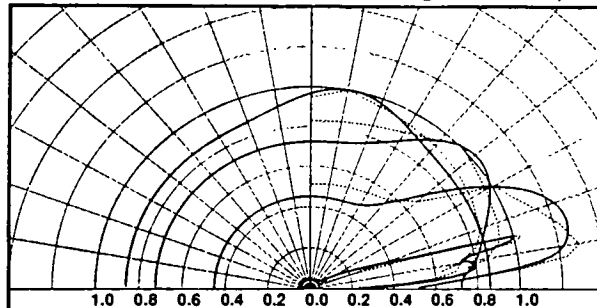


figure 5.1.c Strong Uniform Diffuse Characteristic
(for incidence angles 10, 45, 60, & 75)

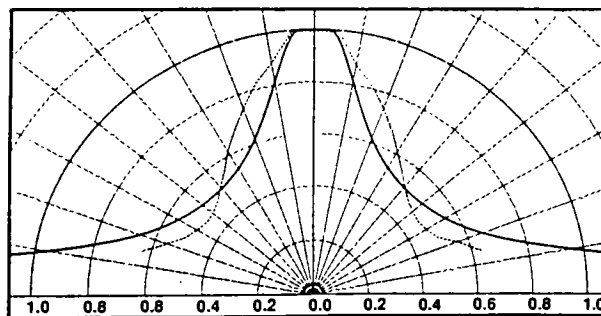


figure 5.1.d 'Grazing' Angle Characteristic
of Diffuse Surfaces
(for incidence angle of 0)

The in-plane reflectance versus view angle plots of an *actual* surface are contained in figures 5.2.a-c, as published by Feng (1990). These plots show the characteristics of roofing material, which is a mostly diffuse surface. They display effects of back scatter and increased magnitude with increased illumination angle.

By measuring the reflectivity at view angles throughout the hemisphere, a plot of the full hemispheric BDRF effects can be formed. These plots give a comprehensive portrayal of the modification energy undertakes as it is reflected in various directions. Figure 5.2.d contains Feng's (1990) full hemispheric BDRF plots for the roofing material at both 15 and 45 degrees view angle. These display a uniform diffuse reflectance at view angles outside the specular lobe. The height of the specular lobe is greatest at the in-plane specular viewing position. Note the scale is not the same between the plots, which makes it difficult to observe that the out-of-plane plateau is of similar magnitude in each.

Since this study is geared towards a remote sensing SIG application, the primary concern is to account for the *major* reflectance characteristics of a surface. Feng's plots show how in-plane measurements sufficiently represent all the

main characteristics observed in full hemispheric measurements. For diffuse surfaces such as roofing material, the out-of-plane plateau of the full plot is similar in magnitude to the non-lobe level of the in-plane plot. Also, the magnitude of the full plot's specular lobe, as well as back scatter lobe, is at a maximum within the illumination-target-sensor plane. For strongly specular surfaces with narrow lobes, it is intuitive that the full BDRF plots will add little information about the reflective characteristics.

Therefore, enough information should be inherent in in-plane data to meet our goal of creating view angle dependent reflectivity components that incorporate critical reflectivity effects. The only added information from full hemispherical plots are the azimuthal dispersion of the specular lobe and the levelling off, or plateau, formed over much of the out-of-plane view angles. Within this study, the lobe width is considered symmetrical and the plateau is treated as uniform.

Similar findings are also displayed by Feng's in-plane and full hemispherical BDRF plots of sandpaper (figures 5.3.a-d). These plots depict a diffuse surface like the roofing material, only without the clear back scatter.

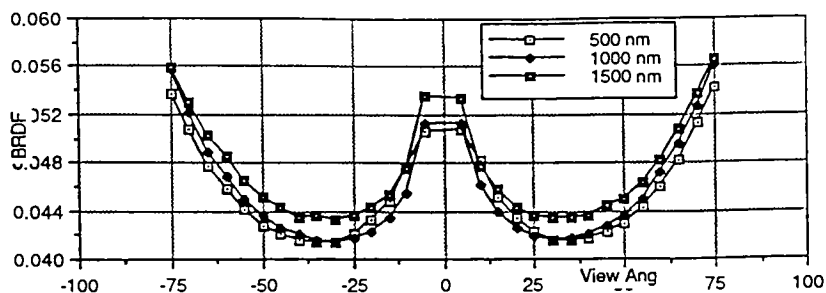


figure 5.2.a In-Plane BDRF of Roofing Material
(at incidence angle of 0 degrees)

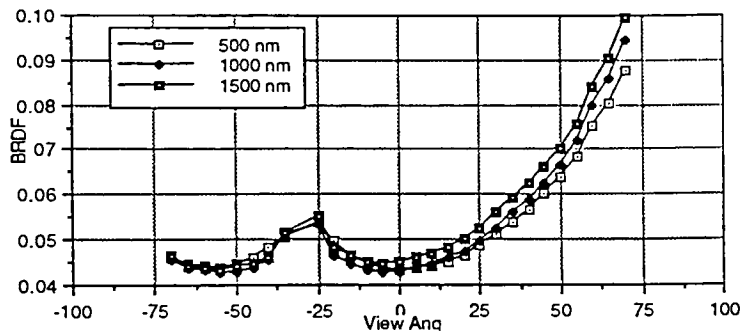


figure 5.2.b In-Plane BDRF of Roofing Material
(at incidence angle of 30 degrees)

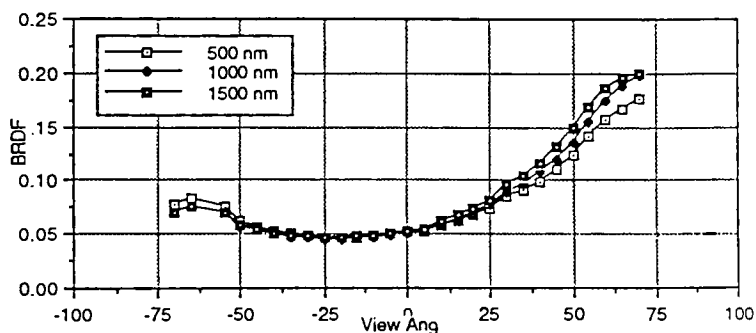


figure 5.2.c In-Plane BDRF of Roofing Material
(at incidence angle of 60 degrees)

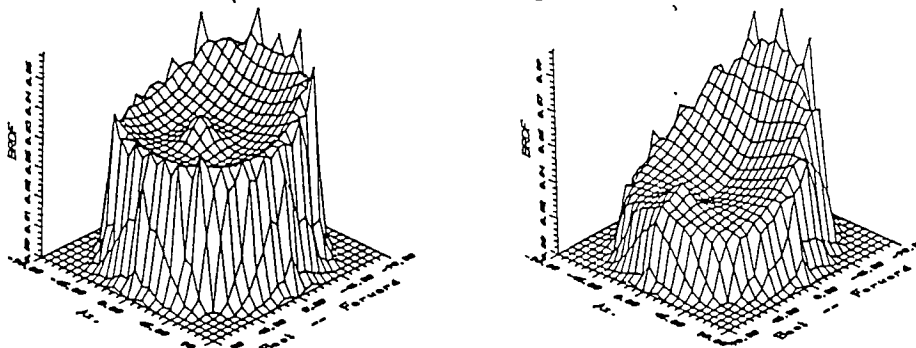


figure 5.2.d Hemispheric BDRF of Roofing Material
(at incidence angles of 15 and 45 degrees)

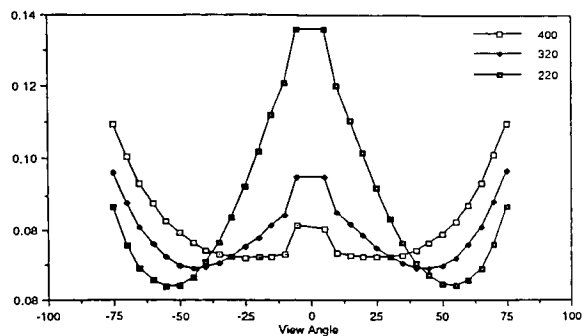


figure 5.3.a In-Plane BDRF of Sandpaper
(at incidence angle of 0 degrees)

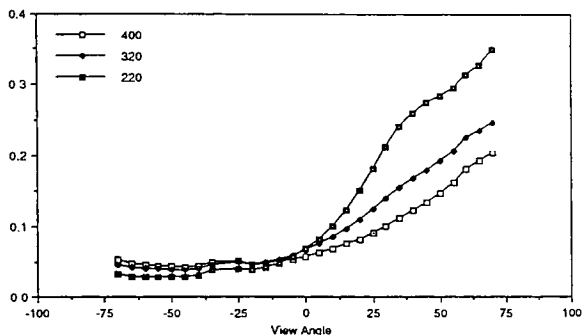


figure 5.3.b In-Plane BDRF of Sandpaper
(at incidence angle of 30 degrees)

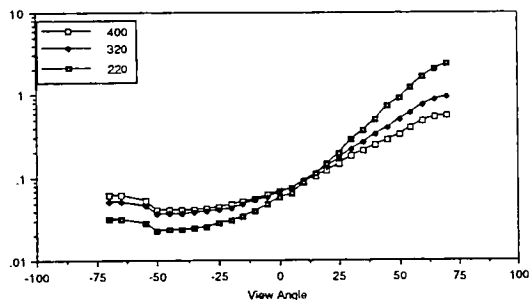


figure 5.3.c In-Plane BDRF of Sandpaper
(at incidence angle of 60 degrees)

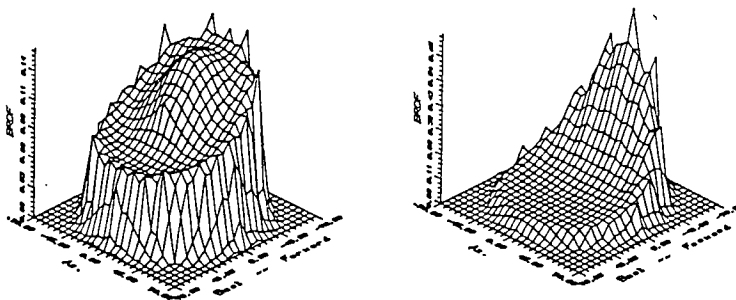


figure 5.3.d Hemispheric BDRF of Sandpaper
(at incidence angles of 15 and 45 degrees)

5.2 Characterizations of Surface Samples for this Study

For this study, the reflectance characteristics of the surfaces used in the modeled scene were acquired by observing in-plane BDRF measurements. These measurements were made with the apparatus and techniques developed by Feng (1990 and 1992) for the DIRS Lab. This entailed measuring BDRF over a series of in-plane view angles for a particular illumination angle, over a set band. Overall, 20 in-plane scans were performed per material, each resulted in a plot similar to those of Feng's shown previously.

band (blue,green,red,NIR)	4
illumination angle (8,30,45,60,75)	5
view angles (8,30,45,60,75,90,-75,-60,-45,-30,-8)	<u>11</u>
TOTAL IN-PLANE SCANS:	20

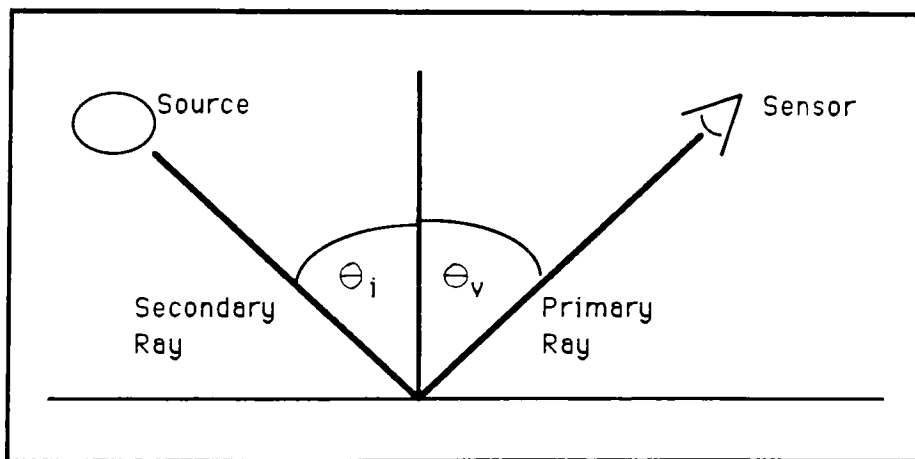


Figure 5.4 Angle Definition for In-Plane Scans

A total of 12 surfaces were intentionally used for this study and their selection is discussed in section 6. Samples of these surfaces were measured in the laboratory to get in-plane BDRF data. Three of these surfaces are discussed in this section. They are; a rough surfaced green painted wood panel, a "less-rough" surfaced white painted wood panel, and a smooth surfaced glossy grey painted wood panel. The in-plane plots for the remaining surfaces can be found in the appendix.

The green panel surface was prepared by mixing a heavy concentration of sand in a flat green paint, and then applying it to a plywood panel. The in-plane measurement data are displayed in figure 5.5. Overall, these plots characterize the surface as diffuse. The evident effects include the lack of a defined specular lobe, a fairly uniform magnitude over all non-grazing view angles, and a noticeable increase in magnitude at grazing angles. This grazing angle effect is more evident as the illumination increases. There is also a slight back scattering effect observed.

The white panel surface was prepared by applying a flat white paint (with no sand) to a roughened plywood panel. The in-plane measurement data is displayed in figure 5.6.

Overall, these plots characterize the surface as non-uniformly diffuse. The evident effects include the emergence of a defined specular lobe and obvious grazing angle effects. Also evident on this surface is a well defined back scatter.

The specular panel surface was prepared by applying a high gloss grey paint to a smooth plywood panel. The in-plane measurement data are displayed in figure 5.7. Overall, these plots characterize the surface as specular. The evident effects include a clearly defined specular lobe and a low, fairly uniform magnitude over all non-specular view angles. The magnitude of the specular lobe also increases with increasing illumination angle as expected.

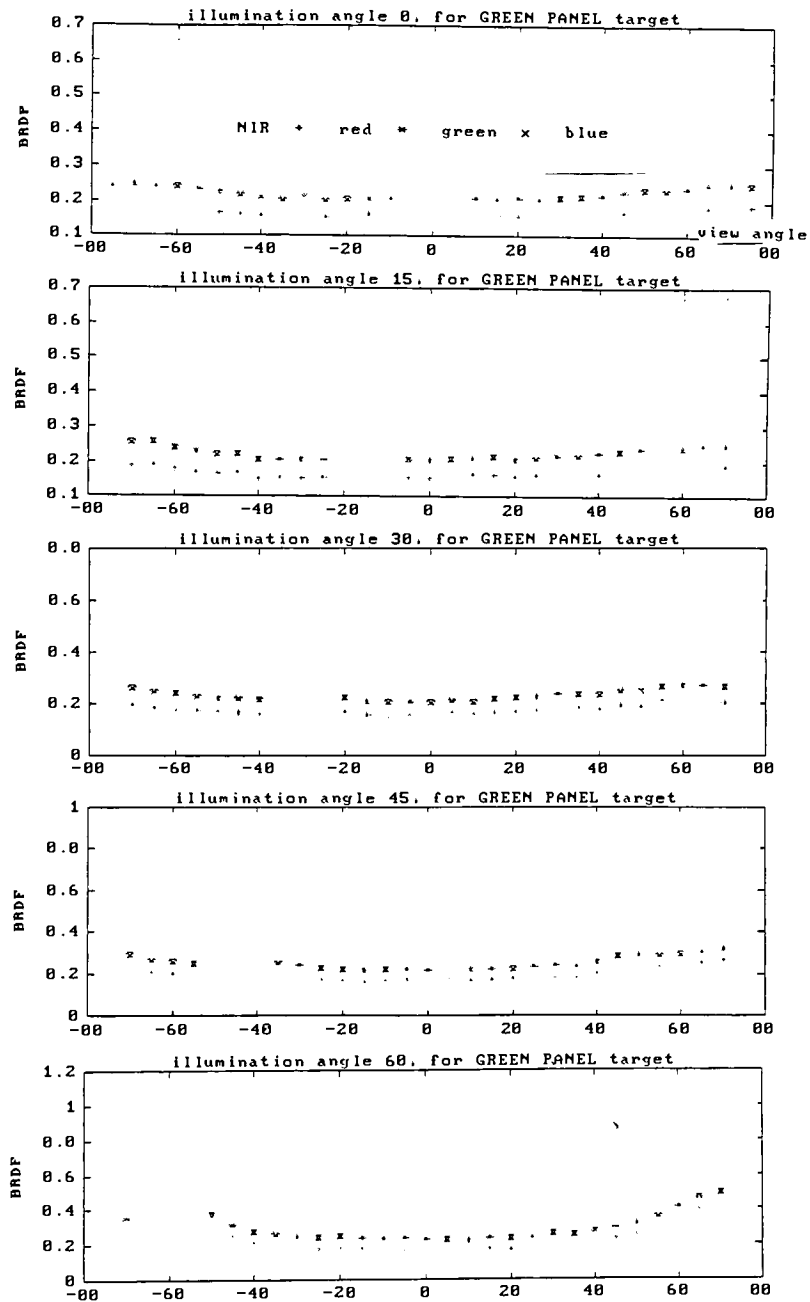


Figure 5.5 In-Plane BRDF Measurements of Green Panel Sample

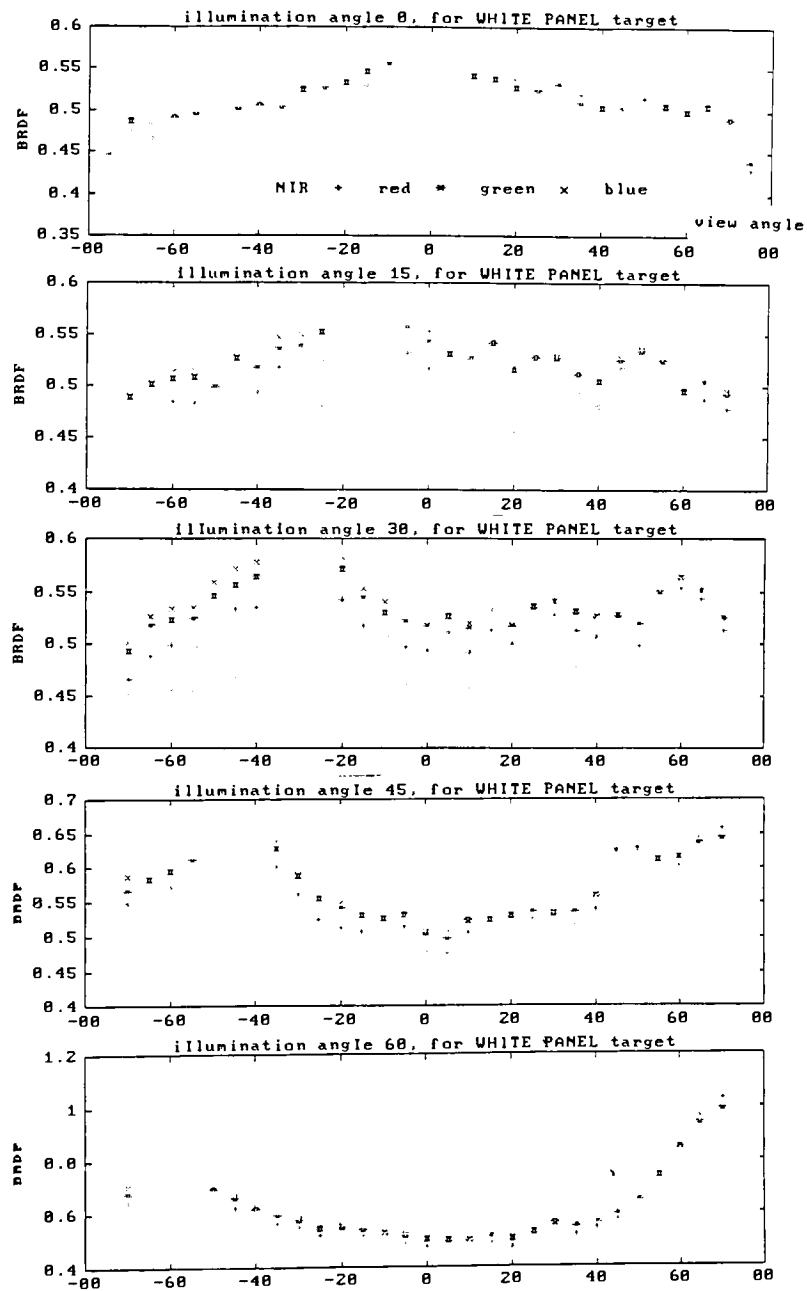


Figure 5.6 In-Plane BDRF Measurements of White Panel Sample

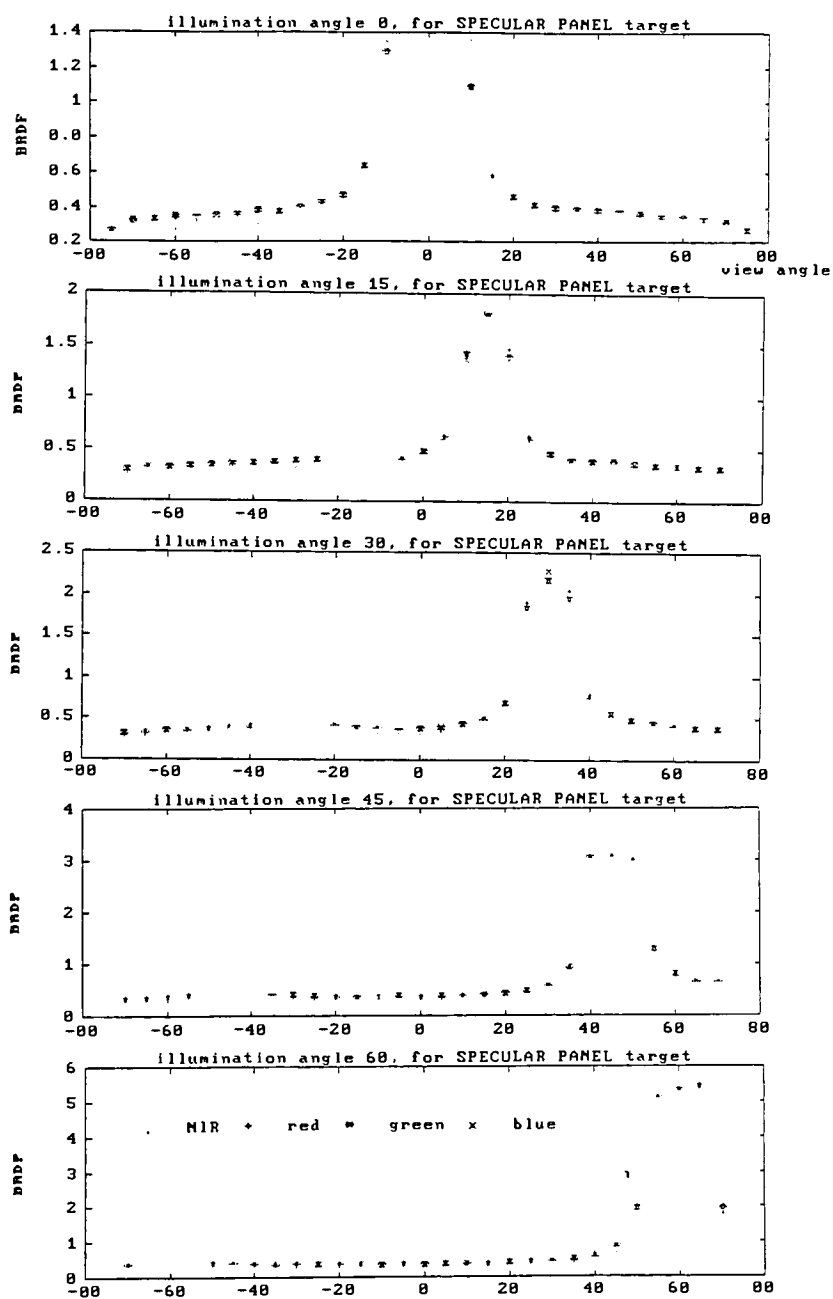


Figure 5.7 In-Plane BDRF Measurements of Specular Panel Sample

To provide data for assessments of assumptions made later in generating the reflectivity components, an "out-of-plane" BDRF scan was also accomplished for the same subset of surface samples. The out-of-plane scan represents a 0-180 degree view angle scan whose plane is 90 degrees apart (in the azimuthal) from the 0-90 degree illumination angle scan plane. The out-of-plane data are displayed in figures 5.8, 5.9, and 5.10. All the surfaces displayed the expected symmetrical plot with increasing values at lower view angles. The increase at the lower view angles is from "picking-up" part of the specular lobe effects due to the sensor's proximity to the illumination-target plane.

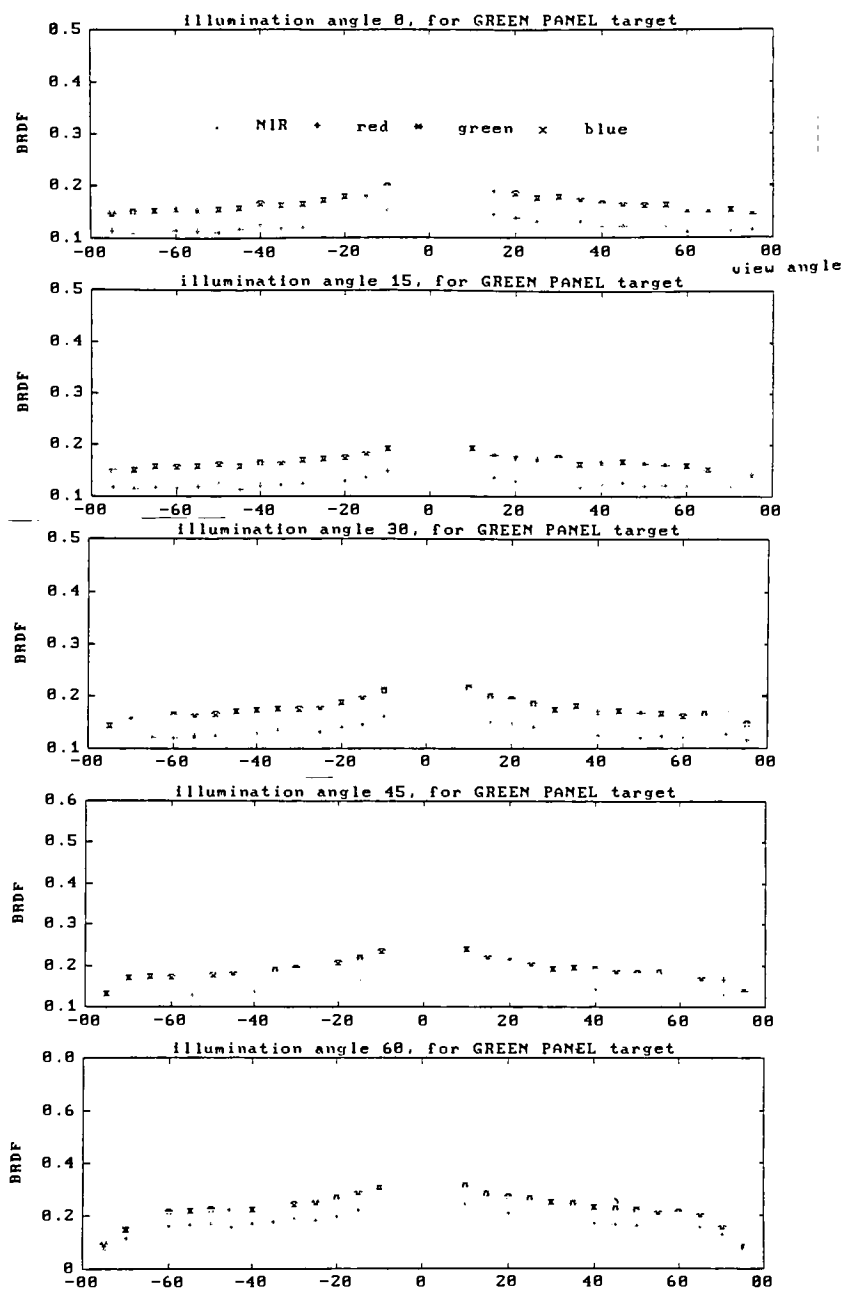


Figure 5.8 Out-of Plane BRDF Measurements of Green Panel Sample

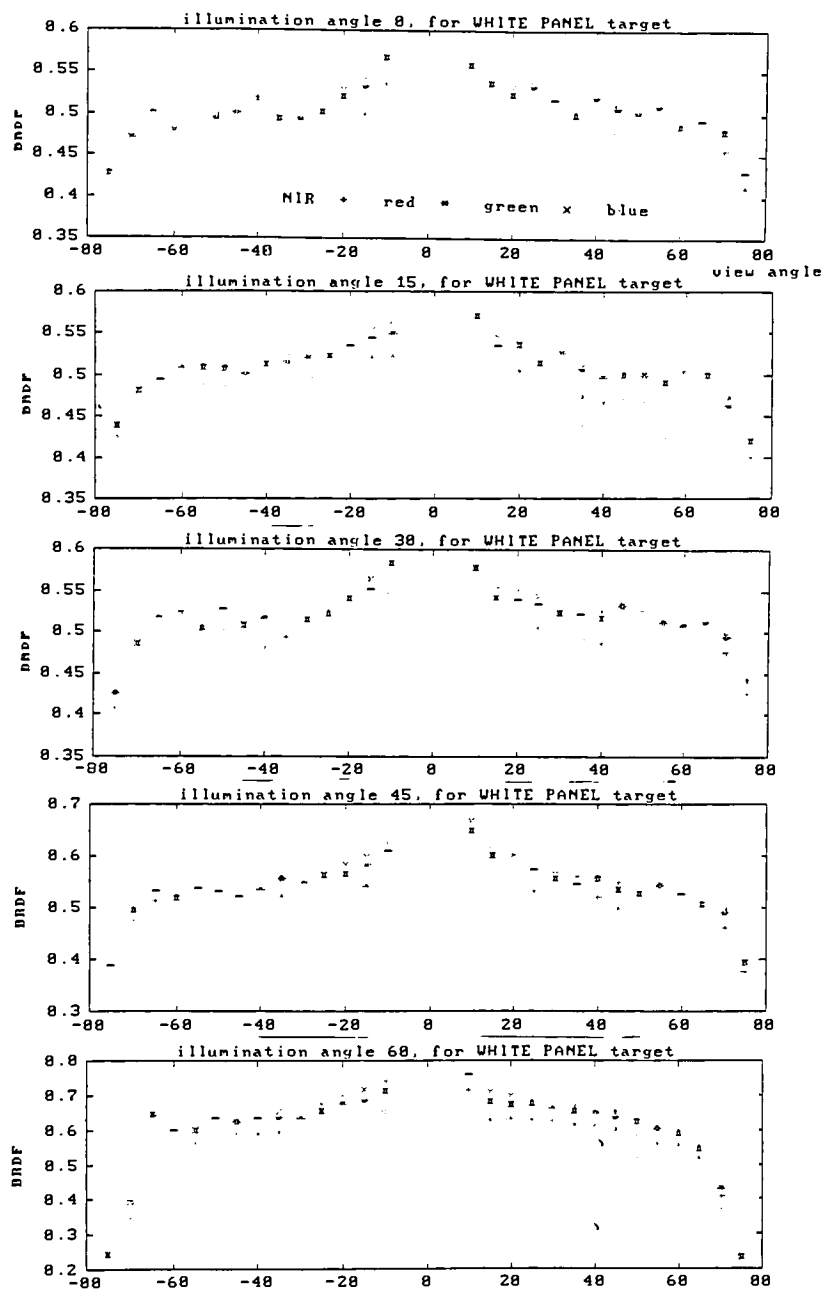


Figure 5.9 Out-of-Plane BDRF Measurements of White Panel Sample

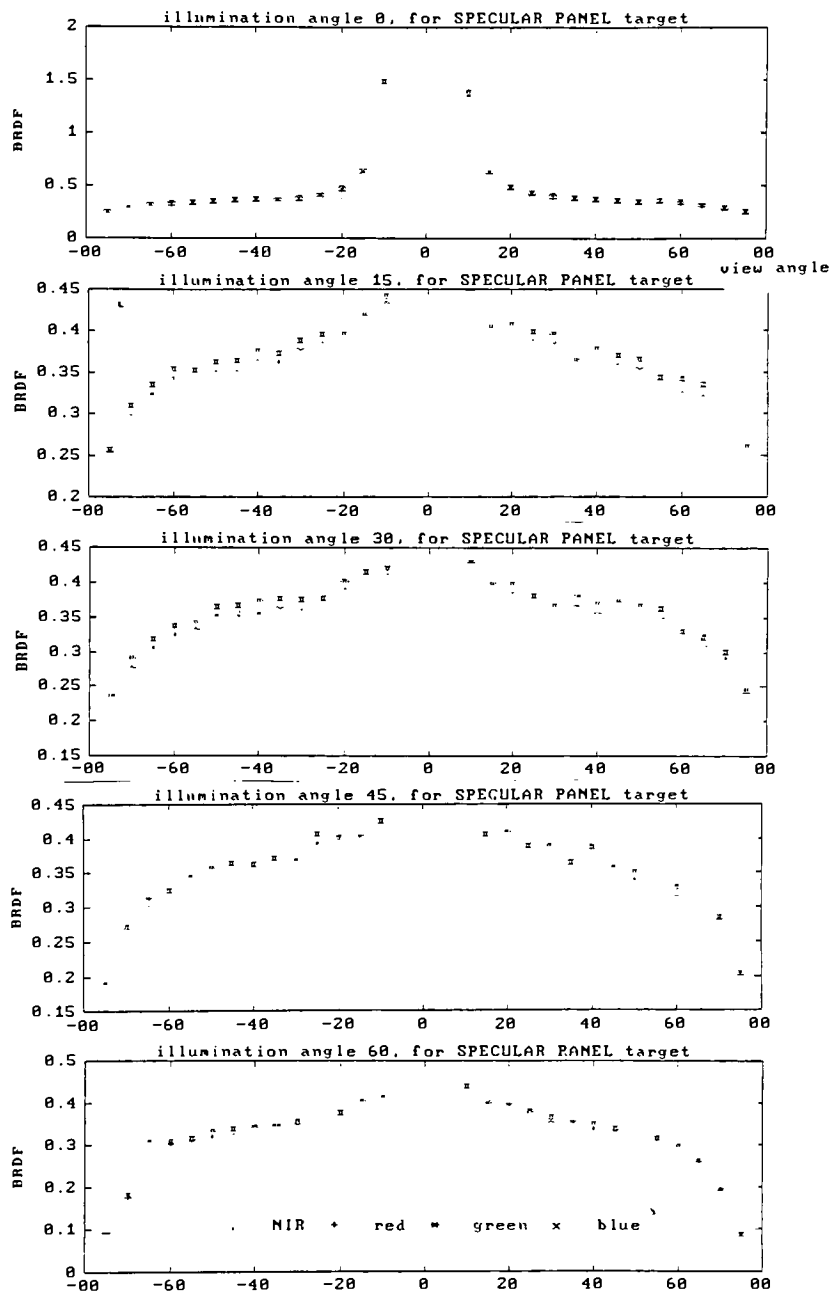


Figure 5.10 Out-of-Plane BRDF Measurements of Specular Panel Samp

5.3 Generation of Reflectivity Components

Sections 5.1-2 described how much of a surface's reflectivity characteristics can be captured by in-plane scans. This section will describe how the data from these in-plane scans will be transformed into reflectivity components applicable to DIRSIG.

How They Are Used

To better understand the approach taken in deriving the reflectivity components, it is helpful to look further into how the DIRSIG model uses them to assess the energy incident onto a surface. The incident energy can consist of a combination of solar irradiance, atmospheric downwelling radiance, and reflected radiance from background objects. DIRSIG will assess this energy first from the specular perspective and then from the diffuse perspective (see figure 5.11). For the specular radiance component, DIRSIG assesses only the energy incident within the specular angle and will attenuate it by the specular reflectivity component (R_s). For the diffuse radiance component, DIRSIG assesses all energy incident from the hemisphere and will attenuate it by the diffuse reflectivity component (R_d). For some

surfaces, the energy incident within the specular angle (defined by the viewer) has a greater reflection due to the presence of a well defined specular lobe.

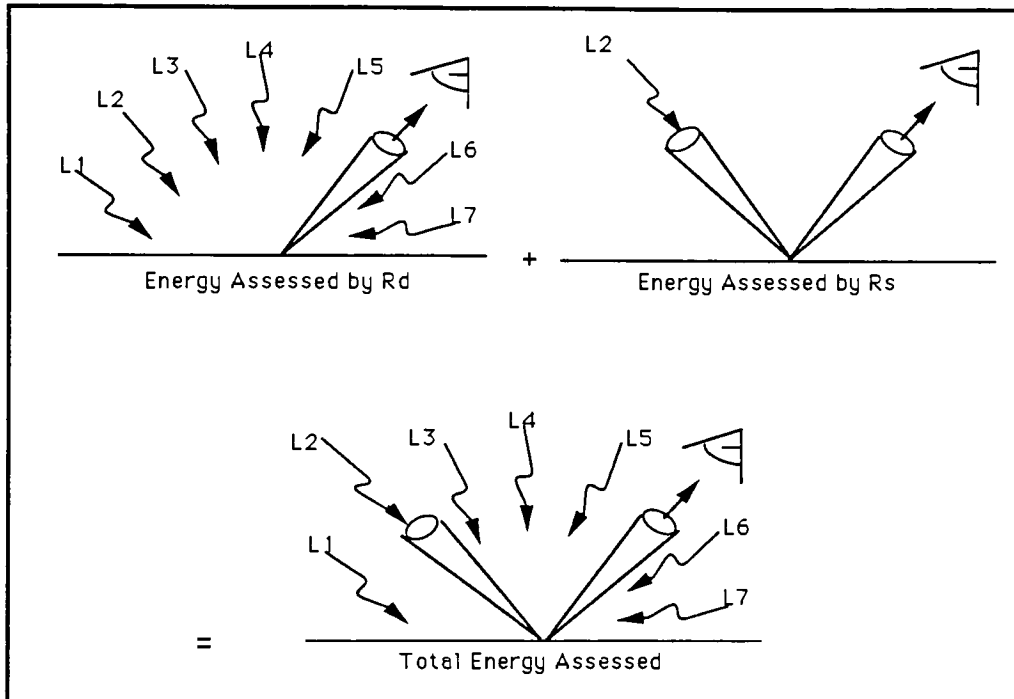


Figure 5.11 Representation of DIRSIG Energy Assessment

What They Represent

The reflectivity components represent the potential for reflecting incident energy towards a given direction. In particular, the specular reflectivity component represents the transfer of incident energy from a specific angle to a specific viewing location. A proper model for this transfer

is defined by the surface's BDRF. On the other hand, the diffuse reflectivity component represents the energy reflected into one direction resulting from incident radiation from all directions. The proper model for this transfer is the surface's hemispherical-directional reflectivity, as defined in section 2.2.

Figure 5.11 exhibits how the modified DIRSIG algorithm assesses energy from location L2 with both reflectivity components. If the "full energy" of the BDRF and hemispherical-directional reflectivity models were applied to the radiance algorithm, excess energy would be accounted for due to "double dipping". This would be more apparent in surface's with a well defined specular lobe.

In reality, these two components don't exist independently, but rather as some combination that represents a surface's degree of "specularity" or "diffuseness". The specularity can be defined as the ratio of the amount of incident energy transferred in the specular direction, to the amount transferred into all directions. Conversely, the diffuseness can be defined as the ratio of the amount of incident energy transferred into all but the specular directions, to the amount transferred into all directions. The term "specular direction" infers some solid angle and

the size of this is open for interpretation.

Furthermore, the location of the sensor is the primary orientation parameter in both the diffuse and specular rendering techniques. It is logical to conclude that the reflectivity components must be view angle dependent. Additionally, DIRSIG assumes all surface reflectances are non-rotationally variant with respect to a particular source-sensor orientation. In other words, if the target is rotated within the scene while the source-sensor positions are held constant, the BRDFs would not change. Therefore the components are view angle dependent on zenith angle only.

The reflectivity components used by DIRSIG are defined as follows:

Diffuse Reflectivity Component = $R_d(\theta_v)$

where, $R_d(\theta_v) = d * R_d'(\theta_v)$
 d = diffuseness
 $R_d'(\theta_v)$ = hemispherical-diffuse reflectivity

Specular Reflectivity Component = $R_s(\theta_v)$

where, $R_s(\theta_v) = s * R_s'(\theta_v)$
 s = specularity = $1 - d$
 $R_s'(\theta_v)$ = bidirectional reflectance factor

The following discussion provides another view of what the reflectivity components represent. Ideally, the best method

of assessing the energy reflected from a surface is by integrating the incident radiance modified by the BRDF over the hemisphere (figure 5.11.A and equation 5.1.).

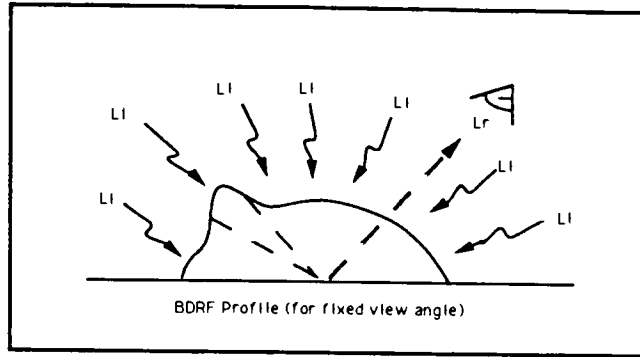


Figure 5.11.A Reflected Energy Assessment

$$L_r = 1/\pi \int_{\text{hemisphere}} \text{BDRF } L_i \cos\theta_i d\omega_i \quad (5.1)$$

As previously discussed, this would require a massive data base and significant computing power. Therefore, this study addresses the radiance-surface interaction by combining the existing specular and diffuse rendering techniques. The diffusely reflected energy is described by integration over the entire reflectivity profile, minus the specular lobe.

$$L_{r \text{ diff}} = 1/\pi \int_{\text{hemisphere - specular lobe}} \text{BDRF } L_i \cos\theta_i d\omega_i \quad (5.2)$$

Conversely, the specular reflected energy is described by integration over the specular lobe portion of the profile.

$$L_{r \text{ spec}} = 1/\pi \int_{\text{specular lobe}} \text{BDRF } L_i \cos\theta_i d\omega_i \quad (5.3)$$

In both cases, the reflectivity and radiance are modified by a geometric factor dependent on the specular lobe width. This lobe width will always be relatively small compared to the entire hemisphere. Therefore, as shown in equation 5.4, the value of this factor nears unity for the diffuse energy component. Similarly, the factor nears zero for the specular energy component and serves to attenuate the large specular reflectivity values of highly specular surfaces.

$$\frac{1}{\pi} \int_{\text{hemispec lobe}} \cos\theta_i d\omega_i = \frac{1}{\pi} \int_0^{2\pi} \int_0^{\pi/2} \cos\theta_i \sin\theta_i d\theta_i d\phi_i = \frac{1}{\pi} * \pi = 1 \quad (5.4)$$

These factors are related to d and s used in this study. The values for s will be near zero and the values for d will be near unity. However, d and s also include the magnitudes of the reflected energy (profile height). This will adjust the values according to the specular characteristics of the surface. Thus, s will be higher for a more specular surface, even though the lobe width is decreasing.

5.3.1 Generating $Rd'(\theta_v)$

As stated, the hemispherical-directional reflectivity of a surface is a good representation of $Rd'(\theta_v)$. This reflectivity was described by equation 2.5. Assuming uniform incident intensity for each incident direction

(which is true with Feng's apparatus), this reduces to:

$$R_{\text{hem-dir}} = \int_{\text{hem}} \text{BRDF} \cos\theta_i \, d\omega_i \quad (5.5)$$

The value of $R_{\text{hem-dir}}$ can be found by integrating a set of complete hemispherical BDRF data as follows:

$$R_{\text{hem-dir}} = \frac{1}{\pi} \sum_{\Phi_i=0}^{2\pi} \sum_{\theta_i=0}^{\pi/2} (\text{BRDF} \cos\theta_i \sin\theta_i \Delta\theta_i) \Delta\Phi_i \quad (5.6)$$

However, it is more practical to approximate $R_{\text{hem-dir}}$ by integrating over an in-plane BDRF data set only, where the summation over Φ equals π . This assumption provides a practical method of generating $R_d'(\theta_v)$.

$$R_d'(\theta_v) = R_{\text{hem-dir}}(\text{in-plane}) \quad (5.7)$$

This in-plane approximation is supported by sections 5.1-2, which demonstrated that the in-plane data set incorporates all the major surface reflectance characteristics contained in the larger hemispherical data set. Also, computation of $R_d'(\theta_v)$ through integration essentially averages out a large portion of the angular information found in BDRF data anyway. Finally, the overall DIRSIG model contains other significant approximations and assumptions that lessen the necessity of the more intensive method.

Therefore, the in-plane approximation of equation 5.6 was used to generate $R_d'(\theta_v)$. This approximation was assessed by comparing the generated values against values computed using a full integration with inclusion of the out-of-plane measurements. The results are presented in section 5.4.

Generating $R_d'(\theta_v)$ With In-Plane Approximation

Within an in-plane BDRF data set, for each view angle there are nine BDRF values corresponding to measurements taken at different illumination angles. (The negative view angle measurements were used to represent negative illumination angles for the corresponding positive view angle.) To determine the component value for a particular view angle, the integration is calculated over the nine illumination angle BDRFs. Figure 5-12 shows the positive illumination angle points used for determining R_d' , at $\theta_v = 30$ degrees.

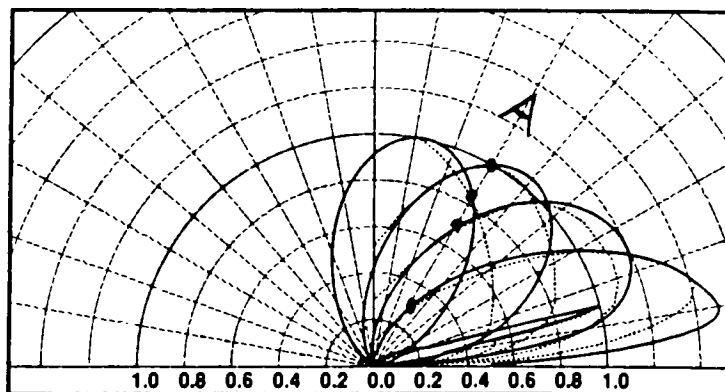


Figure 5.12 Points Used for Averaging to Determine $R_d'(\theta_v)$
[He, et al, 1991]

Note that the diffuse reflectivity component will incorporate the directional diffuse characteristics of a surface reflectance. Referring to the reciprocity of reflectivity, a directionally diffuse lobe will increase the amount of energy reflected by the target surface from illumination just outside the specular illumination angle (see figure 5.13). In other words, if energy is incident within the width of the reciprocal specular lobe, then more of that energy will be reflected by the surface into that view angle. The averaging of the non-specular portions of the lobe in deriving the diffuse component will serve to pick-up any effects from lobe widths, and increase the value of $R_d'(\theta_v)$. This will better account for the proportion of incident energy actually reflected to the sensor.

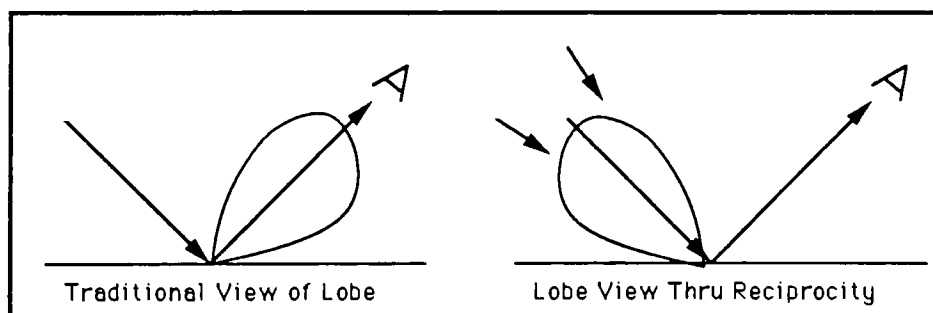


Figure 5.13 A Look at Reflectivity Reciprocity

Actual implementation of this in-plane averaging technique required three approximation steps to be made.

- *First*, the reflectivity component data base needed to include view angles up to 90 degrees, while the Feng apparatus measured scans only up to view angles of 70 degrees. This was "filled in" by regressing the component values of 60, 65, and 70 degrees, and extrapolating a line from 70 to 90 degrees. This approximation is not a crucial one, since the scene to be implemented has a maximum target view angle of approximately 70 degrees.

- *Secondly*, DIRSIG requires view angle dependent components at one degree increments, while the Feng apparatus measured angle increments of 5 degrees. A cubic spline interpolation was employed for expansion of the data.

- *Finally*, this approach was unsuccessful when applied to highly specular surfaces whose specular lobe BDRF maximum was $\gg 1.0$ reflectivity units. It is documented by Siegal and Howell (1981) that the use of bidirectional reflectivity "can be of less practical value" if a surface tends to be highly specular. For these materials, the averaged diffuse component was pulled too high by the large peak values. Therefore, for highly specular materials, the specular lobes

were omitted from the calculations. The only effect this would have, will be on "missing" any lobe width difference between two highly specular materials. With the coarseness of the current scan increments, it is doubtful that such a difference would be effectively "picked up" anyway.

5.3.2 Generating $R_s'(\theta_v)$

Like the diffuse component, the specular reflectivity component was derived from the "in-plane" BDRF data measured on Feng's apparatus. As stated earlier, the measured BDRF of a surface is a good representation of $R_s'(\theta_v)$. Within an in-plane BDRF data set, there are only five view angles measured that correspond to the specular angle of an actual illumination orientation. These were at 0, 15, 30, 45, and 60 degrees. The component value for these view angles are simply the corresponding measured BDRF.

Actual implementation of this in-plane averaging technique required two general approximation steps to be made.

- *First*, DIRSIG requires view angle dependent components at one degree increments. The Feng apparatus measured specular BDRF values at 15 degree increments. Thus, a cubic spline interpolation was employed for expansion of the data.

- *Secondly*, the reflectivity component data base needed to include view angles up to 90 degrees, and the measured specular BDRF values were limited to the highest illumination angle at 60 degrees. This was "filled in" by regressing the component values of 50, 55, and 60 degrees, and extrapolating a line from 60 to 90 degrees. Again, this approximation is not a crucial one, since the implemented scene has a maximum target view angle of approximately 70 degrees. Any error caused by the extrapolation within 10 degrees should be relatively minor.

5.3.3 Results of Generation of $R_d'(\theta_v)$ and $R_s'(\theta_v)$

Figures 5.14, 5.15, and 5.16 display the resulting diffuse and specular reflectivity component databases for the subset of the surfaces used in this study. These are found on the next three pages. The plots for the remaining surfaces are found in the appendix. Note that these databases will be further factored by the values for diffuseness and specularity found in the next section. These factors are considered constant over all view angles and will not effect the shape of the curve.

GREEN PANEL. The green surface's in-plane BDRF plot of figure 5.5 exhibits relatively uniform diffuse characteristics. No specular lobe is present and the grazing angle effects become significant above 60 degrees. Correspondingly, the reflectivity components for the green surface in figure 5.14 display the expected reflectance behavior. The diffuse component is fairly flat, with a slight upward slope at about 60 degrees. The specular component displays almost no specular behavior until about 50 degrees. Thus, both account for the emergence of the grazing effect. Note the increased slope for the NIR band of the specular component. This is due to the increased specular behavior of the surface at longer wavelengths.

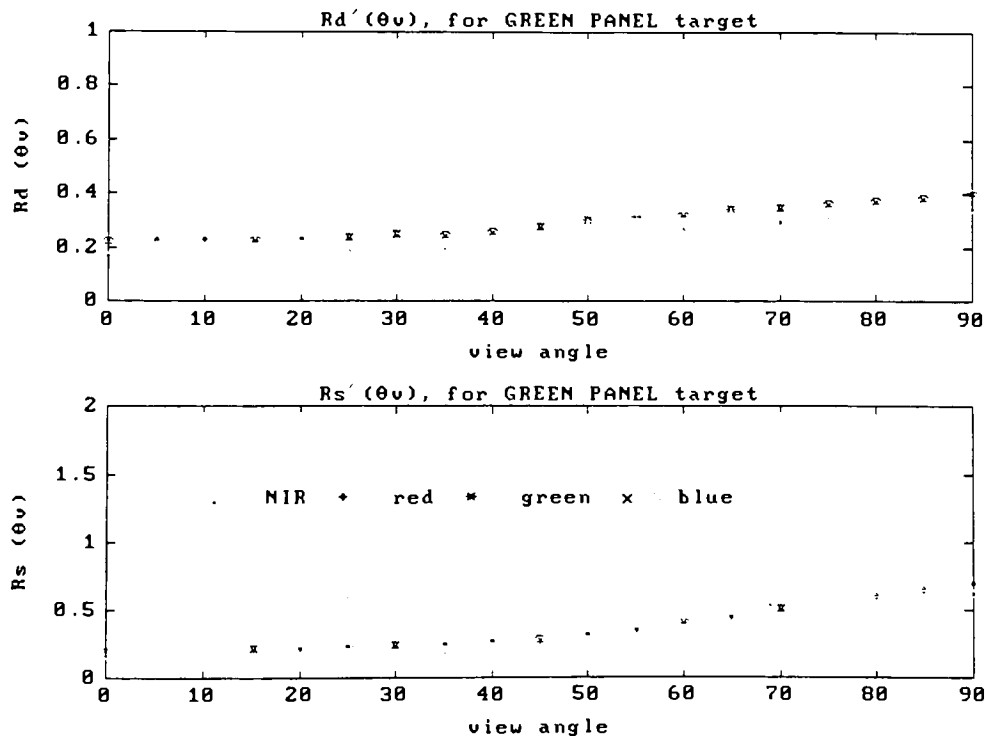


Figure 5.14 Reflectivity Components for Green Sample

WHITE SURFACE. The white surface's in-plane plot of figure 5.6 exhibits directional diffuse characteristics. A specular lobe is present, as well as a noticeable back scatter. The resulting reflectivity component plots in figure 5.15 represent a less diffuse surface. Both the diffuse and specular components display the emergence of a larger defined lobe at increasing angles through a steeper slope that begins to turn up at a slightly lower view angle.

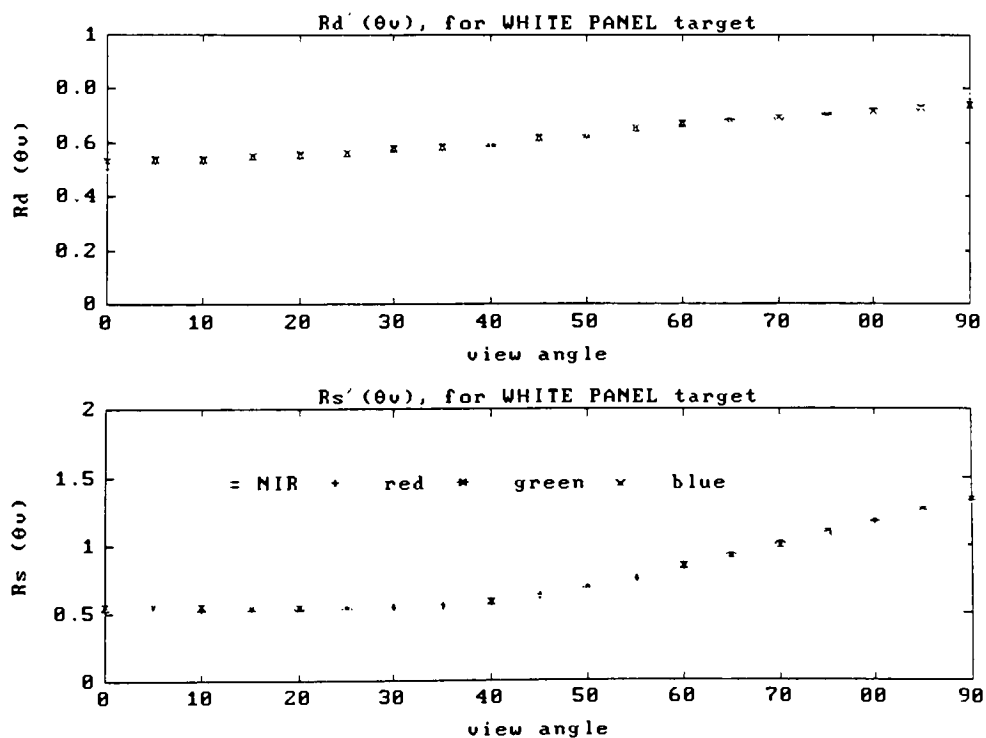


Figure 5.15 Reflectivity Components for White Sample

SPECULAR SURFACE. The specular surface's in-plane plot of figure 5.7 displays strong specular characteristics, and these are well represented by the reflectivity component plots of figure 5.16. The specular component exhibits an increasing slope over the entire plot, which indicates a grazing effect at increasing angles. The diffuse component shows a negative slope at higher angles, which represents the increased specularity at these higher angles and lack of any substantial lobe width.

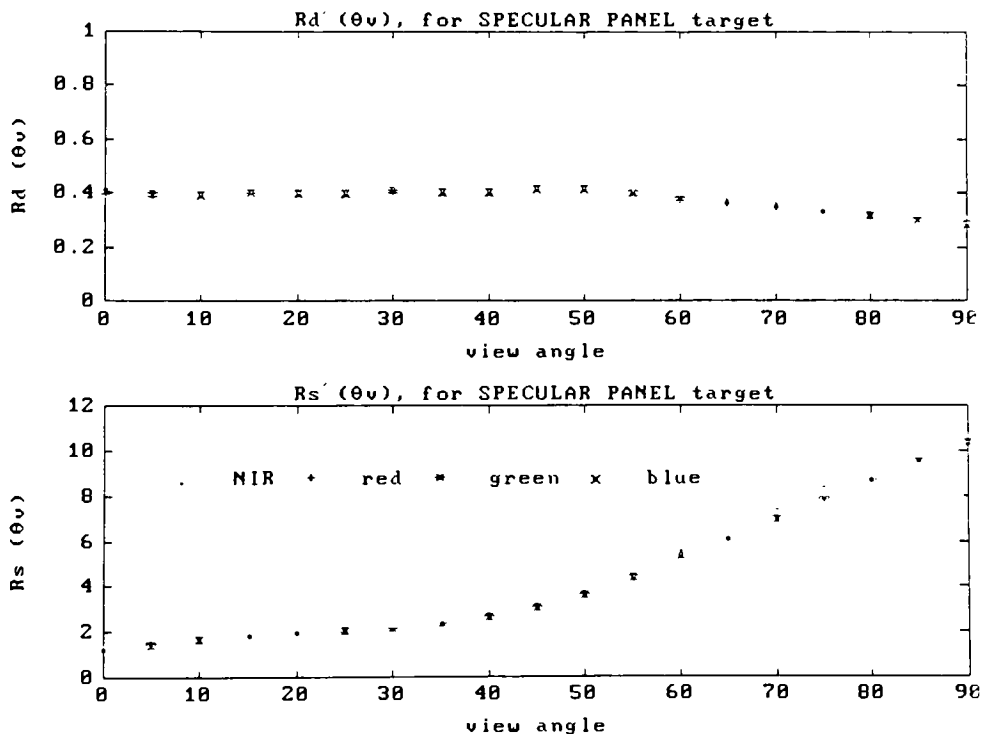


Figure 5.16 Reflectivity Components for Specular Sample

5.3.4 Calculation of Diffuseness and Specularity

While the values found for $R_d'(\theta_v)$ and $R_s'(\theta_v)$ incorporate the view angle dependent characteristics that can be exploited by the DIRSIG rendering technique, the values of diffuseness (d) and specularity (s) provide effective weights for each radiance component. As stated in section 5.3, the diffuseness is defined as the ratio of the amount of incident energy transferred into all but the specular directions, to the amount transferred into all directions of the hemisphere. Also, it was described that the specularity was simply the compliment of the diffuseness ($s = 1 - d$).

Diffuseness can be determined from BDRF measurements by applying equation 5.8, where non-specular angles refer to all angles other than in the specular direction.

$$d = \frac{\begin{array}{c} \text{(non-specular angles only)} \\ 2\pi \quad \pi/2 \\ 1/\pi \sum_{\Phi_i=0} \left(\sum_{\theta_i=0} \text{BDRF} \cos\theta_i \sin\theta_i \Delta\theta_i \right) \Delta\Phi_i \end{array}}{\begin{array}{c} \text{(all angles)} \\ 2\pi \quad \pi/2 \\ 1/\pi \sum_{\Phi_i=0} \left(\sum_{\theta_i=0} \text{BDRF} \cos\theta_i \sin\theta_i \Delta\theta_i \right) \Delta\Phi_i \end{array}} \quad (5.8)$$

A problem is realized when calculating diffuseness from an in-plane data set. The values are pulled artificially low due to consideration of non-specular angles within a single plane. Intuitively, the values of d would be closer to

unity if full hemispherical data was considered. However, this will require more data than originally desired and the quality of the value is still suspect due to the coarse integration steps resulting from measurement limitations.

Alternatively, a simple solution would be to measure the total reflectivity of the sample with an integrating sphere. Most of these devices allow operation in two modes, one that measures energy reflected into the entire hemisphere and one that measures all *but* the energy reflected into the specular direction. The ratio of these two values can be used to determine the value of "d" very quickly.

In all of these techniques, the width of the excluded solid angle in the specular direction is open for interpretation. For the BDRF integration method, a specular cone of ± 5 degrees was applied. For the integrating sphere, the Munsell Color Lab's portable Minolta Spectrophotometer CM-2002 was used (with unknown omitted specular cone size). The results from each of these techniques are provided in table 5.1. Initial tests proved the values for "s" from the BDRF measurement methods were too high, resulting in excessive saturation. Therefore, the diffuseness and specularity values from the integrating sphere method were applied in this study.

<u>Material</u>	Integration of In-Plane Data		Integration of Hemispherical Data		Integrating Sphere	
	<u>d</u>	<u>s</u>	<u>d</u>	<u>s</u>	<u>d</u>	<u>s</u>
Green Panel	.86	.14	.98	.02	.99	.01
White Panel	.86	.14	.98	.02	.98	.02
Specular Panel	.53	.47	.89	.11	.96	.04

Table 5.1 Measured Diffuseness and Specularity

For each material, the values for d and s will be multiplied by $R_d'(\theta_v)$ and $R_s'(\theta_v)$, respectively, to create the final reflectivity values of $R_d(\theta_v)$ and $R_s(\theta_v)$. These values were used by the DIRSIG algorithm for the reflectivity components.

5.4 Assessment of Reflectance Generation Method

This section describes the estimated error for the generated reflectivity components. No error was attached to the theoretically derived, empirically generated, diffuseness and specularity factors. Therefore, all error is due to the generation of the $R_d'(\theta_v)$ and $R_s'(\theta_v)$ values.

Since the specular reflectivity component is directly proportional to the actual measured BDRF, the measurement error can be applied directly. The amount of measurement error for the BDRF technique was estimated by Feng (1990) to be approximately 1 percent.

The diffuse reflectivity component's error is estimated in two steps. First, determine the RMS difference between the $R_d'(\theta_v)$ values generated by in-plane data and the more complete hemispherical-directional reflectivity values generated by integrating both in-plane and out-of-plane data. Secondly, these values are compounded with the measurement error of BDRF.

Figure 5.17 displays the plots of the hemispherical-directional reflectivity values calculated from equation 5.2 for the subset of samples. The corresponding $R_d'(\theta_v)$ values from in-plane data were shown in figures 5.14-16.

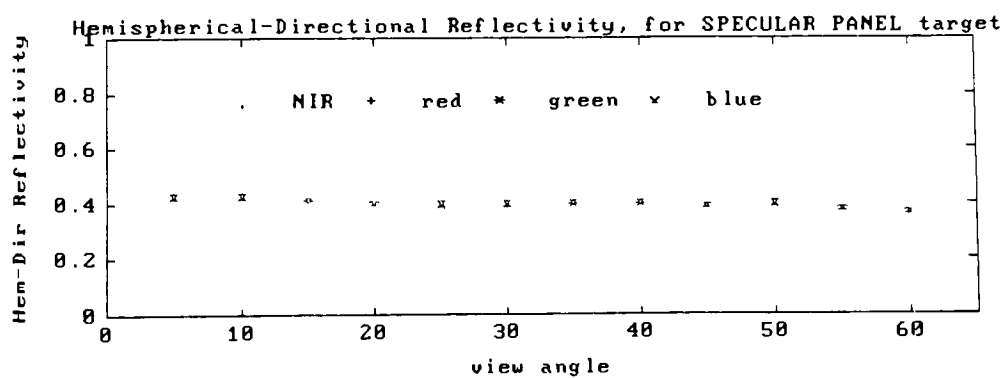
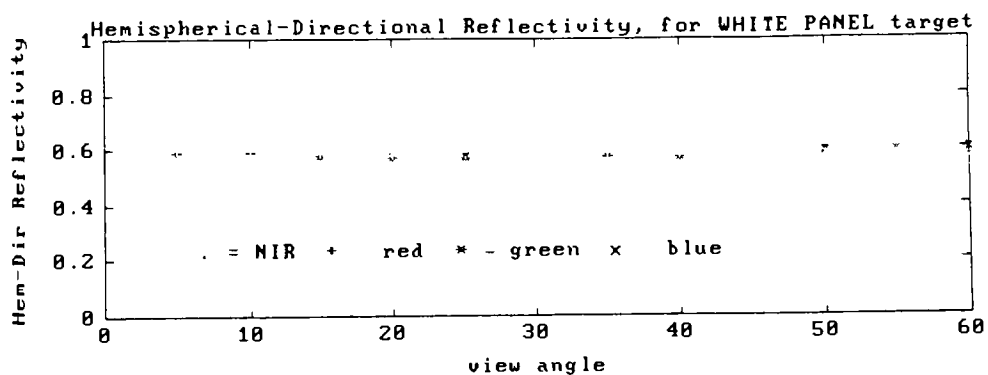
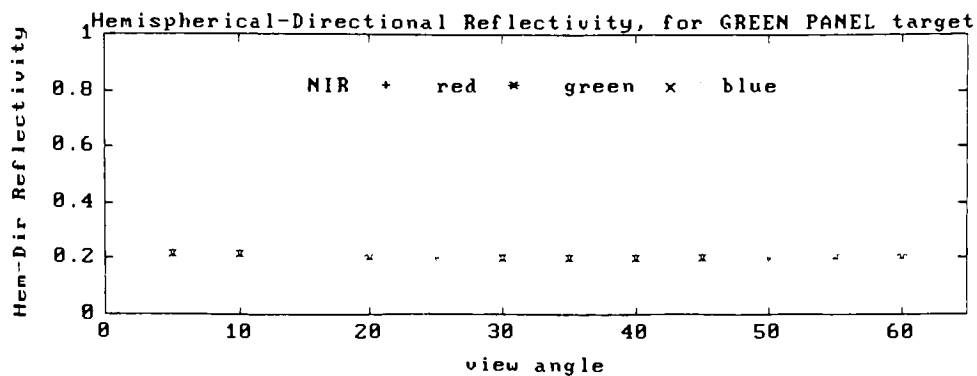


Figure 5.17 Hemispherical-Directional Reflectivity Values for Subset of Samples

The hemispherical-directional reflectivity values were not computed beyond 70 degrees, because those values would have been based on extrapolated data only. Thus, the RMS error was computed with data between 0 and 70 degrees view angle only. The RMS calculation is described in equation 5.9 and was applied over all measured angles in a given data set.

$$\text{RMS Error} = \left(\left(\sum_{k=1}^N (X_{\text{truth}} - X_{\text{experiment}})^2 \right) / N \right)^{0.5} \quad (5.9)$$

where, X is a data point
 N is the number of data pairs

<u>Surface</u>	<u>NIR</u>	<u>RED</u>	<u>GREEN</u>	<u>BLUE</u>
Green Panel	.039(.49)	.017(.16)	.022(.21)	.021(.20)
White Panel	.026(.50)	.032(.55)	.040(.58)	.044(.59)
Specular Panel	.017(.32)	.017(.39)	.018(.40)	.020(.39)

Overall	.029(.44)	.023(.36)	.029(.40)	.030(.40)

[This error is for data from 0 to 70 degrees view angle.
Average $R_d'(\theta_v)$ within parenthesis in reflectivity units.]
Table 5.2 RMS Error of In-Plane Assumption

Feng's estimated measurement percent error is applied to the average $R_d'(\theta_v)$ value for each in-plane data set to provide a measurement error in reflectivity units. Finally, this error is then compounded with RMS error by simply calculating the square root of the sum of the squares of the two errors. The 1 percent measurement error was much smaller than the RMS error, and its effect on the compounded error was insignificant. Therefore, table 5.2 summarizes the resulting RMS error for $R_d'(\theta_v)$ for each surface.

5.5 Models for Non-BDRF Measured Surfaces

What about materials not easily measured? In many instances, samples of scene objects are not conducive to laboratory analysis. A method was established to generate appropriate reflectivity components by creating "model" reflectivity component curves for five categories of reflectivity. In addition to these curves, diffuseness and specularity values will be assigned to each category. The categories selected for modeling are; highly specular, moderately specular, directional diffuse, moderately diffuse, and diffuse.

The sample set of materials discussed thus far were used to create models for three of the categories; moderately diffuse (green panel), directional diffuse (white panel), and highly specular (specular panel). Models for the other categories (highly diffuse and moderately specular) will be created by a "loose" interpolation from the other three.

The model reflectivity curves represent the percentage increase of energy reflected towards the sensor with increasing view angle. This will capture the general angular reflectivity characteristics of the various surface types. From the established reflectivity component data

bases for the green, white, and specular panels, the percentage changes in reflectivity were calculated for view angle increments 0 -> 25 degrees, 25 -> 50 degrees, and 50 -> 90 degrees. The moderately specular was then created by arbitrarily factoring the highly specular effects by 1/6. The highly diffuse was simply established as having no variability with view angle. Table 5.3 lists the model reflectivity curves.

Model Type	Band	Diffuse Component			Specular Component			"u"
		0->25	25->50	50->90	0->25	25->50	50->90	
Highly Diffuse	NIR	0%	0%	0%	0%	0%	0%	0
	RED	0	0	0	0	0	0	0
	GRE	0	0	0	0	0	0	0
	BLU	0	0	0	0	0	0	0
Moderately Diffuse	NIR	3%	16%	47%	13%	37%	88%	.8
	RED	5	22	41	9	47	145	1.0
	GRE	4	19	40	9	38	122	.9
	BLU	4	18	42	9	38	123	.9
Directional Diffuse	NIR	1	8	50	- 5	36	167	.9
	RED	4	5	34	+ 0.5	29	98	.9
	GRE	3	5	32	- 3	27	95	.9
	BLU	2	5	31	- 4.2	27	92	.9
Moderately Specular	NIR	.3	- 1.2	- 4	10	11	36	.4
	RED	.5	- 1.3	- 5	12	13	31	.4
	GRE	.5	- 1.2	- 5	7	13	31	.4
	BLU	.7	- 1.3	- 5	13	14	32	.4
Highly Specular	NIR	2	- 7	- 24	59	64	220	2.5
	RED	3	- 8	- 28	69	79	184	2.5
	GRE	3	- 7	- 30	71	78	186	2.5
	BLU	4	- 8	- 30	80	81	190	2.5

* "u" is a ratio of Rs(0)/Rd(0)

Table 5.3 Reflectivity Curves (Incremental Percent Increases)

Similarly, the values for diffuseness and specularity for the three materials in the sample subset were determined by direct measurement as described in section 5.3.4. The highly diffuse values are simply set at the extreme and the moderately diffuse values are set between the directional diffuse and highly specular. Table 5.4 lists these values.

<u>Model Type</u>	<u>Diffuseness (d)</u>	<u>Specularity (s)</u>
Highly Diffuse	1.00	.00
Moderately Diffuse*	.99	.01
Directional Diffuse*	.98	.02
Moderately Specular	.97	.03
Highly Specular*	.96	.04

* These values are based on actual measurements

Table 5.4 Diffuseness and Specularity Values

The following steps should be applied to generate a reflectivity database for surfaces not conducive to laboratory BDRF measurement.

- *First*, choose a category that best fits the material's general reflectivity characteristics.

- *Second*, determine a starting point for applying the appropriate diffuse reflectivity curve. A logical value will be the surface's normal hemispheric reflectance. This value is commonly defined as the proportion of energy reflected to the normal of the surface and is usually documented for most materials. If not, this value can be easily measured in the field with a portable instrument.

- *Third*, determine the starting point for the specular reflectivity curve by multiplying the diffuse starting point by the value "u" found in the table. This value is equivalent to the ratio $R_s(0)/R_d(0)$.

- *Fourth*, create the reflectivity curves by applying the percentage increases, beginning with the starting points, for each angle increment.

- *Fifth*, modify the diffuse and specular reflectivity curves with the appropriate values of *d* and *s*, respectively.

- *Finally*, create the reflectivity component database by interpolating the curve to create values at one degree increments.

For those surfaces in this study that could not be measured with the BDRF apparatus, the total diffuse reflectance values were obtained from a variety of sources. *These surfaces are described in section 6.1 when the scene set-up is presented.* For the CONCRETE and PAVEMENT, the values were derived from spectral total reflectivity curves plotted from measurements on a Shimadzu spectrophotometer and integrating sphere assembly. For GLASS, the value was "pulled" from a spectral total reflectance plot in an optics text by Hecht (1974). The value for GRASS was pulled from a spectral reflectance plot by Sabins (1987). The values for the remaining surfaces were obtained from a spectral diffuse

reflectance data base (SETS Technology, Inc., 1991). Of these remaining surfaces, only white sand was not represented in the database. Therefore, the total reflectance value of bare wood was used as a substitution for white sand.

The $\theta_v = 0$ starting points (normal hemispheric reflectance) for each of the non-BDRF measured surfaces used in the study are provided in table 5.5.

<u>Surface</u>	<u>Rd(0)</u>				<u>Rs(0)</u>				<u>Chosen</u>	
	<u>NIR</u>	<u>RED</u>	<u>GRE</u>	<u>BLU</u>	<u>NIR</u>	<u>RED</u>	<u>GRE</u>	<u>BLU</u>	<u>Model</u>	<u>Type</u>
Concrete	.62	.61	.54	.47	.5	.61	.49	.42	Mod-Diff	
Pavement	.29	.16	.12	.11	.23	.16	.11	.10	Mod-Diff	
Rubber	.04	.04	.04	.04	.03	.04	.036	.036	Mod-Diff	
Fiberglass	.81	.57	.35	.37	.32	.23	.14	.15	Mod-Spec	
Bumper	.04	.04	.04	.04	.016	.016	.016	.016	Mod-Spec	
Sand	.85	.30	.25	.21	.0	.0	.0	.0	High-Diff	
Water	.02	.02	.02	.02	.05	.05	.05	.05	High-Spec	
Glass	.04	.04	.04	.04	.1	.1	.1	.10	High-Spec	
Grass	.90	.08	.10	.05	.0	.0	.0	.0	High-Diff	

Table 5.5 Rd'(0) and Rs'(0) Values of Non-BDRF Measured Surfaces

The infrared values for fiberglass, sand, and grass appear to be too high. These surfaces should be treated with caution when assessing the data. This highlights an important problem with the available reflectivity data bases. Many are incomplete and often inconsistently populated. There is still a great deal of confusion among researchers regarding standard definitions and measurement methods for terms such as normal hemispheric reflectance and total reflectivity.

The reflectivity component plots for pavement, derived from this method, are displayed in figure 5.18.

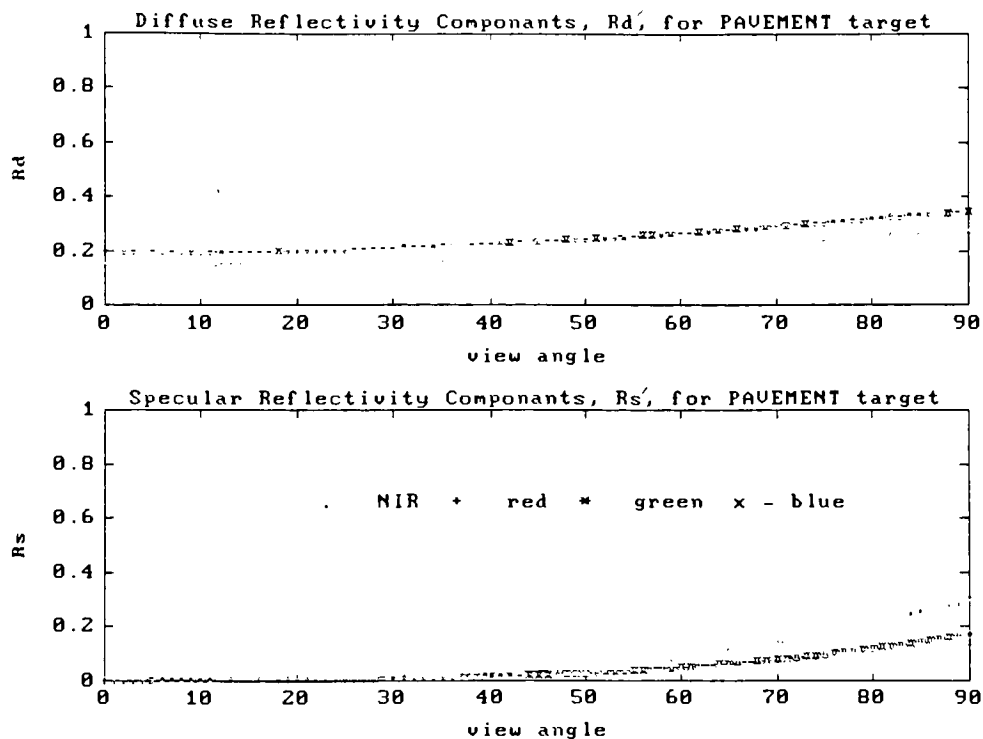


Figure 5.18 Model-Derived Reflectivity Components for Pavement

6. Obtaining Truth Data

6.1 The Scene

The ground truth data for this study consists of actual images of a scene collected from a fixed view angle over varying solar orientations. The scene was constructed at ground level outside RIT's Chester Carlson building and was imaged from a sensor located on the building's roof. The location of the sun's path, sensor, and scene, roughly provided an in-plane orientation with varying illumination angles at a fixed viewing angle. Figures 6.1 and 6.2 diagram the scene set-up.

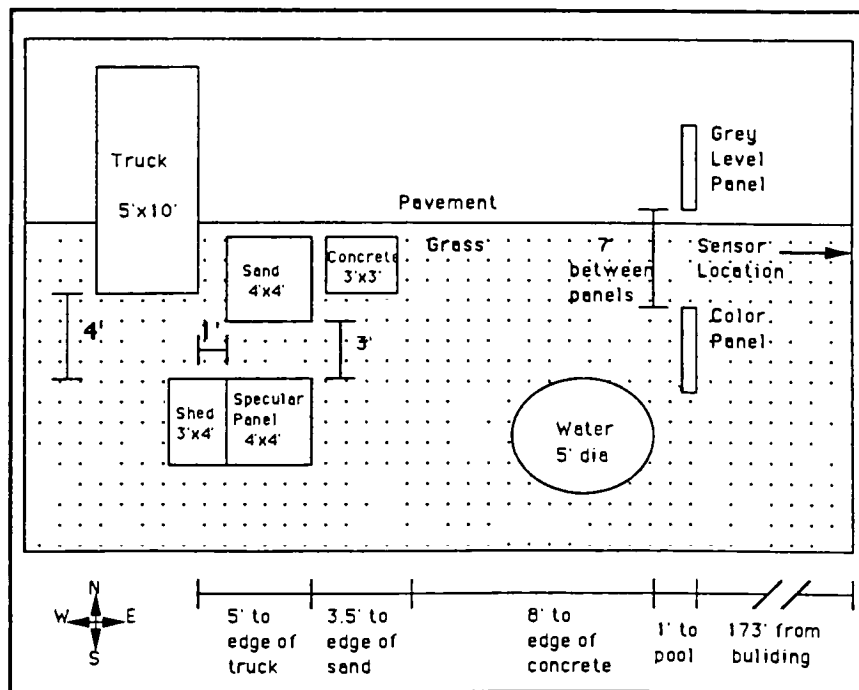


Figure 6.1 Top View of Scene

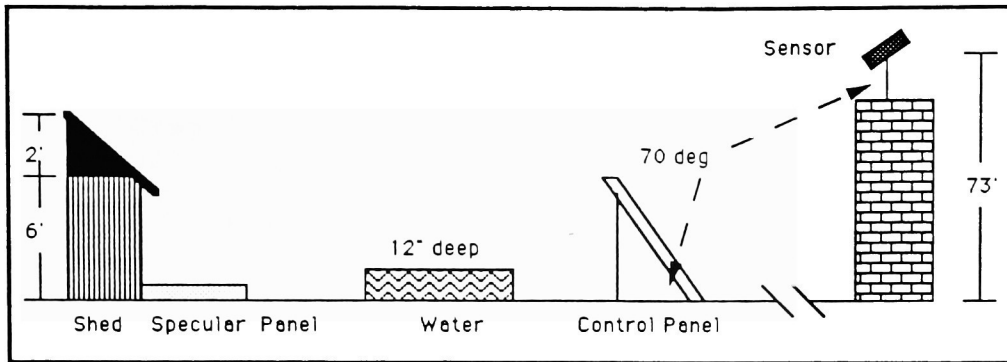


Figure 6.2 Side View of Scene

The contents of the scene were chosen to support concurrent experiments in both the mid-wave IR and long-wave IR, as well as the visible region. For the visible region, a subset of the in-scene objects were considered primary and samples of these were characterized in the laboratory with BDRF measurements. The other objects are considered secondary and are in the scene mainly to provide pertinent data to the IR study, but will also be assessed in the visible region, where appropriate.

Table 6.1 provides a list of all primary and secondary surfaces within the scene, along with the general classification of surface reflectivity. This list corresponds directly to the categorization in the previous section. The main object groups within the scene are the control panels, the shed/specular panel, and the truck/pavement.

<u>Primary Objects</u>	<u>(Category)</u>
Grey Level 1 Panel	(moderately diffuse)
Grey Level 2 Panel	(moderately diffuse)
Grey Level 3 Panel	(moderately diffuse)
Grey Level 4 Panel	(moderately diffuse)
Green Panel	(moderately diffuse)
Red Panel	(moderately diffuse)
Blue Panel	(moderately diffuse)
White Shed Front	(directional diffuse)
Black Shed Front	(directional diffuse)
Specular Panel	(highly specular)
Shingles	(moderately diffuse)
Truck Metal	(highly specular)
<u>Secondary Objects</u>	<u>(class)</u>
Concrete	(moderately diffuse)
Pavement	(moderately diffuse)
Rubber Tires	(moderately diffuse)
Fiberglass Truck Cap	(moderately specular)
Bumper	(moderately specular)
Sand	(highly diffuse)
Water	(highly specular)
Truck Glass	(highly specular)
Grass	(highly diffuse)

Table 6.1 Primary and Secondary In-Scene Objects

The two control panels provided a standard within the scene. They are each divided into four 2'x 2' quadrants with a moderately diffuse surface created by applying a flat latex paint, fully saturated with fine grained sand. Each quadrant of the grey level control panel contained a distinctly different brightness. The color panel was sectioned into red, green, blue, and an arbitrary grey level. These surfaces, positioned normal to the sensor viewing vector, serve both a qualitative and quantitative function. Qualitatively, the spectral images should retain the relative radiance signatures. Quantitatively, the

panels provided well behaved surfaces to permit in-scene radiance measurements for determination of upwelling radiance and atmospheric transmission.

The shed/specular panel group was included to observe background interactions. The shed's directionally diffuse front surface was painted half white and half black. This high contrast surface was placed directly behind, and perpendicular to, a highly specular surfaced panel. The background interactions can be observed by viewing the reflection of the shed front on the specular panel. Additionally, the shed roof consisted of layered shingles.

Another area of interest within the scene is the truck and pavement combination. This group is less controlled due to the curvature of the truck exterior and the non-uniformity of the pavement reflectivity. However, it provided another location to observe general shadowing and background effects.

6.2 Collection of Data

The scene image was captured with a 610 x 488 pixel CCD monochrome frame transfer sensor and frame grabber board. With a 6.0 mm x 4.5 mm CCD array area and a 1/2 inch lens, the resolution at the fixed sensor position was approximately 5 cm. Attached to the front of the camera system was a filter wheel containing four band-pass filters (NIR, red, green, and blue). For maximum dynamic range throughout the imaging cycle, it was experimentally determined to set the camera's F-stop at F#16 and the electronic gain of the external circuitry at 3.7 volts.

The goal was to capture images every 30 minutes from sunrise until sunset to provide a variety of solar illumination angles. At each 30 minute interval, four consecutive images were captured, one for each band-pass filter. Since the simulated scene was not to be generated with clouds included, it was crucial that the collected truth images be captured when the sun was not blocked by clouds, and the remainder of the sky was relatively cloud free. This proved difficult as Rochester experienced one of the worst summers "weather-wise" in the twentieth century. Therefore, it was necessary to piece together images from two collection days, the 22nd and 30th of July. The approximate illumination

orientations for my truth data are depicted in figure 6.3.

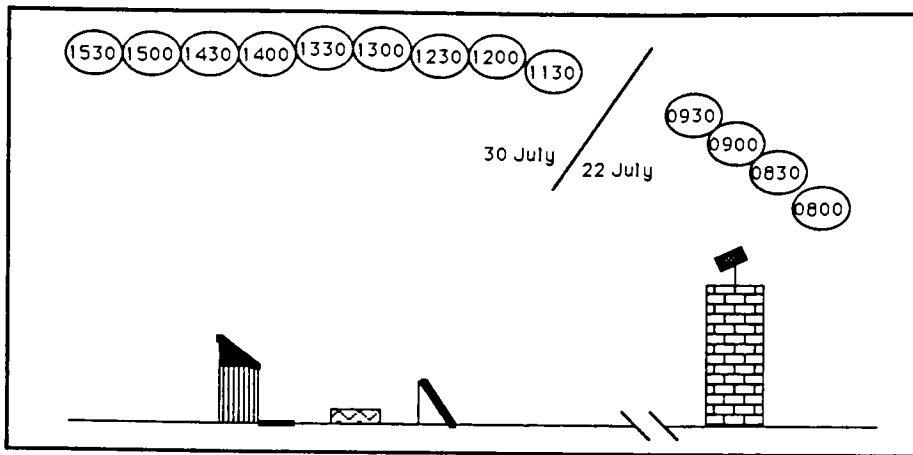


Figure 6.3 Illumination Angles of Truth Data Set

Besides the actual image data, two other measurements were taken concurrently to find the degree of error within DIRSIG's derived downwelled radiance and atmospheric transmittance. First, a series of directional downwelled radiance measurements were made over the sky hemisphere using the Munsell Color Lab's PhotoResearch linear array spectrometer located on the roof. Spectral readings were recorded at nadir, plus 6 different elevations each along the north, south, east, and west axis. Figure 6.4 displays the targeted measurement points as the spectrometer was rotated throughout the hemisphere.

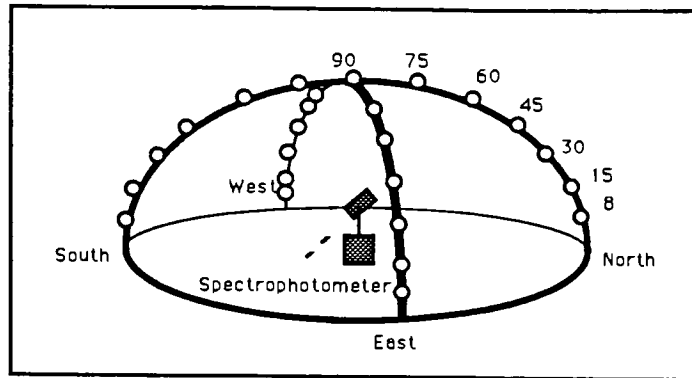


Figure 6.4 Measurement of Directional Downwelled Radiance

Secondly, in-scene radiance measurements were recorded for each of the grey level and color control panels using a simple radiometric detector (United Detector Technology, Model QED-200). Four filters identical to the CCD sensor filters were rotated in front of the radiometer for each panel measurement. The intent of this measurement was to collect the radiance reflected towards the sensor as close as possible to the object without blocking a significant amount of illumination. To accomplish this, the radiometer was attached to a tomato cage at a distance of 24 inches from the surface, as sketched in figure 6.5.

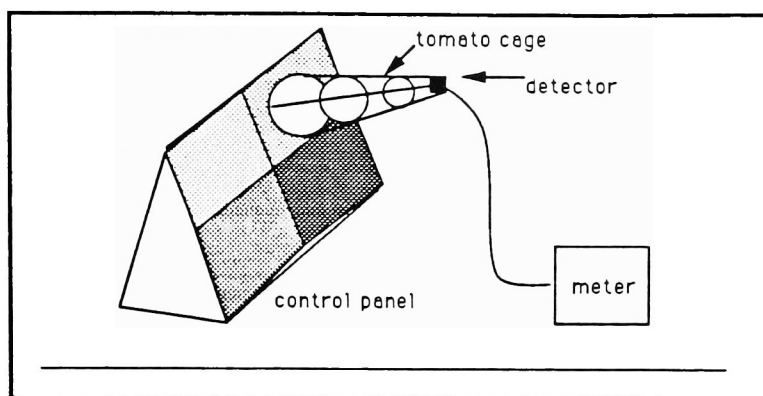


Figure 6.5 Sketch of Radiometer Placement for In-Scene Measurement

The directional downwelled radiance scans were conducted at 0900 on 22 July and 1230 & 1500 on 30 July. In-scene radiance measurements were conducted at 0900 on 22 July and 1200 & 1500 on 30 July. As stated, the downwelled radiance measurements provided ground truth hemispheric and directional downwelled radiance values. In-scene radiance measurements were made to provide scene-to-sensor upwelled radiance and atmospheric transmissivity ground truth values. The results are provided in section 7.1.

Finally, atmospheric data was acquired for the collection days by ordering radiosonde data for the Buffalo airport from the National Weather Service. This data provides an atmospheric profile which includes temperature, pressure, and dew point at various elevations. DIRSIG requires this information to properly simulate the atmosphere using LOWTRAN7. The radiosonde data is provided in the appendix.

6.3 Equipment Calibrations

The digital counts stored for the truth data images represent the radiance reaching the detector. In order to compare with DIRSIG images, the relation must be determined between the truth data digital counts and the absolute radiance reaching the front of the sensor. This relation was found by calibrating the CCD camera system against a known radiance source for each band. The calibration was performed by aligning the known source, a series of neutral density diffuse filters, the appropriate band-pass filters, and the camera system, on an optical bench. Average pixel digital counts were recorded for each radiance level exposed to the front of the camera system, accounting for the attenuation factor of the filters used. The linear transformation equations resulting from a least squares regression are as follows:

NIR:	Radiance = 16.8709 * DC - 44.7149
RED:	Radiance = 7.7995 * DC - 6.4140
GREEN:	Radiance = 5.1244 * DC - 0.6035
BLUE:	Radiance = 7.0883 * DC + 0.1161

[units; uW/(sr*cm²)]

Table 6.2 CCD Camera Calibration Transformations

A similar calibration was performed on the portable QED radiometer. Since the radiometer output is a relative digital count value, the calibration permits transformation

of this value into absolute radiance reaching the front of the detector. The linear transformation equations resulting from a least squares regression are as follows:

NIR:	Radiance =	5.8040 * DC +	8.9203
RED:	Radiance =	7.6453 * DC +	0.6951
GREEN:	Radiance =	4.8353 * DC +	0.0144
BLUE:	Radiance =	5.7922 * DC -	0.2449

[units; uW/(sr*cm²)]

Table 6.3 QED Radiometer Calibration Transformations

The linear array spectrometer used in measuring the downwelled radiance provided accurate absolute radiance values. This instrument was precalibrated prior to collection.

7. Assessment of DIRSIG's Sensitivity of Radiance Reaching the Sensor

The different variables in the DIRSIG model will be assessed for their predicted error and relative impact on the final radiance reaching the sensor. Many non-spectral portions, such as ray tracing and structure modeling, have already been validated in studies of performance in the mid-wave and long-wave IR regions. These should perform to the same degree of error in the visible region. However, depending on their function, they may have a different impact on the final radiance error.

The uncertainty of the total radiance reaching the front end of the sensor was investigated by applying the error propagation technique of Yardley Beers (1957). This approach defines the overall uncertainty as a composite of the uncertainties involved in each of the variables. Therefore, each variable's contribution to the overall uncertainty can be determined.

7.1 Comparison of Truth and DIRSIG Parameters

The first step in applying Beers' technique was identifying the standard error of each of the variables of equation

4.1.a. The standard error of the non-spectral variables were well established by the mid-wave assessment of DIRSIG and directly transported to this study. Schott, et al (1993) provides a detailed explanation of how these were obtained. Since the device available to both the visible and mid-wave studies for measurement of direct insolation integrates over the entire 0.28 - 2.8 μm region, the error for the direct insolation found in the mid-wave study will be applied to the visible. The variables whose errors were determined explicitly by this visible study are the downwelled radiances, upwelled radiances, atmospheric transmission, and reflectivity components. The reflectivity component errors were established in section 5.4. The errors for the other three parameters are discussed in the remainder of this section.

Downwelled Radiance Error

The ground truth directional downwelled radiances were measured as described in section 6.2, using the linear array spectrophotometer. For each of the 25 directions measured, the readings were integrated spectrally to provide an estimated value of the directional downwelled radiance for each of the bands. The truth values for downwelled radiance

were not available in the NIR, since the spectrometer was only sensitive in the 400 - 750 nm region.

Figure 7.1 displays the ground truth data against the corresponding modeled radiance values of LOWTRAN7 for each of the measured times within the blue region. The plots on the left refer to the NORTH/SOUTH plane, while those on the right refer to the EAST/WEST plane. Figures 7.2 and 7.3 plot the comparison for the green and red regions, respectively. The percent RMS errors were computed for each data set by dividing the RMS error by the average truth value. The results are listed below in table 7.1.

		<u>BLUE</u>	<u>GREEN</u>	<u>RED</u>
0900:	RMS	3.8	5.2	6.2
	% RMS	35.0	80.6	62.1
1230:	RMS	5.5	8.2	4.0
	% RMS	43.2	115.8	40.3
1500:	RMS	5.1	7.1	3.0
	% RMS	51.0	136.2	45.6

Overall:	RMS	4.9	7.0	4.6
	% RMS	43.3	111.1	52.2

[units; W/(sr*m²)]

Table 7.1 RMS Error for Directional Downwelled Radiance

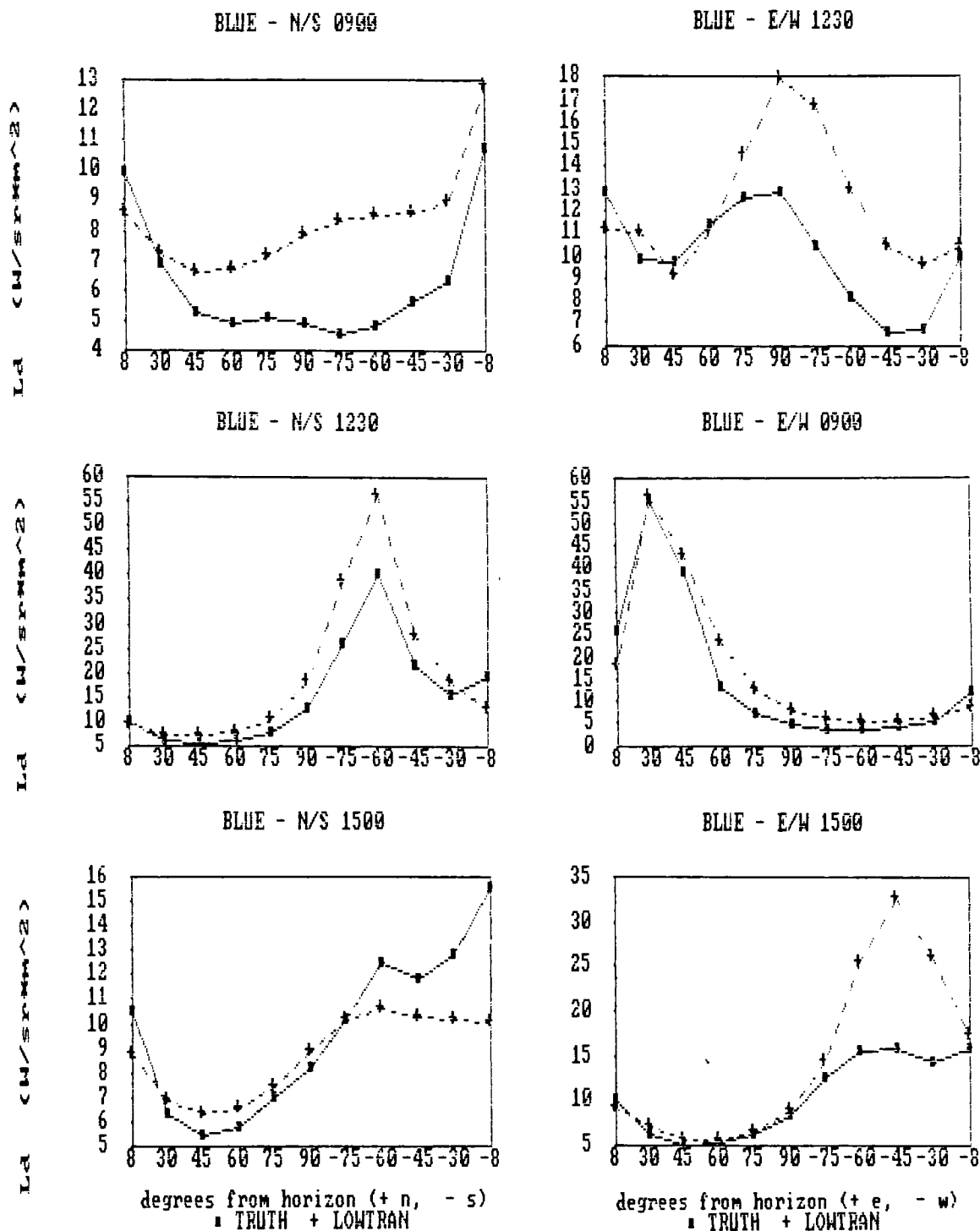


Figure 7.1 Measured Directional Downwelled Radiance vs LOWTRAN7's Calculated Directional Downwelled Radiance (in BLUE Band)

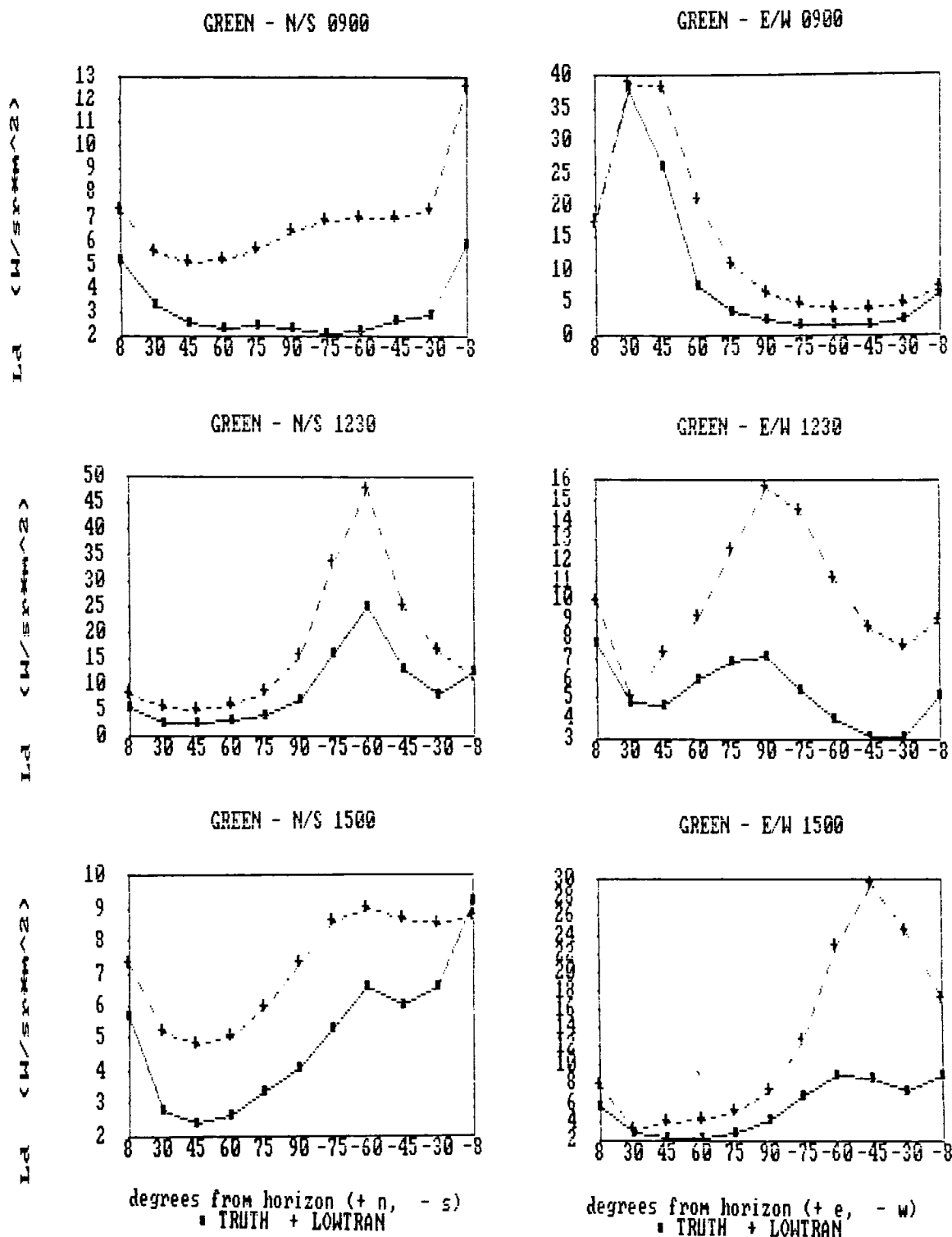


Figure 7.2 Measured Directional Downwelled Radiance vs LOWTRAN7's Calculated Directional Downwelled Radiance (in GREEN Band)

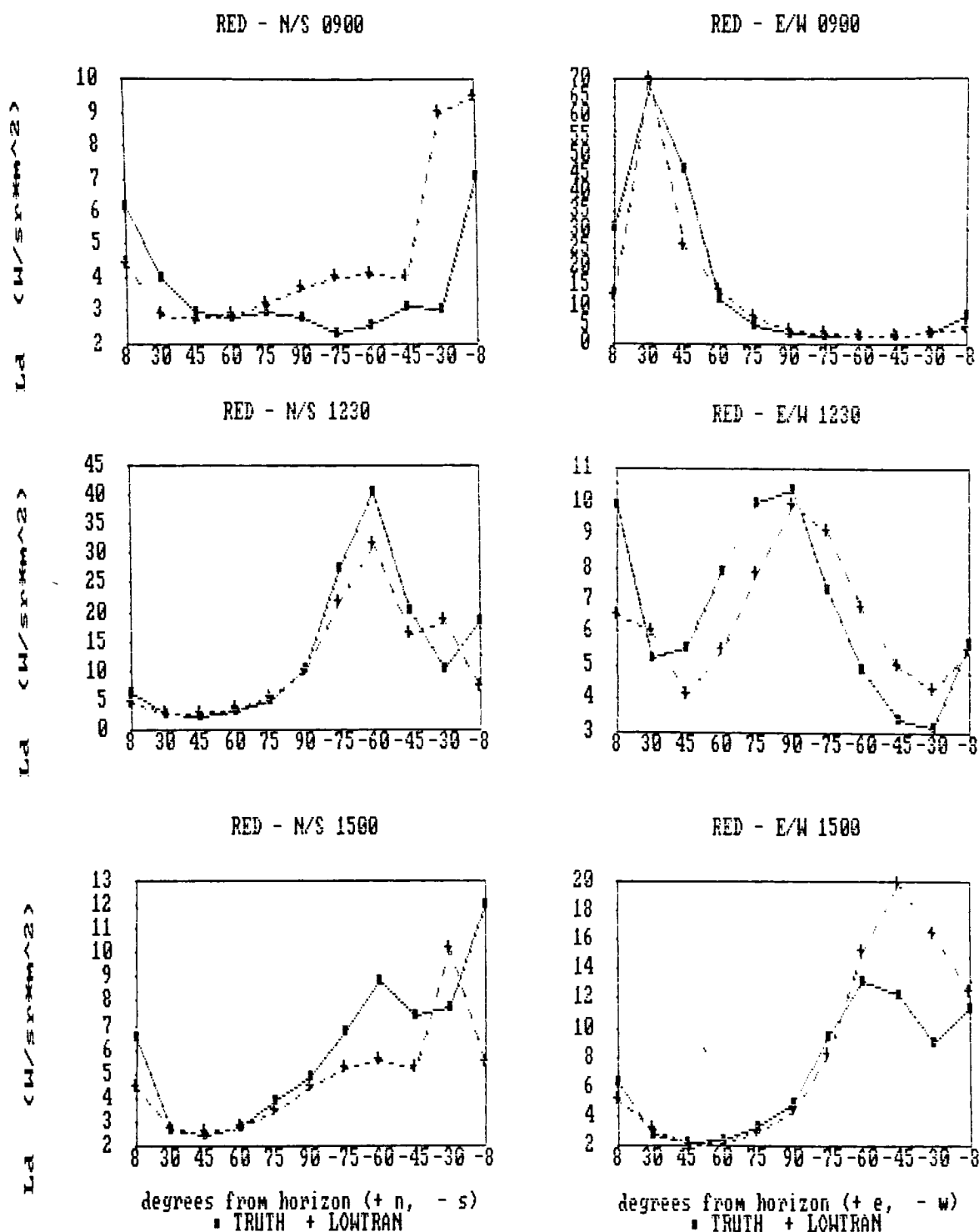


Figure 7.3 Measured Directional Downwelled Radiance vs LOWTRAN7's Calculated Directional Downwelled Radiance (in RED Band)

To determine the ground truth hemispherical downwelled radiance within each of the bands, the measured directional downwelled radiance data was further integrated geometrically according to equation 7.1. These were then compared with the hemispherical values derived by LOWTRAN7 to produce the RMS errors listed in table 7.2.

$$L_D = 1/\pi \sum (\sum L_D(\theta_i, \Phi_i) \cos\theta_i \sin\theta_i \Delta\theta_i) \Delta\Phi_i \quad (7.1)$$

		<u>BLUE</u>	<u>GREEN</u>	<u>RED</u>
0900:	RMS	6.8	1.8	13.6
	% RMS	36.6	14.9	68.8
1230:	RMS	0.7	4.4	3.1
	% RMS	4.9	59.9	29.6
1500:	RMS	4.5	6.7	2.1
	% RMS	55.6	169.3	47.3

Overall:	RMS	4.7	4.8	8.2
	% RMS	35.3	61.7	70.6

[units; W/(sr*m²)]

Table 7.2 RMS Error for Hemispherical Downwelled Radiance

Overall, a large degree of error was displayed between the magnitudes of the LOWTRAN7 derived and experimentally measured downwelled radiance values. The following plots show the trend in percent RMS as a function of time. These plots indicate that the actual atmosphere probably changed its composition significantly throughout the day, which

alters its effects on visible energy. Many factors can change the atmospheric composition at any given time. By applying radiosonde data collected only two times in a 24 hour period from as far as Buffalo, a good deal of disparity can exist between the modeled and actual atmosphere at the time of the image capture. Clearly these errors could be reduced by the input of more representative atmospheric data.

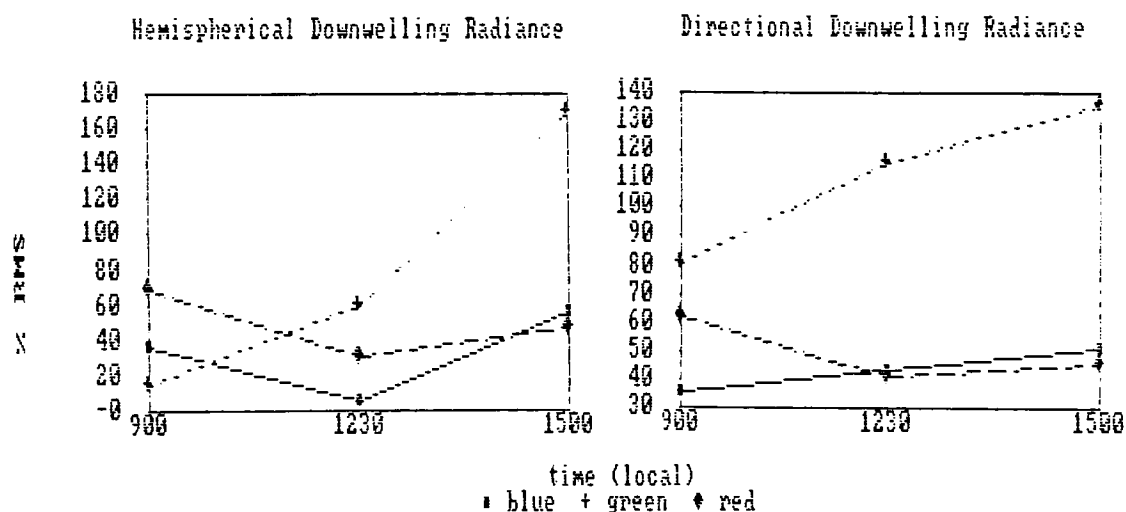


Figure 7.4 Percent RMS Error vs Time of Day for Both Directional and Hemispherical Downwelled Radiance

Upwelled Radiance and Atmospheric Transmission Error

Ground truth for scene-to-sensor upwelled radiance and atmospheric transmissivity was to be established from observing the relation between the measured in-scene

radiance values and the concurrent image radiance values for the panels. Figure 7.5 shows the relationship between the radiance reaching the camera (L_c), the in-scene object radiance (L_s), the upwelled radiance (L_u), and the transmissivity (τ). By plotting the radiance values against each other, the slope would equal the transmissivity and the intercept would equal the upwelled radiance.

$$L_c = \tau * L_s + L_u \quad (7.2)$$

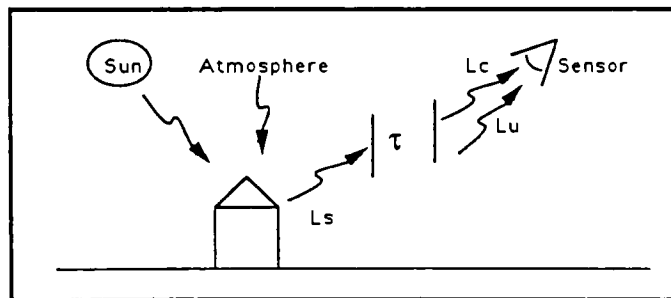


Figure 7.5 Relationship Establishing Upwelled Radiance and Atmospheric Transmission

Unfortunately, the observed transmissivity ranged from 1.2 to 5.3, while the observed upwelled radiance values (L_u) ranged from -114 to +145 $\mu\text{W}/(\text{sr} \cdot \text{cm}^2)$. The magnitude of the radiance values were correct, however the data relating in-scene radiance and at-sensor radiance contained a great deal of variance from linearity. Therefore, the error for these two components could not be estimated from this experiment.

This failure most likely occurred because the method of measuring the in-scene radiance with the QED radiometer proved inadequate. First of all, the detector did not have any optical components to assist in proper alignment with the target. Additionally, to reduce the interference by the detector housing on the incident illumination, the detector was kept approximately two feet from the target surface. The resulting large spot size, along with the possible non-normal alignment, may have combined to destroy the efficacy of the measurement. Another contributor to the failure may have been a systematic error in the QED calibration. The lack of optics made it difficult to ensure exact alignment of the components on the optical bench. In the future, a radiometer with alignment optics should be used for these in-scene measurements.

Since the experiment had the sensor only 210 feet from the in-scene targets, the impact of the upwelled radiance and the atmospheric transmission on the total radiance will be minimal. Therefore, the standard error of the transmission factor will be assumed equal to zero. Additionally the error of the upwelled radiance will be assumed equal to the estimated error for the directional downwelling radiance. This is acceptable due to the fact that LOWTRAN7 models both upwelling and downwelling radiances in the same fashion.

Summary of Variable Errors

<u>VARIABLE</u>	<u>RMS ERROR</u>				<u>%RMS ERROR</u>			
	<u>NIR</u>	<u>RED</u>	<u>GREEN</u>	<u>BLUE</u>	<u>NIR</u>	<u>RED</u>	<u>GREEN</u>	<u>BLUE</u>
Ld hem	-	-	-	-	N/A	70.6	61.7	35.3
Ld dir	-	-	-	-	N/A	52.2	111.1	43.3
Lu dir	-	-	-	-	N/A	52.2	111.1	43.3
τ_2	-	-	-	-	0	0	0	0
Rd(θ_v)	.029	.023	.029	.030	-	-	-	-
Rdb(θ_v)	.029	.023	.029	.030	-	-	-	-
Rs(θ_v)	-	-	-	-	1	1	1	1
(Es/ π)(τ_1)(cos θ)*	-	-	-	-	17.7	17.7	17.7	17.7
F *	-	-	-	-	10	10	10	10
all θ 's *	7.5	7.5	7.5	7.5	-	-	-	-

[The reflectivity component errors are from assessing measured samples only and listed in reflectivity units. The "*" estimates are from the MWIR study (Schott, *et al*, 1993). Angles listed in degrees.]

Table 7.3 Summary of Errors Associated With Each Variable

7.2 Error Propagation

Next, the uncertainty of the total radiance reaching the front of the sensor was determined. Applying the Beers technique to DIRSIG's radiance algorithm requires solving the relation shown in equation 7.3. The partial derivatives were computed using a MATHCAD Symbolic Processor and are listed in the appendix. The measurements of all variables were considered independent. The upwelled radiance and atmospheric transmission are actually inversely correlated, but this was not a factor since the transmission error was assumed irrelevant.

$$\sigma_L = \{ (\delta L / \delta((E_s/\pi)\tau_1))^2 \sigma_{((E_s/\pi)\tau_1)}^2 + (\delta L / \delta \theta_s)^2 \sigma_{\theta_s}^2 + \dots \}^{0.5} \quad (7.3)$$

where; - L, E_s, τ₁, and θ_s are from equation 4.1.a
 - σ is the standard error

Once the overall radiance error is found, each variable's contribution to the overall uncertainty can be determined. This is found by comparing the standard error of the radiance with respect to each variable, to the overall standard error of the radiance. Equation 7.4 shows this relation for determining the contribution of the sun-target normal angle (θ_s).

$$\text{Error Contribution of } \theta_s = ((\delta L / \delta \theta_s)^2 \sigma_{\theta_s}^2)^{0.5} / \sigma_L \quad (7.4)$$

The model's sensitivity was assessed for two different target interactions encountered by the primary ray cast from the sensor. First, referred to as CASE A, was the ray hitting a target (grey control panel) and its secondary ray bouncing to the sky. Second, CASE B, was the ray hitting a target (specular panel) and its secondary ray intersecting a background object (black shed front). These two cases are representative of the energy-surface interactions of interest for this study.

To solve for these relationships, values for the variables

were extracted from the DIRSIG process using a software "debugging" tool. The appropriate errors were then assigned to each variable. The values and errors are listed in table 7.4. The variable data is from an image generated in the green band at 1230 hours.

VARIABLE	CASE A	CASE B
	TARGET TO SKY values (errors)	TARGET TO BACKGROUND values (errors)
Ld hem	.0009552 (.0005894)	.0009552 (.0005894)
Ld dir	.0005864 (.0006514)	-
Lu dir	3.444e-6 (3.827e-6)	3.970e-6 (4.411e-6)
τ_2	.99 (0)	.99 (0)
Rd(θ_v)	.25 (.031)	.32 (.031)
Rdb(θ_v)	-	.07 (.031)
Rs(θ_v)	.0029 (.00029)	.29 (.0029)
(Es/ π)(τ_1)	.002724 (.000482)	.002724 (.000482)
F	.956 (.0956)	.716 (.0716)
θ_s	65.3 deg (7.5 deg)	47.8 deg (7.5 deg)
θ_b	-	79.1 deg (7.5 deg)
Lr	.000561 (-)	.0008047 (-)

[Radiance values in W/(sr*cm²)]

Table 7.4 Observed Parameter Values and Associated Error for Green Band at 1230 Hours

The errors were propagated to find the total error according to equation 7.3. The error contributions for each of the variables were then computed as in equation 7.4. The results are listed in table 7.5.

VARIABLE	ERROR CONTRIBUTIONS	
	CASE A	CASE B
	<u>Target to Sky</u>	<u>Target to Background</u>
Ld hem	0.7678 (1)	0.6765 (1)
Ld dir	0.0103 (7)	-
Lu dir	0.0214 (6)	0.0206 (8)
τ_2	0.0 (9)	0.0 (10)
Rd(θ_v)	0.3521 (3)	0.3636 (4)
Rdb(θ_v)	-	0.0655 (6)
Rs(θ_v)	0.0009 (8)	0.0011 (9)
(Es/ π)(τ_1)	0.2744 (4)	0.4901 (2)
F	0.1244 (5)	0.1007 (5)
θ_s	0.4418 (2)	0.3915 (3)
θ_b	-	0.0432 (7)
L error	1.675e-4 (8.3%)	1.996e-4 (7.9%)

[Rankings for variables in parenthesis. The last line lists the radiance error, with equivalent reflectance unit error in parenthesis (Radiance units in $W/(sr \cdot cm^2)$)].

Table 7.5 Error Contributions of Variables

7.3 Error Propagation Results

It is important to understand for a limited study such as this "that the theoretical error propagation serves more as a sensitivity indicator than as a predictor of absolute radiance error" (Schott, et al, 1993). For both cases, the top four contributors of error are the hemispherical downwelling radiance, effective solar radiance, target-normal/sun-vector angle (θ_s), and the diffuse

reflectivity component. This is not surprising since these variables are associated with the majority of energy within the scene. Each of the error contributions for the components common to both cases are of the same magnitude for all except the effective solar radiance, which was twice as high in case B.

Regarding the energy sources, the hemispherical downwelling radiance error is the major contributor in both cases. This is probably due to the large associated percent error. Little effort was made to ensure LOWTRAN7 accurately modeled atmospheric effects. These effects were based on the expected molecular constituents for a standard atmosphere at this latitude, concentrated in various amounts determined by exploiting radiosonde data recorded over Buffalo. LOWTRAN7 calculates the downwelling radiances by modeling the energy scattered, absorbed, and transmitted within the defined atmosphere. Since downwelling radiance is a primary source of energy in the visible region, the effectiveness of LOWTRAN7 to model the atmospheric effects in this wavelength region is an important area to pursue in future studies. Of particular concern is proper modeling of aerosol and cloud cover effects. The degree of overcast and clouding can be monitored by periodically imaging the entire sky through a wide-view lens. This information can be used to adjust the

LOWTRAN7 input data.

The actual direct solar radiance reaching a surface is described by attenuation the effective solar radiance reaching the scene $((E_s/\pi)(\tau_1))$ by the factor $\cos(\theta_s)$. Both of these terms contribute a large portion of error to the overall error. It is intuitive that any errors in solar energy will have significant impact in the visible region. In case B, the solar radiance error contribution is higher since the background surface provides an additional source of solar energy onto the target. The expected error in θ_s is strictly a function of the resolution applied in rendering the scene. The impact of the θ_s error underscores the importance of directional information when operating in the visible region.

Beyond the energy sources, the target surface's diffuse reflectivity component is the largest contributor to error. The effects of this error could be reduced by improving the BDRF measurement resolution within the in-plane scans, which would produce a more accurate representation of the hemispherical-directional reflectivity. To further reduce error, a full hemispherical BDRF scan could be performed, at the expense of processing resources.

The specular reflectivity component is not a large contributor to error since it plays a relatively small role in the percentage of energy propagated within the scene. In fact, with the exception of τ_2 (assumed errorless), R_s is the lowest contributing variable to total error. The shape factor is found by casting rays about the hemisphere and determining the percentage of the sky blocked by background objects. Like θ_s , the error in shape factor is only limited by the angular resolution of its computation. This error could be decreased at the expense of computational resources.

The overall final radiance error for both cases was found to be approximately the equivalent of an 8% reflectance error. Efforts to reduce the degree of total error should be geared to improving LOWTRAN7's ability to model the atmosphere, by increasing the accuracy of the input data. Additionally, the amount of SIG processing can be increased to allow a finer angular resolution in image rendering. These combined efforts would significantly reduce the error from the major contributors. If further error reduction is desired after these improvements, the resolution of the BDRF measurements can be addressed.

8. DIRSIG Image Evaluation

Synthetic images were generated for a subset of the truth data image set. It was assumed that trends in the data over time would be sufficiently represented by the green band. Additionally, comparisons between all bands were assessed for only three distinct illumination angles. A matrix of those images generated and assessed is found in table 8.1.

		NIR	RED	GREEN	BLUE
T I M E	0800			X	
	0830			X	
	0900	X	X	X	X
	0930			X	
	1130			X	
	1200			X	
	1230	X	X	X	X
	1300			X	
	1330			X	
	1400			X	
	1430			X	
	1500	X	X	X	X
	1530			X	

Table 8.1 Matrix of Assessed Images

Evaluation involved comparing the radiance values reaching the front of the sensor between the simulated and truth images for various points in the scene. The actual camera system radiance-to-digital count calibration curves from section 6.3 were applied to the radiance values of simulated images. Therefore, the DIRSIG image digital counts were calibrated and direct comparisons could be made between the pixel values.

Figure 8.1 provides a map of where in the scene the digital counts were extracted. The points 11-24 represent surfaces that were actually characterized in the laboratory. Points 1-10 represent surfaces that were modeled. The extracted digital counts are the average from a 10x10 pixel box. Plates 1-3 show the truth and DIRSIG images for each band at 0900, 1230, and 1500 hours, respectively. The 0900 truth images were questionable due to suspected equipment variations, and thus only used for qualitative assessments.

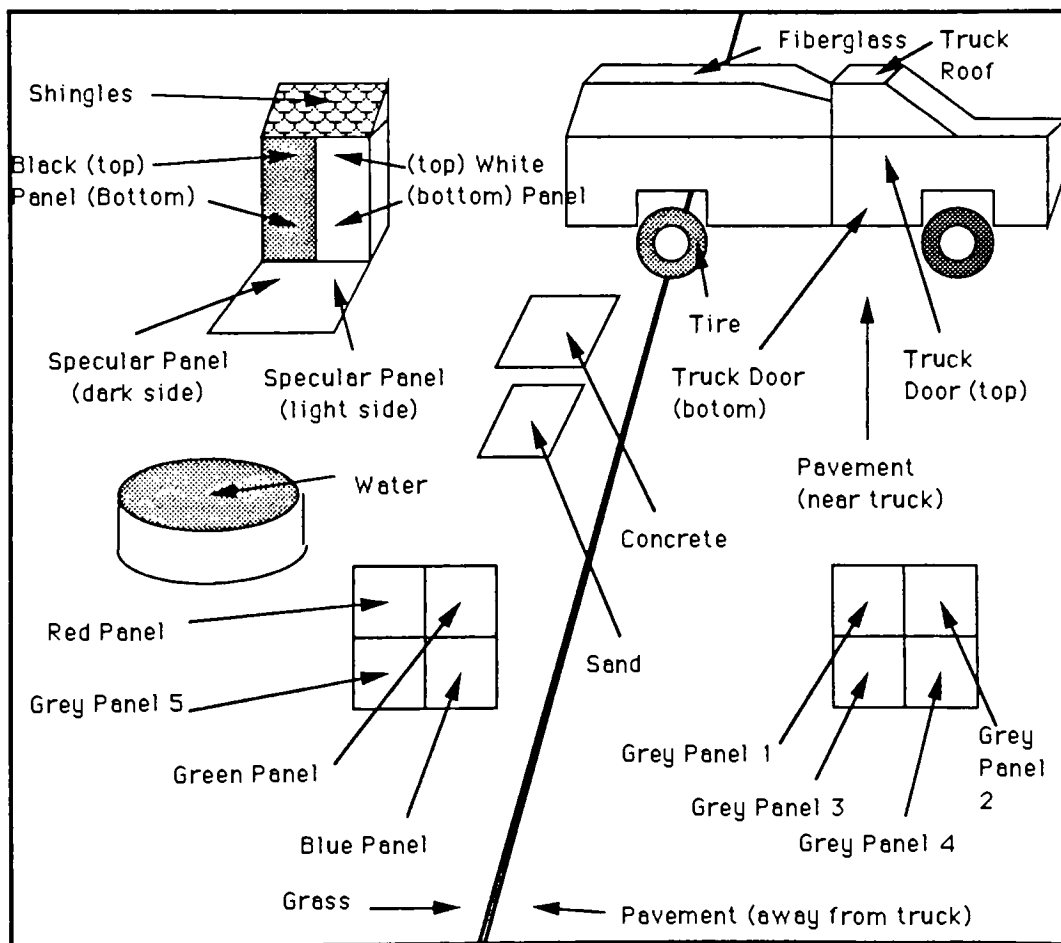
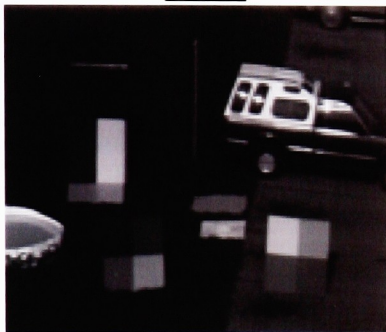


Figure 8.1 Map of Digital Count Extraction Points

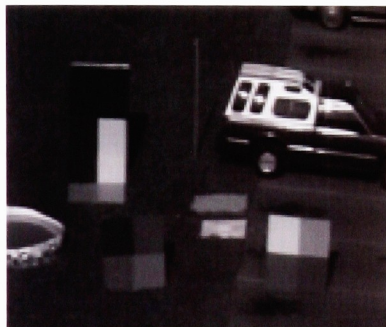
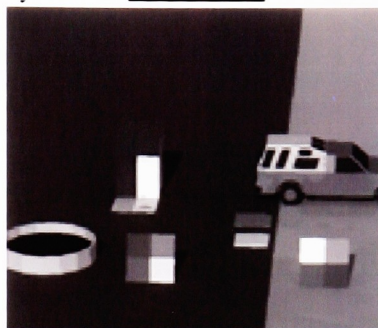
Truth

0900 Local Time, 22 July 92

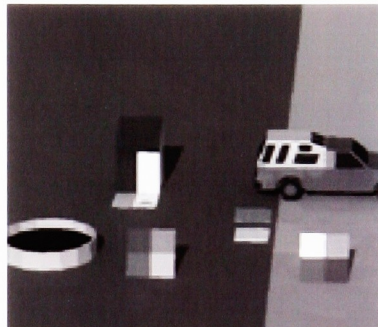
Simulated



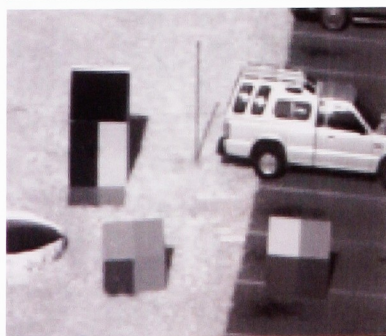
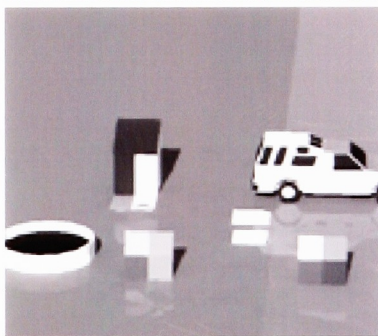
1.1 Blue



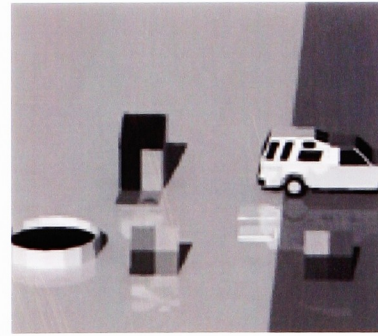
1.2 Green



1.3 Red



1.4 NIR



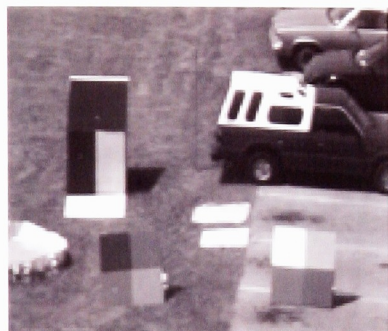
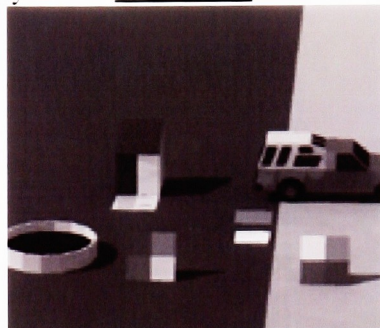
Truth

1230 Local Time, 30 July 92

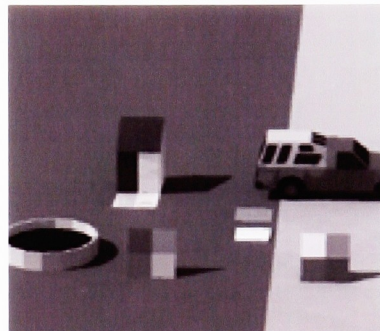
Simulated



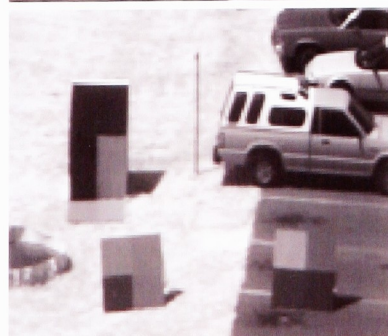
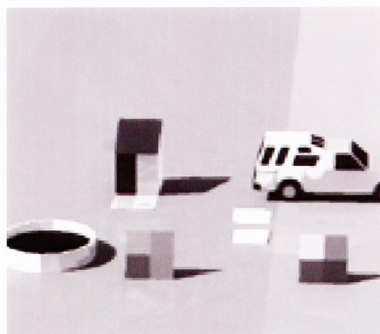
2.1 Blue



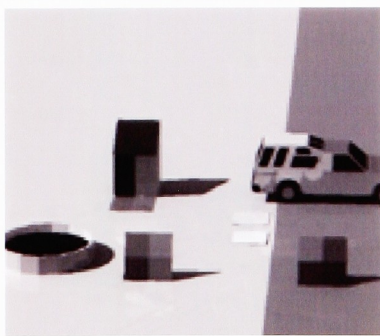
2.2 Green



2.3 Red



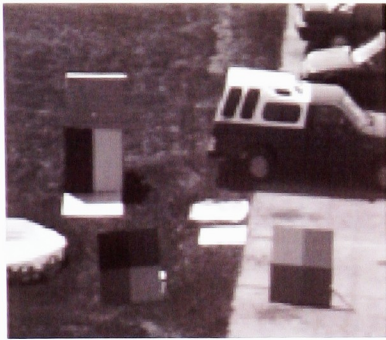
2.4 NIR



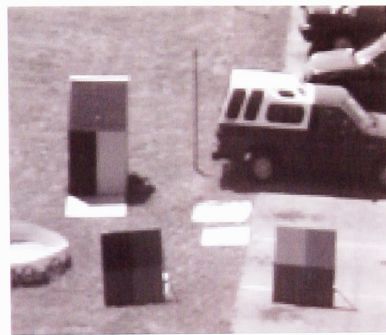
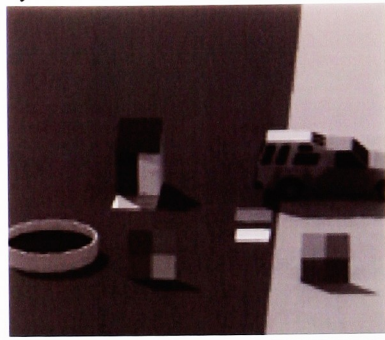
Truth

1500 Local Time, 30 July 92

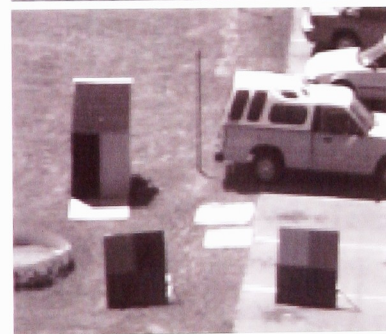
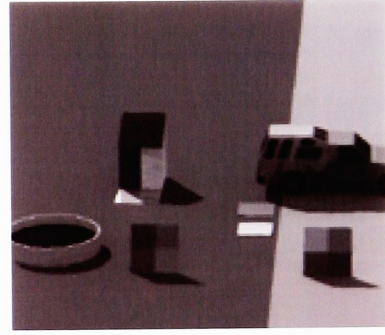
Simulated



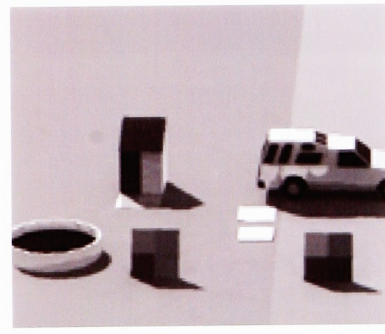
3.1 Blue



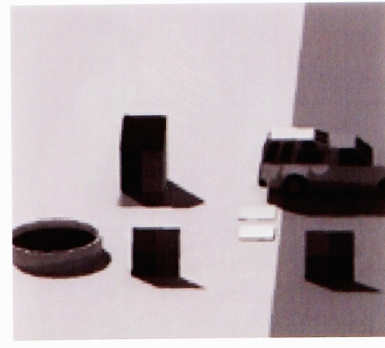
3.2 Green

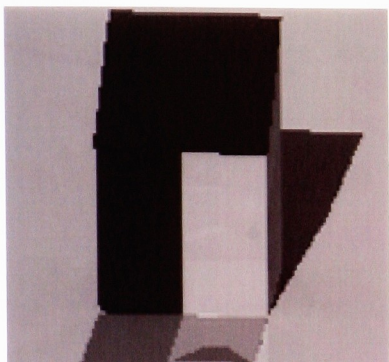


3.3 Red

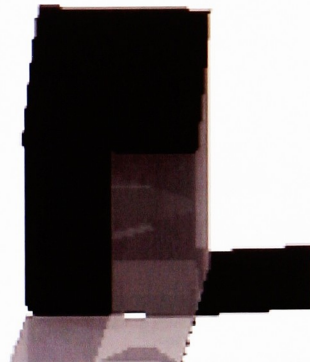


3.4 NIR

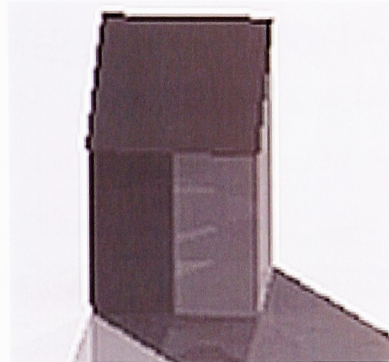




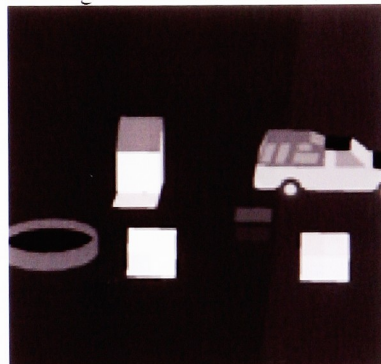
4.1 Magnification of NIR, 0900



4.2 Magnification of NIR, 1230



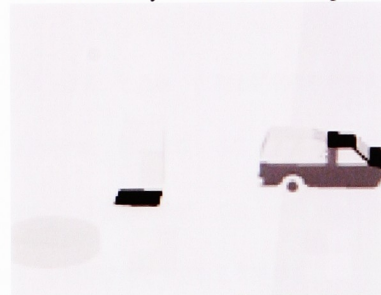
4.3 Magnification of NIR, 1500



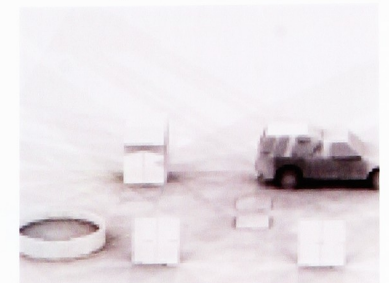
4.4 Primary Material Map



4.5 Target Diffuse Reflectivity



4.6 Target Specular Reflectivity



4.7 Target Shape Factor



4.8 Background Diffuse Reflectivity

8.1 Quantitative Assessment

8.1.1 Comparison of *Calibrated* Image Pixel Values

The images were compared by plotting the calibrated synthetically generated digital counts verses the ground truth digital counts. Perfect correlation would result in the data lying along the unity line. Variations about this line indicate relative errors in the treatment of surface reflectance. If the data shows a strong linear relation about a line other than unity, then an image-wide error may exist.

Figure 8.2 shows the scatter plots of the characterized surfaces (points 11-24) for the green band at 1230 and 1500 hours. These both display a strong linear relationship indicating a good modeling of the energy-surface interactions. However, an image-wide offset is observed which drives the data above the target line. Additionally, the slope of the data is slightly greater than one. This may result from a minor error in the camera system calibration curves. These same tendencies were found in the NIR, red, and blue regions. These plots can be found in the appendix.

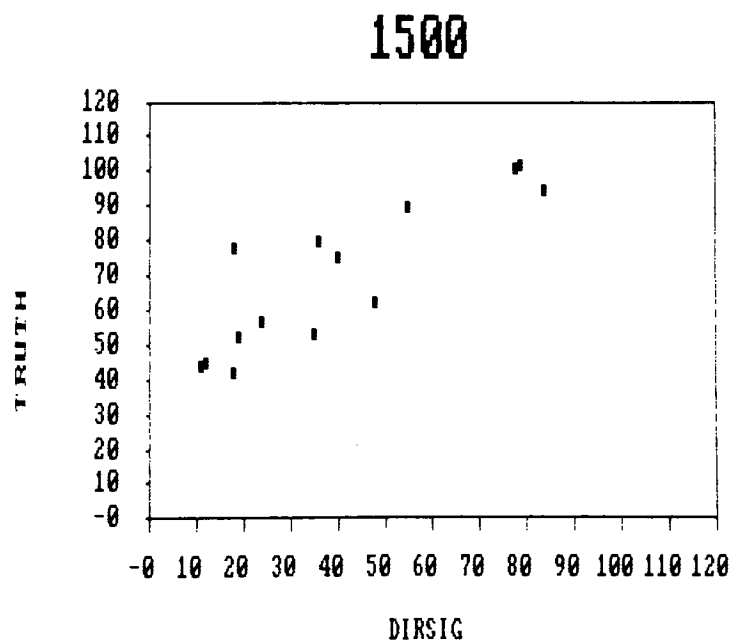
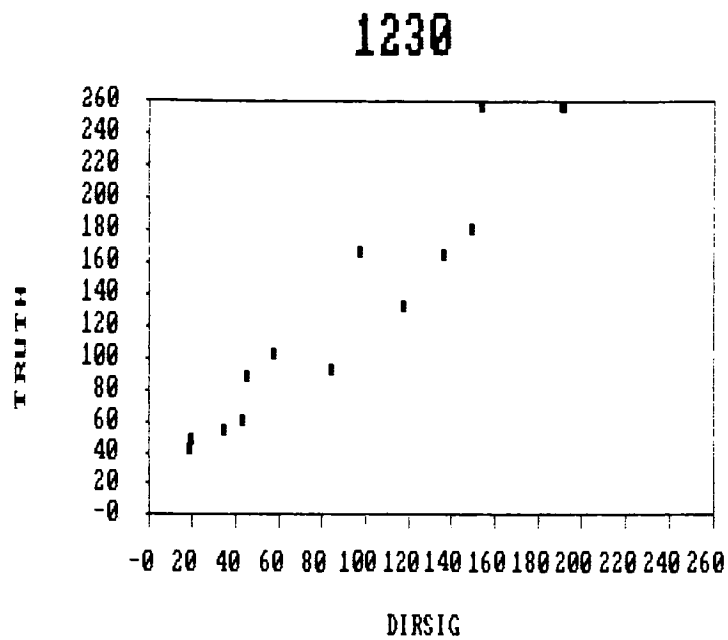


Figure 8.2 Calibrated Synthetic DC vs Truth DC
[Green band/1230 and 1500 hrs]

An image-wide offset may be the result of equipment calibration problems or source-energy/atmospheric-interaction errors in LOWTRAN's modeling. A high degree of confidence is placed in the calibration of the camera system due to the control of optical alignment and field of view. Therefore, the image-wide offset is probably a result of LOWTRAN7's limitations.

As mentioned earlier, the atmospheric data input to LOWTRAN7 is not very accurate. The aerosol levels and cloud cover may have differed enough between Buffalo and Rochester during the collection to lower the relative DIRSIG pixel counts. Schott, *et al* (1993), reports that in earlier experiments, LOWTRAN7's predicted insolation was 17.7 percent lower than measured. Such an error would serve to drive the data above the unity line as observed. However, figures 7.1-3 show that, for this experiment at least, the predicted downwelling radiance was actually higher than measured. This would tend to drive the data the other way. The previous section on error propagation shows both sources of energy are important potential error contributors and depending on the environmental factors, either one could result in a dominant image-wide offset.

Since a strong linear relationship in the image digital count data is easily observed, it is not necessary to characterize the strengths of this linearity through regression statistics. However, the degree of variance about the line does provide some indication of how well the surface reflectances performed. The traditional look at the variance in the data doesn't adequately describe the relative value of the synthetic image. To practically exploit the image, it is important that relative contrasts are maintained in order to relate different objects within the scene. A good method for this is the Spearman's Rank Order Correlation Coefficient (r), which provides a measure of the relative radiance values between the truth and DIRSIG images (Lehmann, 1975). The coefficient is found by applying equation 8.1. Much like the traditional correlation coefficient, values will fall between 0 and 1, with 1 indicating a strong association.

$$r = 1 - (6 \cdot D) / (N(N^2 - 1)) \quad (8.1)$$

where, $D = \sum (x - y)^2$,
of all points in a data set
 N = the # points assessed

Lehmann uses this coefficient to test the null hypothesis that two data sets are randomly matched with no correlation. The sampling distribution of the randomly matched data is approximated as normal. Therefore, the Z test statistic is

used to test the significance of the correlation.

$$Z = r * (N-1)^{.5} \quad (8.2)$$

This test is applied against a given level of significance (α), which defines the probability of falsely rejecting the null hypothesis. This critical region is divided into upper and lower tails of the distribution, each consisting of an $\alpha/2$ probability.

The process followed for testing the coefficient for each image data set is as follows:

1. Null Hypothesis (H_0): correlation = 0
Alternate Hypothesis (H_1): correlation \neq 0
2. Define level of significance as $\alpha = 0.01$ or 1%
3. Find the Spearman Correlation Coefficient
where $D = \sum(\text{truth rank} - \text{DIRSIG rank})^2$
and $N = 14$ for points 11-24
4. Define critical regions from normal distribution table, $Z_{\alpha/2} = \pm 2.575$
5. Find the Z-statistic for each image et.
6. If $Z > 2.575$ or $Z < -2.575$, then reject the null hypothesis of no correlation. This provides a high confidence in the correlation

Table 8.2 provides a list of the Spearman coefficients and Z statistics for the twelve image comparisons in this study. Note that the fourteen sampled points represent the surfaces

with measured reflectivity data. The coefficient values are all high (range:.72-.98, mean:.88) showing strong contrast sensitivity of the images. The extracted digital count values and associated ranks can be found in the appendix. Furthermore, all Z values are above 2.575, rejecting the hypothesis of no correlation in the data with only a 1 percent probability of error. This gives a high level of confidence in the correlation. Note that the lowest coefficient, 0.72, has a "Z" statistic of 2.59, which is just within the rejection zone. All the other image pairs will have an even stronger rejection of the null hypothesis.

<u>Time/Date</u>	<u>NIR</u>		<u>RED</u>		<u>GREEN</u>		<u>BLUE</u>	
	<u>r</u>	<u>Z</u>	<u>r</u>	<u>Z</u>	<u>r</u>	<u>Z</u>	<u>r</u>	<u>Z</u>
0900/22JUL92	.83	2.99	.78	2.81	.95	3.43	.97	3.50
1230/30JUL92	.72	2.59	.90	3.24	.98	3.53	.90	3.24
1500/30JUL92	.93	3.35	.78	2.81	.88	3.17	.88	3.17

[Z = 2.59 is significant for $\alpha=0.01$]

Table 8.2 Spearman Rank Order Correlation Coefficients (r) and Z Statistics

The Spearman coefficient assessment displays strong rank order correlation which indicates that the energy-surface interactions are well characterized. If they weren't, severe image degradation such as saturation or contrast reversal could result. These effects would seriously compromise any value for synthetic image exploitation. The error present is mainly from image-wide offset. These errors alter the average digital count throughout the image,

resulting in a darker or lighter scene. Depending on the image exploitation application, these types of errors may be annoying but are usually not catastrophic.

8.1.2 Comparison of *Corrected* Image Pixel Values

Another useful assessment is to compare the surface's relative reflectivity errors. This provides insight into how well each surface's reflectivity was characterized. To observe this, the data was "corrected" to remove the offset due to the image-wide errors. A linear regression line was determined for the data, and then the original synthetic pixel values were transformed about the unity line. This re-mapped the variations about unity without inclusion of the offset effects. Figure 8.3 displays the result of this simple transformation for the green band at 1230 and 1500 hours. This data is used in further analysis and is referred to as "corrected" data.

The relative pixel value difference between the images provide information on what surfaces may be better characterized. A general comparison was made of the overall RMS digital count errors for the combined data over all four bands at 1230 and 1500 hours. These results are listed in

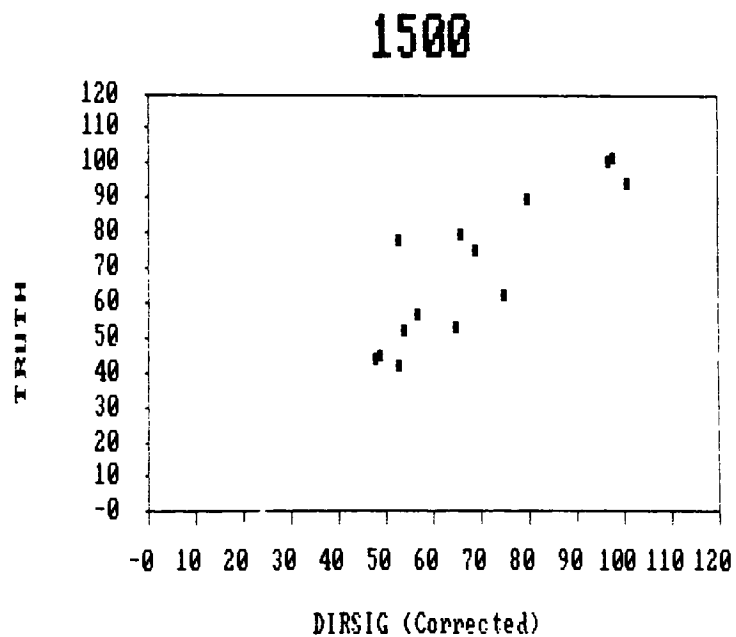
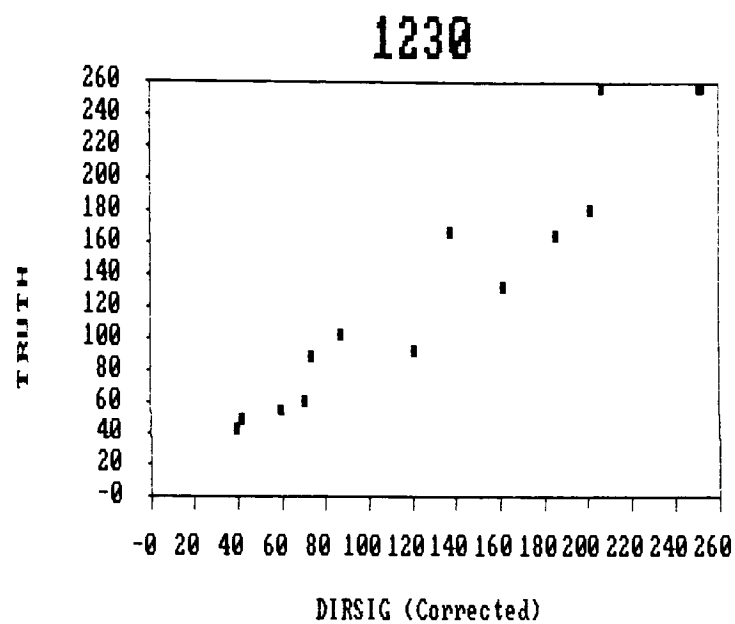


Figure 8.3 *Corrected* Synthetic DC vs Truth DC
[Green band/1230 and 1500 hrs]

table 8.3 and graphically portrayed in figure 8.4.A. The digital count differences displayed in the figure are linearly related to radiance. However, it may be more intuitive to assess these differences in relative reflectivity units. Figure 8.4.B displays the pixel count error as a "rough" error in reflectivity units. This is considered rough due to the varying nature of the reflectivity by band and view angle. The data displays that the energy-surface interactions at those surfaces characterized by actual BDRF measurements generally performed better than the strictly modeled surfaces.

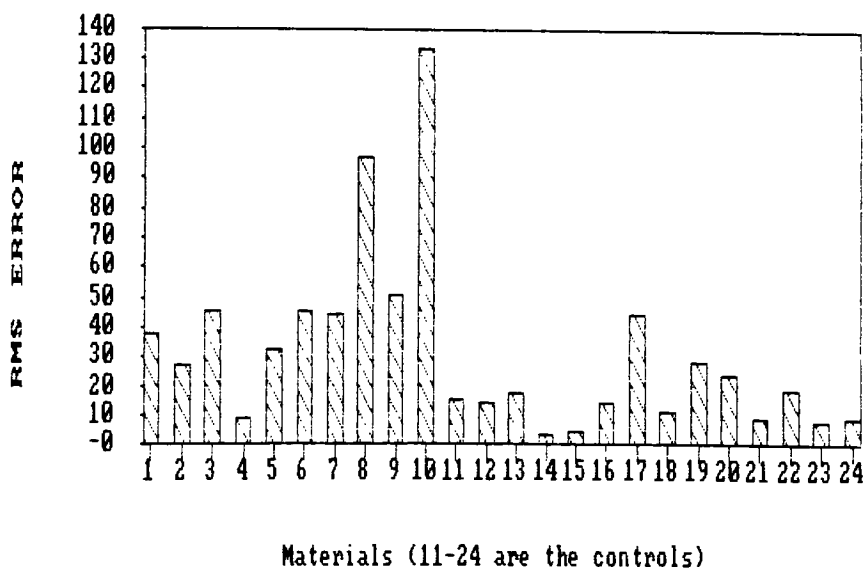


Figure 8.4.A Overall RMS Digital Count Error
[All Bands / Corrected / 1230 & 1500]

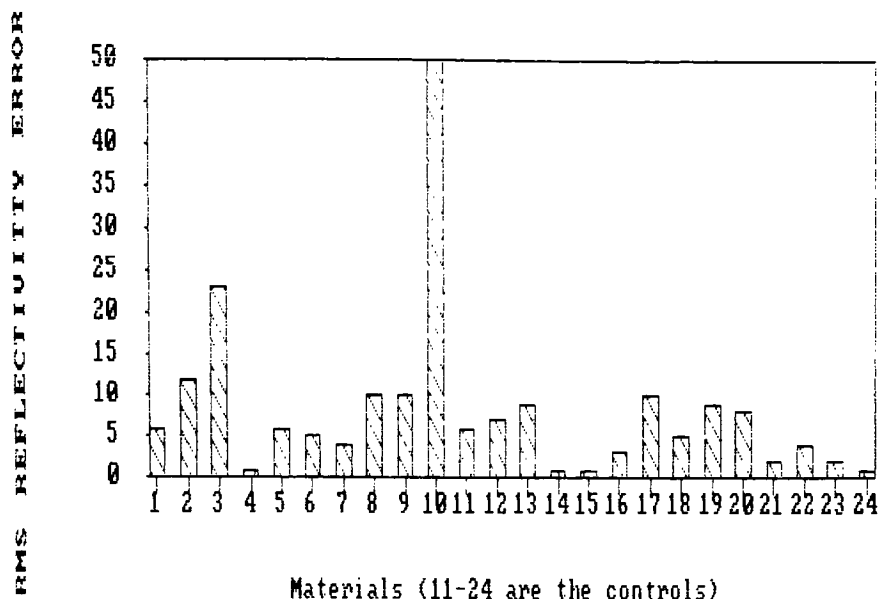


Figure 8.4.B Overall RMS Relative Reflectivity Error
[All Bands / Corrected / 1230 & 1500]

KEY	SURFACE	RMS DC ERROR	ROUGH RELATIVE REFLECTIVITY ERROR (% ref units)
1	Truck Top	38.2	6
2	Truck Door(T)	27.1	12
3	Truck Door(B)	45.1	23
4	Tire	8.9	1
5	Pavement(NT)	32.1	6
6	Pavement(AFT)	45.5	5
7	Grass	44.3	4
8	Sand	96.9	10
9	Concrete	50.9	10
10	Water	132.9	NA
11	Shingles	15.8	6
12	White Panel(T)	13.9	7
13	White Panel(B)	17.8	9
14	Black Panel(T)	3.3	1
15	Black Panel(B)	4.9	1
16	Specular Panel(L)	14.1	3
17	Specular Panel(D)	43.8	10
18	Red Panel	10.9	5
19	Green Panel	28.1	9
20	Blue Panel	24.1	8
21	Grey Panel 1	8.4	2
22	Grey Panel 2	18.7	4
23	Grey Panel 3	8.3	2
24	Grey Panel 4	8.4	1

[Combined Red, Green, Blue, & NIR Bands and 1230 & 1500 Hrs]

Table 8.3 Overall RMS Digital Count and
Relative Reflectivity Error

The drastic difference in the performance of the two specular panel measurements suggest that the specular reflectivity treatment may not be adequate. Even though both light and dark background surfaces performed relatively well when interrogated directly, the half of the specular panel reflecting the dark background performed significantly worse than the half reflecting the light background. This suggests either the BDRF effects were not modeled adequately or else an error was made when extracting the digital count value from the dark side of the specular panel. Given the differences present in the shadowing effects due to geometrical errors in the modeled scene, the latter is a likely cause.

The data for the non-BDRF measured surfaces point out two general limitations to how this particular scene was modeled. First, the water results were too dark. This is because the water was modeled as a non-transmissive surface. In reality, the red, green, and blue wavelengths penetrate a pool of clear water quite efficiently, and then reflect off the pool interior. The ability to place transmissive surfaces within a DIRSIG scene is being developed. A good deal of data is available in the literature characterizing the transmissivity of water in the visible-NIR region.

Secondly, the truck doors suffered from a large degree of error. This is easily explained in that the autoCAD model of the truck side consisted of flat facets, when in reality the sides are quite curved. For specular surfaces, such an approximation is intuitively not sufficient.

The behavior of the relative reflectivity was further assessed by breaking out the data by both band and time. Individual plots describing the data relationships for each band and at each time (1230 and 1500 hrs) are provided in the appendix. The same general trends hold throughout. However, the error in water is reduced in the NIR, since water is highly absorbing in this region and little energy is reflected off the bottom.

8.1.3 Time Trend Comparisons in Image Pixel Values

Another important assessment compares the digital count trend over time. This provides insight into the relative treatment of incident energy. Over the course of the day, the overall strength of the incident energy rises than falls. Figure 8.5 displays the overall energy levels estimated by DIRSIG for the three categories of incident energy in the green band at the specular reflection angle

defined by the fixed viewing location. Additionally, as the solar position changes in the hemisphere, the strengths of energy incident from individual points in the hemisphere change.

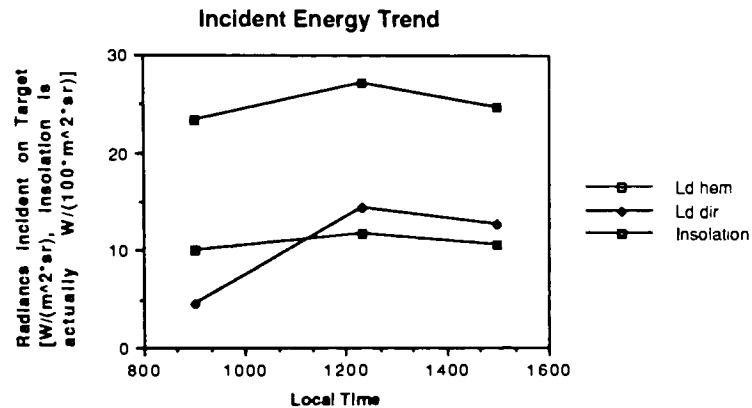


Figure 8.5 Trend in Incident Energy for Green Band
[Insolation in $\text{W} \cdot 100 / (\text{m}^2)$, Ld in $\text{W} / (\text{sr} \cdot \text{m}^2)$]

A controlled test of these effects was performed by constructing a simple autoCAD scene of five flat rectangular objects, positioned horizontally one after another. These objects were given the surface characteristics of the truck, fiberglass cap, white panel, green panel, and grass. This scene was synthetically generated in the green band at 0900, 1230, and 1500 hours. Figure 8.6 plots the calibrated digital counts extracted for each surface.

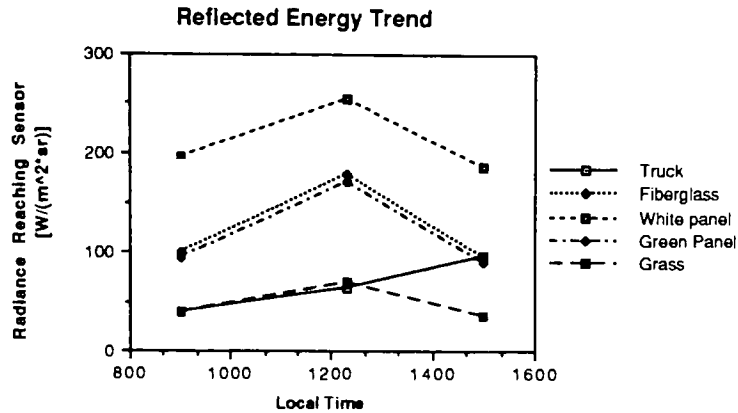


Figure 8.6 Trend in Reflected Energy for Green Band
[in calibrated digital counts]

Notice how the reflected energy from the "more diffuse" surfaces followed the trend of the overall incident energy levels in figure 8.5. However, the reflected energy of the specular surface of the truck doesn't become lower as the overall incident energy lowers. Instead, the reflected energy increases. This highlights the increasing energy found within the specular cone angle (as defined by the sensor location) as the relative position of the sun changes. Also, notice that the fiberglass cap surface followed the same trend as the more diffuse surfaces. The fiberglass was characterized as moderately diffuse. However, these findings suggest this surface may be more appropriately modeled diffuse.

The trends over time were also assessed in the complete scene by generating images in the green band every half hour from 1130 to 1530. The calibrated digital counts were extracted from all 24 surface points for both the simulated and associated truth images. Additionally, the digital counts for each synthetic image were also corrected to account for image wide errors, as done before. The trends in truth DC, calibrated DC, and corrected DC were plotted together.

Overall, the materials displayed good agreement in the trends. The corrected DC plots were closely correlated to the truth data, supporting earlier findings that image-wide offsets were the main cause of error. The individual trend plots of uncorrected data for the 14 BDRF measured surface points show that this image-wide error is minimum (about 20 DCs) at 1130 and largest (about 60 DCs) at 1330. This trend roughly follows the trend in incident energy magnitudes, which were previously found to be the largest contributors to total radiance error. Only a subset of the surface point trend plots are presented here. The plots for the remaining surface points are found in the appendix.

The surfaces of the control panels, shingles, and tires were all characterized by a mostly diffuse surface and their

trend plots were very similar. Figure 8.7 displays the plot for the grey level 3 panel. After correcting for the image-wide offset, the DIRSIG digital counts matched well.

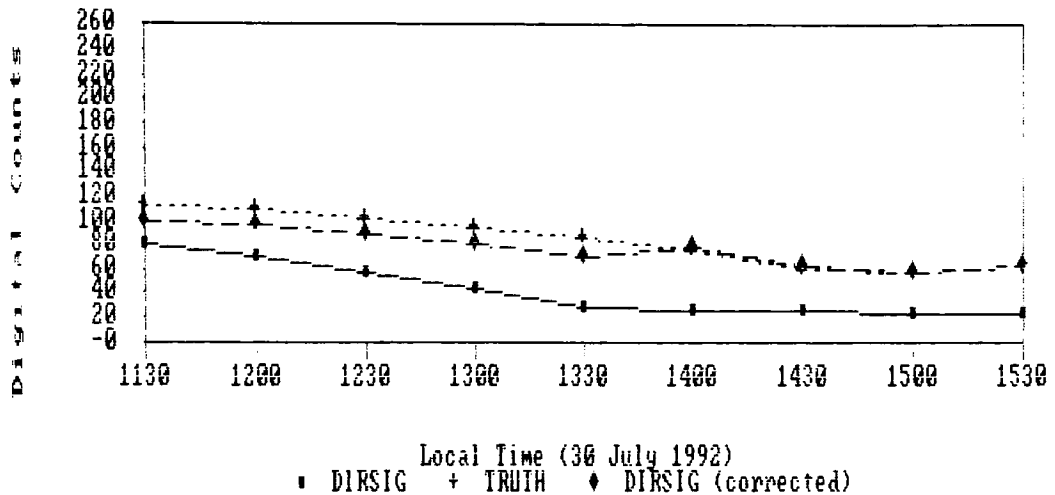


Figure 8.7 Digital Count Trends for Grey Level 3 Panel [Green Band / 1130-1530 hrs]

The trend in the specular panel is generally a good match, as shown in figure 8.8. However, the truth image data was saturated until 1430 hours. At 1500 and 1530 hours the panel becomes shaded and the digital count drops accordingly. In the simulated image, the trend plot for the light half shows it moves into shadow an hour earlier, at 1330. This is due to an error in the geometric relations within the modeled scene. This highlights the sensitivity modeling in the visible region has to geometric and directional errors.

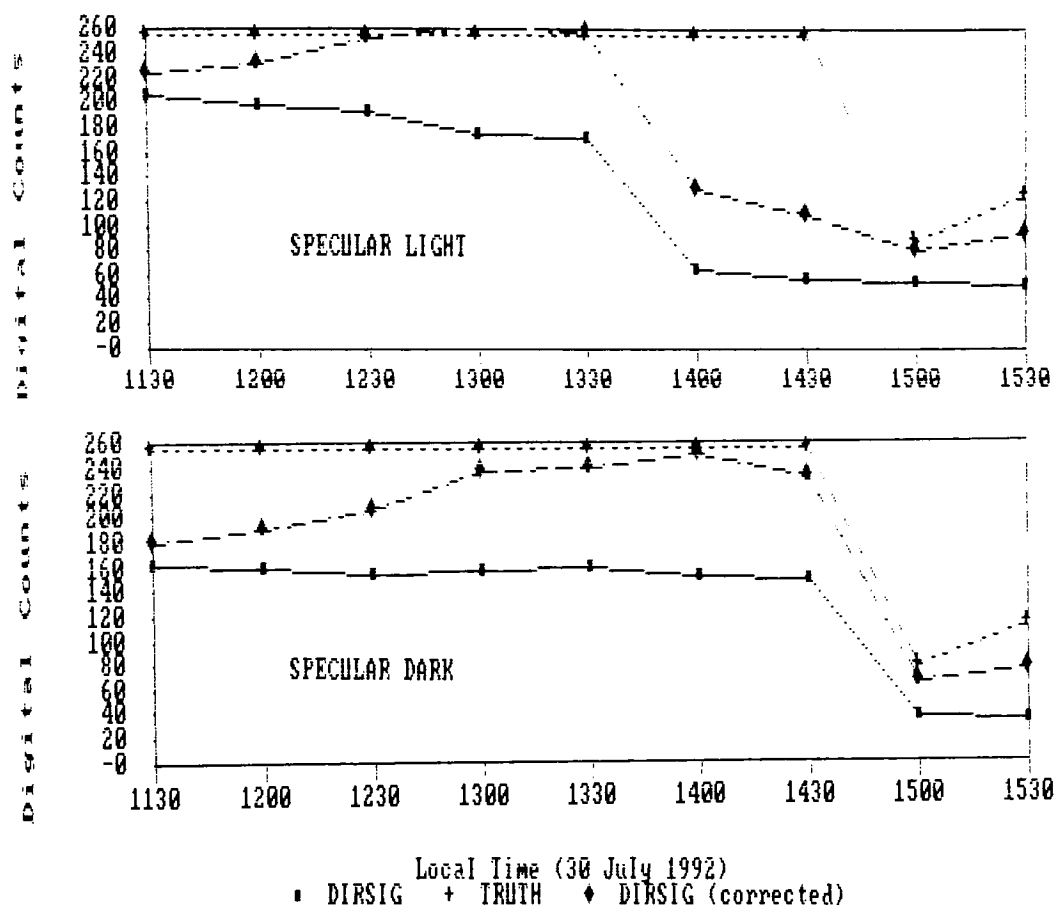


Figure 8.8 Digital Count Trends for Specular Panel's
Light and Dark Halves
[Green Band/1130-1530 hrs]

The trend in the shed front panels also matched fairly well. At 1300 hrs, a change is apparent where the panels were no longer directly illuminated by the sun. After that, the digital counts decrease slowly, following the trend in the downwelling radiance. Figure 8.9 shows the trend plot for the top of the white panel.

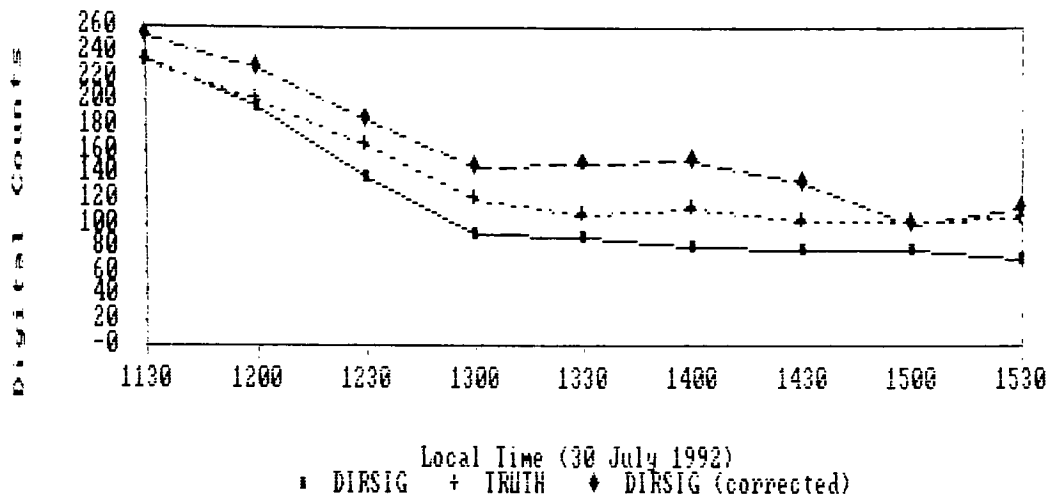


Figure 8.9 Digital Count Trend for Top of White Panel
[Green Band / 1130-1530 hours]

The overall trends for the non-BDRF measured surface points provided similar results. The pavement near the truck had the same early response to the shadowing as the specular panel did. The sand and pavement plots provided little information as they were saturated throughout in the truth image.

The grass trend plot of figure 8.10 is of particular interest. The grass surface was modeled in this study as completely diffuse, with a specular reflectivity component of zero. However, the truth plot increases slightly as the relative solar position moves into the specular incident angle. This infers that the grass surface has some degree

of specularity and is picking up the increase in energy incident from the west. Deering (1988) characterized the surface reflectance of a prairie grassland at peak greenness as having some specular effects, especially at higher view angles. Deering's hemispherical BRDF plots suggest grass may be better modeled as a moderately diffuse surface in DIRSIG.

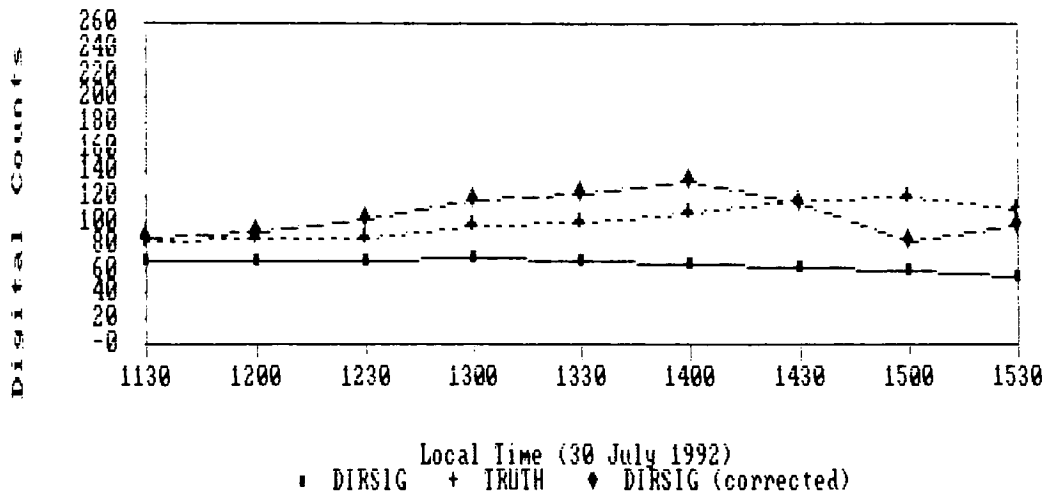


Figure 8.10 Digital Count Trend for Grass
[Green Band / 1130-1530 hrs]

8.2 Qualitative Observations of Images

The quantitative assessments favorably compared DIRSIG's accuracy for modelling the radiance reflected from many of the 24 specific surface points in the scene. This section compares some of the more general aspects of DIRSIG's radiometric modeling. Overall, the synthetic images provide a good representation of the corresponding truth images.

8.2.1 Observations of General Limitations

An obvious limitation to the images is the "cleanness" of their surfaces. Most notably are the absence of spectral variations in the energy reflected from the grass and pavement. Techniques can be applied to add texture, which provides a more realistic appearance by modeling expected natural variations. However, these were specifically not applied in this study in order to permit observation of subtle "first order" radiometric differences.

Additionally, the scene is not on flat ground. The pavement has a slight slope down to the north and the grass actually forms a slight ravine running east-to-west, down the middle of the scene. These create an instant barrier to reality for an observer when comparing to the actual images.

To provide insight to many of the synthetic image artifacts, plate 4 contains maps representing relative data values used in generating an image in the green band at 1230 hours. The PRIMARY MATERIAL map simply identifies the different surface types used in the scene at each pixel. The SHAPE FACTOR map identifies the relative shape factor (F) seen by each pixel for use in the radiometry algorithm. The TARGET DIFFUSE REFLECTIVITY map and TARGET SPECULAR REFLECTIVITY map identify the appropriate relative reflectivity component value used in the algorithm for the target surface. Finally, the BACKGROUND DIFFUSE REFLECTIVITY map and BACKGROUND SPECULAR REFLECTIVITY map identify the relative diffuse reflectivity component value used for the background surface during computation of the diffuse and specular radiance components, respectively.

The two most useful maps are the shape factor (SF) and background diffuse reflectivity (BDR). The shape factor is computed for each pixel by casting rays out into the hemisphere at 30 degree increments. The percentage of rays that do not intersect an object is the value assigned as F. Besides, the large angular increments, this routine is limited in that it treats all surfaces as horizontal. Thus, vertical surfaces such as the control panels will include the shed, truck, and pool in its shape factor computation.

This problem is further compounded because the model uses the shape factor routine to assign the background diffuse reflectivity value used during the calculation of the diffuse radiance component. During the shape factor computation, a histogram is maintained of how many times each secondary surface type is intersected. The surface type intersected the most then has its diffuse reflectivity component value (at $\theta_v=0$) assigned as the diffuse background reflectivity component for the target pixel. These values are depicted in the BDR map. The problems are evident in many areas in the scene and the degree of impact any particular one of these will have depends on a combination of many environmental factors. For instance, the bright "splotches" on the side of the truck bed severely degrade the final images. However, the "wheel" located on the left control panel has little apparent effect on the final image.

Furthermore, the solar energy reflected off the background is effected. As depicted in the radiance equation, the solar radiance reaching the background surface is supposed to be attenuated by $\cos(\theta_b)$. However, when the diffuse radiance component is calculated, the background surface applied is found by the shape factor histogram method already discussed. This method only retains the type of surface and not the surface's orientation. Therefore, the

proper value for θ_b is not known and the algorithm substitutes $\theta_b = 0$, which essentially doesn't modify the radiance at all. The result of this can be dramatic. For example, the pavement in front of the truck has radiance reflected onto it from the side of the truck. At 1230 hrs, $\theta_b = 79$ degrees and $\cos(\theta_b) = 0.19$. By not properly attenuating the solar radiance, five times as much is reflected to the pavement than should be. The effects are apparent in the strong mirroring evident in the mostly diffuse grass and pavement areas. The mirroring is no longer present at 1500 hrs because the sun is not directly illuminating these vertical (or near vertical) surfaces.

8.2.2 Observations of Specific Phenomenon

The image simulations did produce certain effects that are intuitively understood, or even desired!

Shed

One of the desired effects is the reflection of the shed front contrast in the specular panel. Plate 4 contains magnified simulated images of the specular panels at 0900, 1230, and 1500 hours. Contrast and brightness adjustments were made to the magnified images from 1230 and 1500 to enhance the variations within the shadows. At 0900 the sun is directly illuminating the shed front and its reflection is clearly observed in the specular panel. At 1230, the sun position is directly above and to the left of the shed. In this environment, the downwelling radiance is becoming greater from the western portion of the hemisphere and a slight shadow appears across the panel. At 1500, the shadow is more defined. The reflected contrast within the shadow is due to the downwelling radiance illuminating the background object next to the specular panel. This capability was added as part of the visible modifications. Previously, no contrast would have been reproduced in the shadow.

This contrast was observed in the truth images for the NIR bands. However, in the other bands the specular panel was mostly saturated due to limitations in the dynamic range of the sensor. The contrast reflections were actually evident in these bands when observed with the eye. Compromises were made in selecting a single gain and bias for the camera system to provide maximum sensitivity over all bands and expected illumination conditions. The compromise resulted in severe saturation of the specular panels, as well as the concrete and sand.

Additionally, the model correctly provided a variation between the top and bottom of the shed front panels. The bottoms were brighter than the top for the 0900 and 1230 images. This is due to the background reflection off of the specular panels incident onto the lower portion of the shed front. Note the diffuse reflectivity component for the specular panel (as background) is 0.3 at 70 degrees view angle. Even though the surface is highly specular, the R_d value is substantial and reflects a large amount of energy.

Truck

The truck roof and door demonstrated characteristic effects of a specular surface. At 0900 the truck top is darker than the door, because the door is reflecting the strong solar energy located behind the sensor. At 1230 this reverses and the truck top is lighter, since the top is now getting more energy into its specular incident angle as the relative sun position shifts. Then at 1500 the disparity increases as more solar energy is reflected from the roof. This effect is observed clearly in the green bands images.

This example also provides one of the only areas in the scene where the view angle dependency of reflectivity can be observed. Compare the relative reflected radiances between the truck top and door at 0900 and 1500 hrs, in the green band. During these times the incident radiances are fairly close in magnitude. Notice that in both the truth and DIRSIG images, the door at 0900 is significantly darker than the top at 1500. This is due in large part to the lower specular component value at the smaller view angle of the door surface. The reflectivity components for the truck are:

	Top($\theta_v=70$)	Door($\theta_v=20$)
Rd	0.075	0.11
Rs	0.32	0.07

Table 8.4 Truck Reflectivity Component Values

Another area of interest is the side of the truck bed. The rear portion is brighter due to the large reflection from the sand and concrete. The 1500 hrs NIR image pair display this phenomenon most clearly. However, the simulated image is too bright and too well defined. This results from a combination of the surface being modeled as flat rather than curved and the limitations in current shape factor calculations. Note the large "splotches" evident on the side of the truck bed, just to the rear of the cab. These are artifacts of the problem discussed earlier with the selection of background diffuse reflectivity.

Additionally, the 0900 truth images display a solar glint in the truck cap windows which is absent from the simulations. This glint results from the shape of these windows, which "bow" out in the middle, capturing the reflection of the solar disk. This glint could be simulated with the implementation of a more detailed autoCAD model.

Control Panels

The spectral integrity of the DIRSIG simulation is observed by comparing the relative radiance values reflected by the panels. First of all, the grey level panels all maintain the correct rank order throughout the matrix of simulated

images. The red, green, and blue (RG&B) panels' rank ordering was also consistent for the green and blue bands. However, the green and blue panels consistently switched order in the red band. This may result from the panels being soaked by a heavy rain during initial attempts to collect truth image data. The green paint was not an exterior grade and much of it "ran" down into the blue panel. Enough pigment probably remained on the blue surface to alter the results. Unfortunately the surface samples used to measure the BDRF *were* brought in from the rain!

Notice that within the green band the blue panel's reflected radiance is higher than that of the green panel for both the truth and simulated images. At first glance this seems to infer that the green panel would appear blue in an RG&B composite image. However, it is important to remember that the the relative reflected radiances are a function of the particular bands defined by the filters selected and not those defined by the human vision system.

Finally, the control panels provide a good display of the decreasing radiance levels reaching their surfaces as the relative solar position shifts west. At 0900, $\cos(\theta_s)$ is near 1, at 1230 it is near 0.15, and at 1500 no direct solar energy is incident on the panels. The reduction in contrast

of the panels matches well in all bands.

Other Objects

The reflected radiance from the grass and pavement maintained relative contrasts throughout, including the contrast reversal in the NIR band. The reflectivity of vegetation in general increases dramatically in the NIR as a result of scattering by the cell structures. The radiance interactions with the pool water were not modeled correctly. These limitations were discussed in section 8.1.2. The original reflectivity values for the sand and concrete derived from the SETS Technology (1991) data base were altered a good deal to provide some degree of matching with the truth scene. This was done for aesthetic purposes only.

As mentioned, there is a good deal of variability among, and within, available reflectivity data bases. The problem of effectively matching a material's surface characteristics is further hampered by the multitude of materials that fall under a common name. For example, concrete can vary by both constituents and amount of exposure to the environment.

9. Conclusions

The broad intent of this study was to create a baseline for future DIRSIG activity in the visible region. This was to be achieved by modifying the infrared based software to account for the characteristics of visible energy, and then evaluating the model's overall performance.

9.1 Summary

A modification was made to the model's radiance algorithm by dividing surface reflectivity into a combination of view angle dependent (zenith angle only) diffuse and specular components. For every pixel-defined surface, the model applies two different energy interaction approaches, one for diffuse and one for specular.

Therefore, a reflectivity component database was required to effectively characterize those surface effects exploited by the algorithm. These diffuse and specular reflectivity components are most appropriately modeled by a surface's hemispherical-directional reflectance and bidirectional reflectance factor, respectively. To permit the combination of the reflected radiance of each of these approaches, the reflectivity values are further weighted by a surface's

relative degree of specularity and diffuseness as proposed by the Cook-Torrence (1982) reflectivity model.

An underlying desire was to keep the generation of a data base as practical as possible. It was demonstrated that much of a surface's reflection characteristics are contained within in-plane BDRF scans and the data base can be sufficiently developed from these. In fact, the values generated from in-plane data compared within 4.8-10.8 % RMS against full-hemispherical generated values. No trends were evident in the errors according to wavelength or surface type.

A simple method was developed to generate reflectivity component values for surfaces not conducive to laboratory BDRF measurements. This entails using the reflectivity component data from measured surfaces to create models that describe the percent changes in reflected energy as a function of view angle.

To evaluate the model's performance, images of an actual scene were recorded, along with appropriate environmental data. Synthetic images were created of the scene and compared against the truth image data. The assessment supported the hypothesis that the changes would provide

realistic energy-surface interactions, and any significant errors could be attributed to specific problems in the model.

The improvements in the radiance algorithm provide a better representation of the energy interactions occurring in a scene within the visible region. A major change was the inclusion of downwelling sky radiance reflections off of background objects. This permits background contrast information to be maintained and was successfully demonstrated by observing a black and white contrast background reflected by a specular target.

The digital counts of 24 specific surface points were compared over the entire matrix of image pairs. As a group, the BDRF measured surfaces performed better than those simply modeled. All image pairs displayed strong relative contrast correlation for the BDRF measured subset. This was very important, because if the relative contrasts were not maintained, exploitation of the images would be severely limited.

All simulated images contained an image-wide offset which varied by time of day and band. It was determined that a major contributor to this error was the downwelling radiance

predicted by LOWTRAN7. LOWTRAN7's predicted values were generally larger than measured. The directional downwelling radiance errors had percent RMS values of 43.3% (BLUE), 111.1% (GREEN), and 52.2% (RED). The hemispherical downwelling radiance errors had values of 35.3% (BLUE), 61.7% (GREEN), and 70.6% (RED).

Another important problem was with how the shape factors for each pixel are computed. The model considers all pixels as horizontally positioned. Thus, vertical objects will be given shape factors that incorporate input from objects not in line-of-sight of the target. Depending on a variety of factors, this problem may result in catastrophic artifacts.

This limitation is further compounded in two areas affecting the calculation of the diffuse radiance component. The first is the assignment of background reflectivity values, which is based on what surface is intercepted the most during the shape factor computation. The selected surface may be highly reflective and not even in the line-of-sight of the target. To make matters worse, the surface orientation of the selected background is not retained and its zero degree reflectivity components are always used.

The second area affecting calculation of the diffuse

radiance component is the computation of the effective solar radiance reaching the background surface. Since the orientation of the background is not known, the background normal-to-sun angle is always assumed zero making the cosine factor always equal to one. This can greatly effect the amount of energy reflected onto a surface by the background. This problem was observed in an enhanced mirroring effect on the pavement in front of the truck.

9.2 Recommendations

Most importantly, additional study must be done to improve the atmospheric modeling by LOWTRAN7. This may entail more detailed modeling of the constituent effects on visible radiation or a method to provide better input data of the atmospheric profile.

Visible synthetic images are affected a great deal by relative object and source orientations, as well as angular resolution. From shape factor computations, to shadowing effects, to computation of effective solar radiance, an improvement in the accuracy of the physical scene model and the angular resolution of the rendering would make significant improvements in image realism.

The value of view angle dependent reflectivity components is understood theoretically, but was not sufficiently demonstrated in this experiment due to the fixed sensor position. The only example of its merit lies on the relative contrasts of the truck side and top. This was the only instance of the same material in two distinct orientations with respect to the sensor. Future studies should better document the effects of the view angle dependency of the reflectivity components. If possible, the sensor position should be rotated about the zenith angle. If this isn't practical, then many surface types can be duplicated and positioned at different orientations within the scene.

9.3 Closing

Within the visible region, proper accounting of the surface reflection characteristics, through BRDF, are important. However, this study demonstrates that other components of the model are equally important. According to Arnold and Beard (1989): "[For remote sensing applications] the collection of BRDF data is not an end to itself, but rather only one step in the understanding of the radiative transfer of complex objects (targets and backgrounds).... We must balance our consideration of BRDF (its accuracy, etc.) with

respect to the other parameters (sensors, backgrounds, atmosphere, etc.) that also influence the performance of the exploitation technology. BRDF measurements and models are important but represent only one aspect of the exploitation technology that is our central focus".

Based on this study, emphasis should be placed initially on improving LOWTRAN7's atmospheric modeling and DIRSIG's rendering shortfalls. Optimizing these components will go a long way towards producing a more accurate image. After these are improved, then methods can be investigated to further optimize the treatment of surface reflectance.

References

- Arnold, C.B. and J.L. Beard, "An ERIM perspective on BRDF measurement technology," *Scatter from Optical Components*, J.C. Stover, Editor, Proc. SPIE 1165, pp 112-135 (1989)
- Beers, Y., Introduction to the Theory of Error, Addison-Wesley Publishing Company, Inc., Reading Mass., 1957
- Blinn, J.F., "Models of Light Reflection for Computer Synthesized Pictures," *Computer Graphics*, Vol 11, No 2, pp 192-198, July 1977
- Bouville, C. and K. Bouatouch, "Developments in Ray Tracing," Advances in Computer Graphics IV, Eurographic Seminars, W.T. Hewitt, M. Grave, and M. Roch (editors), Springer-Verlag, New York, 1991
- Cathcart, J.M., A.D. Sheffer, and W.L. Wooten, "Synthetic Visible Imagery for Multi-Attribute Target Identification," *Signal and Image Processing Systems Performance Evaluation*, SPIE 1310, pp 150-160 (1990)
- Cook, R.L. and K.E. Torrence, "A Reflectance Model for Computer Graphics," *ACM Transactions on Graphics*, Vol 1, No 1, pp 7-24, January 1982
- Deering, Donald W., "PARABOLA Directional Field Radiometer for Aiding in Space Sensor Data Interpretations," *Recent Advances in Sensors, Radiometry, and Data Processing for Remote Sensing*, SPIE 924, pp 249-261 (1988)
- Environmental Institute of Michigan, "Polarized Emittance Vol 1: Polarized Bidirectional Reflectance with Lambertian or Non-Lambertian Diffuse Components," prepared for the USA Ballistic Research Laboratories (BRL), BRL Contract Report No 154, May 1974
- Feng, X., J.R. Schott, and T. Galligher, "Comparison of Methods for Generation of Absolute Reflectance Factor Values for BRDF Studies," submitted for journal publication by Rochester Institute of Technology, Center for Imaging Science, November 1992
- Feng, X., "Comparison of methods for generation of absolute reflectance factor measurements for BRDF studies," M.S. Thesis, Rochester Institute of Technology, Center for Imaging Science, December 1990

Goral, C.M., K.E. Torrence, D.P. Greenberg, and B. Battaille, "Modeling the Interaction of Light Between Diffuse Surfaces," *Computer Graphics*, Vol 18, No 3, pp 213-222, July 1984

Greenberg, D.P., "Light Reflection Models for Computer Graphics," *Science*, Vol 244, pp 166-173, April 1989

He, X.D., K.E. Torrence, F.X. Sillion, and D.P. Greenberg, "A Comprehensive Physical Model for Light Reflection," *Computer Graphics*, Vol 25, No 4, pp 175-186, July 1991

Hecht, E. and A. Zajac, Optics, Addison-Wesley Publishing Company, Reading, Massachusetts, 1974

Lehman, E.L., Nonparametrics; Statistical Methods Based on Ranks, Holden-Day, Inc., San Francisco, 1975

Lillesand, T.M. and R.W. Kiefer, Remote Sensing and Image Interpretation, 2nd ed., John Wiley and Sons, Inc., New York, 1987

Lindahl, C., A. Cockcroft, T. Derryberry, J. Sigler, and M. Yablonski, "Synthetic, multisensor, database generation and validation," *Signal and Image Processing Systems Performance Evaluation*, SPIE 1310, pp 88-94 (1990)

Magenat-Thalmann, N. and D. Thalmann, Image Synthesis: Theory and Practice, Springer-Verlag, New York, 1987

Mason, J., "DIRSIG Validation in the Mid-Wave Infrared Region," Presentation at DIRS Lab Meeting, Rochester Institute of Technology, Center for Imaging Science, December 1992

Nicodemus, F.E., "Directional Reflectance and Emissivity of an Opaque Surface," *Applied Optics*, Vol 4, No 7, pp 767-772, July 1965

Rankin, D., "DIRSIG Validation in the Long Wave Infrared Region," Presentation at DIRS Lab Meeting, Rochester Institute of Technology, Center for Imaging Science, November 1992

Raqueno, R., C. Salvaggio, J.S. Warnick, E. Kraus, and J.R. Schott, "A thermal infrared synthetic image generation model," Final Report RIT/DIRS 90/91-63-142, prepared for the Central Intelligence Agency, Office of Development and Engineering, April 1991

Reeves, R., D. Anding, and F. Mertz, "First-Principles Deterministic Simulation of IR and Visible Imagery," *Multispectral Image Processing and Enhancement*, SPIE 933, pp 207-230 (1988)

Sabins, Floyd F., Remote Sensing; Principles and Interpretation, 2nd ed, W.H. Freeman and Company, New York, 1987

Salvaggio, C., G. Braun, and J.R. Schott, "SVGM: a spectral vector generating model using the LOWTRAN 7 and SCATTRAN atmospheric propagation codes," RIT/DIRS 90/91-63-141, prepared for Eastman Kodak Company, Federal Systems Division, January 1991

Schott, J.R., M. Fairchild, X. Feng, R. Raqueno, B. Brower, and T. Galligher, "Techniques for measurement of the optical properties of materials," Final Report RIT/DIRS 89/90-51-134, prepared for United States Department of Energy, January 1990

Schott, J.R., J.E. Mason, C. Salvaggio, J.D. Sirianni, R.A. Rose, E.O. Kulp, and D.K. Rankin, "DIRSIG-Digital Imaging and Remote Sensing Image Generation Model: Description, Enhancement, and Validation," RIT/DIRS Report 92-93-51-146, prepared for the Central Intelligence Agency, Office of Development and Engineering, July 1993

SETS Technology, Inc., "Spectral Catalog, Appendix A; Catalog of Spectral Reflectance Measurements", Ver 1, Vol 1, September 1991

Sillion, F.X., J.R. Arvo, S.H. Westin, and D.P. Greenberg, "A Global Illumination Solution for General Reflectance Distributions," *Computer Graphics*, Vol 25, No 4, pp 187-195, July 1991

Torrence, K.E. and E.M. Sparrow, "Theory of Off-Specular Reflection From Roughened Surfaces," *Journal of the Optical Society of America*, Vol 57, No 9, pp 1105-1112, Sep 1967

Wallace, J.R., M.F. Cohen, and D.P. Greenberg, "A Two-Pass Solution to the Rendering Equation: A Synthesis of Ray Tracing and Radiosity Methods," *Computer Graphics*, Vol 21, No 4, pp 311-320, July 1987

***** Appendix 1 *****

Image Analysis

***** 1.a *****

Image Digital Counts
for All 24 Surface Points for Truth and DIRSIG Images

(see following pages)

FOR BLUE 30 1230

	SURFACE	DIRSIG DC	X-FORM DC	TRUTH DC
	-----	-----	-----	-----
1	truck top	62	101	70
2	truck door(t)	35	64	38
3	truck door(b)	35	64	36
4	tire	7	26	39
5	pavement(nt)	121	180	140
6	pavement(aft)	133	196	148
7	grass	39	70	85
8	sand	91	140	255
9	concrete	197	283	255
10	water	9	29	187
11	shingles	32	60	55
12	shed lite(t)	126	187	164
13	shed lite(b)	147	215	179
14	shed dark(t)	13	41	43
15	shed dark(b)	20	44	48
16	specular(l)	156	241	255
17	specular(d)	143	210	255
18	red	41	72	60
19	green	79	124	92
20	blue	55	91	132
21	grey1	130	260	255
22	grey2	94	144	166
23	grey3	56	92	101
24	grey4	44	75	38

FOR BLUE 30 1500

	SURFACE	DIRSIG DC	X-FORM DC	TRUTH DC
	-----	-----	-----	-----
1	truck top	93	117	135
2	truck door(t)	17	47	43
3	truck door(b)	10	40	43
4	tire	3	34	42
5	pavement(nt)	34	61	50
6	pavement(aft)	114	131	174
7	grass	33	61	119
8	sand	77	99	233
9	concrete	168	173	255
10	water	9	40	227
11	shingles	17	47	77
12	shed lite(t)	73	100	101
13	shed lite(b)	83	103	94
14	shed dark(t)	12	42	43
15	shed dark(b)	13	43	44
16	specular(l)	55	80	39
17	specular(d)	40	67	79
18	red	19	48	42
19	green	36	63	53
20	blue	63	91	62
21	grey1	82	103	100
22	grey2	43	69	75
23	grey3	26	54	56
24	grey4	20	49	52

FOR GREEN 30 1230

	SURFACE	DIRSIG DC	X-FORM DC	TRUTH DC
	-----	-----	-----	-----
1	truck top	64	96	70
2	truck door(t)	30	54	38
3	truck door(b)	31	55	36
4	tire	7	26	39
5	pavement(nt)	138	187	140
6	pavement(aft)	147	198	148
7	grass	68	101	85
8	sand	118	162	255
9	concrete	214	255	255
10	water	10	29	187
11	shingles	35	60	55
12	shed lite(t)	137	186	164
13	shed lite(b)	150	202	179
14	shed dark(t)	19	40	43
15	shed dark(b)	20	42	48
16	specular(l)	192	253	255
17	specular(d)	154	207	255
18	red	44	71	60
19	green	85	122	92
20	blue	118	162	132
21	grey1	191	252	255
22	grey2	98	138	166
23	grey3	58	88	101
24	grey4	46	74	88

FOR GREEN 30 1500

	SURFACE	DIRSIG DC	X-FORM DC	TRUTH DC
	-----	-----	-----	-----
1	truck top	117	125	135
2	truck door(t)	14	50	43
3	truck door(b)	13	49	43
4	tire	3	42	42
5	pavement(nt)	33	64	50
6	pavement(aft)	130	135	174
7	grass	60	84	119
8	sand	102	114	255
9	concrete	185	175	255
10	water	10	47	227
11	shingles	18	53	77
12	shed lite(t)	79	98	101
13	shed lite(b)	84	101	94
14	shed dark(t)	11	48	43
15	shed dark(b)	12	49	44
16	specular(l)	55	80	89
17	specular(d)	36	66	79
18	red	18	53	42
19	green	35	65	53
20	blue	48	75	62
21	grey1	78	97	100
22	grey2	40	69	75
23	grey3	24	57	56
24	grey4	19	54	52

FOR RED 30 1230

	SURFACE	DIRSIG DC	X-FORM DC	TRUTH DC
	-----	-----	-----	-----
1	truck top	194	226	255
2	truck door(t)	148	175	122
3	truck door(b)	148	175	76
4	tire	12	24	39
5	pavement(nt)	159	187	147
6	pavement(aft)	164	192	157
7	grass	154	181	82
8	sand	255	293	255
9	concrete	255	293	255
10	water	12	24	118
11	shingles	43	58	51
12	shed lite(t)	139	165	149
13	shed lite(b)	161	189	170
14	shed dark(t)	21	34	40
15	shed dark(b)	23	36	45
16	specular(l)	220	254	255
17	specular(d)	182	212	255
18	red	137	162	157
19	green	112	135	74
20	blue	106	128	97
21	grey1	204	237	253
22	grey2	101	122	158
23	grey3	60	77	94
24	grey4	48	64	78

FOR RED 30 1500

	SURFACE	DIRSIG DC	X-FORM DC	TRUTH DC
	-----	-----	-----	-----
1	truck top	242	176	255
2	truck door(t)	76	80	76
3	truck door(b)	76	80	70
4	tire	4	38	38
5	pavement(nt)	33	55	44
6	pavement(aft)	147	121	179
7	grass	138	116	113
8	sand	255	183	255
9	concrete	255	183	255
10	water	15	44	151
11	shingles	21	48	66
12	shed lite(t)	69	76	82
13	shed lite(b)	77	80	73
14	shed dark(t)	10	41	38
15	shed dark(b)	13	43	38
16	specular(l)	51	65	67
17	specular(d)	33	55	60
18	red	46	62	57
19	green	37	57	41
20	blue	36	56	47
21	grey1	68	75	82
22	grey2	35	56	62
23	grey3	21	48	48
24	grey4	17	45	46

FOR NIR 30 1230

	SURFACE	DIRSIG DC	X-FORM DC	TRUTH DC
	-----	-----	-----	-----
1	truck top	75	116	160
2	truck door(t)	76	117	82
3	truck door(b)	76	117	53
4	tire	7	34	35
5	pavement(nt)	85	128	81
6	pavement(aft)	86	129	89
7	grass	170	230	202
8	sand	184	247	220
9	concrete	204	271	249
10	water	7	34	78
11	shingles	18	47	39
12	shed lite(t)	50	86	99
13	shed lite(b)	56	93	96
14	shed dark(t)	9	37	36
15	shed dark(b)	10	38	37
16	specular(l)	80	122	157
17	specular(d)	66	105	141
18	red	53	89	110
19	green	77	113	104
20	blue	56	93	95
21	grey1	74	115	128
22	grey2	36	69	80
23	grey3	22	52	52
24	grey4	13	47	46

FOR NIR 30 1500

SURFACE	DIRSIG DC	X-FORM DC	TRUTH DC
1 truck top	88	143	167
2 truck door(t)	38	73	44
3 truck door(b)	38	73	40
4 tire	3	24	28
5 pavement(nt)	14	40	25
6 pavement(aft)	76	126	79
7 grass	150	230	222
8 sand	160	244	203
9 concrete	181	273	250
10 water	8	31	74
11 shingles	10	34	39
12 shed lite(t)	24	54	62
13 shed lite(b)	25	55	48
14 shed dark(t)	6	28	30
15 shed dark(b)	6	28	30
16 specular(l)	16	42	39
17 specular(d)	13	38	36
18 red	16	42	48
19 green	22	51	50
20 blue	17	44	45
21 grey1	22	51	45
22 grey2	12	37	33
23 grey3	8	31	28
24 grey4	7	30	26

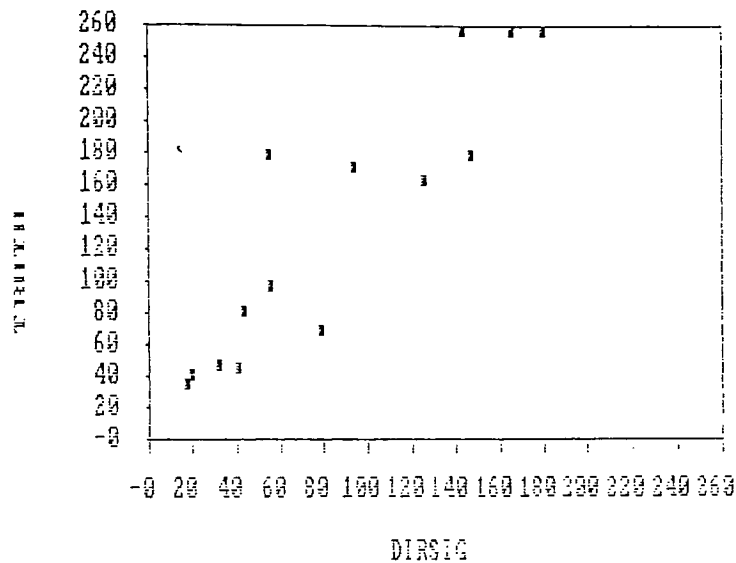
***** Appendix 1 *****
Image Analysis
***** 1.b *****

Remaining Image Digital Counts Plots
for 14 BDRF-Measured Surface Points
for Truth and DIRSIG Images

(see following pages)

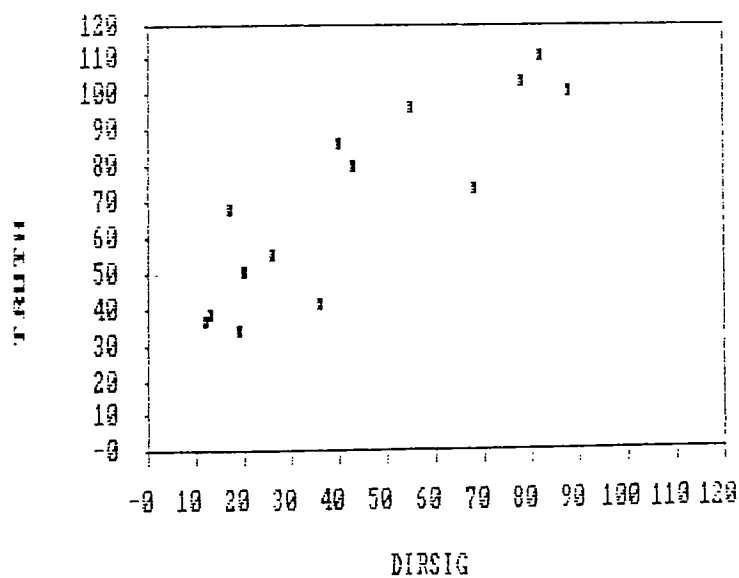
DIRSIG vs TRUTH (B 30 1230)

(in calibrated digital counts)



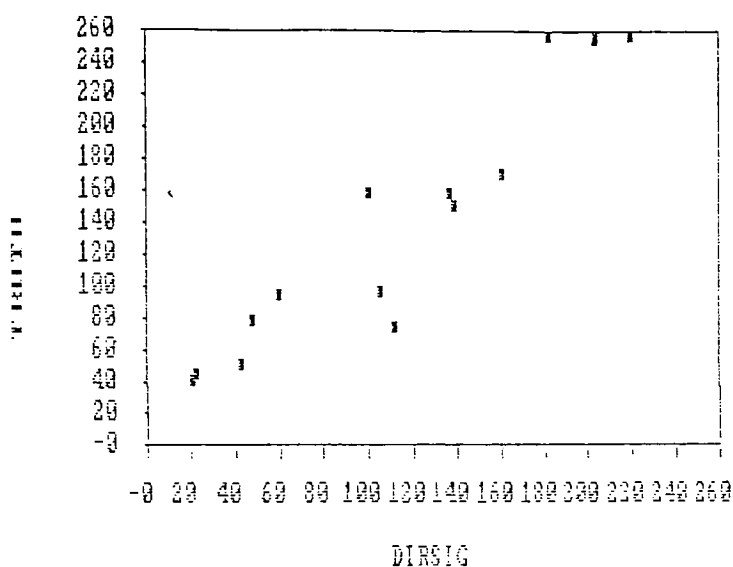
DIRSIG vs TRUTH (B301500) M

(in calibrated digital counts)



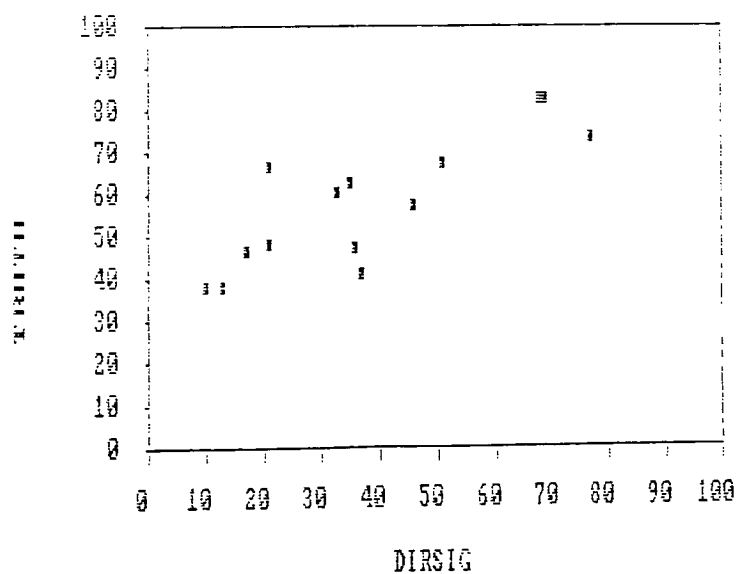
DIRSIG vs TRUTH (R301230) M

(in calibrated digital counts)



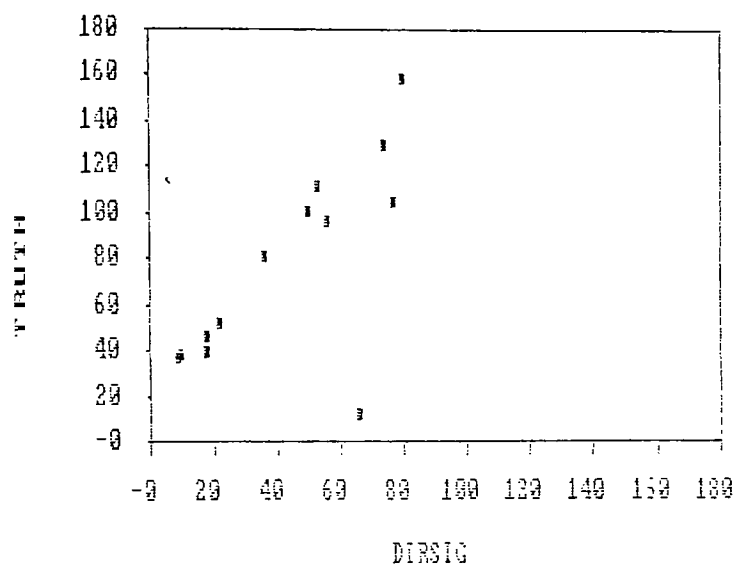
DIRSIG vs TRUTH (R301500) M

(in calibrated digital counts)



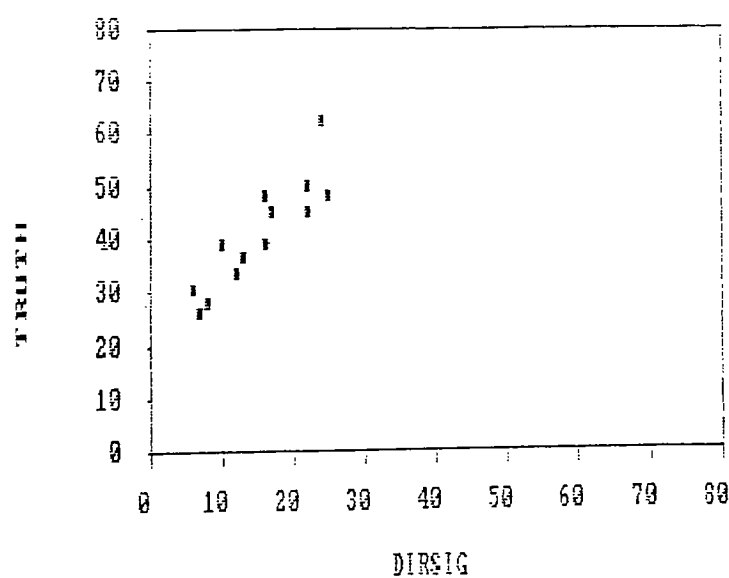
DIRSIG vs TRUTH (N 30 1230)

(in calibrated digital counts)



DIRSIG vs TRUTH (N 30 1500)

(in calibrated digital counts)



***** Appendix 1 *****

Image Analysis

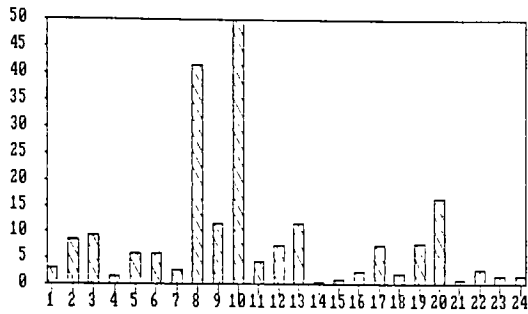
***** 1.c *****

Various Relative Reflectivity Error Plots
for all 24 BDRF-Measured Surface Points
for Truth and DIRSIG Images

(see following pages)

RMS REFLECTIVITY ERROR

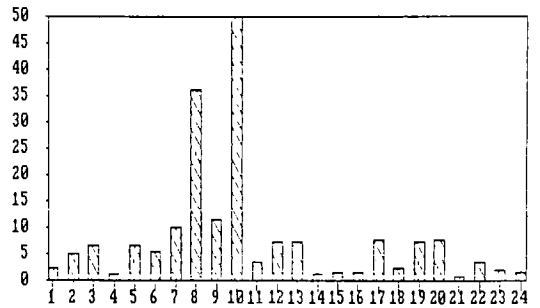
Blue Band / 1230&1500 / Corrected



Materials (11-24 are the controls)

RMS REFLECTIVITY ERROR

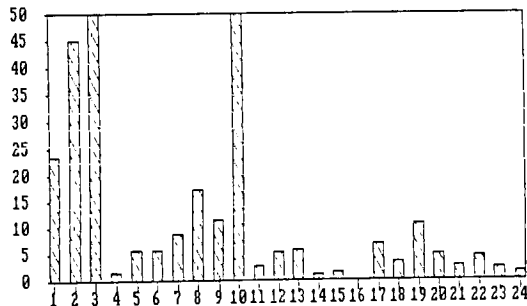
GREEN Band / 1230&1500 / Corrected



Materials (11-24 are the controls)

RMS REFLECTIVITY ERROR

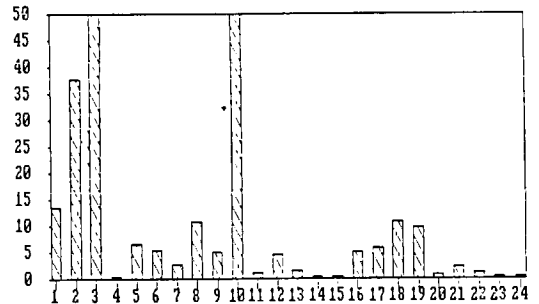
BED Band / 1230&1500 / Corrected



Materials (11-24 are the controls)

RMS REFLECTIVITY ERROR

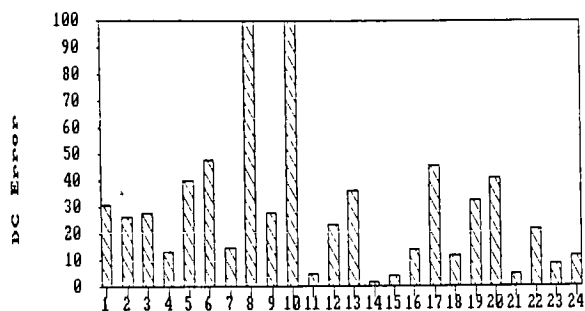
NIB Band / 1230&1500 / Corrected



Materials (11-24 are the controls)

DIGITAL COUNT ERROR

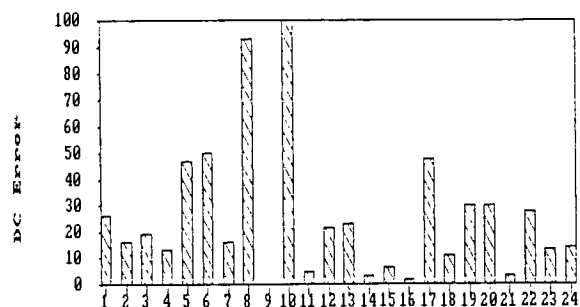
Corrected Digital Counts, BLUE @1230



Materials(11-24 are measured materials)

DIGITAL COUNT ERROR

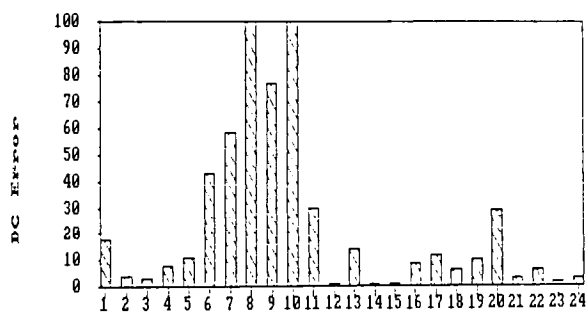
GREEN Band / 1230 / Corrected



Materials(11-24 are measured materials)

DIGITAL COUNT ERROR

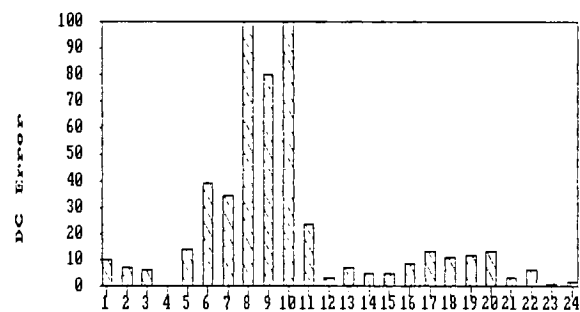
BLUE Band / 1500 / Corrected



Materials(11-24 are measured materials)

DIGITAL COUNT ERROR

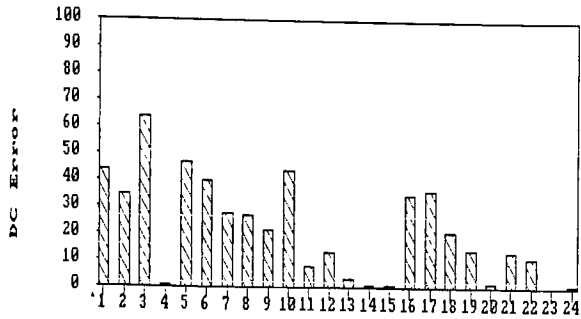
GREEN / 1500 / Corrected



Materials(11-24 are measured materials)

DIGITAL COUNT ERROR

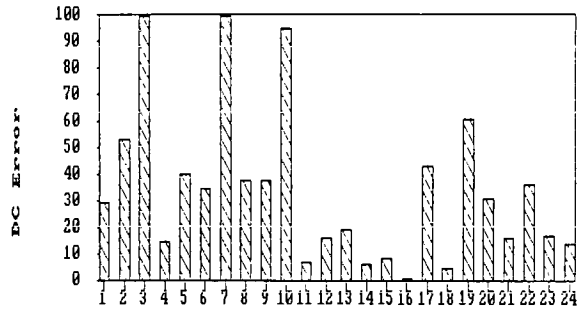
NIR Band / 1230 / Corrected



Materials(11-24 are measured materials)

DIGITAL COUNT ERROR

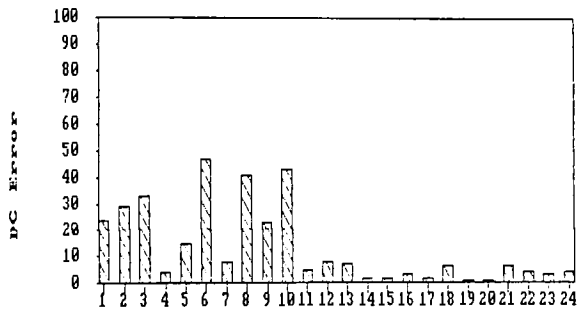
RED Band / 1230 / Corrected



Materials(11-24 are measured materials)

DIGITAL COUNT ERROR

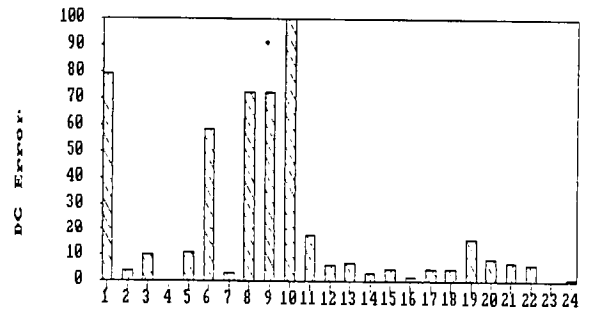
NIR Band / 1500 / Corrected



Materials(11-24 are measured materials)

DIGITAL COUNT ERROR

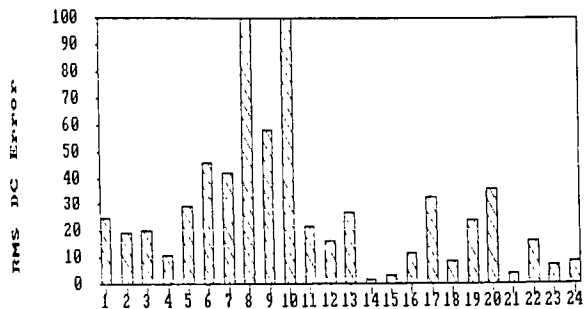
RED Band / 1500 / Corrected



Materials(11-24 are measured materials)

RMS DIGITAL COUNT ERROR

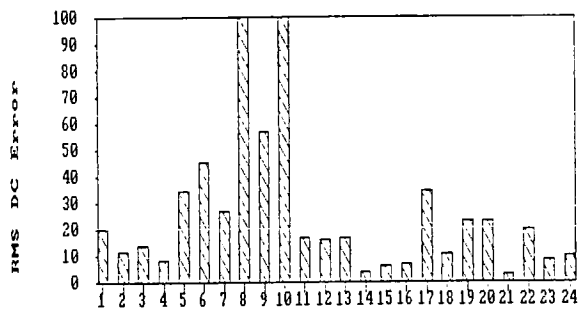
Blue Band / 1230&1500 / Corrected



Materials (11-24 are the controls)

RMS DIGITAL COUNT ERROR

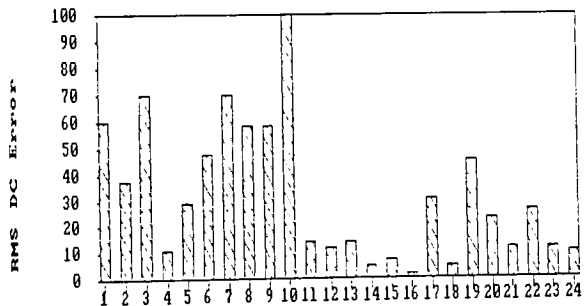
GREEN Band / 1230&1500 / Corrected



Materials (11-24 are the controls)

RMS DIGITAL COUNT ERROR

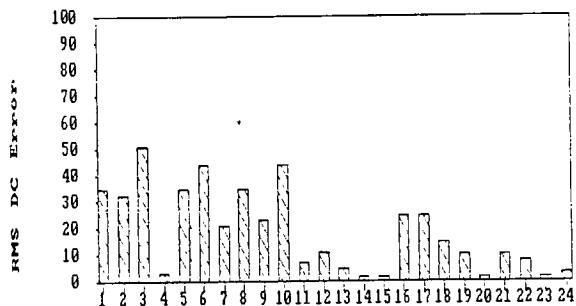
RED Band / 1230&1500 / Corrected



Materials (11-24 are the controls)

RMS DIGITAL COUNT ERROR

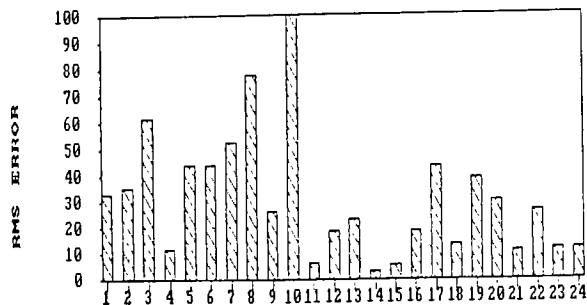
NIR Band / 1230&1500 / Corrected



Materials (11-24 are the controls)

RMS DIGITAL COUNT ERROR

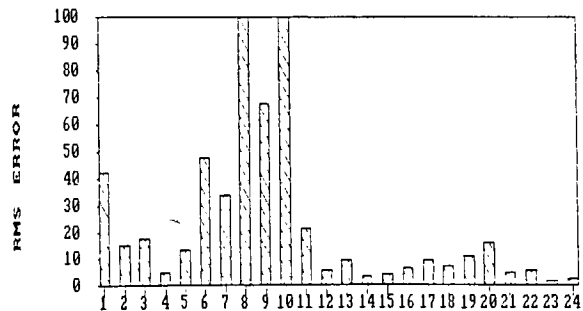
(All bands / 1230 / Corrected)



Materials (11-24 are the controls)

RMS DIGITAL COUNT ERROR

(All bands / 1500 / Corrected)



Materials (11-24 are the controls)

***** Appendix 1 *****

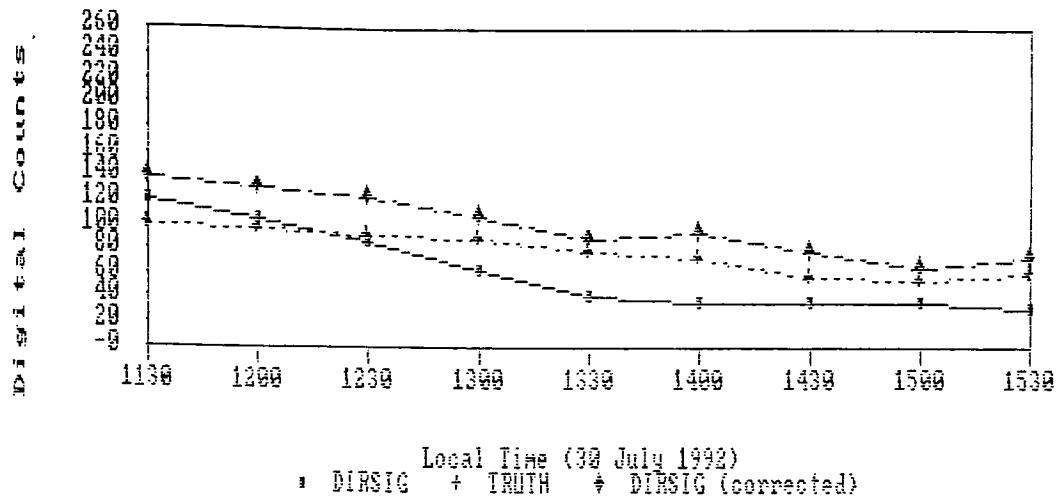
Image Analysis

***** 1.d *****

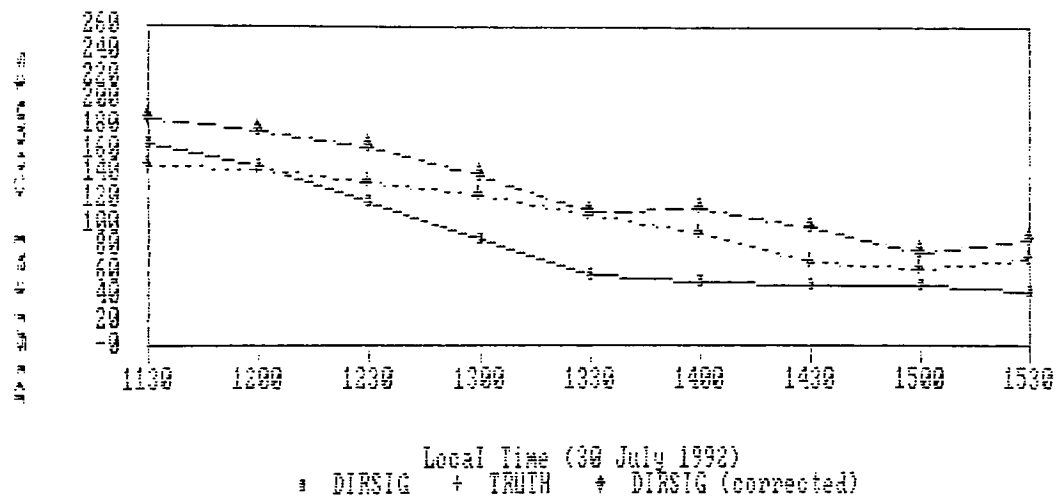
Remaining Trend Plots for Surface Points
for Truth and DIRSIG Images
from 1130 - 1530 Hours in Green Band

(see following pages)

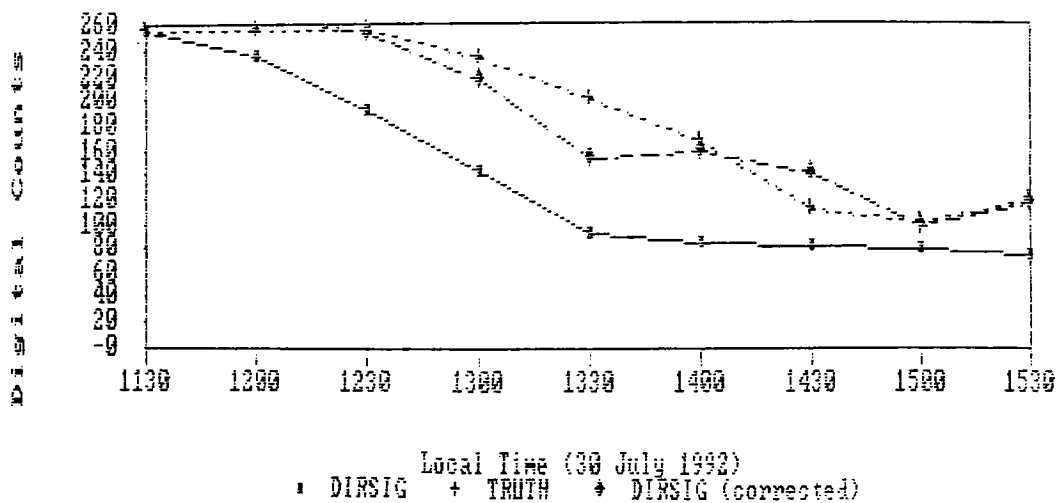
(GREEN PANEL, Within Green Band)



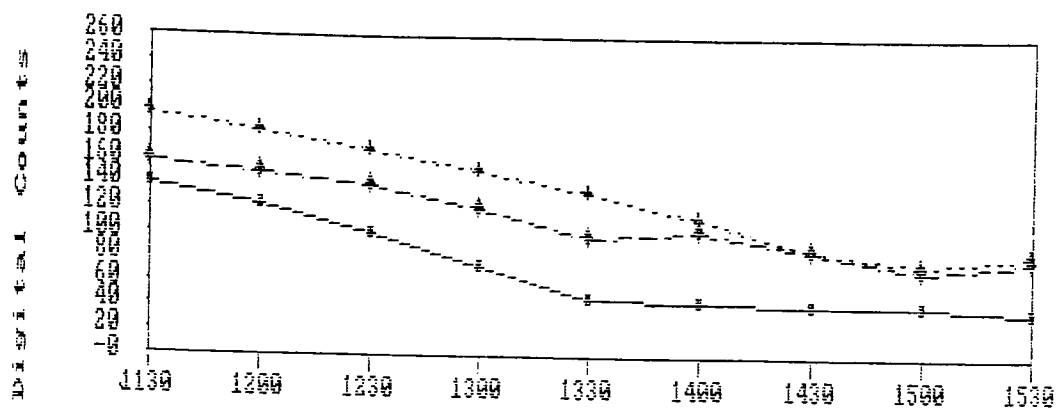
(BLUE PANEL, Within Green Band)



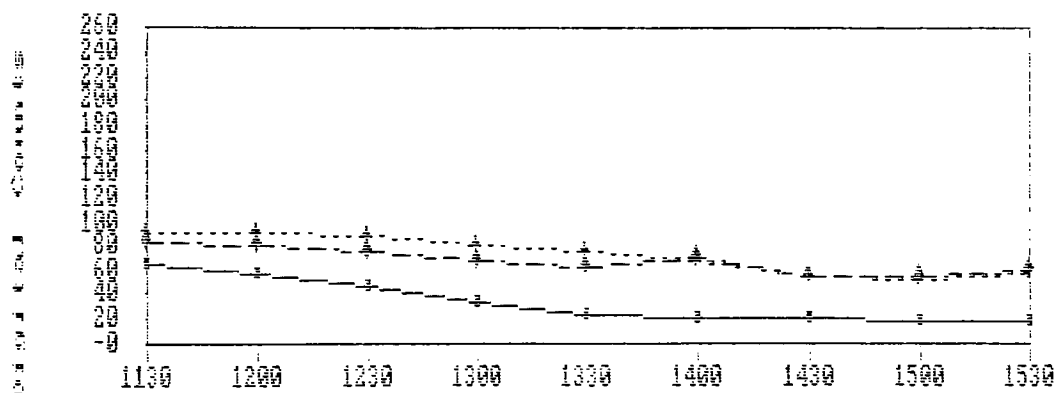
(GREY 1 PANEL, Within Green Band)



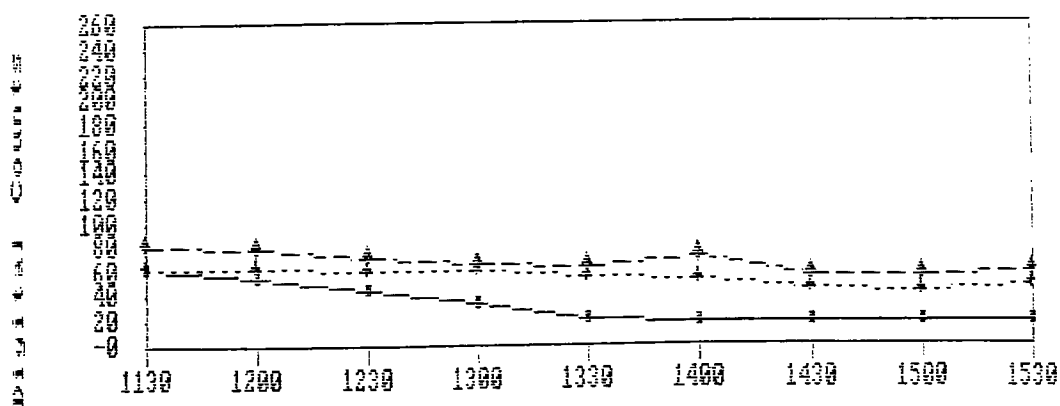
(GREY 2 PANEL, Within Green Band)



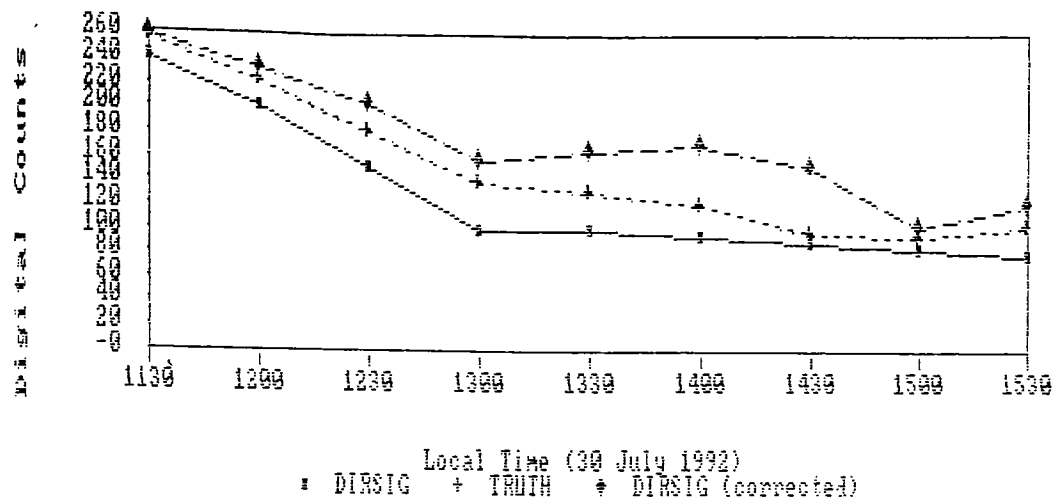
(GREY 4 PANEL, Within Green Band)



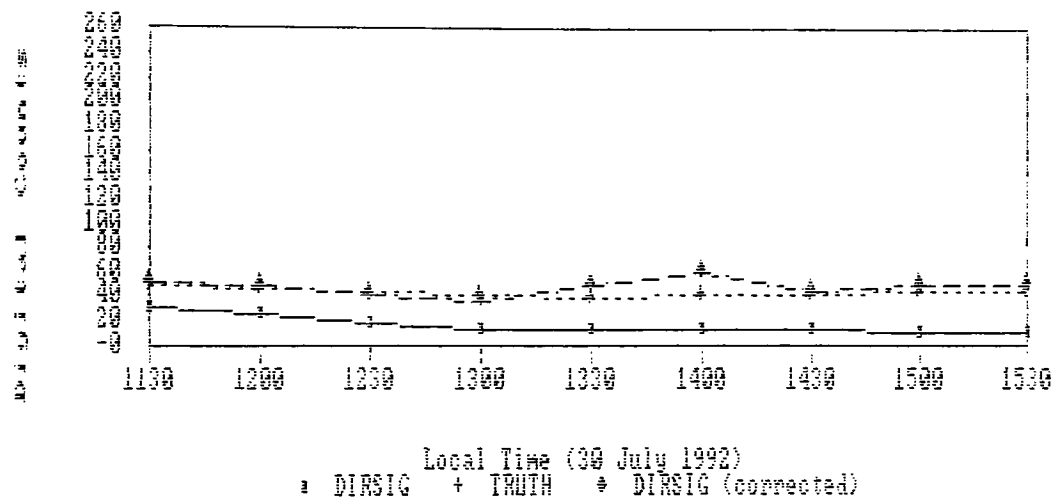
(RED PANEL, Within Green Band)



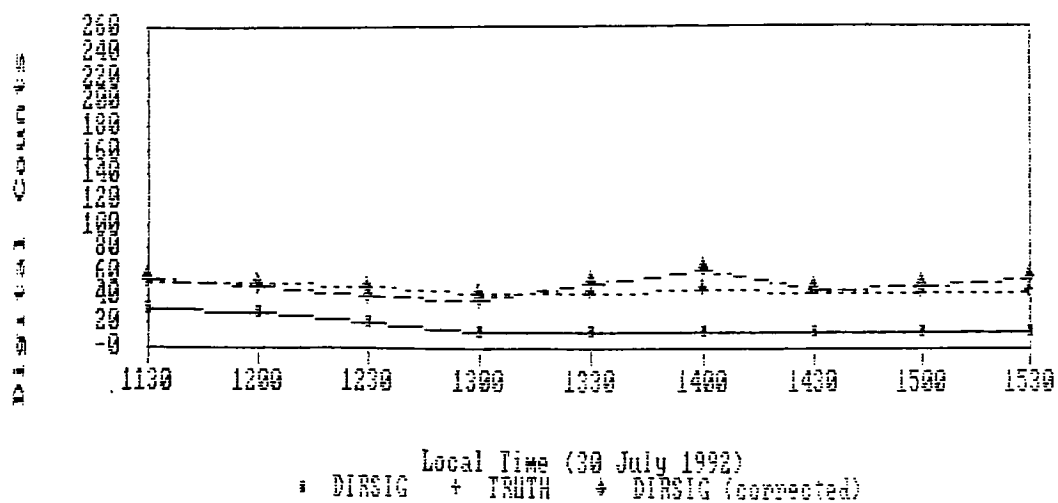
(WHITE PANEL-B, Within Green Band)



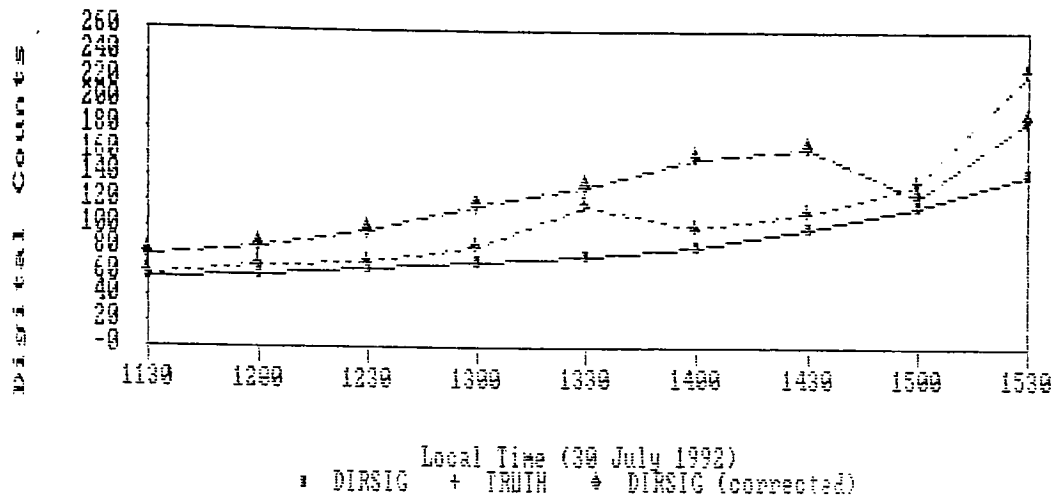
(BLACK PANEL-T, Within Green Band)



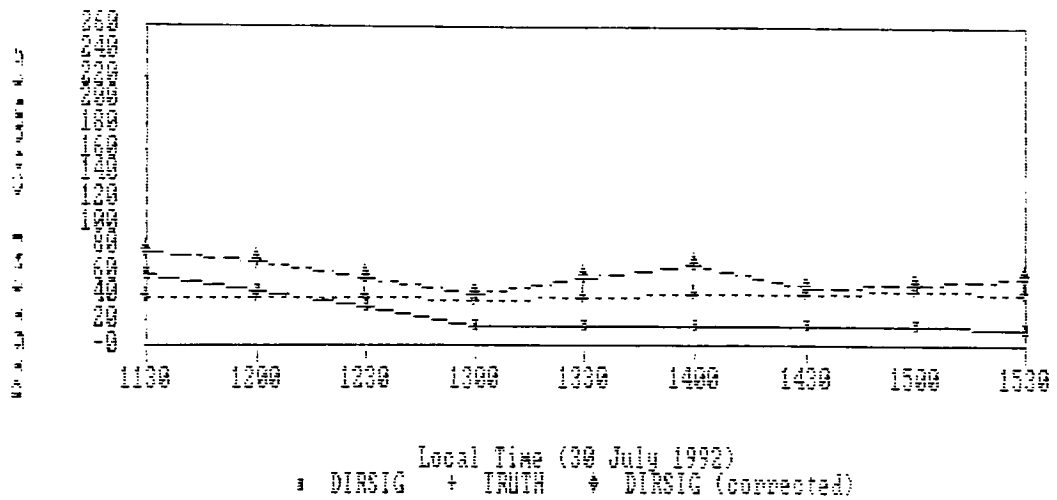
(BLACK PANEL-B, Within Green Band)



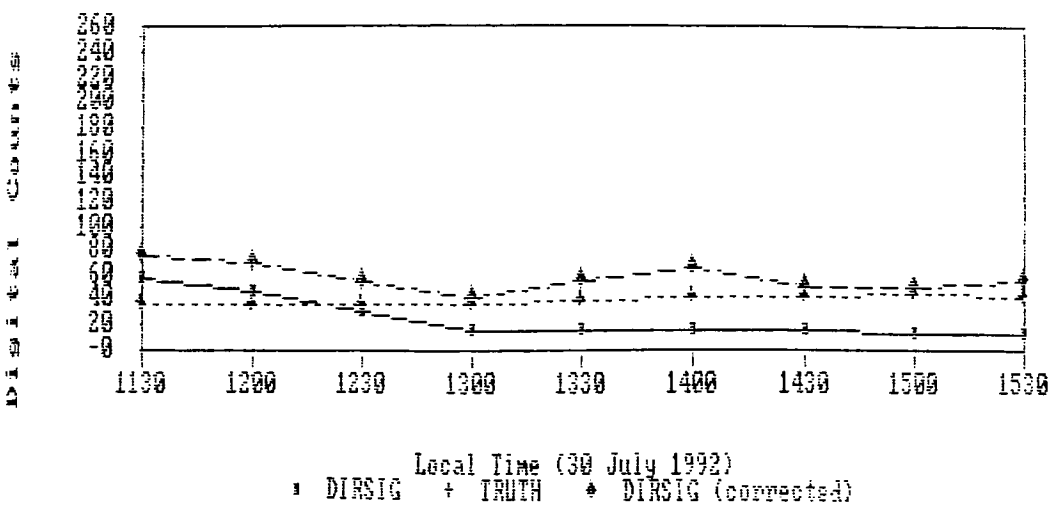
(TRUCK ROOF, Within Green Bandpass)



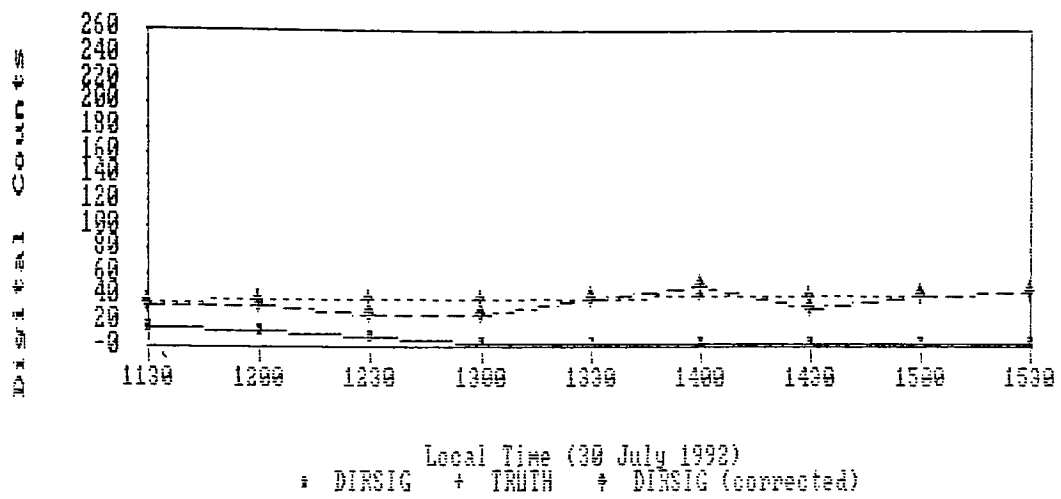
(TRUCK DOOR TOP, Within Green Bandpass)



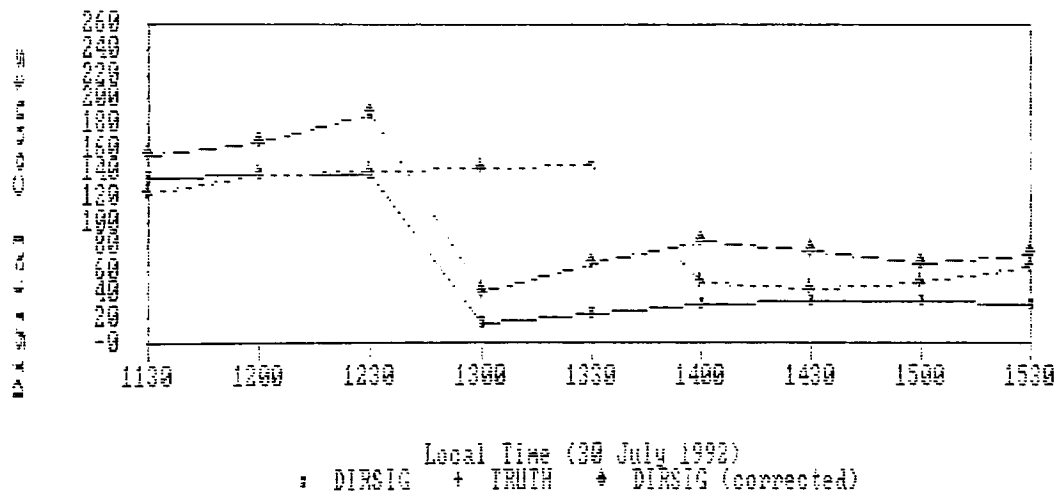
(TRUCK DOOR BOTTOM, Within Green Band)



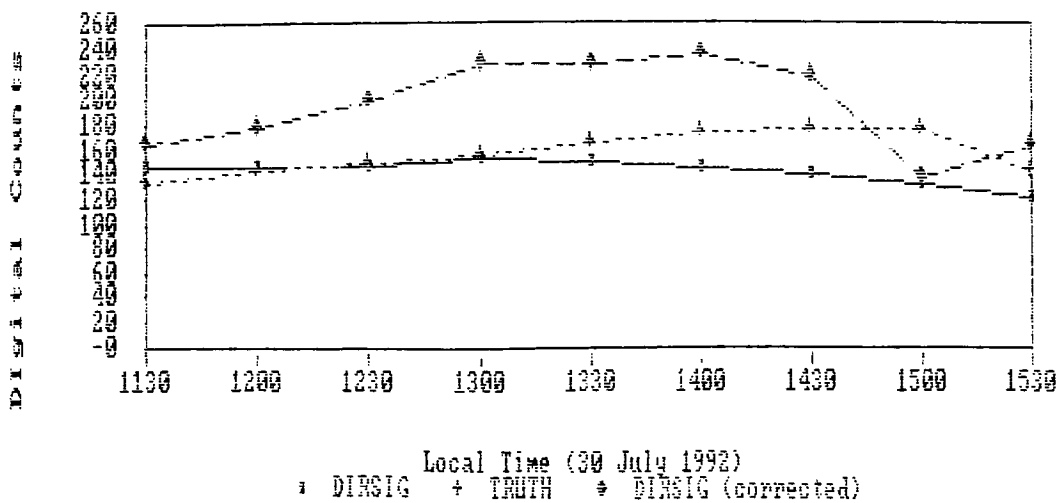
(TIRE, Within Green Band)



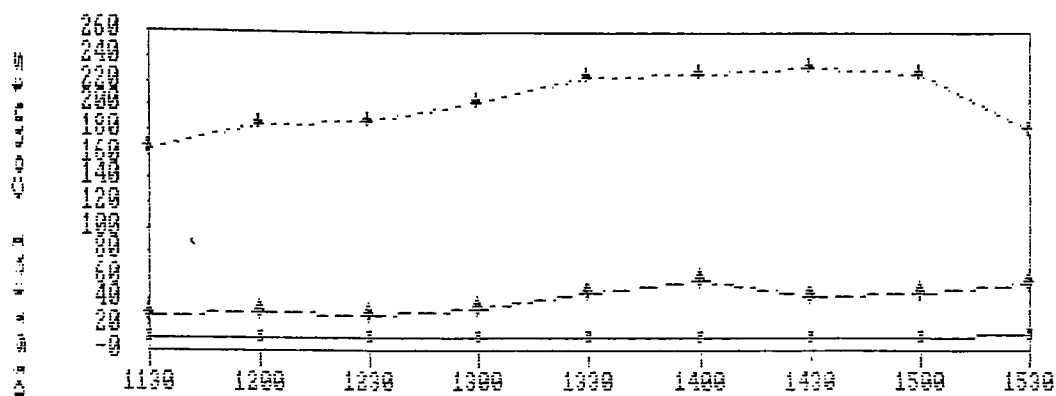
(PAVEMENT-NT, Within Green Band)



(PAVEMENT-AFT, Within Green Band)



(WATER, Within Green Band)



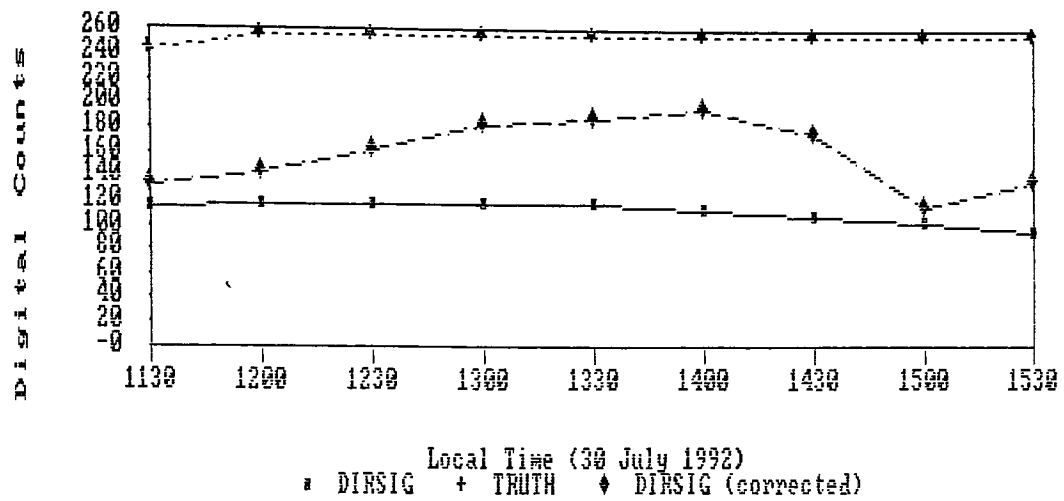
Local Time (30 July 1992)
 * DIRSIG + TRUTH ♦ DIRSIG (corrected)

(SHINGLES, Within Green Band)

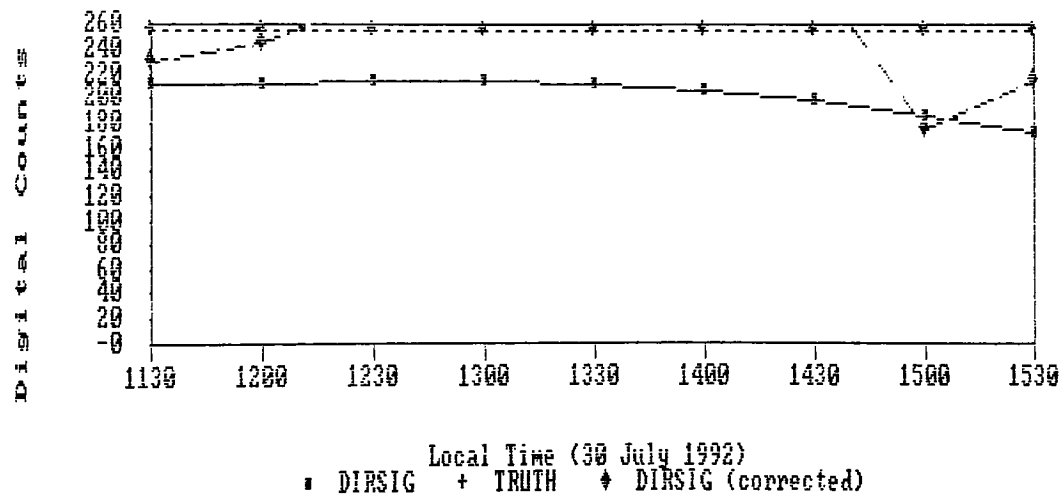


Local Time (30 July 1992)
 * DIRSIG + TRUTH ♦ DIRSIG (corrected)

(SAND, Within Green Band)



(CONCRETE, Within Green Band)



***** Appendix 2 *****
Truth Data Collection
***** 2.a *****

Atmospheric Data
(Radiosonde Data)

(see following pages)

BUFFALO, NEW YORK

22 JULY 1992

RADIOSONDE/RAWINSONDE OBSERVATION WBAN NO. 14733

TIME (GMT) 12

TROPOPAUSE DATA - PRESS (MBS): 200.0 HEIGHT (M-MSL): 12188 TEMP (DEG C):-57.1

ELAPSED TIME (MIN)	PRESSURE (MBS)	HEIGHT (M-MSL)	TEMP (DEG C)	DEW POINT (DEG C)	RH %	WIND DIR (DEG)	WIND SPD (KTS)
.0	999.0	218	10.0	9.5	96	110	004
.2	993.5	264	11.6	9.0	84	098	004
.5	984.8	338	12.4	7.2	70	076	004
1.1	968.4	479	11.6	5.9	68	043	004
1.4	961.5	539	11.6	3.1	56	049	004
1.6	954.5	600	11.6	5.9	68	055	002
1.7	950.0	640	11.3	5.9	69	058	002
2.6	925.0	862	9.3	6.0	80	344	002
2.8	919.8	909	9.1	7.0	86	315	002
3.4	902.6	1065	8.0	6.8	92	310	004
3.4	900.0	1089	8.0	6.7	92	310	004
4.3	878.1	1292	7.2	4.9	85	317	010
4.6	870.3	1366	7.7	-4.5	42	320	010
4.8	865.2	1414	8.1	-4.6	40	322	012
4.9	862.7	1438	8.6	-1.6	49	322	012
5.1	857.8	1485	9.4	-3.2	41	323	012
5.4	850.0	1561	9.5	-3.6	39	324	012
6.0	835.3	1706	8.5	-4.7	39	325	012
6.4	824.8	1811	8.5	-9.1	28	321	012
6.9	812.2	1938	7.5	-11.0	25	315	012
7.3	800.0	2063	7.5	-11.5	25	312	012
7.6	794.3	2122	7.5	-11.8	24	309	012
9.2	754.4	2544	4.6	-14.5	23	292	012
9.3	750.0	2592	4.5	-14.6	23	291	012
11.5	700.0	3151	2.1	-16.7	23	278	021
12.7	672.7	3471	-0.1	-20.0	20	277	025
13.7	650.0	3745	-0.8	-27.5	20	275	029
14.3	639.2	3879	-1.2	-31.2	19	274	033
16.1	600.0	4381	-3.9	-33.9	19	273	037
17.7	570.7	4774	-6.1	-36.1	19	275	037
18.7	550.0	5062	-8.1	-38.1	19	277	041
19.0	545.2	5130	-8.6	-38.6	19	278	043
19.6	533.5	5298	-9.4	-39.4	19	277	047
20.5	515.5	5563	-9.2	-27.4	21	273	049
21.0	506.1	5705	-10.0	-20.5	42	271	049
21.3	500.0	5798	-10.8	-20.4	45	270	049
22.3	482.5	6071	-13.5	-21.5	51	268	051
22.7	475.2	6187	-14.2	-20.5	59	267	052
23.0	469.7	6275	-14.0	-17.2	77	267	054
23.5	461.4	6410	-14.6	-18.4	73	268	054
24.2	450.0	6599	-15.9	-20.6	68	269	054
24.8	441.1	6749	-17.1	-22.5	63	268	054
27.0	407.8	7332	-21.9	-24.4	80	266	054
27.5	400.0	7474	-22.5	-25.5	76	266	052
28.8	381.4	7822	-25.4	-27.3	84	269	056
29.6	370.3	8036	-26.2	-28.4	81	272	058
31.1	350.4	8433	-29.0	-33.5	65	275	054
31.1	350.0	8444	-29.0	-33.6	65	275	054
32.7	329.6	8868	-32.1	-39.9	45	272	058
33.6	318.4	9111	-34.3	-41.2	49	270	060

BUFFALO, NEW YORK

22 JULY 1992

RADIOSONDE/RAWINSONDE OBSERVATION WBAN NO. 14733

TIME (GMT) 12 (CONTD)

TROPOPAUSE DATA PRESS (MBS): 200.0 HEIGHT (M-MSL): 12188 TEMP (DEG C): -57.1

ELAPSED TIME (MIN)	PRESSURE (MBS)	HEIGHT (M-MSL)	TEMP (DEG C)	DEW POINT (DEG C)	RH %	WIND DIR (DEG)	WIND SPD (KTS)
33.7	317.4	MISDA					
34.9	302.2	9474	-37.7	-42.8	58	269	068
35.1	300.0	9524	-38.1	-43.0	59	269	068
35.8	291.1	9730	-40.0	-44.6	60	269	064
38.0	265.9	10341	-45.5			270	076
39.4	250.0	10750	-47.6				
42.0	222.7	11503	-54.2				
43.3	211.4	11836	-56.1				
44.6	200.0	12188	-57.1				
46.6	182.8	12757	-57.1				
47.6	175.0	13033	-57.6				
48.6	167.9	13294	-58.2				

BUFFALO, NEW YORK

WIND DATA AT ONE MINUTE INTERVAL WBAN NO. 14733

22 JULY 1992
TIME (GMT) 12

MAXIMUM WIND DATA - DIR:270 DEG SPD: 076 KTS HEIGHT (M-AS): 10123

MINUTE	HEIGHT (M-AS)	WIND DIR (DEG)	WIND SPD (KTS)	MINUTE	HEIGHT (M-AS)	WIND DIR (DEG)	WIND SPD (KTS)
0	0	110	004				
1	237	041	004				
2	487	073	002				
3	743	302	002				
4	998	313	008				
5	1244	323	012				
6	1488	325	012				
7	1746	314	012				
8	2010	306	012				
9	2273	295	012				
10	2537	282	014				
11	2801	278	019				
12	3066	278	023				
13	3329	276	025				
14	3584	275	031				
15	3844	273	035				
16	4109	273	037				
17	4372	274	037				
18	4638	276	037				
19	4912	278	043				
20	5198	276	049				
21	5487	271	049				
22	5771	268	049				
23	6057	267	054				
24	6322	269	054				
25	6583	268	054				
26	6849	265	054				
27	7114	266	054				
28	7390	267	052				
29	7658	270	056				
30	7924	273	058				
31	8188	275	054				
32	8459	274	056				
33	8731	271	058				
34	9004	270	062				
35	9281	269	068				
36	9567	269	064				
37	9845	267	070				
38	10123	270	076				
39	10415	273	058				

BUFFALO, NEW YORK

RADIOSONDE/RAWINSONDE OBSERVATION

WBAN NO. 14733

30 JULY 1992

TIME (GMT) 12

TROPOPAUSE DATA - PRESS (MBS):7339.2 HEIGHT (M-MSL): 7301 TEMP (DEG C):-51.9

ELAPSED TIME (MIN)	PRESSURE (MBS)	HEIGHT (M-MSL)	TEMP (DEG C)	DEW POINT (DEG C)	RH %	WIND DIR (DEG)	WIND SPD (KTS)
.0	991.6	218	11.8	9.7	87	120	004
.3	983.0	291	13.8	9.7	76	068	002
.5	977.5	338	14.0	8.1	67	030	004
1.4	950.0	578	13.0	4.6	57	001	010
2.3	925.0	802	12.0	1.2	47	360	014
2.8	911.8	922	11.0	2.4	55	355	016
3.2	900.6	1025	10.3	-0.2	48	350	016
3.2	900.0	1031	10.3	-0.5	48	350	016
3.6	889.5	1128	10.1	-6.7	30	340	014
3.9	881.7	1201	10.1	-8.8	25	332	014
4.1	876.2	1253	9.9	-6.0	32	326	014
5.0	850.0	1505	9.1	-7.3	30	295	014
5.6	836.0	1642	8.5	-7.1	32	289	017
6.2	821.9	1782	8.2	-12.0	22	284	021
6.6	811.9	1883	7.6	-4.5	42	281	023
6.9	804.6	1957	6.8	3.3	78	279	027
7.0	800.0	2004	6.5	3.1	78	278	027
7.1	799.8	2006	6.4	3.0	79	277	027
7.2	797.4	2031	6.1	4.4	89	277	027
7.9	779.3	2219	4.6	3.2	90	273	029
8.2	771.7	2299	4.1	1.1	81	272	029
8.6	762.3	2399	4.3	-13.0	27	273	027
8.9	755.2	2475	5.0	-15.3	21	274	025
9.1	750.0	2531	4.8	-15.4	21	274	025
11.4	700.0	3091	2.8	-16.4	23	280	027
13.1	663.8	3519	1.0	-18.9	21	275	033
13.7	651.8	3665	0.0	-12.3	39	274	033
13.7	650.0	3687	-0.1	-12.3	39	274	033
14.3	639.7	3815	-1.2	-11.9	44	273	033
15.1	623.6	4018	-1.8	-16.0	33	273	035
15.3	619.6	4069	-1.9	-13.6	40	272	035
15.6	613.6	4146	-2.7	-9.2	61	271	037
15.8	609.5	4199	-3.2	-9.4	62	270	037
15.9	607.3	4228	-3.4	-11.7	53	269	037
16.0	605.1	4257	-3.4	-20.9	24	269	037
16.1	602.9	4286	-3.4	-22.8	20	268	037
16.2	600.0	4324	-3.6	-23.0	20	267	037
16.9	585.9	4512	-4.9	-24.2	20	261	039
17.1	581.8	4567	-5.3	-22.9	23	260	039
17.5	573.8	4676	-6.1	-14.4	52	260	041
18.0	563.8	4813	-7.2	-17.2	45	260	043
18.3	557.9	4895	-7.9	-13.6	63	262	045
18.5	554.0	4950	-8.3	-14.1	63	263	045
18.7	550.2	5003	-8.6	-14.0	65	264	045
18.7	550.0	5006	-8.6	-14.1	65	264	045
19.1	542.6	5111	-9.0	-18.6	46	265	047
19.3	538.8	5165	-9.4	-13.7	71	265	047
19.7	531.4	5272	-10.0	-14.4	70	266	049
20.0	526.0	5351	-10.4	-12.0	88	266	049
20.8	512.2	5555	-11.6	-14.5	79	264	049

BUFFALO, NEW YORK

30 JULY

1992

RADIOSONDE/RAWINSONDE OBSERVATION WBAN NO. 14733

TIME (GMT) 12 (CONTD)

TROPOPAUSE DATA - PRESS (MBS):7339.2 HEIGHT (M-MSL): 7301 TEMP (DEG C):-51.9

ELAPSED TIME (MIN)	PRESSURE (MBS)	HEIGHT (M-MSL)	TEMP (DEG C)	DEW POINT (DEG C)	RH %	WIND DIR (DEG)	WIND SPD (KTS)
21.5	500.0	5740	-12.6	-15.1	81	261	049
23.9	459.9	6373	-17.3	-18.6	89	266	058
24.3	454.1	6468	-17.4	-21.1	73	266	058
24.5	450.0	6536	-17.9	-21.9	72	266	058
24.6	449.8	6539	-18.0	-22.0	71	265	058
26.9	416.5	7109	-22.5	-24.1	86	262	058
28.0	400.0	7405	-24.7	-27.9	74	264	064
28.3	396.4	7471	-24.9	-29.3	66	265	066
28.5	393.7	7521	-24.7	-33.5	43	265	066
28.6	392.4	7545	-24.8	-34.5	40	265	066
29.2	384.8	7687	-25.4	-35.8	37	266	068
31.8	350.0	8370	-30.9	-41.1	36		
36.1	300.0	9441	-39.8	-49.8	32		
36.5	295.5	9544	-40.5				
37.3	286.2	9762	-39.6	-50.7	28		
37.5	284.0	9815	-40.0	-51.3	27		
38.8	267.6	10218	-43.3				
40.0	250.0	10672	-47.5				
41.2	236.3	11042	-50.8				
44.8	204.0	11992	-54.3				
45.3	200.0	12119	-54.0				
46.1	193.5	12331	-54.1				
46.4	190.8	12422	-52.7				
47.0	185.5	12604	-52.5				
47.7	178.8	12841	-53.6				
48.1	175.0	12979	-54.7				
49.5	164.0	13391	-58.1				
50.3	158.0	13625	-59.3				
50.8	154.0	13786	-58.7				
51.4	150.0	13951	-59.5				
52.9	139.0	14429	-58.0				
53.4	136.2	14557	-58.2				
53.9	133.0	14707	-56.5				
54.9	126.3	15034	-58.3				
55.1	125.0	15099	-58.2				
55.4	123.1	15196	-57.9				
56.7	115.3	15608	-59.2				
57.5	111.1	15841	-58.8				
58.7	105.3	16180	-56.0				
59.8	100.0	16508	-57.3				
60.8	95.2	16818	-58.9				
61.0	94.3	16878	-57.9				
61.4	92.6	16993	-57.7				
62.6	87.0	17385	-59.5				
63.1	84.9	17538	-58.6				
63.5	83.2	17665	-59.1				
64.0	81.1	17826	-57.7				
64.2	80.0	17912	-57.5				
65.5	75.3	18296	-56.5				
66.1	73.0	18493	-56.8				
66.9	70.0	18760	-55.6				
68.0	66.0	19138	-52.1				

66.9	70.0	18760	-55.6
68.0	66.0	19138	-52.1

69.4	62.3	19510	-54.5		
70.1	60.0	19751	-54.2		
73.8	50.0	20926	-52.2		
77.8	40.0	22376	-50.6		
82.2	31.5	23940	-48.8		
83.1	30.0	24260	-49.7		
86.0	25.0	25458	-47.9		
89.6	20.0	26939	-45.5	075	019
94.2	15.0	28866	-43.5	100	016
100.8	10.0	31611	-40.6	084	023
101.6	9.7	31818	-41.3	094	023

BUFFALO, NEW YORK

30 JULY 1992

WIND DATA AT ONE MINUTE INTERVAL

WBAN NO. 14733

TIME (GMT) 12

MAXIMUM WIND DATA - DIR:266 DEG SPD: 068 KTS HEIGHT (M-AS): 7422

MINUTE	HEIGHT (M-AS)	WIND DIR (DEG)	WIND SPD (KTS)	MINUTE	HEIGHT (M-AS)	WIND DIR (DEG)	WIND SPD (KTS)
0	0	120	004	50	13319	(M)	(M)
1	249	360	008	51	13623	(M)	(M)
2	507	003	012	52	13924	(M)	(M)
3	756	354	016	53	14237	(M)	(M)
4	1009	329	014	54	14522	(M)	(M)
5	1287	295	014	55	14848	(M)	(M)
6	1517	286	019	56	15168	(M)	(M)
7	1764	278	027	57	15477	(M)	(M)
8	2028	272	029	58	15764	(M)	(M)
9	2282	274	025	59	16051	(M)	(M)
10	2528	277	023	60	16352	(M)	(M)
11	2774	280	027	61	16660	(M)	(M)
12	3024	279	029	62	16971	(M)	(M)
13	3276	275	033	63	17289	(M)	(M)
14	3522	273	033	64	17608	(M)	(M)
15	3775	273	035	65	17921	(M)	(M)
16	4039	269	037	66	18242	(M)	(M)
17	4322	260	039	67	18330	(M)	(M)
18	4595	260	043	68	18392	(M)	(M)
19	4866	265	047	69	18453	(M)	(M)
20	5133	266	049	70	18514	(M)	(M)
21	5390	263	049	71	18575	(M)	(M)
22	5654	260	051	72	18637	(M)	(M)
23	5918	263	054	73	18698	(M)	(M)
24	6179	266	058	74	18759	(M)	(M)
25	6420	265	058	75	18821	(M)	(M)
26	6668	262	056	76	18888	(M)	(M)
27	6918	262	058	77	18950	(M)	(M)
28	7187	264	064	78	19011	(M)	(M)
29	7422	266	068	79	19072	(M)	(M)
30	7671	267	068	80	19133	(M)	(M)
31	7925	267	068	81	19195	(M)	(M)
32	8179	(M)	(M)	82	19256	(M)	(M)
33	8434	(M)	(M)	83	19317	(M)	(M)
34	8688	(M)	(M)	84	19379	(M)	(M)
35	8942	(M)	(M)	85	19440	066	012
36	9197	(M)	(M)	86	19508	075	019
37	9462	(M)	(M)	87	19569	072	014
38	9752	(M)	(M)	88	19630	082	012
39	10075	(M)	(M)	89	19691	097	017
40	10454	(M)	(M)	90	19753	102	016
41	10762	(M)	(M)	91	19814	089	025
42	11035	(M)	(M)	92	19875	097	023
43	11299	(M)	(M)	93	19937	080	023
44	11562	(M)	(M)	94	19998	081	023
45	11825	(M)	(M)	95	20059	098	021
46	12087	(M)	(M)	96	20127	089	025
47	12386	(M)	(M)	97	20188	098	023
48	12714	(M)	(M)	98	20250	098	023
49	13020	(M)	(M)	99	20311	083	021

BUFFALO, NEW YORK

30 JULY 1992

WIND DATA, AT ONE MINUTE INTERVAL WBAN NO. 14733

TIME (GMT) 12 (CONTD)

MAXIMUM WIND DATA - DIR:266 DEG SPD: 068 KTS HEIGHT (M-AS): 7422

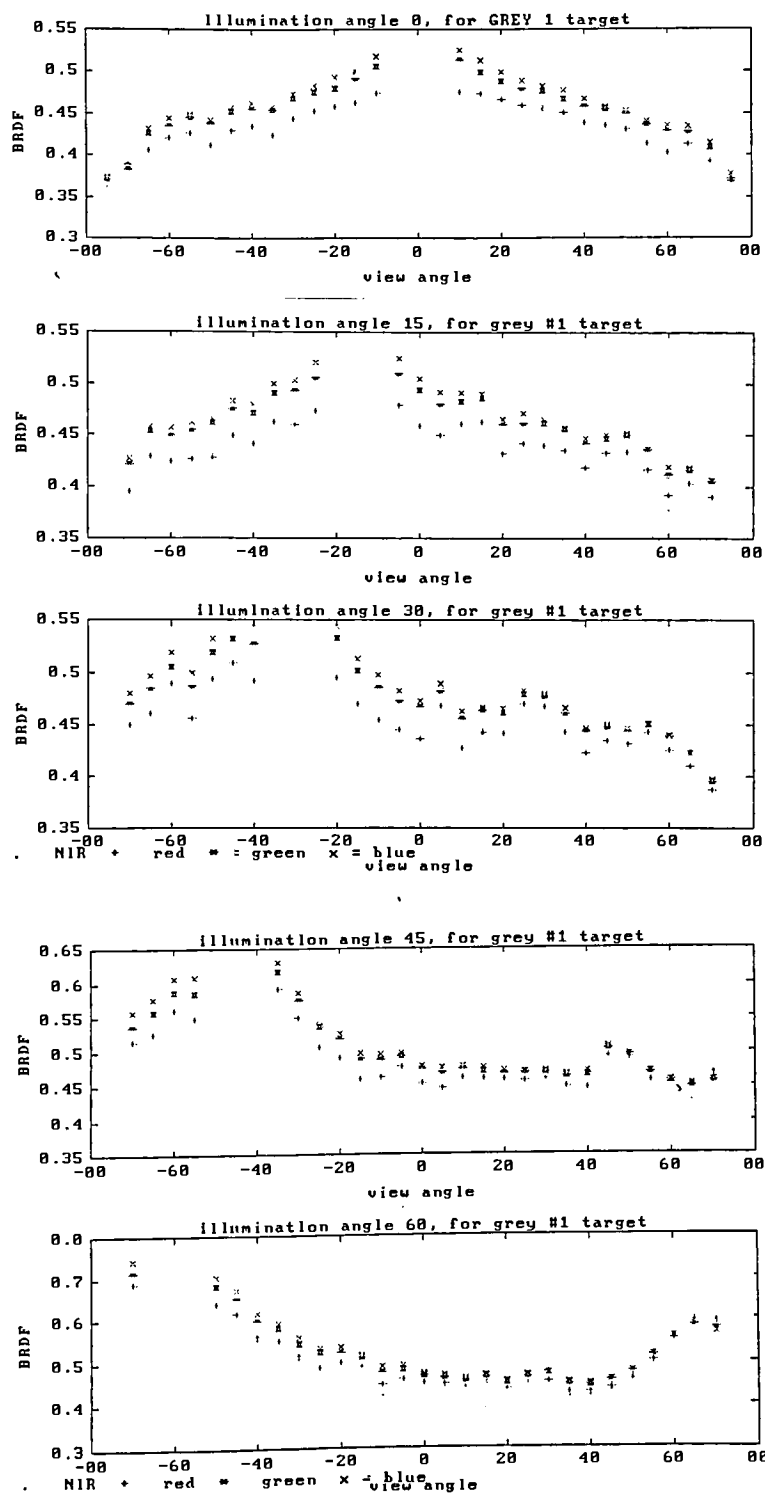
MINUTE	HEIGHT (M-AS)	WIND DIR (DEG)	WIND SPD (KTS)	MINUTE	HEIGHT (M-AS)	WIND DIR (DEG)	WIND SPD (KTS)
100	20372	083	025				
101	20433	097	023				

***** Appendix 3 *****
Generation of Reflectivity Curves
***** 3.a *****

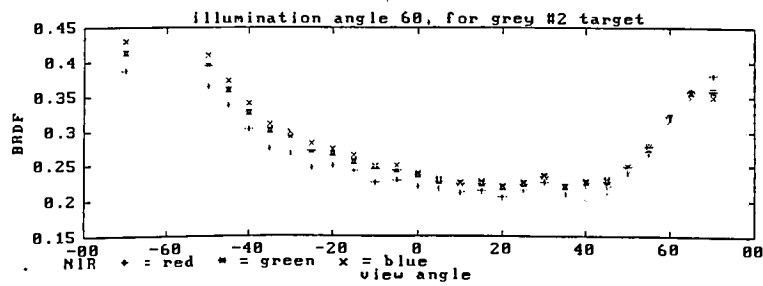
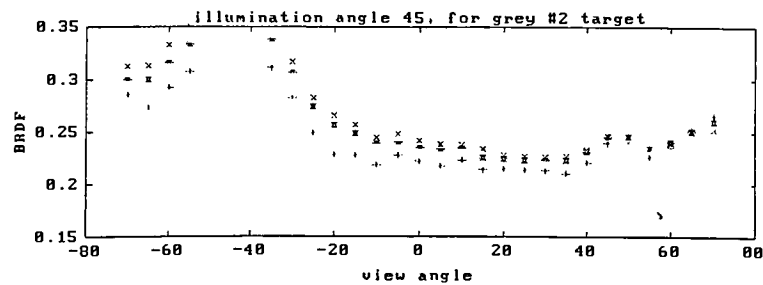
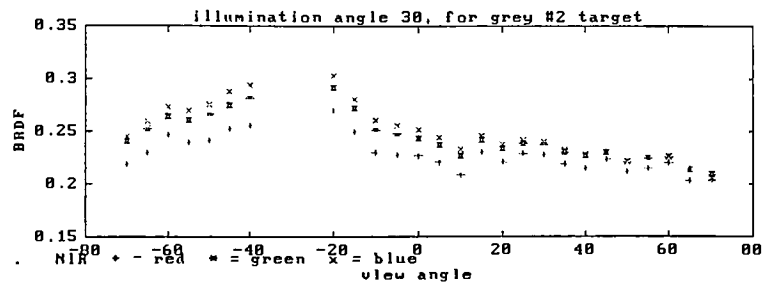
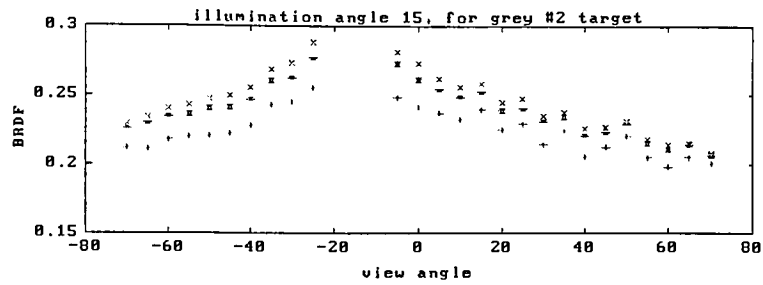
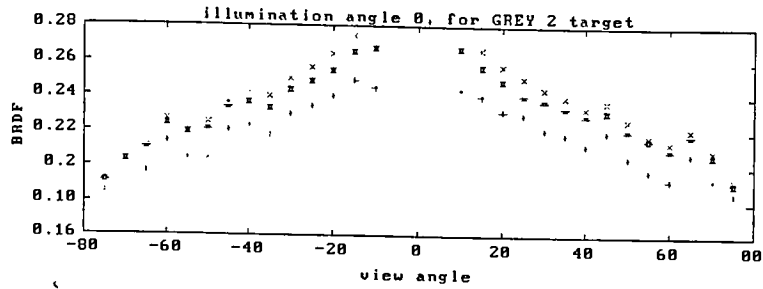
Remaining Measured In-Plane BDRF Plots

(see following pages)

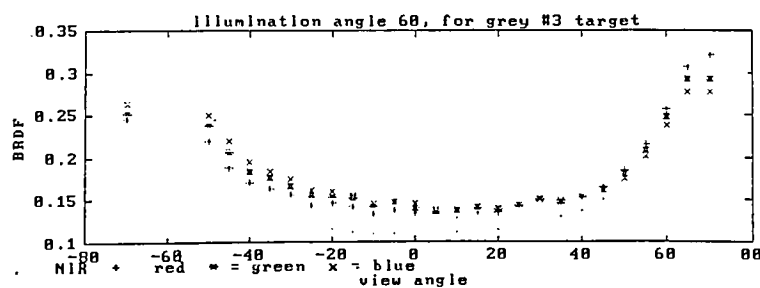
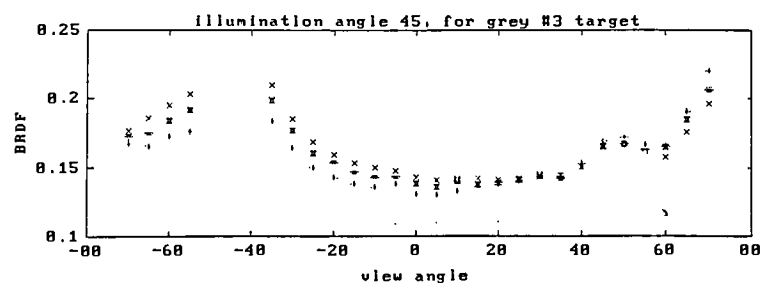
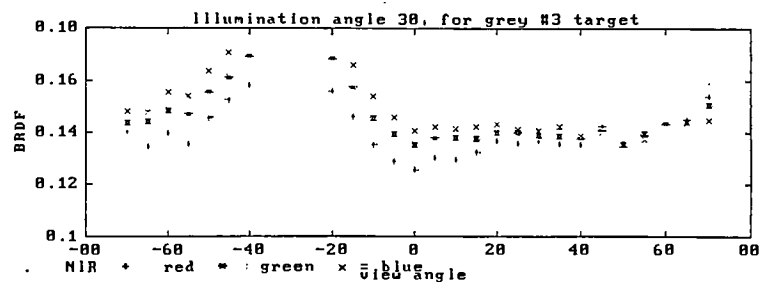
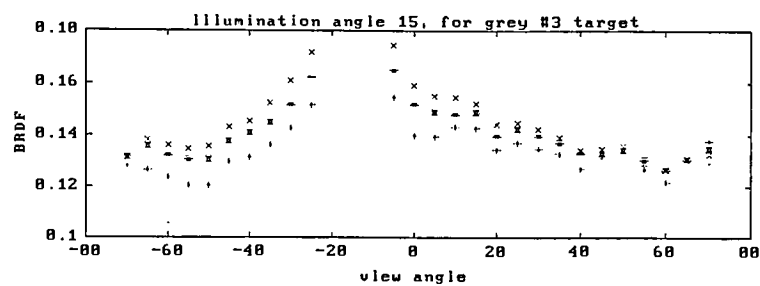
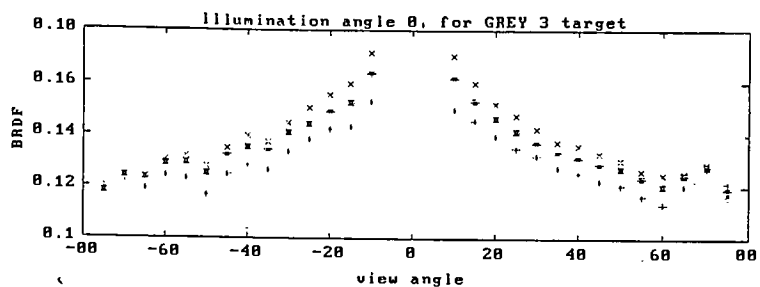
In-Plane BDRF Measurements



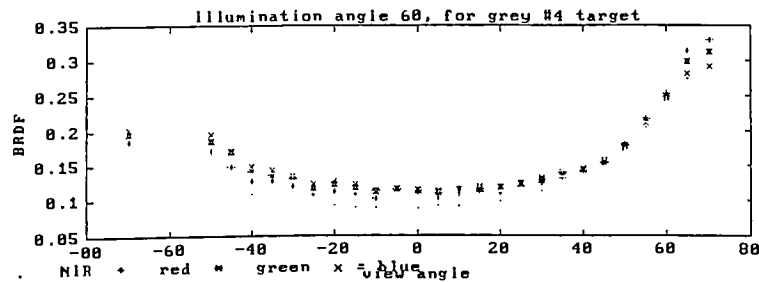
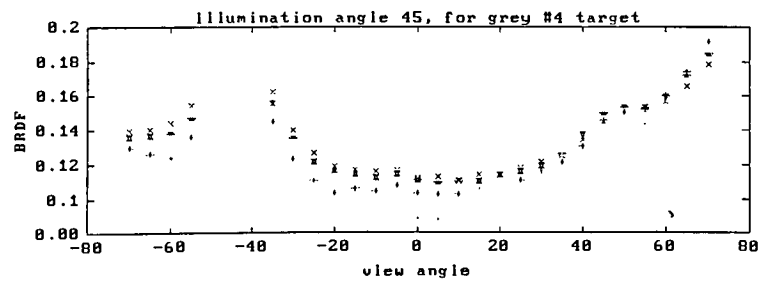
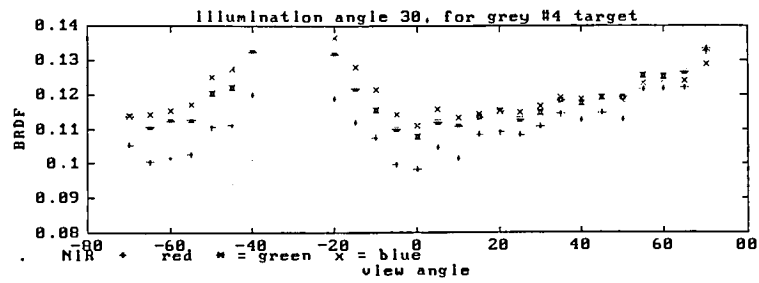
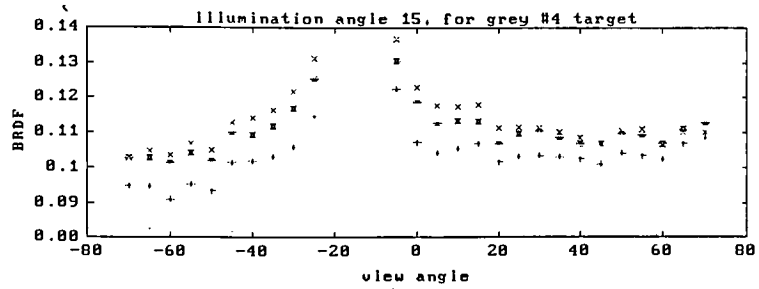
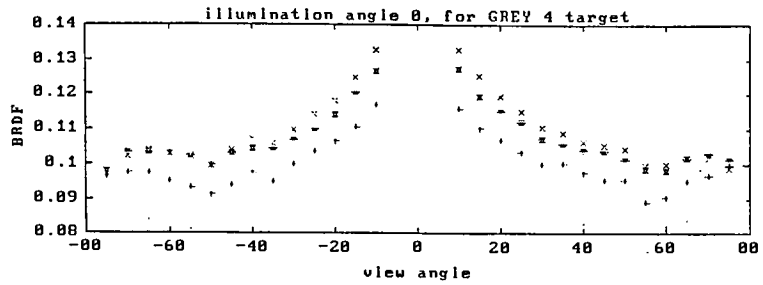
In-Plane BDRF Measurements



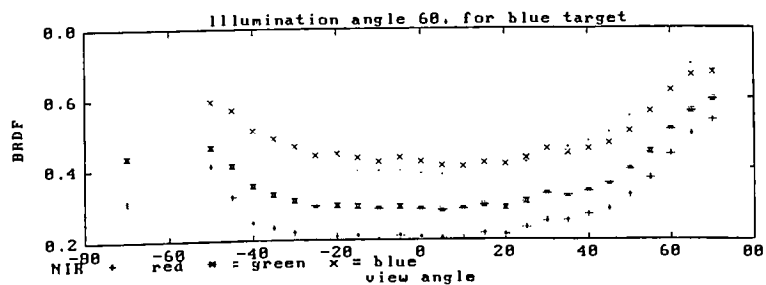
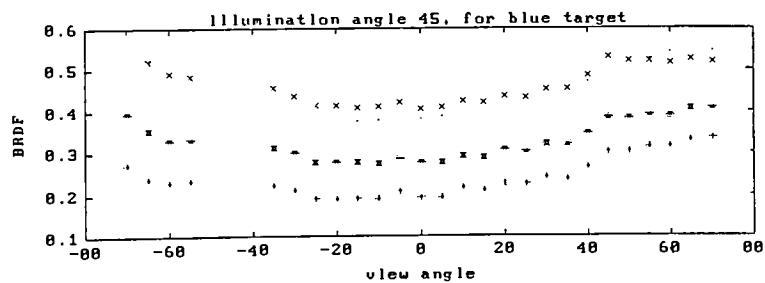
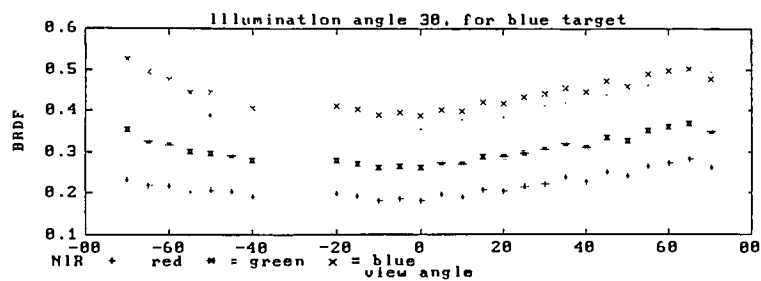
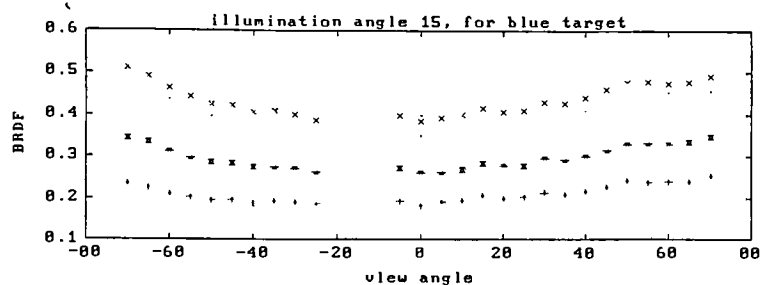
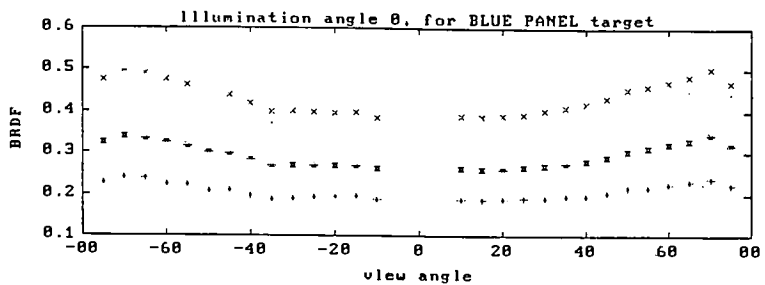
In-Plane BDRF Measurements



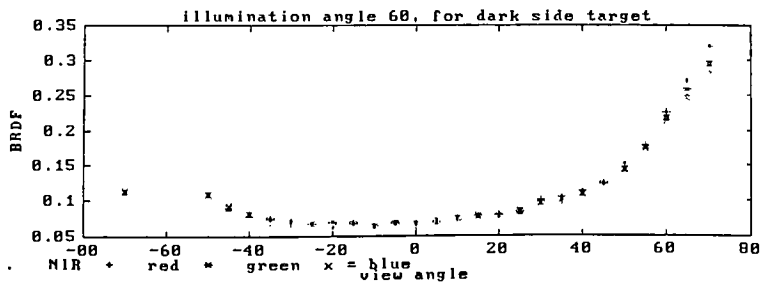
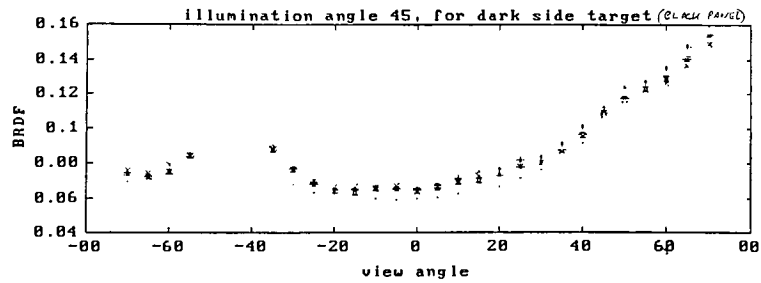
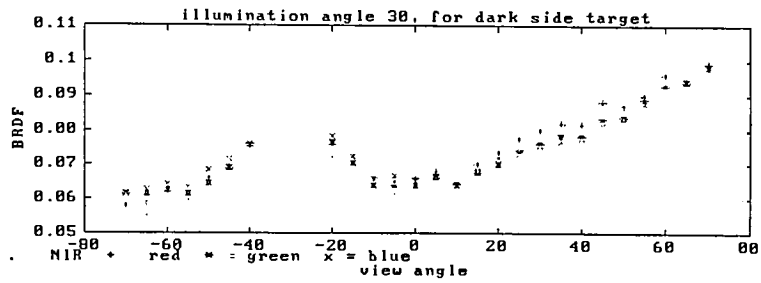
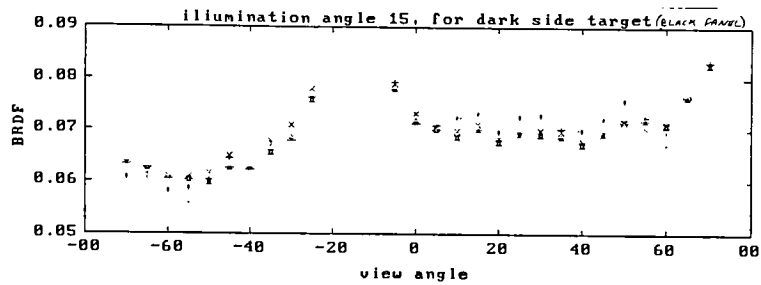
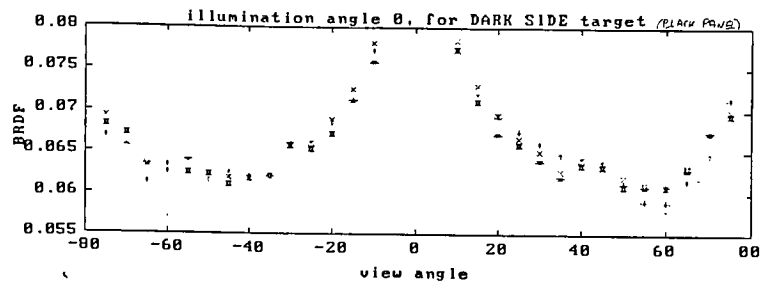
In-Plane BDRF Measurements



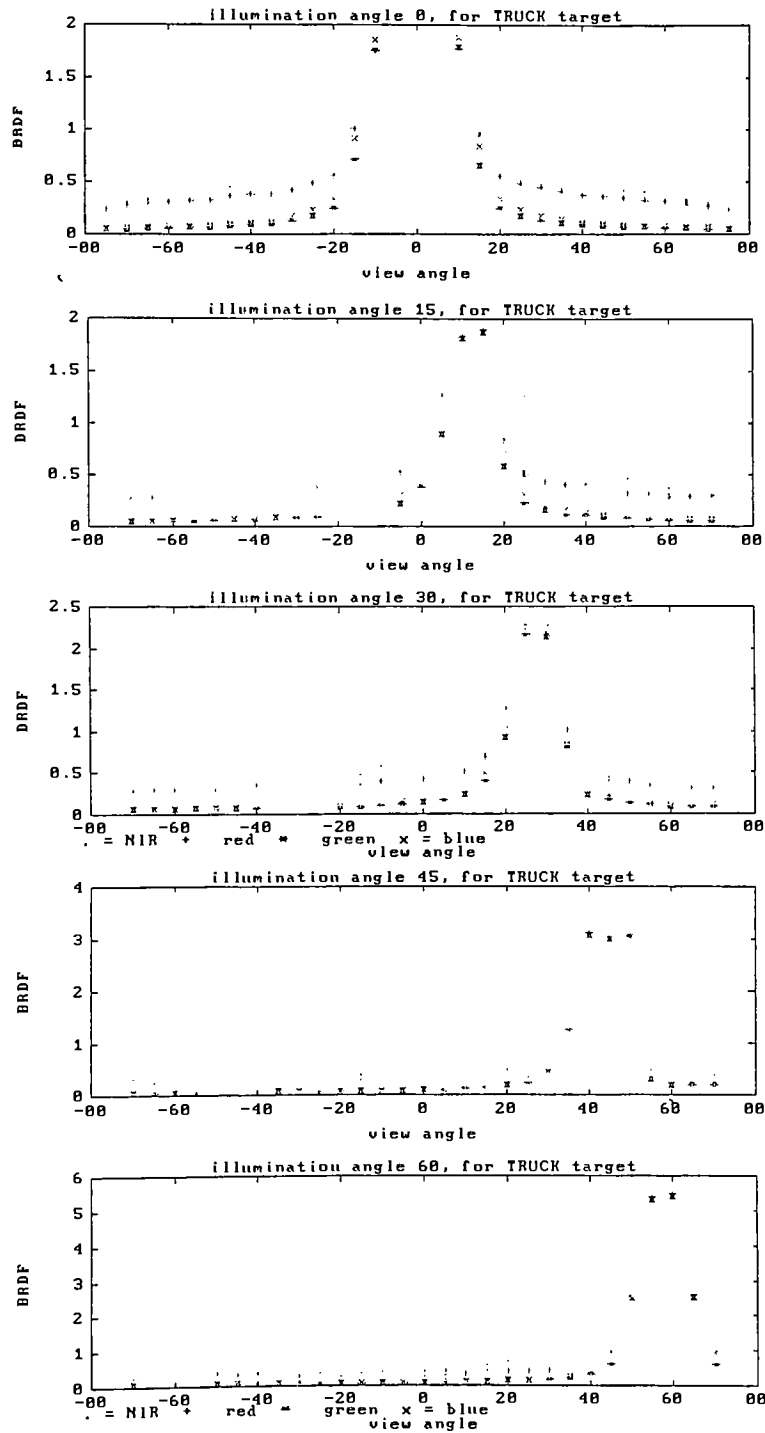
In-Plane BDRF Measurements



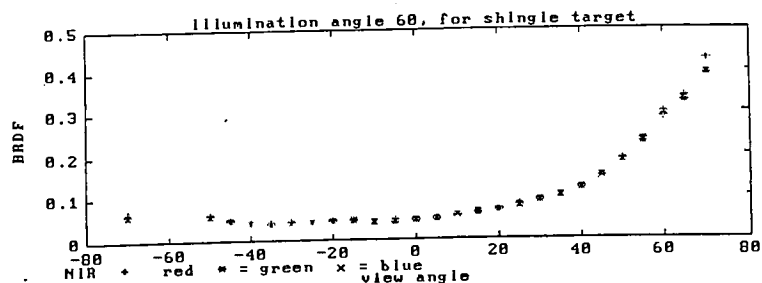
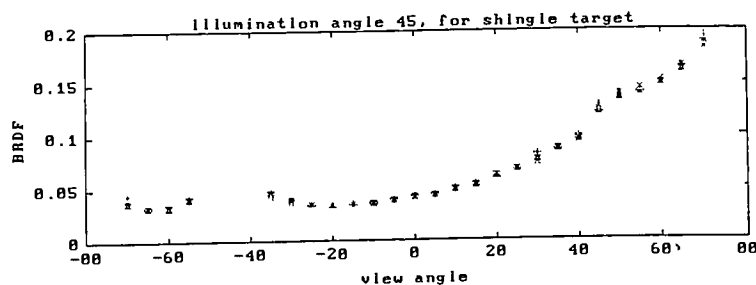
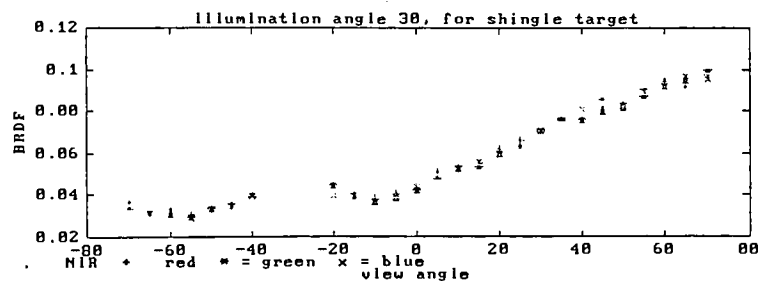
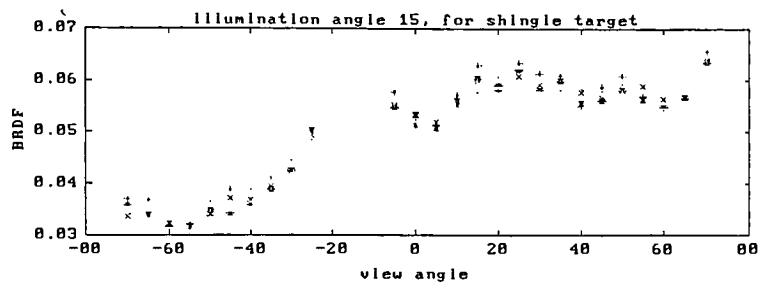
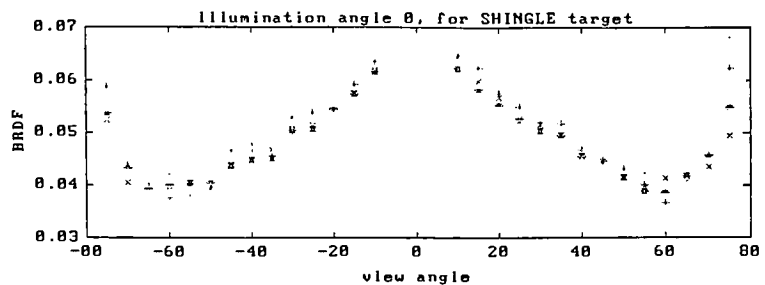
In-Plane BDRF Measurements



In-Plane BDRF Measurements



In-Plane BDRF Measurements

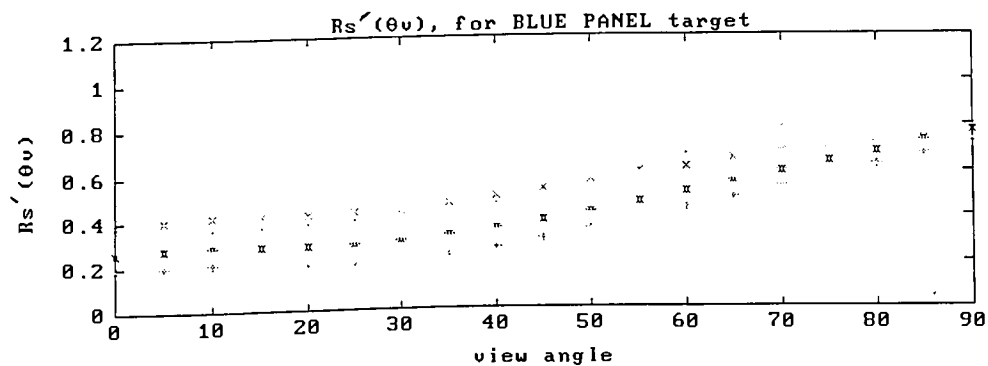
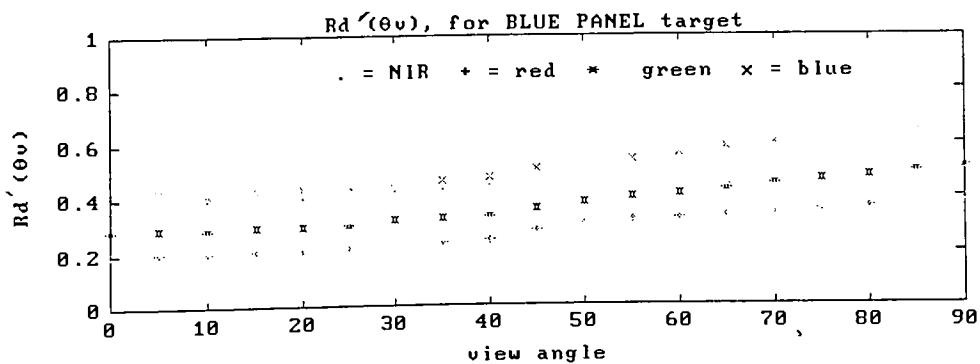
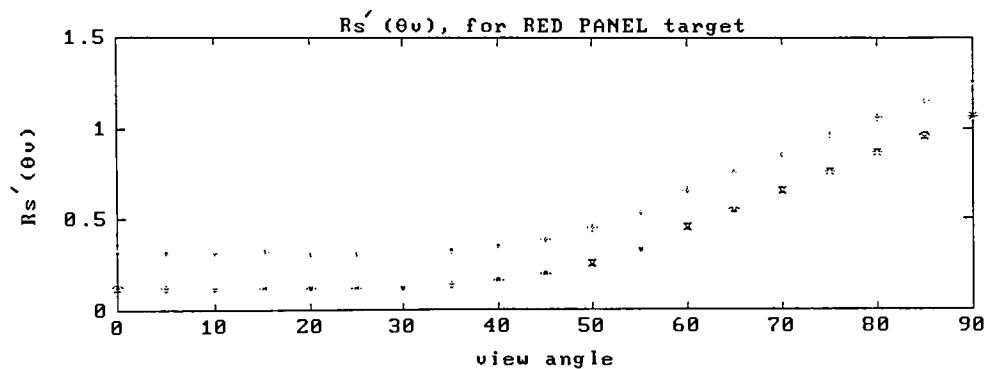
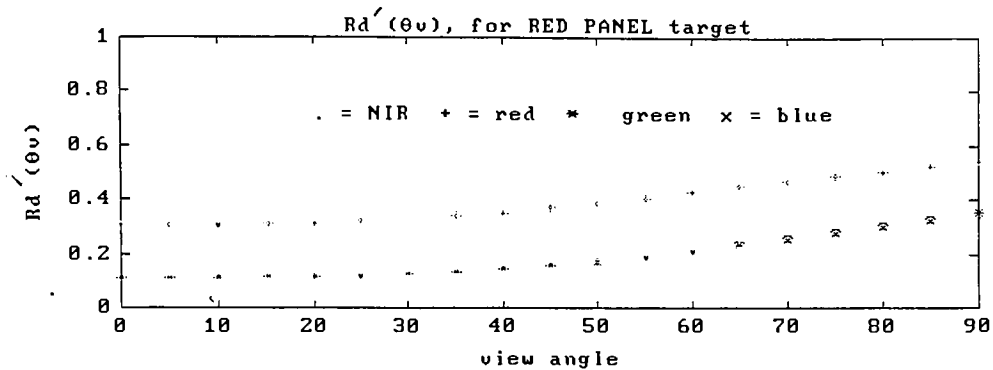


***** Appendix 3 *****
Generation of Reflectivity Curves
***** 3.b *****

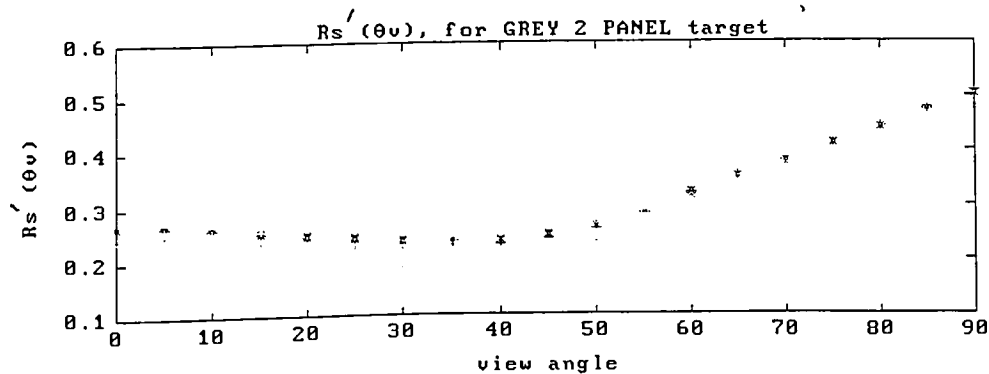
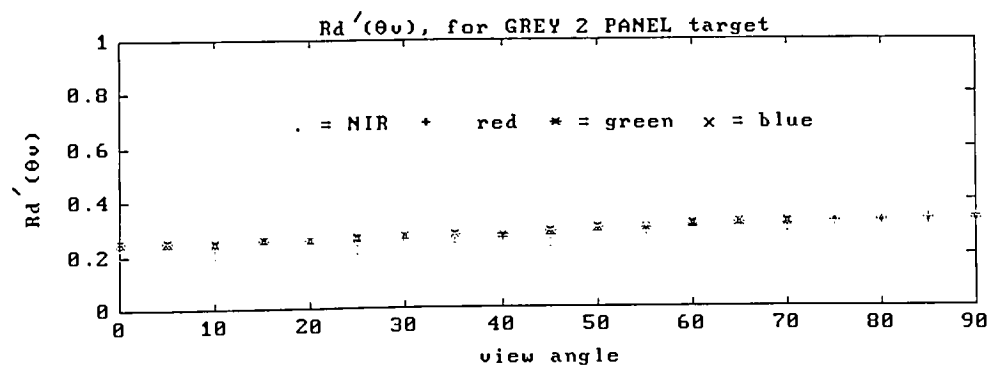
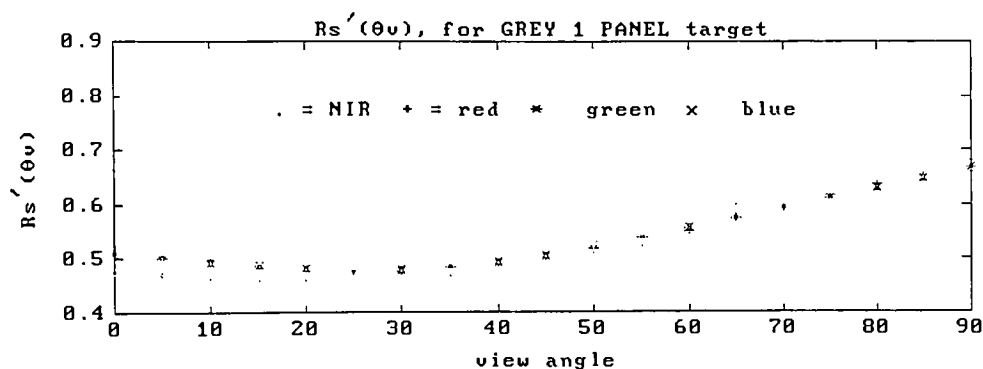
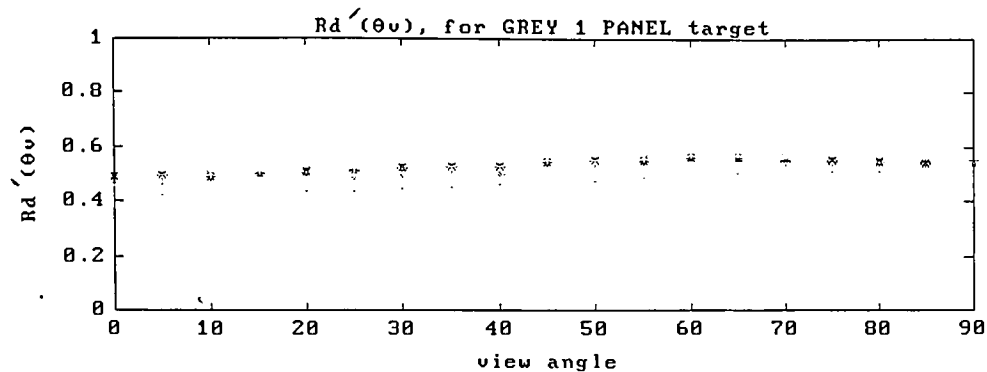
Remaining Primary Target Reflectivity Component Plots

(see following pages)

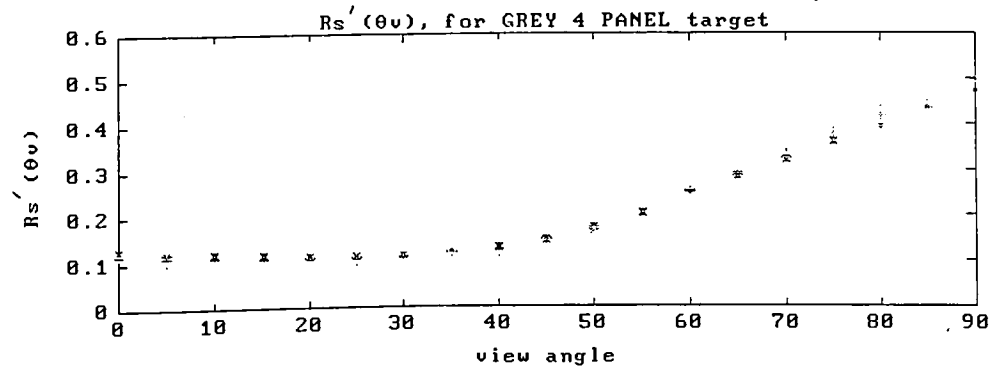
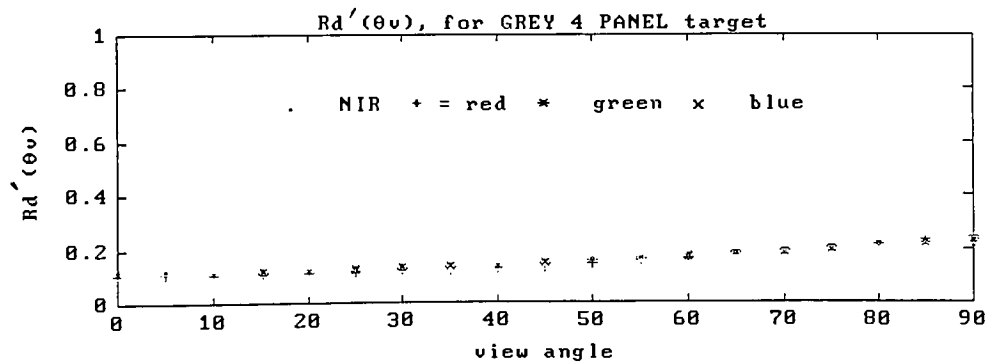
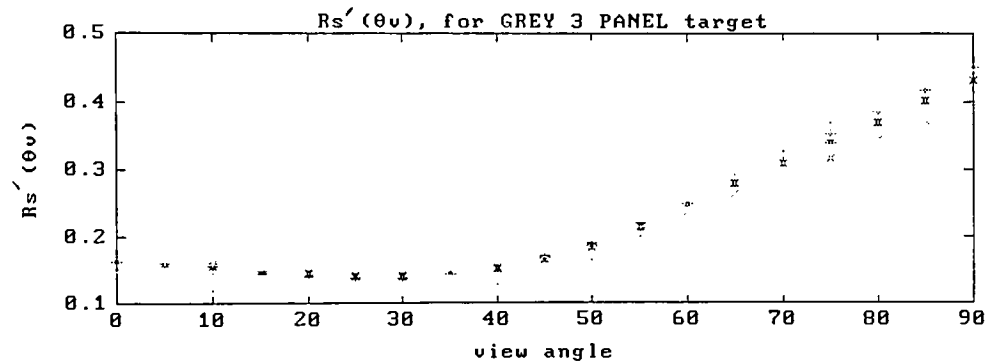
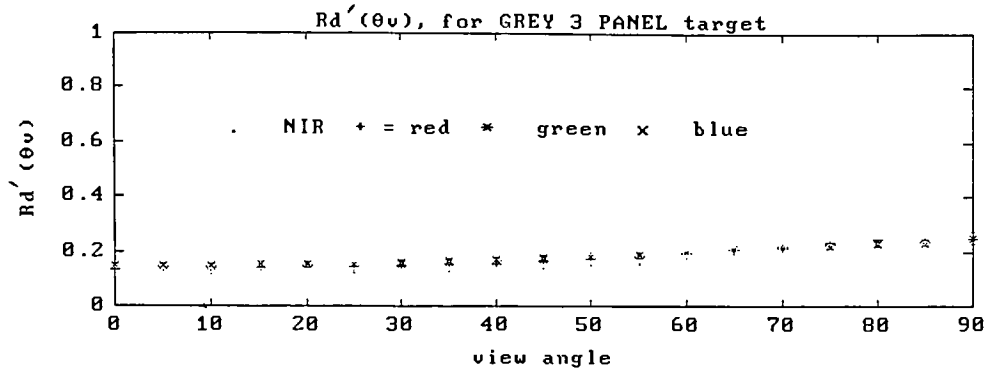
Primary Target Reflectivity Component Plots



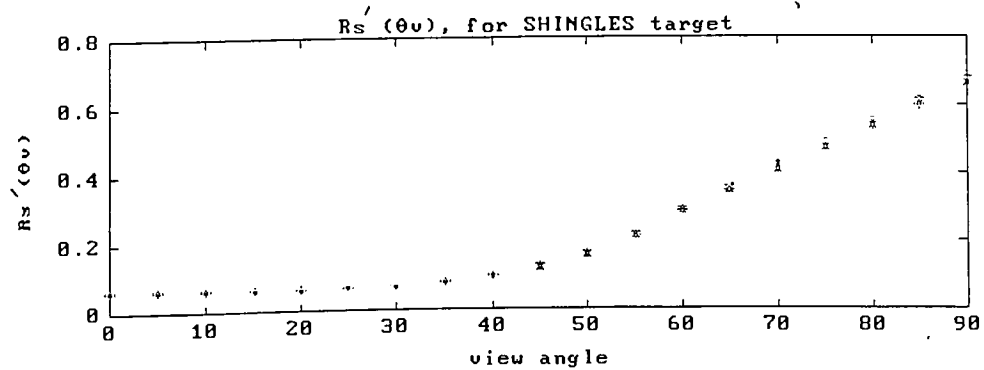
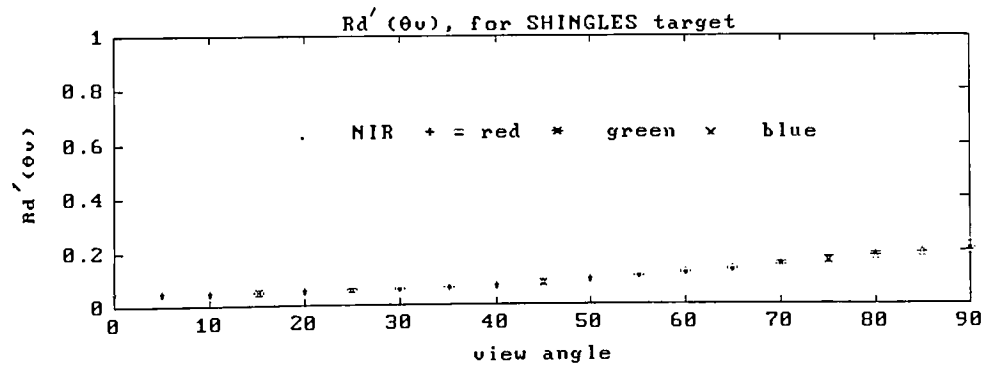
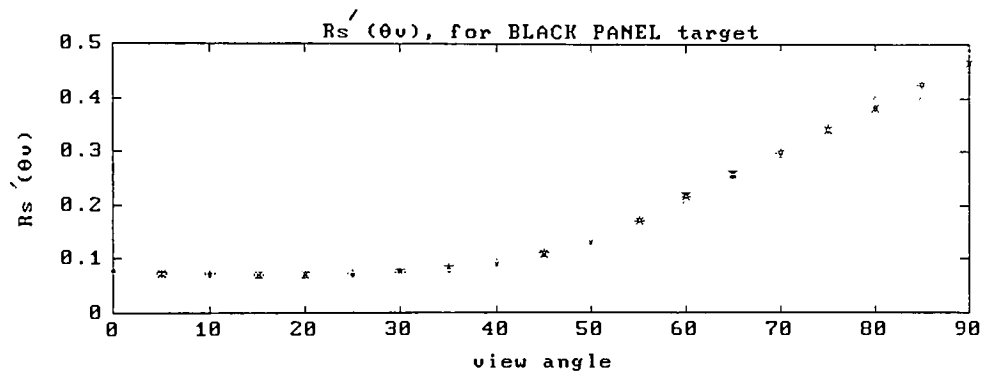
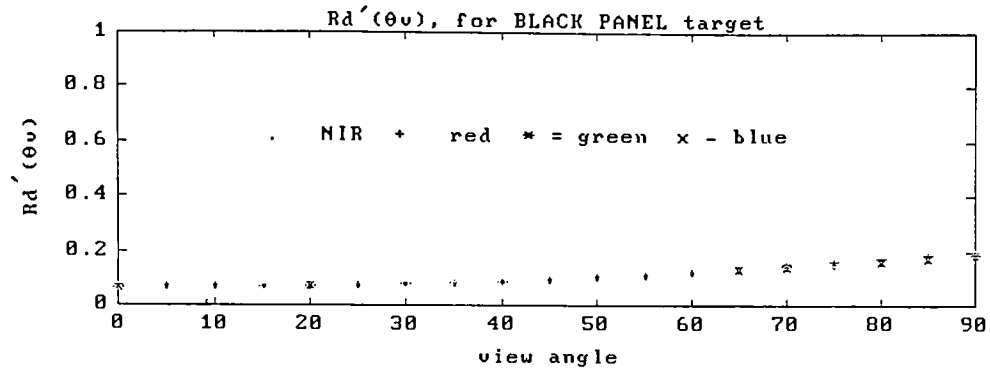
Primary Target Reflectivity Component Plots



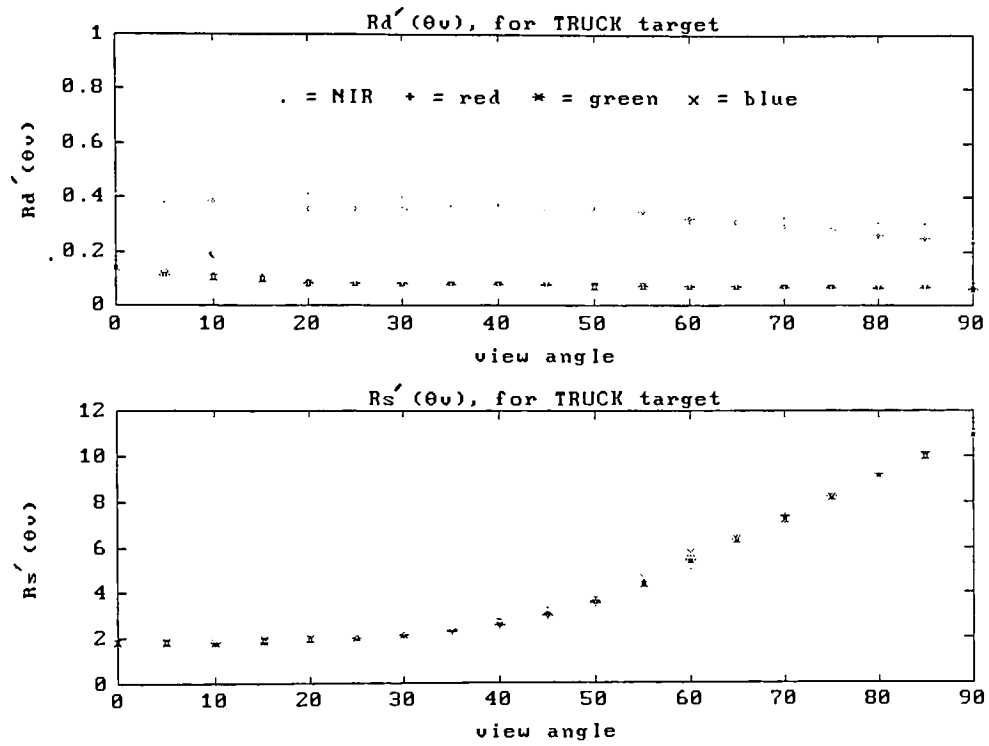
Primary Target Reflectivity Component Plots



Primary Target Reflectivity Component Plots



Primary Target Reflectivity Component Plots



***** Appendix 3 *****
 Generation of Reflectivity Curves
 ***** 3.c *****

Total Reflectivity Measurements
 used to Find Diffuseness and Specularity

Measured using Munsell Lab's Portable Minolta Spectrophotometer

nm	Specular Panel		White Panel		Green Panel	
	SCI	SCE	SCI	SCE	SCI	SCE
400	29.4	28.1	5	4.97	34.1	33.6
410	37	35.7	5.5	5.5	46.8	46.2
420	39.2	37.9	6	5.9	50.9	50.3
430	39.6	38.3	6.7	6.6	51.2	50.7
440	40.4	39	7.8	7.7	51.4	50.9
450	40.9	39.5	8.7	8.6	51.5	51
460	40.8	39.4	9.1	9	51.4	51
470	40.6	39.2	9.3	9.2	51.4	51
480	40.4	39	9.7	9.6	51.3	50.8
490	40.4	39	10.3	10.2	51.2	50.9
500	40.6	39.1	11.4	11.3	51.2	50.8
510	40.9	39.4	12.8	12.7	51.1	50.7
520	41.1	39.6	14.3	14.1	50.9	50.5
530	41.4	39.9	15.1	14.9	50.8	50.5
540	41.5	40	14.7	14.5	50.6	50.4
550	41.6	40	13	12.9	50.4	50.2
560	41.7	40.1	11	10.8	50.2	50
570	41.7	40.2	9.5	9.4	50	49.7
580	41.7	40.2	8.9	8.8	49.7	49.5
590	41.6	40	8.5	8.4	49.5	49.3
600	41.4	39.8	8.3	8.11	49.2	49
610	41.1	39.5	8	7.9	48.9	48.8
620	40.7	39.1	8.1	8	48.6	48.5
630	40.4	38.8	8.8	8.6	48.5	48.3
640	40.1	38.4	9.7	9.5	48.2	48.2
650	39.7	38.1	10.6	10.4	48	48
660	39.5	37.8	11.1	10.8	47.9	47.8
670	39.2	37.5	10.8	10.6	47.9	47.6
680	38.9	37.2	10	9.8	47.5	47.5
690	38.6	36.9	9.4	9.2	47.3	47.3
700	38.3	36.5	9.4	9.2	47.2	47.1

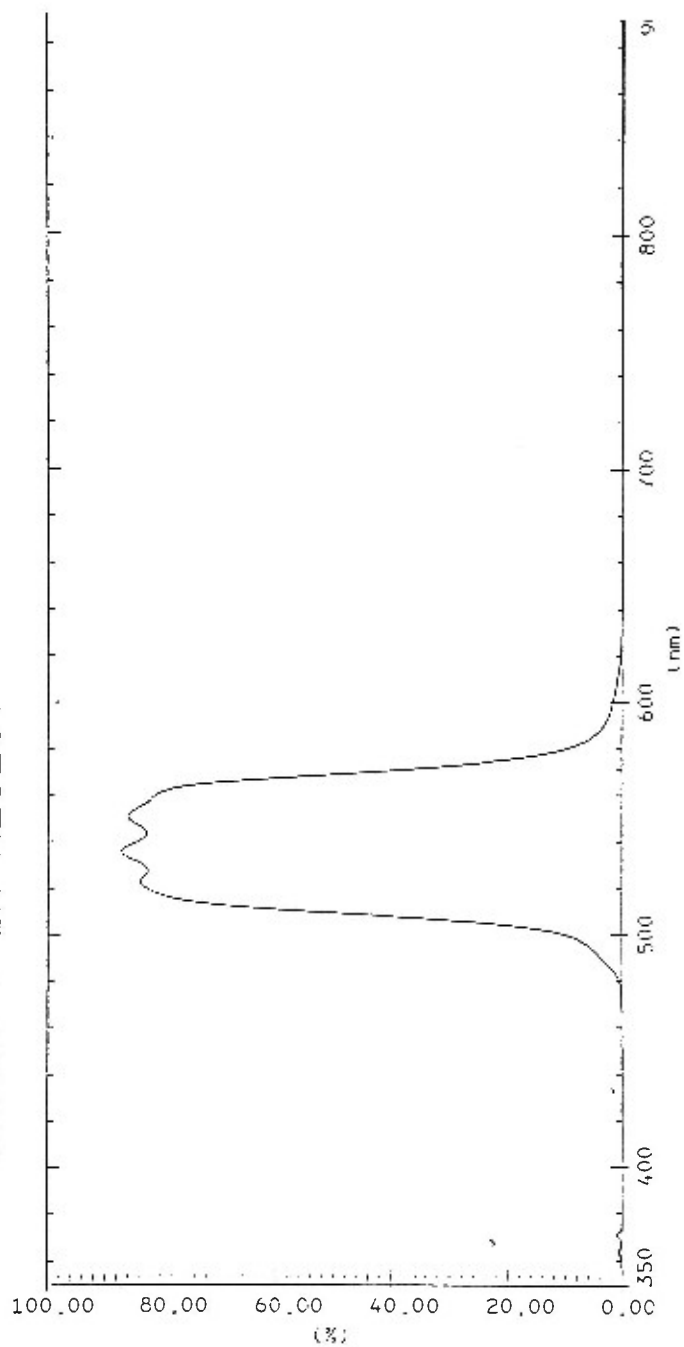
SCI is with specular reflection included.
 SCE is with specular reflection excluded.

***** Appendix 4 *****
Equipment
***** 4.a *****

Transmission Plots of Filters used to Collect Truth Data

(see following pages)

GREEN + IR REJECT



SAMPLE : 1
CONC. :

COMMENT :

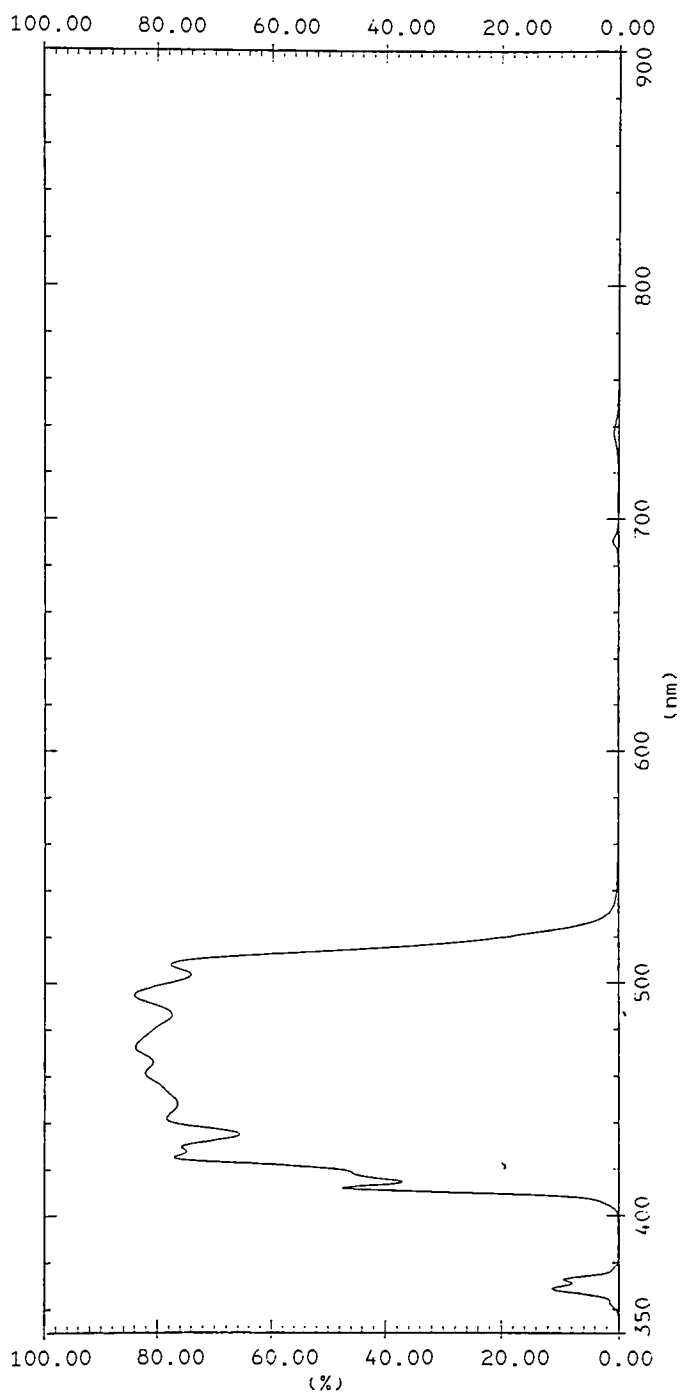
REFERENCE :
PATHLENGTH :

SPEED : MID.
DATE :

ANALYST :

SLIT :

BLUE + IR REJECT

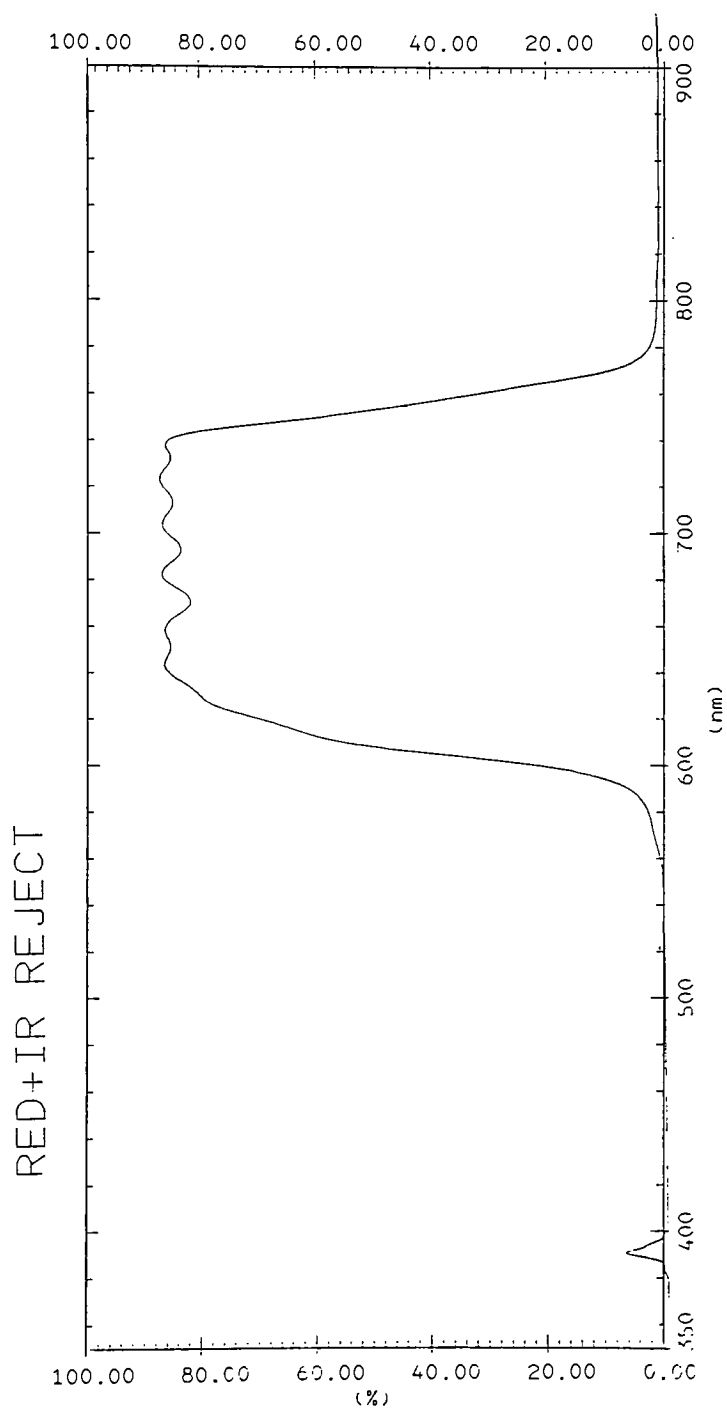


SAMPLE : T
CONC. :

COMMENT :

REFERENCE :
PATHLENGTH :

SPEED : MID.
DATE :
ANALYST :
SLIT : 2.0



SLIT : 2.0

SPEED : MID.

REFERENCE :

DATE :

ANALYST :

SAMPLE : T

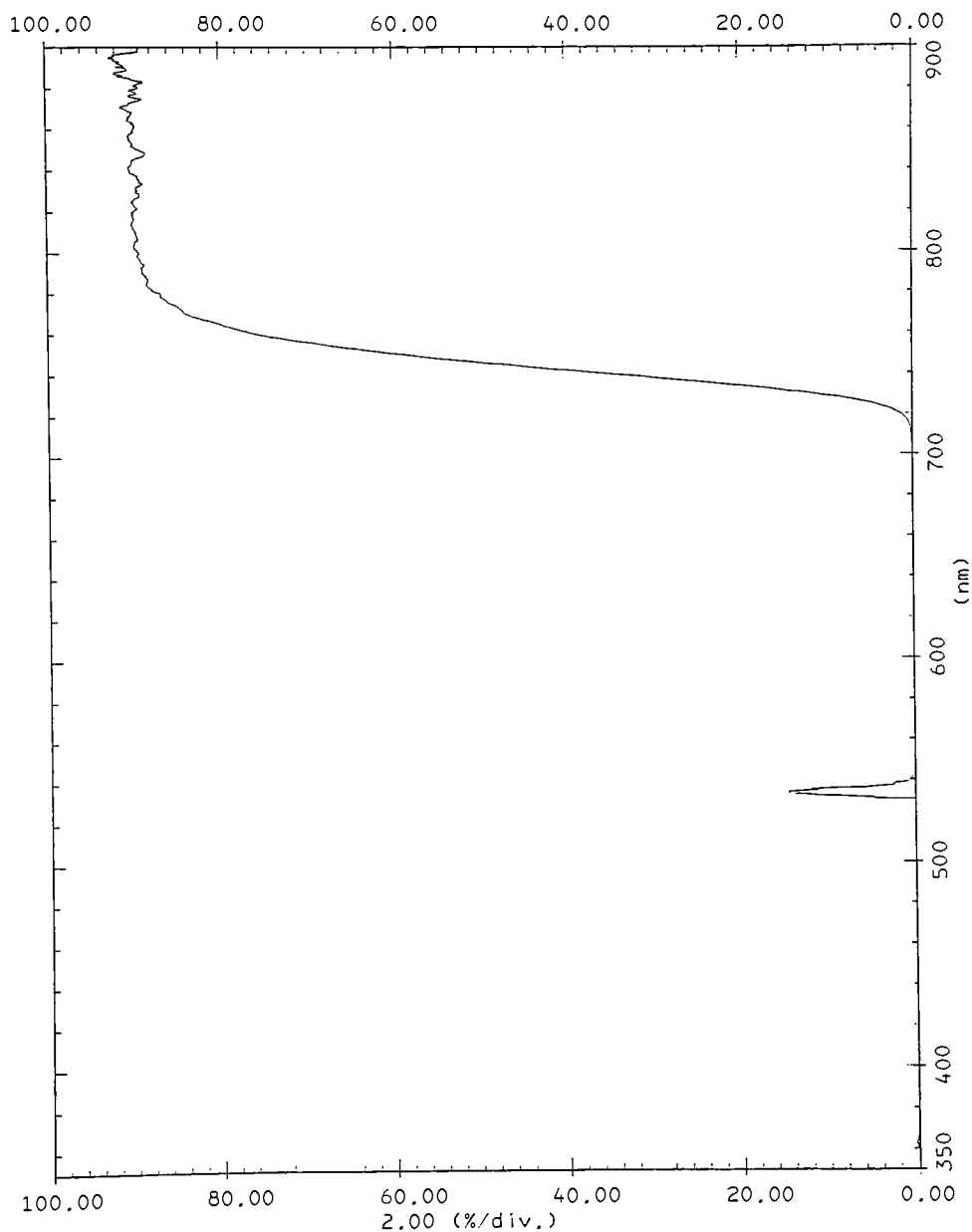
WLENGTH :

WINT :

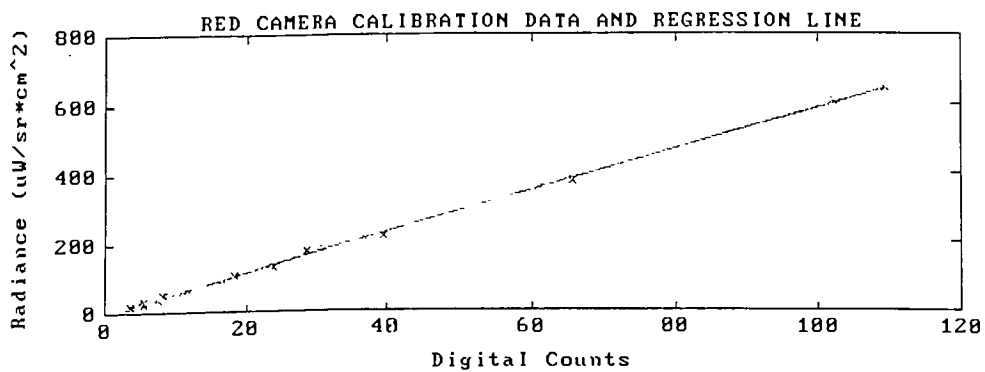
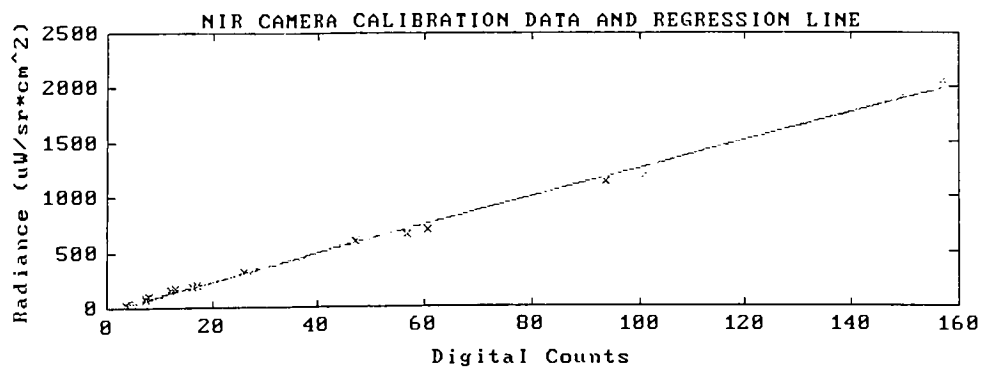
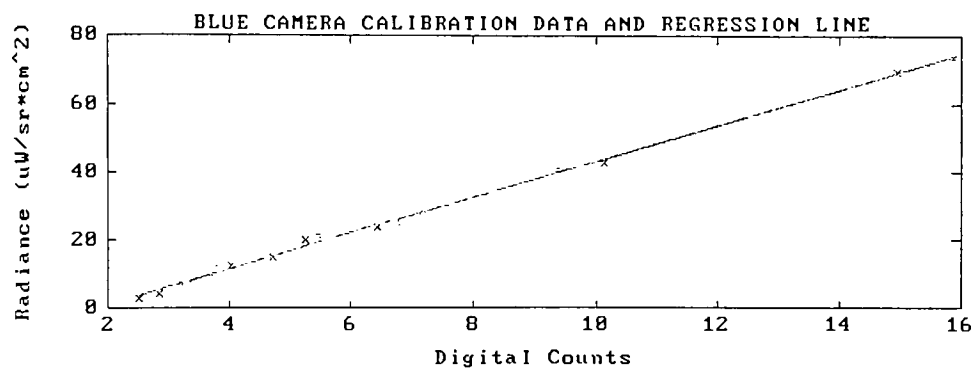
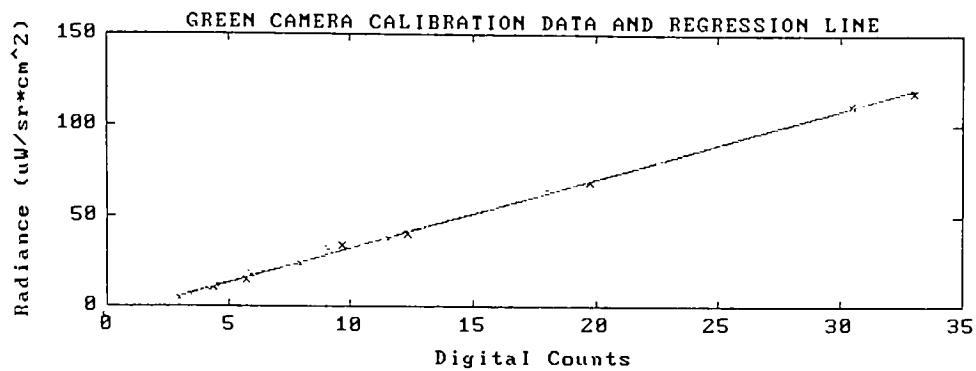
SCALE (nm/div.) SPEED SLIT (nm) REPEAT T (sec) N
20.0 FAST 5.0 0 1

MEASURE MODE ; T%

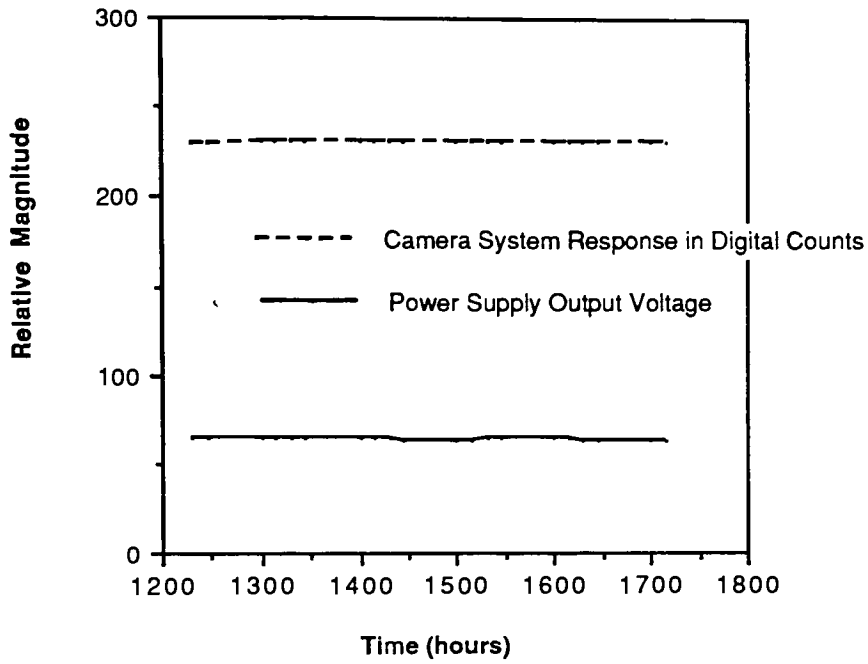
DATE & TIME ; 23:46:54 07/20 '92



SAMPLE NAME ; MIR



Camera Stability Test (Every 15 minutes for 5 hours)



TIME	POWER	CAMERA
1230.000	63.920	229.986
1245.000	63.858	230.422
1300.000	63.819	230.549
1315.000	63.837	230.910
1330.000	63.788	230.845
1345.000	63.806	231.062
1400.000	63.793	231.221
1415.000	63.761	230.900
1430.000	63.695	230.853
1445.000	63.654	230.959
1500.000	63.620	231.117
1515.000	63.619	231.196
1530.000	63.726	231.475
1545.000	63.775	231.124
1600.000	63.714	230.574
1615.000	63.665	230.533
1630.000	63.637	230.599
1645.000	63.612	230.661
1700.000	63.568	230.664
1715.000	63.538	230.573

***** Appendix 5 *****
 Other
 ***** 5.a *****

Modified Algorithm
 as Implemented with Two-Pass Method

The emissivities are not treated correctly. They were included only to remind the software engineer (Dr Salvaggio) where they should be placed in the algorithm. They have no effect in the visible region.

$$L = \left\{ I_{Diffuse} \frac{\epsilon_{ST}(\theta) + \epsilon_{DT}(\theta)}{2} L_T + \right. \\
\left[I_S I_T \frac{E_S}{\pi} \tau_1 \cos(\theta_S) + I_{Diffuse} F(L_{DE} + L_{DS}) + (1 - I_{Diffuse})(1 - I_{SH}) [L_{DL}(\phi, \theta_{SK}) + L_{DS}(\phi, \theta_{SK})] + \right. \\
\left. I_{SH} (1 - I_{Diffuse} F) \left(\frac{\epsilon_{SB}(\theta_{BT}) + \epsilon_{DB}(\theta_{BT})}{2} L_{TB} + \left[I_B \frac{E_S}{\pi} \tau_1 \cos(\theta_B) + F(L_{DE} + L_{DS}) \right] [1 - \epsilon_{DB}(\theta_{BT})] \right) \right] \\
\left. \left((1 - I_{Diffuse}) [1 - \epsilon_{ST}(\theta)] + I_{Diffuse} [1 - \epsilon_{DT}(\theta)] \right) \right\} \tau_2(\theta_E) + I_{Diffuse} [L_{uE}(\theta_E) + L_{uS}(\theta_E)]$$

where

$$I_{Diffuse} = \begin{cases} 1 & \text{for diffuse pass,} \\ 0 & \text{for specular pass} \end{cases}$$

$$I_{SH} = \begin{cases} 1 & \text{for diffuse pass,} \\ 1 \text{ or } 0 & \text{for specular pass depending on background hit(1) / miss(0) status} \end{cases}$$

$$I_T = \begin{cases} 1 & \text{for diffuse pass,} \\ 1 \text{ or } 0 & \text{for specular pass depending on solar disk hit(1) / miss(0) status} \end{cases}$$

***** Appendix 5 *****
Other
***** 5.b *****

Partial Derivatives of Radiance Equation For Error Analysis

NOTE: The partials from an early version of the equation were actually used. The earlier version is listed below and its partial derivatives are on the next page. The equations are actually identical if the different flags are set correctly.

$$L = \left\{ \left[(E_s/\pi) I'_s \tau_1 \cos\theta_s + L_d(\theta_{sky}) \tau_{bsp} + ((E_s/\pi) I'_b \tau_1 \cos\theta_b + F L_{dsky}) R_{db}(\theta_{bt}) (1 - \tau_{bsp}) \right] R_s(\theta_v) \right. \\
+ \left. \left[(E_s/\pi) I'_t \tau_1 \cos\theta_s + F L_{dsky} + (1-F) ((E_s/\pi) I'_b \tau_1 \cos\theta_b + F L_{dsky}) R_{db}(\theta_{bt}) \right] R_d(\theta_v) \right\} \tau_2(\theta_v) \\
+ L_u(\theta_v)$$

$R_s(\theta_v)$	specular component of the angular dependent reflectivity
$R_d(\theta_v)$	diffuse component of the angular dependent reflectivity
$R_{db}(\theta_{bt})$	diffuse component of the angular dependent reflectivity of the background
L	spectral radiance reaching front of the sensor
L_{dsky}	downwelled spectral radiance due to scattering integrated over the skydome
$L_d(\theta_{sky})$	directional downwelled spectral radiance due to scattering
$L_u(\theta_v)$	upwelled spectral radiance due to scattering along the target-sensor path
E_s/π	exoatmospheric solar spectral radiance
τ_1	atmospheric spectral transmission along the source - target path
$\tau_2(\theta_v)$	atmospheric spectral transmission along the target-sensor path
τ_{bsp}	transmission of an object in the target-sky specular bounce direction
I'_t	target sun/shadow flag (1 or 0)
I'_b	background sun/shadow flag (1 or 0)
I'_s	specular incidence/sun intersection flag (1 or 0)
F	shape factor, the fraction of the exposed skydome
θ_s	angle between the normal to the surface and the sun-target path
θ_{sky}	angle between the normal to the earth and the specularly reflected ray from the sensor to target cast.
θ_b	angle between the normal to the background and the target hit point
θ_{bt}	angle between the normal to the background and the target hit point
θ_v	angle between the normal to the earth at the target and the sensor-target path

$$L = \left[\left[\left(\frac{E_s}{\pi} \right) \cdot l_s \cdot \tau_1 \cdot \cos(\theta_s) + L_{ddir} \cdot \tau_{bsp} + \left[\left(\frac{E_s}{\pi} \right) \cdot l_b \cdot \tau_1 \cdot \cos(\theta_b) + F \cdot L_{dhem} \right] \cdot R_{db} \cdot (1 - \tau_{bsp}) \right] \cdot R_s + \left[\left(\frac{E_s}{\pi} \right) \cdot l_l \cdot \tau_1 \cdot \cos(\theta_s) + F \cdot L_{dhem} + (1 - F) \cdot \left[\left(\frac{E_s}{\pi} \right) \cdot l_b \cdot \tau_1 \cdot \cos(\theta_b) + F \cdot L_{dhem} \right] \cdot R_{db} \right] \cdot \tau_2 + L_u \right]$$

$$dL_{dEs} = \left[l_s \cdot \cos(\theta_s) + l_b \cdot \cos(\theta_b) \cdot R_{db} \cdot (1 - \tau_{bsp}) \right] \cdot R_s + \left[l_l \cdot \cos(\theta_s) + \frac{(1 - F)}{\pi} \cdot l_b \cdot \cos(\theta_b) \cdot R_{db} \right] \cdot R_d \cdot \tau_2 \quad ; \quad \text{Actually } dL_d \frac{E_s \tau_1}{\pi}$$

$$dL_{d\theta_s} = \left(\frac{E_s}{\pi} \cdot l_s \cdot \tau_1 \cdot \sin(\theta_s) \cdot R_s - \frac{E_s}{\pi} \cdot l_l \cdot \tau_1 \cdot \sin(\theta_s) \cdot R_d \right) \cdot \tau_2$$

$$dL_{dL_{dir}} = \tau_{bsp} \cdot R_s \cdot \tau_2$$

$$dL_{d\theta_b} = \left[\frac{E_s}{\pi} \cdot l_b \cdot \tau_1 \cdot \sin(\theta_b) \cdot R_{db} \cdot (1 - \tau_{bsp}) \cdot R_s - (1 - F) \cdot \frac{E_s}{\pi} \cdot l_b \cdot \tau_1 \cdot \sin(\theta_b) \cdot R_{db} \cdot R_d \right] \cdot \tau_2$$

$$dL_{dF} = \left[L_{dhem} \cdot R_{db} \cdot (1 - \tau_{bsp}) \cdot R_s - \left[L_{dhem} - \left(\frac{E_s}{\pi} \cdot l_b \cdot \tau_1 \cdot \cos(\theta_b) + F \cdot L_{dhem} \right) \cdot R_{db} + (1 - F) \cdot L_{dhem} \cdot R_{dl} \right] \cdot R_d \right] \cdot \tau_2$$

$$dL_{dL_{dhem}} = (F \cdot R_{db} \cdot (1 - \tau_{bsp}) \cdot R_s - (F + (1 - F) \cdot F \cdot R_{db}) \cdot R_d) \cdot \tau_2$$

$$dL_{dR_{db}} = \left[\left(\frac{E_s}{\pi} \cdot l_b \cdot \tau_1 \cdot \cos(\theta_b) + F \cdot L_{dhem} \right) \cdot (1 - \tau_{bsp}) \cdot R_s - (1 - F) \cdot \left(\frac{E_s}{\pi} \cdot l_b \cdot \tau_1 \cdot \cos(\theta_b) + F \cdot L_{dhem} \right) \cdot R_d \right] \cdot \tau_2$$

$$dL_{dR_s} = \left[\frac{E_s}{\pi} \cdot l_s \cdot \tau_1 \cdot \cos(\theta_s) + L_{ddir} \cdot \tau_{bsp} + \left(\frac{E_s}{\pi} \cdot l_b \cdot \tau_1 \cdot \cos(\theta_b) + F \cdot L_{dhem} \right) \cdot R_{db} \cdot (1 - \tau_{bsp}) \right] \cdot \tau_2$$

$$dL_{dR_d} = \left[\frac{E_s}{\pi} \cdot l_l \cdot \tau_1 \cdot \cos(\theta_s) - F \cdot L_{dhem} + (1 - F) \cdot \left(\frac{E_s}{\pi} \cdot l_b \cdot \tau_1 \cdot \cos(\theta_b) + F \cdot L_{dhem} \right) \cdot R_{db} \right] \cdot \tau_2$$

$$dL_{d\tau_2} = \left[\frac{E_s}{\pi} \cdot l_s \cdot \tau_1 \cdot \cos(\theta_s) + L_{ddir} \cdot \tau_{bsp} + \left(\frac{E_s}{\pi} \cdot l_b \cdot \tau_1 \cdot \cos(\theta_b) + F \cdot L_{dhem} \right) \cdot R_{db} \cdot (1 - \tau_{bsp}) \right] \cdot R_s + \left[\frac{E_s}{\pi} \cdot l_l \cdot \tau_1 \cdot \cos(\theta_s) + F \cdot L_{dhem} + (1 - F) \cdot \left(\frac{E_s}{\pi} \cdot l_b \cdot \tau_1 \cdot \cos(\theta_b) + F \cdot L_{dhem} \right) \cdot R_{db} \right] \cdot R_d$$

$$dL_{dLu} = 1$$